To my parents

STUDIES OF THE OPTICAL CONSTANTS OF SOME RARE EARTH FILMS

by

WASIMUL HASAN

A thesis submitted for the degree of Doctor of Philosophy in the University of London

Department of Physics,
Royal Holloway College.

February 1975

A B S T R A C T

The electronic band structures of some rare earth metals have been investigated by optical reflection spectroscopy. Newly developed optimization methods have been used on specimens produced in vacuo and measured by means of a reflectometer constructed in laboratory.

Optical properties of these rare earth films have also been studied as a function of ageing. The results have been compared with a model based on the growth of dielectric layers on the film surface.

The electronic band structure of iron has also been investigated by observing and measuring optical and magneto-optical properties.

CONTENTS

CHAPTER I

THE ROLE OF OPTICAL AND MAGNETO-OPTICAL CONSTANTS IN SOLID STATE PHYSICS.

1.1. Introduction

Optics is concerned with the interaction of electromagnetic waves with matter. This interaction forms one of the fundamental and continuing concerns of Physics, and is the basis of innumerable technical devices. Maxwell's electromagnetic theory provides a basic description of the interaction, and leads to relationships between the behaviour of electromagnetic waves in a medium and the properties of that medium.

Studies of the optical properties of metals as a function of frequency provide valuable information about their electronic band structure.

1.2. Interaction of the Electromagnetic Waveswith the Medium

The Maxwell's macroscopic equations for a source-free and isotropic medium can be written as

$$\begin{aligned} \nabla . \vec{E} &= 0 \\ \nabla \times \vec{E} &= - \frac{\mu}{c} \frac{\partial \vec{H}}{\partial t} \\ \nabla . \vec{H} &= 0 \\ \nabla \times \vec{H} &= \frac{\epsilon}{c} \frac{\partial \vec{E}}{\partial t} + \frac{4\pi\sigma}{c} \vec{E} \end{aligned} \qquad (1.1.)$$

where

E is the electric field,

H is the magnetic field,

μ is the magnetic permeability,

c is the velocity of light in vacuo,

ϵ is the dielectric Constant,

and σ is the conductivity.

Using the vector identity

$$\nabla \times (\nabla \times \vec{E}) = \nabla(\nabla . \vec{E}) - \nabla^2 . \vec{E} \qquad (1.2.)$$

and equations (1.1.), we get the equation for a plane wave propagating in an energy-absorbing medium:

$$\nabla^2 . \vec{E} = \frac{\epsilon \mu}{c^2} \cdot \frac{\partial^2 \vec{E}}{\partial t^2} + \frac{4\pi\sigma\mu}{c^2} \frac{\partial \vec{E}}{\partial t} \qquad (1.3.)$$

The solutions are necessarily restricted to transverse plane waves because $\nabla . \vec{E} = 0$ in the absence of a net charge density. The conductivity which appears in equation (1.3) should be called the optical conductivity. This is because the energy absorption with which we are concerned is that arising from electronic transitions accompanying photon absorption. These transitions correspond to a transverse current density that does not include the conventional current such as is obtained with a battery connected across the sample. The latter is a longitudinal current, it originates from a longitudinal electric field which is derivable from a scalar potential function.

Since experiments on optical properties of solids are usually conducted with monochromatic light, we shall consider first the propagation of a single plane wave within an isotropic medium. Anticipating that the wave vector must be complex to describe energy dissipation of the wave, we write

$$\vec{E} = \vec{E}_o \exp i\,(\omega.t - \vec{q}.\vec{r}) \qquad (1.4)$$

where $\vec{E}_o$ is perpendicular to the wave vector $\vec{q}$. We may assume a sinusoidal (plane wave) variation of $\vec{E}$ only in a region large compared with the lattice constant. This is possible and quite satisfactory for a theory of the optical properties of solids, but it is not suitable for the x-ray region.

Substituting eq.(1.4) into (1.3), we find

$$\tilde{q}^2 = \mu \frac{\omega^2}{c^2} \left(\epsilon - i \frac{4\pi\sigma}{\omega} \right) \qquad (1.5)$$

We now define a complex refractive index $\tilde{n}$ such that

$$\tilde{q} = \left(\frac{\omega}{c}\right) \tilde{n} = \frac{\omega}{c} (n - ik) \qquad (1.6)$$

where n is the refractive index and k is the extinction coefficient. Now we can rewrite equation (1.4) as

$$\vec{E} = \vec{E}_o \left[\exp - \left(\frac{\omega}{c} \vec{k}.\vec{r} \right)\right] \exp\text{-}i \left(\frac{\omega}{c} \vec{n}.\vec{r} - \omega t\right) \qquad (1.7)$$

The first exponential factor in equation (1.7) describes the attenuation of wave amplitude with distance. The absorption coefficient, which describes the fractional decrease in intensity with distance, is defined as

$$\alpha = - \frac{1}{I} \frac{dI}{dr} \qquad (1.8)$$

where I is the intensity. Since the intensity is proportional to the square of the wave amplitude, we find from Eqs. (1.7) and (1.8) that

$$\alpha = \frac{2\omega k}{c} = \frac{4\pi . k}{\lambda} \qquad (1.9)$$

where λ is the wavelength of the light in vacuo.

The second exponential factor in eq. (1.7) describes a wave travelling with phase velocity $\frac{c}{n}$, hence the identification of n as the refractive index.

Equations (1.5) and (1.6) can be used to obtain the expressions for ϵ and σ in terms of n and k. Thus,

$$\epsilon = (n^2 - k^2)/\mu \qquad (1.10)$$

$$\sigma = \frac{nk}{\mu} \quad \frac{\omega}{2\pi} = \frac{nk\nu}{\mu} \qquad (1.11)$$

Sometimes it is convenient to use a complex dielectric function defined as

$$\tilde{\epsilon} = \epsilon_1 - i\epsilon_2 = \frac{\tilde{n}^2}{\mu} \qquad (1.12)$$

where ϵ_1, is the old ϵ of eq. (1.10), the ϵ that appears in the usual versions of Maxwell's equations when the properties of the medium are included. Thus

$$\epsilon_1 = (n^2 - k^2)/\mu \qquad (1.13)$$

$$\epsilon_2 = 2nk/\mu \qquad (1.14)$$

(μ can be taken as unity at optical frequencies).

1.3. Transverse Kerr Effect and Magneto-Optical Parameters

The effect on the state of polarisation of light reflected

from a ferromagnetic mirror in the presence of magnetic field, whose magnetising vector is parallel to the surface of the mirror and perpendicular to the plane of incidence is known as transverse Kerr effect.

A macroscopic discussion of magneto-optical effects in a ferromagnetic can be based on the general differential equations for the electromagnetic field

$$\frac{1}{c}\frac{\partial \vec{B}}{\partial t} = -\operatorname{curl}\vec{E} \qquad (1.15)$$

$$\frac{1}{c}\frac{\partial \vec{D}}{\partial t} = \operatorname{curl}\vec{H} \qquad (1.16)$$

and the tensor equations

$$\vec{D} = \epsilon.\vec{E} \qquad (1.17)$$

$$\vec{B} = \mu.\vec{H} \qquad (1.18)$$

where ϵ and μ are the permittivity and the magnetic permeability tensors of the magnetised ferromagnetic metal.

The permittivity tensor of a magnetised ferromagnetic can be constructed on the basis of induced anisotropy. An isotropic magnetised medium may be regarded as a birefringent crystal whose optical properties are determined by the permittivity tensor. Without loss of generality, it may be supposed that the magnetisation vector (residual magnetisation, or the magnetisation 'produced' by the external field) is parallel to z-axis. All planes passing through this special direction are equivalent. It follows that the permittivity tensor of a magnetised ferromagnetic must be cylindrically symmetrical, i.e.

$$\epsilon = \begin{bmatrix} \tilde{\epsilon} & -i\tilde{\epsilon}\tilde{Q} & 0 \\ i\tilde{\epsilon}\tilde{Q} & \tilde{\epsilon} & 0 \\ 0 & 0 & \tilde{\epsilon}_o \end{bmatrix} \qquad (1.19)$$

where $\tilde{\epsilon}$ is the complex permittivity defined by equation (1.12) and $\tilde{Q} = Q_1 - iQ_2$ is a complex magneto-optical parameter which is a function of magnetisation of the body. At optical frequencies, $\tilde{\epsilon}_o = \tilde{\epsilon}$, for metals for which there is little observed anisotropy of the ordinary optical properties (Krinchik and Chetkin (1959); Martin, Neal and Dean (1965), Erskine and Stern (1973) etc.).

Some scientists, e.g. Martin, Neal and Dean (1965); Ferguson and Romagnoli (1969), use $\tilde{\epsilon}' = \epsilon_1' - i\epsilon_2'$ as a magneto-optical parameter which is related to Q by the equation

$$\tilde{\epsilon}' = \tilde{\epsilon}.\tilde{Q} \qquad (1.20)$$

Thus

$$\epsilon_1' = \epsilon_1 Q_1 - \epsilon_2 Q_2 \qquad (1.21)$$

$$\epsilon_2' = \epsilon_1 Q_2 + \epsilon_2 Q_1 \qquad (1.22)$$

ϵ_1 and ϵ_2 are defined by equation (1.13) and (1.14).

An expression similar to (1.19) can be written for the magnetic permeability tensor, by assuming that the medium is not only electrically but also magnetically anisotropic. But it has been shown (Krinchik and Chetkin, 1959) that ferromagnetic metals at optical frequencies possess gyroelectic properties whereas at superhigh frequencies (centimeter range) these possess gyromagnetic properties. However, both properties must be taken into account in the intermediate region.

Sometimes it is convenient to describe the magneto-optical effects by relating them to a conductivity tensor, which for a solid with cubic or greater symmetry (Erskine and Stern, 1973), and magnetisation $\vec{M}$ along z-direction can be written in the form

$$\tilde{\sigma}(\vec{M}) = \begin{bmatrix} \tilde{\sigma}_{xx} & -i\tilde{\sigma}_{xy} & 0 \\ i\tilde{\sigma}_{xy} & \tilde{\sigma}_{xx} & 0 \\ 0 & 0 & \tilde{\sigma}_{xx} \end{bmatrix} \qquad (1.23)$$

The conductivity $\tilde{\sigma}$ is related to the commonly used dielectric constant $\tilde{\epsilon}$ by

$$\sigma_{ij} = \frac{\omega}{4\pi} (\tilde{\epsilon}_{ij} - \delta_{ij}) \qquad (1.24)$$

where $\delta_{ij} = 1$ for $i = j$

$= 0$ for $i \neq j$

The imaginary component σ_{xx}^{i} of $\tilde{\sigma}_{xx}$, represents the absorptive part which describes ordinary optical absorption and is the same quantity as given by equation (1.11). The imaginary component σ_{xy}^{i} of σ_{xy} represents the magneto-optical Kerr effect absorptive part. The real components σ_{xx}^{r} and σ_{xy}^{r} represent the dispersive parts.

1.4. Band Structure Calculations

The electronic band structure describes the energy-momentum relationship of electrons in a material in terms of the distribution of their wave vectors throughout the reciprocal lattice of the crystal structure. The calculation of electronic band structures is very

much a specialist task and the techniques employed have been reviewed by Kittel (1963), Slater (1965), Harrison (1970) and Pincherle (1971). The calculations are necessarily approximate since the results will depend on many-body effects and these must be handled in an average sense.

Ideally one would like to calculate band structure of metals from first principles, i.e. setting up of the one- electron Hamiltonian, containing a potential representing the effect of all the electrons in the material, including exchange effects, and the solution of the corresponding Schrodinger equation, using an absolute minimum of experimental information. Unfortunately, many of the quantities, such as effective masses, detailed shape of the Fermi surface of metals, are sensitive to variations in the wavefunctions used, whatever these are, so that the ideal aim has never been completely achieved, and only a combination of theory and experiment can lead to the elucidation of all the details of a band structure. For a completely theoretical band structure to be accurate, total self- consistency must be achieved, electron-electron and electron-phonon interactions must be included, relativistic effects must be considered. The difficulty of the problem is illustrated by the many precise and careful calculations that have had little quantitative success.

On the other hand, with an empirical band model, there is always the danger that it is fitted to an incorrect or incomplete interpretation of experimental results, besides the possibility of

experimental errors. However, between the two extremes of purely "first principles" calculations and purely empirical band models there is ample room for intermediate treatments (Herman et al. 1967), and these empirically adjusted first principles calculationscan be very useful.

More recently relativistic orthogonalised plane wave (OPW) (Soven 1965) and augmented plane wave (APW)(Loucks 1965) calculations have been made using solutions of the Dirac equation (Rose 1961) and have given results which agree favourably with existing experimental data. For rare earths the relativistic augmented plane wave method (RAPW) has exclusively been employed (Loucks 1967).

1.5. Interpretation of Optical Data in Terms of Electronic Band Structure

When light of sufficient energy is incident on a material, it induces transitions of electrons from occupied states below the Fermi energy to unoccupied states above the Fermi energy. Clearly, a quantitative study of these transitions must provide some understanding of the initial and final states for the transitions and hence some knowledge of the band structure.

The most common experiments consist of shining a beam of monochromatic light onto a sample and calculating optical constants by measuring the fraction of the incident beam that is transmitted or reflected (Heavens, 1955).

A very general expression relates the optical conductivity to the electron states throughout Brillouin zones(Kubo, 1957), (Greenwood, 1958). In general we do not know all these states, and any experimental results depend strongly on the properties of the optical surface and other effects not accounted for in the Kubo-Greenwood formula. For these reasons it is not considered worthwhile to attempt comparisons between experimental data and the Kubo-Greenwood formula. Since the optical constants determined by different workersare not generally in good numerical agreement (see, for example Section 6.3.2), it is the shape of the optical conductivity dispersion curve which ought to be interpretable in terms of electronic band structure. We would expect that electron transitions will cause an increase in the optical conductivity.

We will interpret our results using the assumption (Miller, Julien and Taylor, 1974) that structures in optical conductivity curve occur due to vertical transitions in the Brillouin zone and the energies at which these structures occur correspond to energy gaps at symmetry interband points, where the joint density of states between the bands is high. The shape of the optical conductivity curve may be determined by one or more non $\vec{k}$-conserving processes (indirect transitions).

1.6. Interpretation of Magneto-Optical Data in Terms of Electronic Band Structure

The most important result of the band theory of ferromagnetism is that the exchange forces give rise to a relative shift of energy

bands for electrons with opposite spins, and therefore there is an excess of electrons in one of the spin directions.

As mentioned in Section 1.3 that ferromagnetic metals possessgyroelectric properties at optical frequencies, i.e. the interaction between the electro-magnetic radiation and the sample is through the $\vec{E}$ field only, and not through $\vec{H}$ field (because, for a magnetic interaction, a gyrotropic magnetic permeability tensor would be required). This is confirmed by the experimental observation of zero transverse Kerr reflectivity difference for the incident beam polarized with $\vec{E}$ field parallel to the spontaneous magnetisation $\vec{M}$ ($\vec{E}$ field perpendicular to the plane of incidence).

The $\vec{E}$ field can act directly only on the orbital or translational motions of the electrons, not on their spins. On the other hand, the spontaneous magnetisation $\vec{M}$ is predominantly due to the spin moments of unpaired electrons. It is spin-orbit coupling which presumably provides the interaction between $\vec{M}$ and $\vec{E}$ field, leading to magneto-optical effects.

Erskine and Stern (1973) obtained an expression for the off-diagonal absorptive component of $\tilde{\sigma}$, which can be written as

$$\omega \sigma_{xy}^{i}(\omega) = \frac{\pi e^2}{4\pi m^2} \quad \overline{F}(\omega).\, J(\omega) \qquad (1.25)$$

where $\overline{F}(\omega)$ is average matrix element and $J(\omega)$ is the joint density of states.

If we assume $\overline{F}(\omega)$ is constant independent of ω , then the quantity $\omega \sigma_{xy}^{i}$ is directly proportional to the joint density of states in the solid.

We will compare our experimental curve of $\omega\sigma_{xy}^{i}(\omega)$ with the joint density of states curve based on the band structure calculation and will interpret our results using the following assumptions:

(a) The general shape of the curve will be given by the joint density of states curve.

(b) Any structure in the experimental curve already predicted by joint density of states curve will be due to indirect transitions (in an indirect transition, wave vector $\vec{k}$ is not conserved and we assume that all the matrix elements are constant and equal).

(c) Any structure in the experimental curve not predicted by joint density of states curve could be due to direct transitions (in a direct transition, wave vector $\vec{k}$ is conserved and we assume that non-zero optical matrix elements are constant and equal).

CHAPTER II

METHODS OF DETERMINING OPTICAL AND MAGNETO-OPTICAL CONSTANTS

2.1. Introduction

The optical constants of absorbing materials can be determined by measurements on light transmitted through thin films, by measurements on light reflected from thin films or bulk specimens, or by a combination of reflection and transmission measurements on suitably thin films. The reflection methods have been chosen for a detailed study because these are:-

(i) suitable for thick specimens,

(ii) recent work has made these methods computationally the most convenient, and

(iii) the Kerr effect involves the influence of changes in magnetization on the reflection of light.

The reflection methods can be divided into (a) Non-Polarimetric methods, which involve the measurements of changes in light intensity on reflection and (b) Polarimetric methods, which involve the measurements of changes in polarisation on reflection. These methods are discussed in this chapter.

2.2. The Fresnel Reflectance Equations

The generalised Fresnel equations can be written (Heavens, 1955)

$$r_{\parallel} = \frac{n_o \cos\gamma - \tilde{n} \cos\theta}{n_o \cos\gamma + \tilde{n} \cos\theta} \qquad (2.1)$$

$$r_{\perp} = \frac{n_o \cos\theta - \tilde{n} \cos\gamma}{n_o \cos\theta + \tilde{n} \cos\gamma} \qquad (2.2)$$

$$t_{\parallel} = \frac{2n_o \cos\theta}{n_o \cos\gamma + \tilde{n} \cos\theta} \qquad (2.3)$$

$$t_{\perp} = \frac{2n_o \cos\theta}{n_o \cos\theta + \tilde{n} \cos\gamma} \qquad (2.4)$$

where

$r_{\parallel}$ and $r_{\perp}$ are the ratios of the amplitudes of the electric vectors of the reflected beam to the incident beam for light polarised $\parallel$ and $\perp$ to the plane of incidence.

$t_{\parallel}$ and $t_{\perp}$ are the ratios of the amplitudes of the electric vectors of the transmitted beam to the incident beam, for light polarised $\parallel$ and $\perp$ to the plane of incidence.

n_o and $\tilde{n}$ are the refractive indices of the media on either side of the interface.

θ and γ are the angles of incidence and refraction respectively.

Using equations (2.1.), (2.2) and the following equations,

$$R_{\perp} = r_{\perp}^2 \qquad (2.5)$$

$$R_{\parallel} = r_{\parallel}^2$$

$$n_o \sin\theta = \tilde{n} \sin\gamma \quad \text{(Snell's law)}$$

$$n_o = 1 \quad \text{(for vacuo)}$$

$$\tilde{n} = n - ik,$$

the Fresnel reflectance equations for a thick absorbing medium can be written as

$$R_{\perp} = \frac{(Q - \cos\theta)^2 + P^2}{(Q + \cos\theta)^2 + P^2} \qquad (2.6)$$

$$R_{\parallel} = R_{\perp} \frac{(Q - \sin\theta \tan\theta)^2 + P^2}{(Q + \sin\theta \tan\theta)^2 + P^2} \qquad (2.7)$$

Where the parameters P and Q are given by

$$Q^2 - P^2 = n^2 - k^2 - \sin^2\theta \qquad (2.8)$$

$$QP = nk \qquad (2.9)$$

Reflectance is defined as the ratio of reflected to incident intensities, and a 'thick' specimen is one for which multiple reflections can be neglected.

2.3. Normal Incidence Method

In the case of normal incidence ($\theta = 0$) equations (2.6) and (2.7) lead to identical result

$$R_{\parallel} = R_{\perp} = R = \frac{(n-1)^2 + k^2}{(n+1)^2 + k^2} \qquad (2.10)$$

This equation allows the direct determination of n only for transparent materials ($k = 0$). For $k \neq 0$ we can write for the complex amplitude

$$r_{\parallel} = r_{\perp} = r = \frac{1 - (n - ik)}{1 + (n - ik)} = R^{\frac{1}{2}} e^{i\Delta} \qquad (2.11)$$

Here Δ describes the phase shift which the incident wave suffers upon reflection. Solving equations (2.10) and (2.11), we will get

$$n = \frac{(1 - R)}{1 + R + 2R^{\frac{1}{2}}\cos\Delta} \qquad (2.12)$$

and

$$k = \frac{2R^{\frac{1}{2}}\sin\Delta}{1 + R + 2R^{\frac{1}{2}}\cos\Delta} \qquad (2.13)$$

The dispersion relation between Δ at a particular frequency ω_0 and the measured reflectance may be expressed in the form (Bode, 1945).

$$\Delta(\omega_0) = \frac{1}{\pi}\int_0^{\infty} \ln\left|\frac{\omega+\omega_0}{\omega-\omega_0}\right| \frac{d}{d\omega}\left(\ln R_\omega^{\frac{1}{2}}\right) d\omega \qquad (2.14)$$

The phase shift can thus be calculated if R_ω is known over the entire spectral range, and from R and Δ the optical constants are obtained using equations (2.12) and (2.13). The sensitivity of this method has been discussed by Miller, Julien and Taylor (1971).

2.4. One Angle, Non-normal Incidence Method

The Fresnel reflectance equations (2.6) and (2.7) have been solved by Querry (1969). He made the substitutions

$$F = \frac{R_\perp + 1}{R_\perp - 1} \qquad (2.15)$$

$$G = \frac{R_{||} + 1}{R_{||} - 1} \qquad (2.16)$$

into equations (2.6) and (2.7), obtaining

$$Q = \frac{(F - G)\,\mathrm{Sin}\,\theta\,\cot 2\theta}{GF + (1 - F^2)\mathrm{Cos}^2\theta - 1} \qquad (2.17)$$

$$P^2 = -Q^2 - 2FQ\mathrm{Cos}\,\theta - \mathrm{Cos}^2\theta \qquad (2.18)$$

Since F and G are functions of the observables $R_\perp$ and $R_{||}$, P and Q can be calculated for a given θ. By substituting P and Q in equations (2.8) and (2.9), n and k can be obtained.

The optical constants are extremely sensitive to the values of $R_{||}$, $R_\perp$ and θ. Miller, Taylor and Julien (1970) investigated the shape of the boundary enclosing analytical solutions for n and k in terms of $R_\perp$, $R_{||}$ and θ and they found the optimum angle of incidence for experimental measurement to be 74°.

2.5. Two Angles Methods

The optical constants n and k of a bulk material can be

conveniently obtained from measurements of reflectance at two angles of incidence Θ_1 and Θ_2 . Let us suppose for a given angle of incidence that $F(R_\perp , R_{||})$ is an observable function of $R_\perp$ and $R_{||}$ such that, in the linear relationship

$$R_\perp = \alpha R_{||} + \beta , \qquad (2.19)$$

the constants α and β are derivable from $F(R_\perp , R_{||})$. If $F(R_\perp , R_{||})_1$ and $F(R_\perp , R_{||})_2$ are measured at Θ_1 and Θ_2 , then n and k may be obtained by the following procedure.

At angle Θ_1 :

$$R_\perp = \alpha_1 R_{||} + \beta_1 \qquad (2.20)$$

Sets of (n,k) pair are calculated, using the analytical solutions to Fresnel equations (Querry 1969), such that equation (2.20) is satisfied, and these values are used to calculate $F(R_\perp , R_{||})'_2$ at Θ_2 . Here, and subsequently, the calculated values are indicated by prime.

$$d = F(R_\perp , R_{||})'_2 - F(R_\perp , R_{||})_2 \qquad (2.21)$$

is then made arbitrarily small with respect to the (n,k) values generated by equation (2.20). In practice d will be slightly less than the precision to which $F(R_\perp , R_{||})$ can be measured.

Let us now discuss the special cases of equation (2.19) together with the equation

$$R_\phi = R_{||} \cos^2\phi + R_\perp \sin^2\phi \qquad (2.22)$$

where R_ϕ is the reflectance for plane polarized light measured for any fixed incident polarization azimuth ϕ with respect to the plane of incidence.

2.5.1. Reflectance Ratio Method

In this case

$$F(R_\perp, R_\parallel) = \frac{R_\perp}{R_\parallel} = \rho \quad , \text{ i.e. } \alpha = \frac{R_\perp}{R_\parallel} \text{ and } \beta = 0 \qquad (2.23)$$

This method has been discussed in detail by Miller, Julien and Taylor (1972). A flow chart for calculating n and k from two reflectance ratio measurements at θ_1 and θ_2 is shown in figure 1.

2.5.2. Total Reflectance Method

Here $\phi = \frac{\pi}{4}$ and

$$F(R_\perp, R_\parallel) = \frac{R_\perp + R_\parallel}{2} = R, \text{ i.e. } \alpha = -1, \beta = 2R \qquad (2.24)$$

If R_1 is the value of R for $\theta = \theta_1$, equation (2.21) becomes

$$R_\perp = -R_\parallel + 2R_1 \qquad (2.25)$$

i.e. a straight line in $(R_\perp, R_\parallel)$ space, with gradient -1 and intercept $2R_1$ on the $R_\perp$ axis. Possible values of n and k are calculated at equispaced points on this line, using the analytical solutions to the Fresnel reflectance equations. These values of n and k are then used to generate the line

$$R_\perp = -R_\parallel + 2R_2 \qquad (2.26)$$

for θ_2, and the calculation proceeds until $d = R_2' - R_2$ is made arbitrarily small. If the incident light is not completely depolarised, then equation (2.24) does not hold, and the parallel component of incident intensity may be written

$$I_{o\parallel} = C.I_{o\perp}$$

giving

$$R = \frac{R_\perp + CR_\parallel}{1 + C}$$

C may be determined in a preliminary calibration experiment. Alternatively, light linearly polarized with $\phi = \frac{\pi}{4}$ may be used

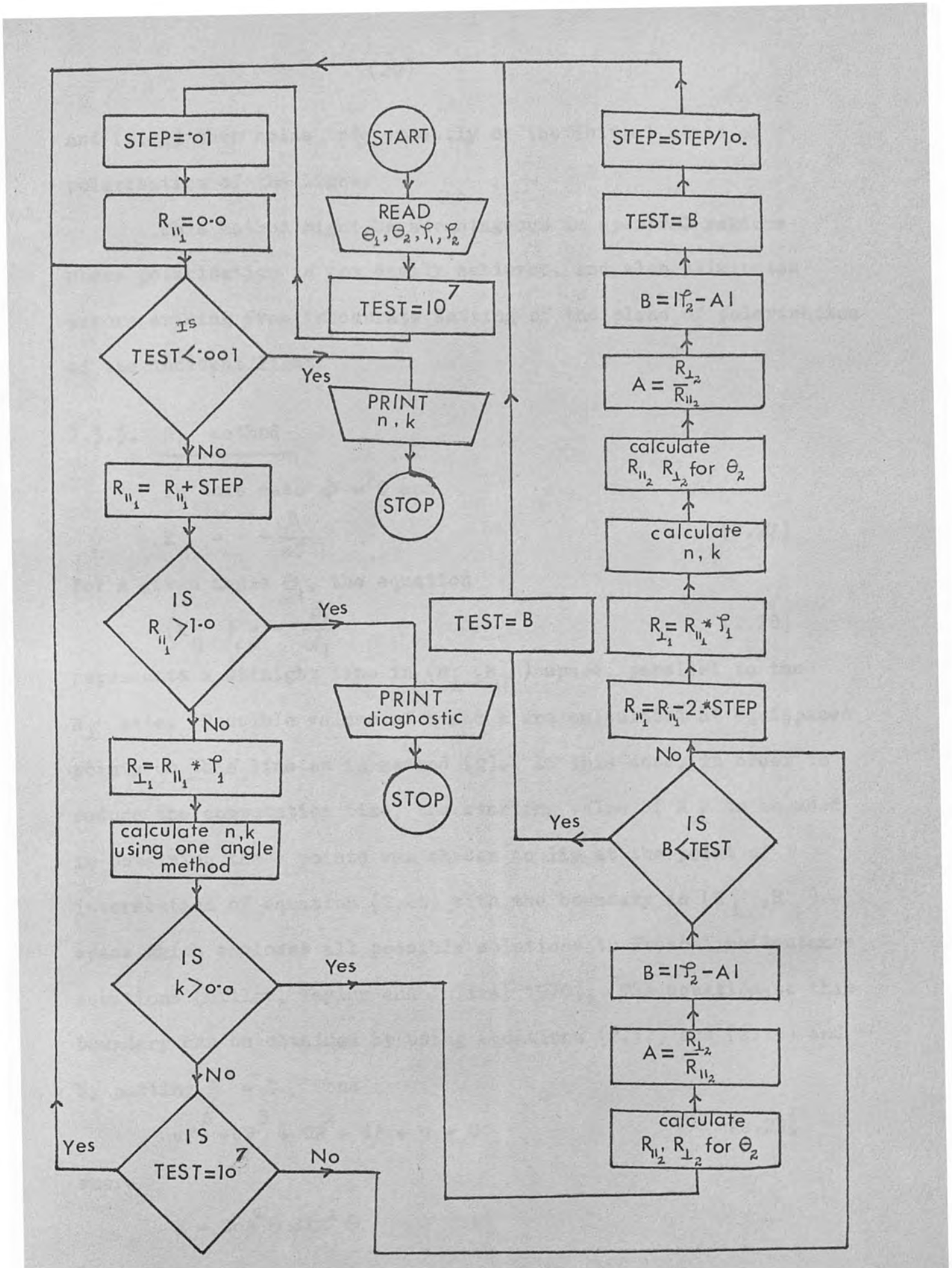

Figure 1: Flow chart of technique for determining n and k from two reflectance ratio measurements.

and (2.24) then holds independently of the initial state of polarisation of the light.

This method might be advantageous in spectral regions where polarisation is not easily achieved, and also eliminates errors arising from inaccurate setting of the plane of polarisation of the incident light.

2.5.3. $R_{||}$ method

In this case $\phi = 0$ and

$$R_{||} = -\frac{\beta}{\alpha} \qquad (2.27)$$

For a given angle θ_1, the equation

$$(R_{||})_1 = -\frac{\beta_1}{\alpha_1} \qquad (2.28)$$

represents a straight line in $(R_\perp, R_{||})$ space, parallel to the $R_\perp$ axis. Possible values of n and k are calculated at equispaced points on this line as in method (2). In this case, in order to reduce the computation time, the starting value of $R_\perp$ to be used in obtaining these points was chosen to lie at the point of intersection of equation (2.28) with the boundary in $(R_\perp, R_{||})$ space which encloses all possible solutions to Fresnel reflectance equations (Miller, Taylor and Julien, 1970). The equation to this boundary can be obtained by using equations (2.17) and (2.18) and by putting $P^2 = 0$. Thus

$$aF^4 + bF^3 + CF^2 + dF + e = 0 \qquad (2.29)$$

where

$$a = \cos^2\theta \sin^2\theta$$

$$b = -G$$

$$c = G^2 + \sin^4\theta + \cos^4\theta + \cot^2 2\theta$$

$$d = -G(1 + 2\,\mathrm{Cot}^2 2\theta)$$

$$e = G^2 \mathrm{Cot}^2 2\theta + \mathrm{Cos}^2\theta \mathrm{Sin}^2\theta$$

A computer subroutine is used to solve equation (2.29) and thus obtain the smallest real value of $R_\perp$, which is then used as the starting value for a series of steps in $R_\perp$ of 0.001, for which n and k are found. These values of n and k are then used to generate lines

$$(R_{||})_2 = -\frac{\beta_2}{\alpha_2} \qquad (2.30)$$

in $(R_\perp, R_{||})$ space, for the angle θ_2, until $d = (R_{||})_2' - (R_{||})_2$ becomes <0.001.

2.5.4. $R_\perp$ method

In this case $\phi = \frac{\pi}{2}$ and

$$R_\perp = \beta, \quad \alpha = 0 \qquad (2.31)$$

For a given angle θ_1, the equation

$$(R_\perp)_1 = \beta_1 \qquad (2.32)$$

represents a straight line in $(R_\perp, R_{||})$ space, parallel to $R_{||}$ axis. Equation (2.29) can be written as

$$AG^2 + BG + C = 0 \qquad (2.33)$$

where

$$A = F^2 + \mathrm{Cot}^2 2\theta$$

$$B = -F^3 - F(1 + 2\mathrm{Cot}^2 2\theta)$$

$$C = (1 + F^4)\,\mathrm{Cos}^2\theta\,\mathrm{Sin}^2\theta + F^2(\mathrm{Sin}^4\theta + \mathrm{Cos}^4\theta + \mathrm{Cot}^2 2\theta)$$

This equation is solved for G, and thus the minimum value of $R_{||}$ is obtained. This value is then used as a starting value for a

series of steps in R_{11} of 0.001 along the line represented by equation (2.32), for which n and k are obtained. These values of n and k are then used to generate lines

$$(R_{\perp})_2 = \beta_2 \qquad (2.34)$$

in $(R_{\perp}, R_{11})$ space, for the angle θ_2, until $d = (R_{\perp})'_2 - (R_{\perp})_2$ becomes < 0.001.

2.6 Three Angles Method

A new method for determining optical constants n and k of bulk materials and opaque films is devised. If I_{11}, $I_{\perp}$ are the reflected intensities and I_{o11}, $I_{o\perp}$ are the incident intensities for the two components of light, then the reflectance ratio can be written as

$$\rho = \frac{R_{\perp}}{R_{11}} = \frac{I_{\perp}}{I_{11}} \cdot \frac{I_{o11}}{I_{o\perp}} = E.C \qquad (2.35)$$

where E is the ratio of the reflected intensities and C is the ratio of the incident intensities, which is constant for a polarizer at a given orientation with respect to the incident beam at a given wavelength.

Let E_1, E_2 and E_3 be the measured reflected intensities ratios at three angles of incidence θ_1, θ_2 and θ_3. Then

$$\begin{aligned} \rho_1 &= E_1.C \\ \rho_2 &= E_2.C \\ \rho_3 &= E_3.C \end{aligned} \qquad (2.36)$$

Equations (2.36) can be represented by straight lines OA, OB and OC on a (ρ, C) diagram as shown in the figure 2.

The method consists of choosing a starting value of C (C generally lies between 0.900 and 1.100, so one can choose 0.900 as a starting value) and then going along x-axis in small steps of 0.001. For each step the values of φ_1, φ_2 and φ_3 have been found out.

Figure 2.

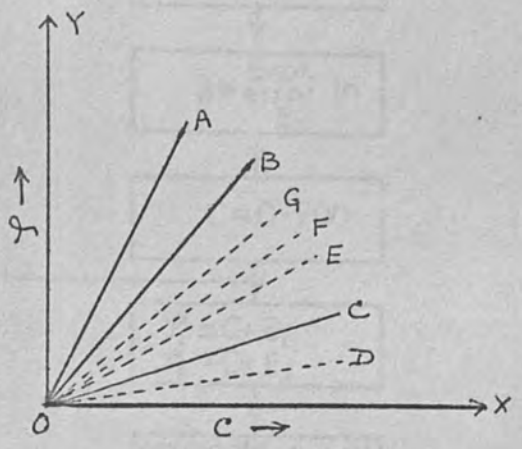

Each pair of φ_1 and φ_2 are used to calculate n and k using the reflectance ratio method. Each pair of n and k are then used in Fresnel reflectance equations to produce lines OD, OE, OF etc.

Each line has different slope $\frac{\varphi}{C}$, and only one pair (n,k) will produce a line which will coincide with OC. This pair of (n,k) will then be the required solution. The whole procedure is represented by a flow chart (Figure 3).

The method may be useful for samples in high vacuum, where it is often difficult to move the sample in order to get the incident beam on to the detector for incident intensity measurements, which are required for calculating reflectance or reflectance ratios.

The three angles method can also be applied to thin films by calculating the quantities defined below:

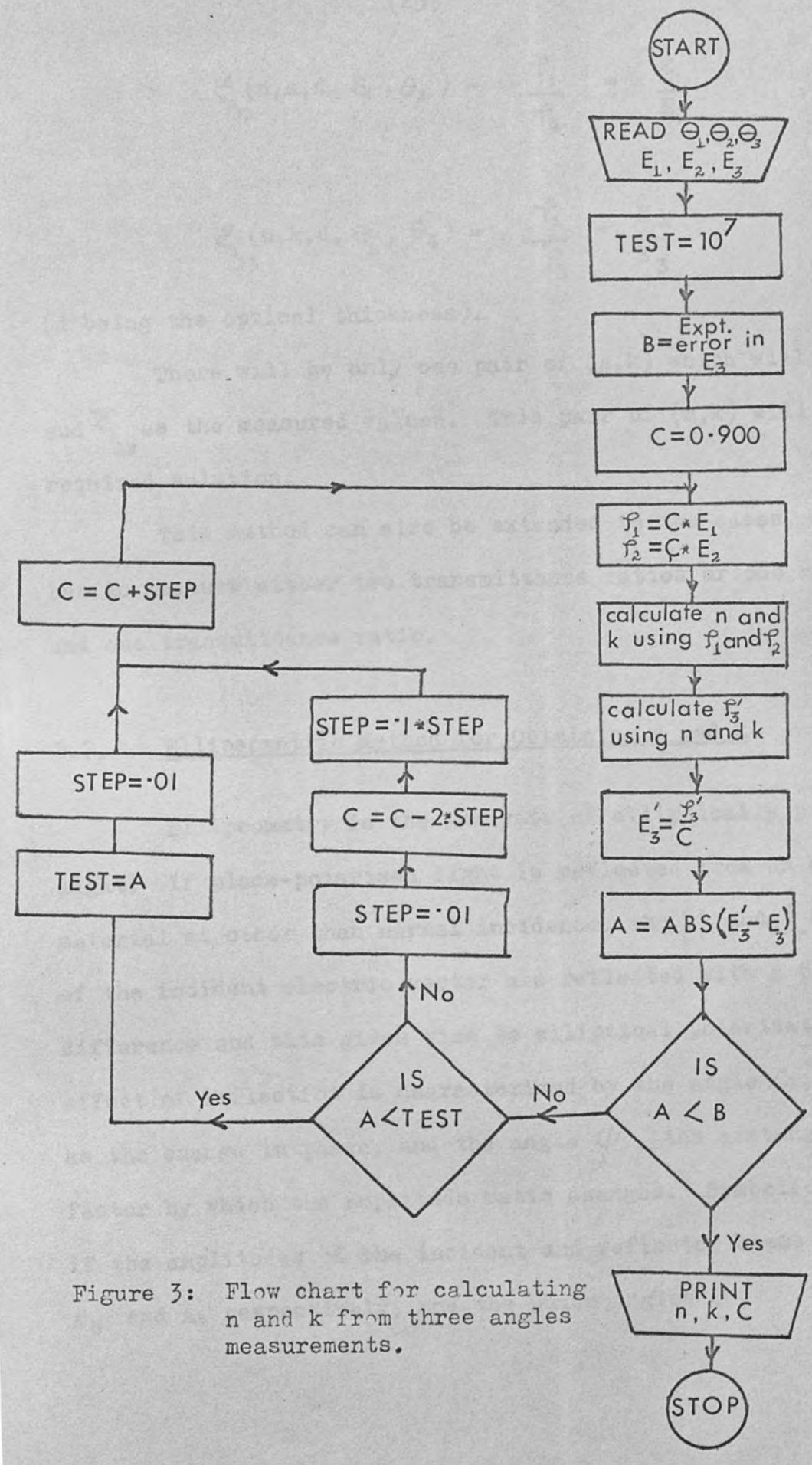

Figure 3: Flow chart for calculating n and k from three angles measurements.

$$\xi_{12}(n,k,d,\theta_1,\theta_2) = \frac{\rho_1}{\rho_2} = \frac{E_1}{E_2}$$

$$\xi_{23}(n,k,d,\theta_2,\theta_3) = \frac{\rho_2}{\rho_3} = \frac{E_2}{E_3} \qquad (2.37)$$

(d being the optical thickness).

There will be only one pair of (n,k) which will give ξ_{12} and ξ_{23} as the measured values. This pair of (n,k) will then be the required solution.

This method can also be extended to the cases, where one has to measure either two transmittance ratios or one reflectance and one transmittance ratio.

2.7. Ellipsometric Method for Obtaining n and k

Ellipsometry is the analysis of elliptically polarised light. If plane-polarised light is reflected from an absorbing material at other than normal incidence, the $||$ and $\perp$ components of the incident electric vector are reflected with a phase difference and this gives rise to elliptical polarisation. The effect of reflection is characterized by the angle Δ, defined as the change in phase, and the angle ψ, the arctangent of the factor by which the amplitude ratio changes. Symbolically, if the amplitudes of the incident and reflected beams are designated A_o and A, respectively, and the phase angles β,

$$\Delta = (\beta_{\parallel} - \beta_{\perp})_{\text{reflected}} - (\beta_{\parallel} - \beta_{\perp})_{\text{Incident}} \quad (2.38)$$

$$\psi = \text{Arctan}\left(\frac{A_{\parallel}}{A_{\perp}} \frac{A_{o\perp}}{A_{o\parallel}}\right) \quad (2.39)$$

Ellipsometry is the measurement of Δ and ψ. The formulae for determining optical constants from values of Δ and ψ for an ideally clean, film-free surface (Archer 1968) are derived from equations (2.1), (2.2) and the equation

$$\frac{r_{\parallel}}{r_{\perp}} = \frac{A_{\parallel}}{A_{\perp}} \frac{A_{o\perp}}{A_{o\parallel}} e^{i\Delta} = \tan\psi\, e^{i\Delta} \quad (2.40)$$

The results are (Ditchburn, 1955)

$$n^2 - k^2 = t^2 \frac{(\text{Cos}^2 2\psi - \text{Sin}^2 2\psi \text{Sin}^2\Delta)}{(1 + \text{Sin}\, 2\psi \text{Cos}\,\Delta)^2} + \text{Sin}^2\theta \quad (2.41)$$

$$2nk = t^2 \frac{\text{Sin}\, 4\psi \text{Sin}\,\Delta}{(1 + \text{Sin}2\psi \text{Cos}\Delta)^2} \quad (2.42)$$

$$t = \text{Sin}\,\theta \tan\theta \quad (2.43)$$

(θ is the angle of incidence and $n_o = 1$)

An alternative method to calculate n and k is to measure the principal angle of incidence $\bar{\theta}$ (the angle of incidence at which $\Delta = 90^{\circ}$) and the principal azimuth $\bar{\psi}$ (the value of ψ at $\bar{\theta}$). The equations (2.41) - (2.43) for this case will reduce to

$$n^2 - k^2 = \bar{t}^2 \text{Cos}4\bar{\psi} + \text{Sin}^2\bar{\theta} \quad (2.44)$$

$$2nk = \bar{t}^2 \text{Sin}4\bar{\psi} \quad (2.45)$$

where $$\bar{t} = \text{Sin}\,\bar{\theta} \tan\bar{\theta} \quad (2.46)$$

Thus by measuring principal angle of incidence $\bar{\theta}$ and principal azimuth $\bar{\psi}$, n and k can be calculated.

Experimental details of measuring Δ, ψ and $\bar{\theta}, \bar{\psi}$ are given in "Manual on ellipsometry" by Archer (1968).

2.8. A Quicker Technique for Obtaining n and k of Thin Films from Reflectance Ratio Measurements at Two Angles of Incidence

A quicker technique for obtaining optical constants n and k from the measurements of reflectance ratios ρ_1 and ρ_2 at angles of incidence θ_1, and θ_2, for thin absorbing films supported by a dielectric substrate, using Hadley and Dennison's formula (1947), has been devised. This technique is a modification of the method described by Miller and Taylor (1971) and is useful for $1<n<3$, $1<k<4$, $.045\leqslant\frac{d}{\lambda}\leqslant.150$ ($\frac{d}{\lambda}$ is the optical thickness), and for all the optimum angles obtained by them.

Miller and Taylor took the starting values of n and k as 1.00 and then by going in small steps in n and k a pair (n,k) is obtained such that the theoretically calculated values of ρ_1' and ρ_2' for the angles of incidence θ_1 and θ_2 and known $\frac{d}{\lambda}$ becomes nearly equal (within the experimental errors) to the experimentally obtained values of ρ_1 and ρ_2.

The technique described here involves the calculation of a starting value of either n or k close to the actual value. The reflectance ratio ρ_1 and ρ_2 for angles of incidence θ_1 and θ_2 are first used to calculate the values n_t and k_t using the bulk specimen formula (method (1) of section 2.5.). If n and k are the real values for the thin film, then for all optimum angles of incidence obtained by Miller and Taylor,

$$n_t \geqslant n \quad \text{for} \quad .045\leqslant\frac{d}{\lambda}\leqslant.080$$

$$k_t \geqslant k \quad \text{for} \quad .080\leqslant\frac{d}{\lambda}\leqslant.150$$

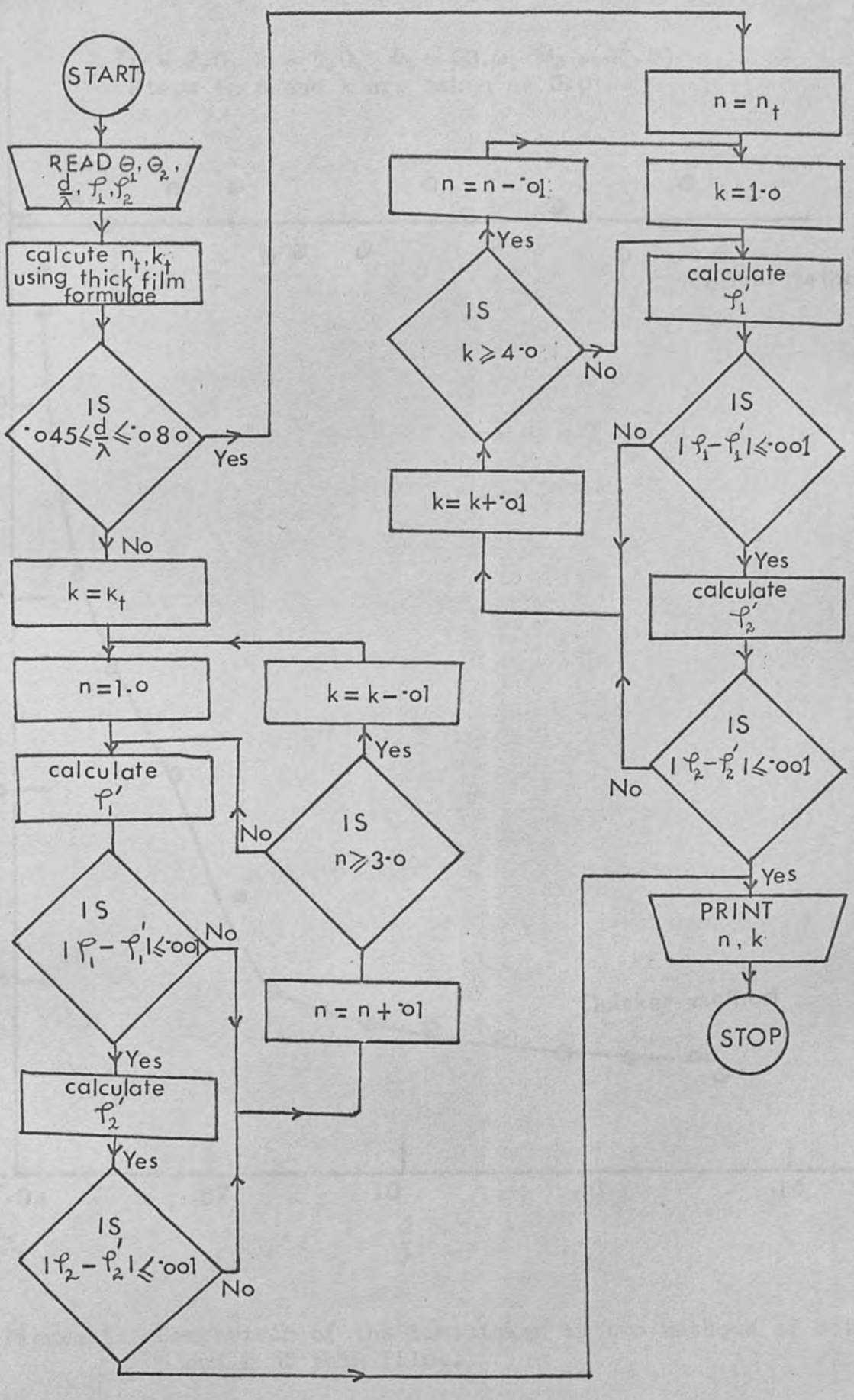

Figure 4: Flow chart for obtaining n and k of thin films from reflectance ratio measurements at two angles of incidence using the quicker technique.

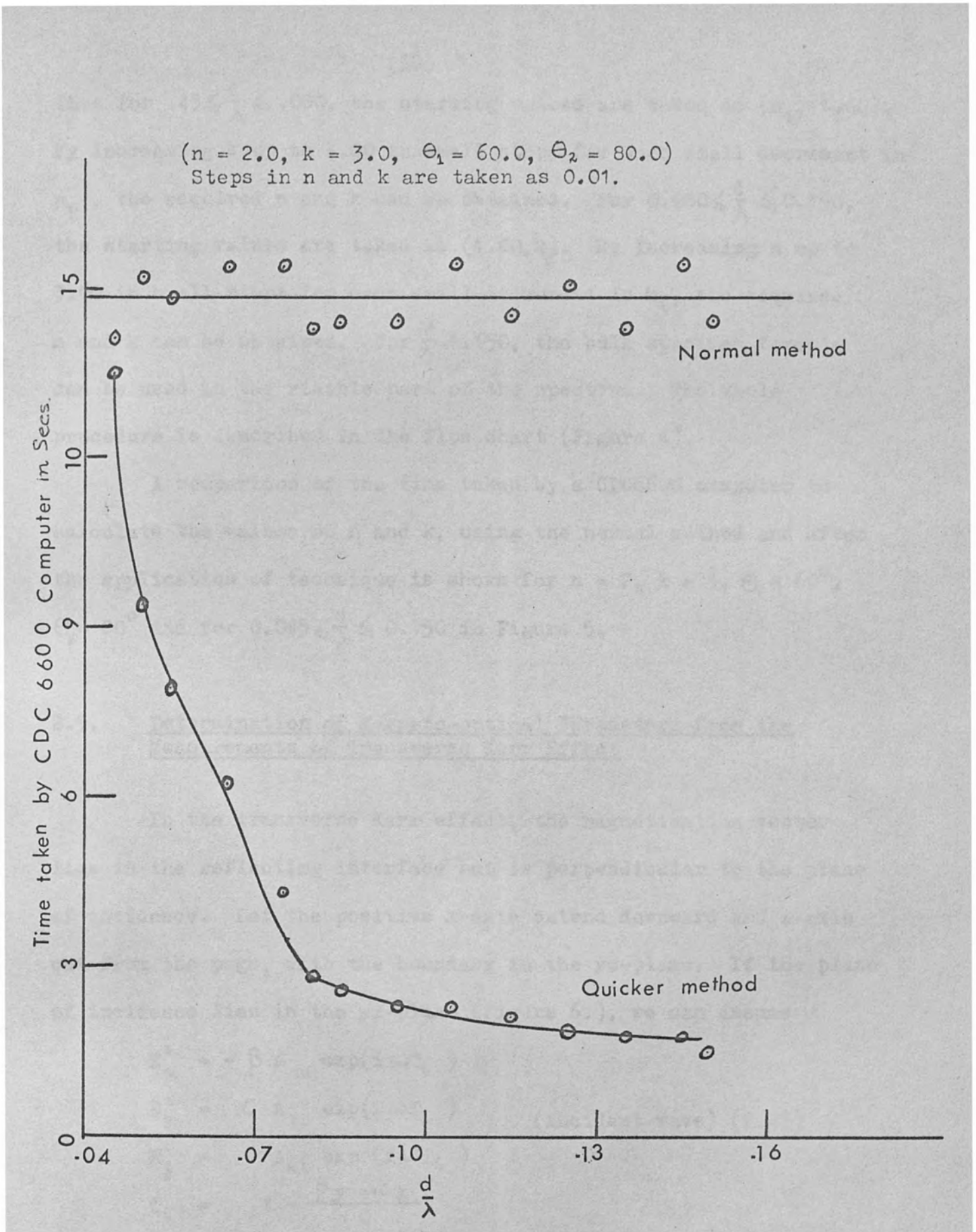

Figure 5: Comparison of the time taken by two methods of obtaining n and k of thin films.

Thus for $.45 \leqslant \frac{d}{\lambda} \leqslant .080$, the starting values are taken as $(n_t, 1.00)$. By increasing k up to 4.00 in small steps for each small decrement in n_t, the required n and k can be obtained. For $0.080 \leqslant \frac{d}{\lambda} \leqslant 0.150$, the starting values are taken as $(1.00, k_t)$. By increasing n up to 3.00 in small steps for each small decrement in k_t, the required n and k can be obtained. For $\frac{d}{\lambda} \geqslant .150$, the bulk specimen formula can be used in the visible part of the spectrum. The whole procedure is described in the flow chart (Figure 4).

A comparison of the time taken by a CDC6600 computer to calculate the values of n and k, using the normal method and after the application of technique is shown for n = 2, k = 3, $\theta_1 = 60^\circ$, $\theta_2 = 80^\circ$ and for $0.045 \leqslant \frac{d}{\lambda} \leqslant 0.150$ in Figure 5.

2.9. Determination of Magneto-optical Parameters from the Measurements of Transverse Kerr Effect

In the transverse Kerr effect, the magnetisation vector lies in the reflecting interface but is perpendicular to the plane of incidence. Let the positive x-axis extend downward and z-axis out from the page, with the boundary in the yz-plane. If the plane of incidence lies in the yx-plane (Figure 6.), we can assume

$$\begin{aligned} E_x^i &= -\beta A_{o\parallel} \exp(i\omega T_i) \\ E_y^i &= \alpha A_{o\parallel} \exp(i\omega T_i) \qquad \text{(incident wave)} \quad (2.47) \\ E_z^i &= A_{o\perp} \exp(i\omega T_i) \\ T_i &= t - \frac{\beta y + \alpha x}{c} \end{aligned}$$

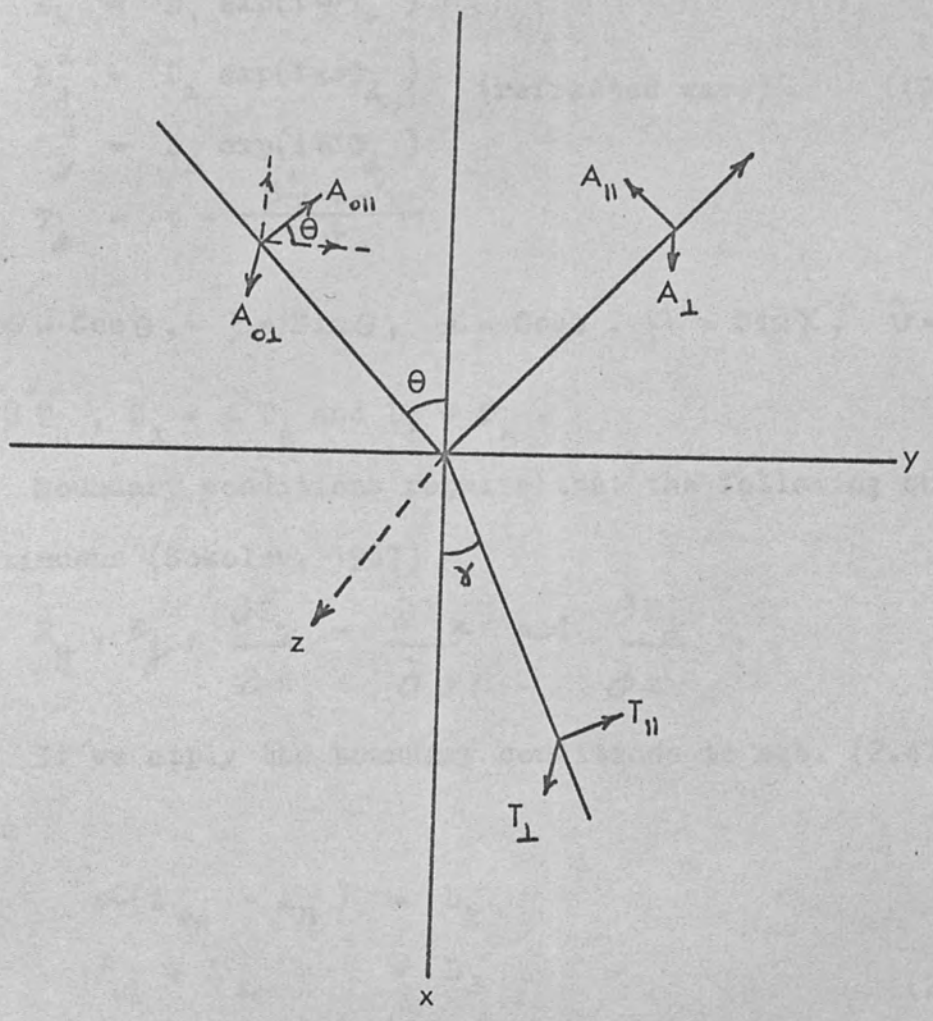

Figure 6: Vectors used in applying the boundary conditions for transverse Kerr effect. ($A_{o\perp}$, $A_{\perp}$ and $T_{\perp}$ vectors are $\perp$ to the page).

$$
\begin{aligned}
E_x^r &= -\beta A_{\parallel} \exp(i\omega T_r) \\
E_y^r &= -\alpha A_{\parallel} \exp(i\omega T_r) \quad \text{(reflected wave)} \\
E_z^r &= A_{\perp} \exp(i\omega T_r) \\
T_r &= t - \frac{\beta y - \alpha x}{C}
\end{aligned}
\tag{2.48}
$$

$$
\begin{aligned}
E_x^d &= D_1 \exp(i\omega T_d) \\
E_y^d &= D_2 \exp(i\omega T_d) \quad \text{(refracted wave)} \\
E_z^d &= D_3 \exp(i\omega T_d) \\
T_d &= t - \frac{\beta' y + \alpha' x}{\tilde{v}}
\end{aligned}
\tag{2.49}
$$

where $\alpha = \cos\theta$, $\beta = \sin\theta$, $\alpha' = \cos\gamma$, $\beta' = \sin\gamma$, $\tilde{v} = \frac{C}{n}$

$D_1 = -\beta' T_{\parallel}$, $D_2 = \alpha' T_{\parallel}$ and $D_3 = T_{\perp}$.

Boundary conditions require that the following quantities be continuous (Sokolov, 1967)

$$E_y, E_z, \frac{\partial E_y}{\partial x} - \frac{\partial E_x}{\partial y} \text{ and } \frac{\partial E_z}{\partial x}$$

If we apply the boundary conditions to eqs. (2.47) - (2.49) we have

$$
\begin{aligned}
\alpha(A_{o\parallel} - A_{\parallel}) &= D_2 \\
A_{o\perp} + A_{\perp} &= D_3 \\
A_{o\parallel} + A_{\parallel} &= \tilde{n}(\alpha' D_2 - \beta' D_1) \\
\alpha(A_{o\perp} - A_{\perp}) &= \tilde{n}\alpha' D_3
\end{aligned}
\tag{2.50}
$$

Substituting equation (1.19) into (1.17) we have

$$
\begin{aligned}
D_x &= \epsilon E_x - i\epsilon Q E_y \\
D_y &= i\epsilon Q E_x + \epsilon E_y \\
D_z &= \epsilon_o E_z
\end{aligned}
\tag{2.51}
$$

If we take curl of equation (1.15) and use equation (1.16), we have

$$c^2 (\Delta \vec{E} - \text{grad. Div. } \vec{E}) = \frac{\partial^2 \vec{D}}{\partial t^2} \qquad (2.52)$$

Substituting equations (2.51) into (2.52) we have

$$\begin{aligned} c^2 (\Delta E_x - \text{grad.}_x \text{ div. } \vec{E}) &= \epsilon \ddot{E}_x - i\epsilon Q \ddot{E}_y \\ c^2 (\Delta E_y - \text{grad.}_y \text{ div. } \vec{E}) &= \epsilon \ddot{E}_y + i\epsilon Q \ddot{E}_x \qquad (2.53) \\ c^2 (\Delta E_z - \text{grad.}_z \text{ div. } \vec{E}) &= \epsilon_o \ddot{E}_z \end{aligned}$$

Using a solution of the form given by equation (2.49), we have

$$\epsilon D_1 - i\epsilon Q D_2 = \tilde{n}^2 \left[D_1 - \alpha' (\alpha' D_1 + \beta' D_2) \right] \qquad (2.54)$$

$$i\epsilon Q D_1 + \epsilon D_2 = \tilde{n}^2 \left[D_2 - \beta' (\alpha' D_1 + \beta' D_2) \right] \qquad (2.55)$$

$$\epsilon_o D_3 = \tilde{n}^2 D_3 \qquad (2.56)$$

Multiplying equations (2.54) and (2.55) by α' and β', adding them and using the identity $\alpha'^2 + \beta'^2 = 1$, we have

$$(\epsilon \alpha' + i\epsilon Q \beta') D_1 + (\epsilon \beta' - i\epsilon Q \alpha') D_2 = 0$$

or $$-(\alpha' D_2 - \beta' D_1) i\beta' Q + \alpha' \beta' D_1 + \beta'^2 D_2 = 0$$

or $$(\alpha' D_2 - \beta' D_1) i\beta' Q + (\alpha' D_2 - \beta' D_1) \alpha' = D_2$$

or $$\alpha' D_2 - \beta' D_1 = \frac{D_2}{\alpha' + i\beta' Q} \qquad (2.57)$$

Substituting (2.57) into (2.50), we have

$$A_{\parallel} \left[(\alpha' + \tilde{n}\alpha) + i\beta' Q \right] = -A_{o\parallel} \left[(\alpha' - \tilde{n}\alpha) + i\beta' Q \right] \qquad (2.58)$$

$$A_{\perp} (\alpha + \tilde{n} \alpha') = A_{o\perp} (\alpha - \tilde{n} \alpha') \qquad (2.59)$$

It is evident from these equations that the component which is perpendicular to the plane of incidence, and is therefore polarised in this plane, is independent of the magnetisation. Physically we should expect this because the vibrations set up by $\vec{E}$ vector of wave cannot be affected by the $\vec{B}$ vector of the medium since the

two vectors are parallel in this case. Owing to the presence of magnetisation, the component which is parallel to the plane of incidence undergoes a change in amplitude and phase.

The Transverse Kerr effect is then described by the expression

$$\delta = \frac{R_{\parallel}' - R_{\parallel}}{R_{\parallel}} = \frac{I_{\parallel}' - I_{\parallel}}{I_{\parallel}} \qquad (2.60)$$

where $R_{\parallel}'$ is the reflectance for the $\parallel$ component for the ferromagnetic, magnetised to saturation, $R_{\parallel}$ is the reflectance for the $\parallel$ component for the ferromagnetic demagnetised, and

$$I_{\parallel}' = I_{o\parallel} R_{\parallel}'$$
$$I_{\parallel} = I_{o\parallel} R_{\parallel} \qquad (I_{o\parallel} \text{ is the incident intensity})$$

are the reflected intensities from the ferromagnetic, magnetised to saturation and demagnetised respectively.

From equation (2.58)

$$r_{\parallel}' = \frac{A_{\parallel}}{A_{o\parallel}} = -\frac{(\alpha' - \tilde{n}\alpha) + i\beta' Q}{(\alpha' + \tilde{n}\alpha) + i\beta' Q}$$

$$= -\left[\frac{\alpha' - \tilde{n}\alpha}{\alpha' + \tilde{n}\alpha} + \frac{2i\beta' Q\tilde{n}\alpha}{(\alpha' + \tilde{n}\alpha)^2}\right] \qquad (2.61)$$

$$= -\left[\frac{\cos\gamma - \tilde{n}\cos\theta}{\cos\gamma + \tilde{n}\cos\theta} + iQ\frac{2\sin\theta\cos\theta}{(\cos\gamma + \tilde{n}\cos\theta)^2}\right]$$

$$= -\left[r_{\parallel} + iQ\frac{2\sin\theta\cos\theta}{(\cos\gamma + \tilde{n}\cos\theta)^2}\right]$$

$$\text{or} \quad \frac{r_{\parallel}'}{r_{\parallel}} = -\left[1 + iQ\frac{\sin 2\theta}{\cos^2\gamma - \tilde{n}^2\cos^2\theta}\right]$$

where terms containing Q^2 have been neglected.

The corresponding ratio of intensities of reflected light is given by

$$\frac{I_{\parallel}'}{I_{\parallel}} = \left[\mathrm{Re}\left(\frac{r_{\parallel}'}{r_{\parallel}}\right)\right]^2 + \left[\mathrm{Im}\left(\frac{r_{\parallel}'}{r_{\parallel}}\right)\right]^2$$

$$= \left[-1 - \frac{\mathrm{Sin}2\Theta(AQ_1 - BQ_2)}{A^2 + B^2}\right]^2 + \left[\frac{\mathrm{Sin}2\Theta(AQ_2 + BQ_1)}{A^2 + B^2}\right]^2$$

Neglecting terms containing second and higher order of Q, we have

$$\frac{I_{\parallel}'}{I_{\parallel}} = 1 + \frac{2\,\mathrm{Sin}2\Theta(AQ_1 - BQ_2)}{A^2 + B^2}$$

Hence

$$\delta = \frac{I_{\parallel}' - I_{\parallel}}{I_{\parallel}} = 2\mathrm{Sin}2\Theta\frac{AQ_1 - BQ_2}{A^2 + B^2} \qquad (2.62)$$

where $A = \epsilon_2 \mathrm{Cos}^2\Theta - q$, $B = \epsilon_1 \mathrm{Cos}^2\Theta - 1 + p$

$$p = \frac{\epsilon_1 \mathrm{Sin}^2\Theta}{(n^2 + k^2)^2} \quad , \quad q = \frac{\epsilon_2 \mathrm{Sin}^2\Theta}{(n^2 + k^2)^2}$$

$$\epsilon_1 = n^2 - k^2 \quad , \quad \epsilon_2 = 2nk$$

Thus, if n and k of the ferromagnetic metals for a given wavelength are known, Q_1 and Q_2 can be determined by measuring δ at two angles of incidence Θ_1 and Θ_2. By knowing Q_1 and Q_2 the other magneto-optical parameters ϵ_1' and ϵ_2' can be calculated using equations (1.21) and (1.22). Alternatively, ϵ_1' and ϵ_2' can be obtained directly from the measurements of δ at two angles of incidence using equation (obtainable from equation (2.61))

$$\delta = 2\,\mathrm{Sin}\,2\Theta\frac{A_1\epsilon_1' + B_1\epsilon_2'}{A_1^2 + B_1^2} \qquad (2.63)$$

where $A_1 = 2\,\epsilon_1\epsilon_2\,\mathrm{Cos}^2\Theta - \epsilon_2$

and $B_1 = (\epsilon_2^2 - \epsilon_1^2)\mathrm{Cos}^2\Theta + \epsilon_1 - \mathrm{Sin}^2\Theta$,

By knowing ϵ_1' and ϵ_2', the real and imaginary parts of the off-diagonal components of the conductivity tensor (equation (1.23)) can be obtained from equation (1.24).

An alternative method to determine magneto-optical parameters is by ellipsometery, which has been discussed in detail by Sokolov (1967).

CHAPTER III

OPTIMIZATION TECHNIQUES FOR ACCURATE DETERMINATION OF OPTICAL AND MAGNETO-OPTICAL CONSTANTS

3.1. Introduction

In this chapter we investigate in detail the sensitivity of values deduced for optical and magneto-optical constants, to small changes in the measured quantities, and how this sensitivity depends on the angles of incidence. Miller et al (1970, 1971) discussed the sensitivity of near-normal incidence and one angle method for optical constants. For the one angle method they obtained the optimum angle 74° and they have shown that large errors in n and k may arise from errors in reflectance $R_{\parallel}$ and $R_{\perp}$, when these are measured at angles of incidence other than 74°. Here we will discuss the sensitivity and optimum conditions for all the other methods described in Chapter II. The values of n and k were selected to be in the ranges $1.0 \leqslant n \leqslant 4.0$, $1.0 \leqslant k \leqslant 4.0$ (typical of metals in visible region). Computer programmes written in FORTRAN IV language for a CDC 6600 computer, allowed a study of a large number of combinations of the parameters concerned.

3.2. Sensitivity and Optimization of Two Angles Methods

Miller et al (1972) examined the sensitivity of the reflectance ratio method and found the optimum angles of incidence

for experimental measurements in angular ranges $58^\circ \leq \Theta_1 \leq 67^\circ$ and $80^\circ \leq \Theta_2 \leq 81^\circ$. They found that errors of less than 2% may be attained in the product nk for $nk \leq 6$, when the reflectance ratios are in error by $\pm .005$, or Θ_1 and Θ_2 are in error by $\pm 0.1^\circ$. Here we will examine the sensitivities of other two-angles methods.

If we define the actual values of the optical constants as n_o and k_o, and the experimentally observed values as n and k, we may calculate σ, the percentage error in $n_o k_o$ produced by an error δR in reflectance measurements, for various combinations of Θ_1, and Θ_2, ϕ and n and k

$$\sigma = \frac{n_o k_o - nk}{n_o k_o} \times 100\% \qquad (3.1)$$

(the product $n_o k_o$ is chosen as a suitable parameter because of its relevance to band structure calculations)

$(R_\phi)_1$ and $(R_\phi)_2$, at Θ_1 and Θ_2, are computed for the given n_o and k_o, using eqs. (2.6) - (2.9) and (2.22). Then it is assumed that $\delta R = 0.001\ R_\phi$, and the quantities $(R_\phi)_1 + \delta R$ and $(R_\phi)_2 - \delta R$ are used to compute n and k. This particular combination has been chosen because it gives largest errors in σ.

Figure 7 shows the variation of σ with ϕ for several values of n_o, k_o, Θ_1 and Θ_2. In general the curves indicate an initial gradual increase in σ with ϕ, rising steeply near $\phi = 90^\circ$. This indicates that method (4) of section 2.5 ($R_\perp$ method) is evidently liable to large errors, and is therefore not generally recommended.

The optimum reflection angles for methods (2) and (3) of section 2.5 will be considered below.

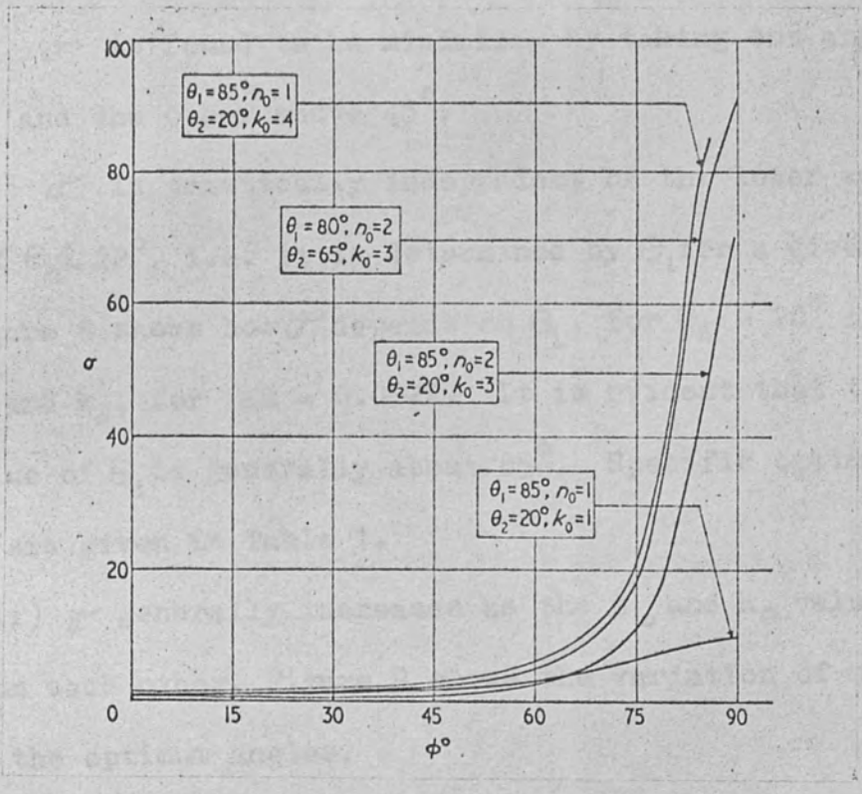

Figure 7: The variation of σ with ϕ.

(a) Optimum angles for the total reflection method

The results of a computation of σ for $\delta R = 0.002R$ and for many combinations of θ_1, θ_2, n_o and k_o may be summarized as follows.

(i) σ is found to be minimized by taking one angle below 45° and the other above 45°.

(ii) σ is practically independent of the lower angle, θ_2, for $2^\circ < \theta_2 < 22^\circ$, i.e. it is determined by θ_1 for a given n_o and k_o. Figure 8 shows how σ depends on θ_1, for $\theta_2 = 20^\circ$ and various n_o and k_o, for $\delta R = 0.002R$. It is evident that the optimum value of θ_1 is generally about 85°. Specific optimum angles θ_1 are given in Table 1.

(iii) σ generally increases as the n_o and k_o values diverge from each other, Figure 9 shows the variation of σ with n_o and k_o at the optimum angles.

Finally, the errors in $(n_o k_o)$ produced by an error of $\pm 0.1^\circ$ in θ_1 and θ_2 (assuming no errors in reflectance) were found. These errors were $< 3\%$ except for $n_o = 3$, $k_o = 1$ and $n_o = 4$, $k_o = 1$, where the errors were between 3% and 5%.

The sensitivity of the method to changes in optical constants is indicated by figure 10, in which R_1 is plotted against R_2, with n_o and k_o as parameters. A similar diagram was produced by Humphreys -Owen (1961) for angles 20° and 70°. As figure 8 indicates, $\theta_1 = 70^\circ$ is the optimum angle only for values of n_o and k_o

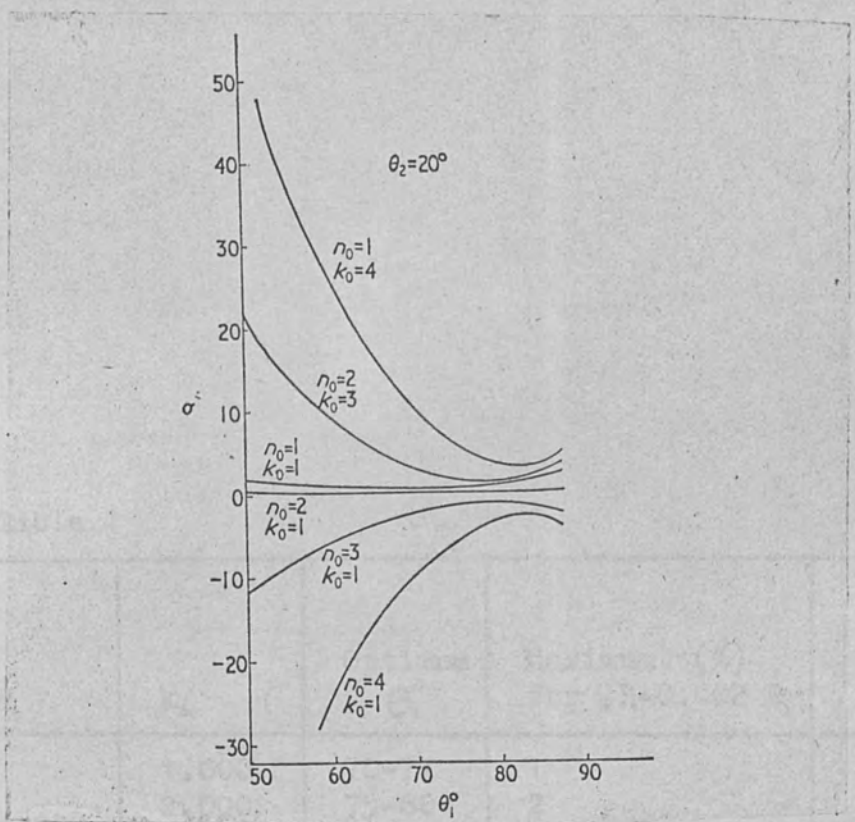

Figure 8: The variation of σ with θ_1 for $\phi = \pi/4$, at $\theta_2 = 20°$.

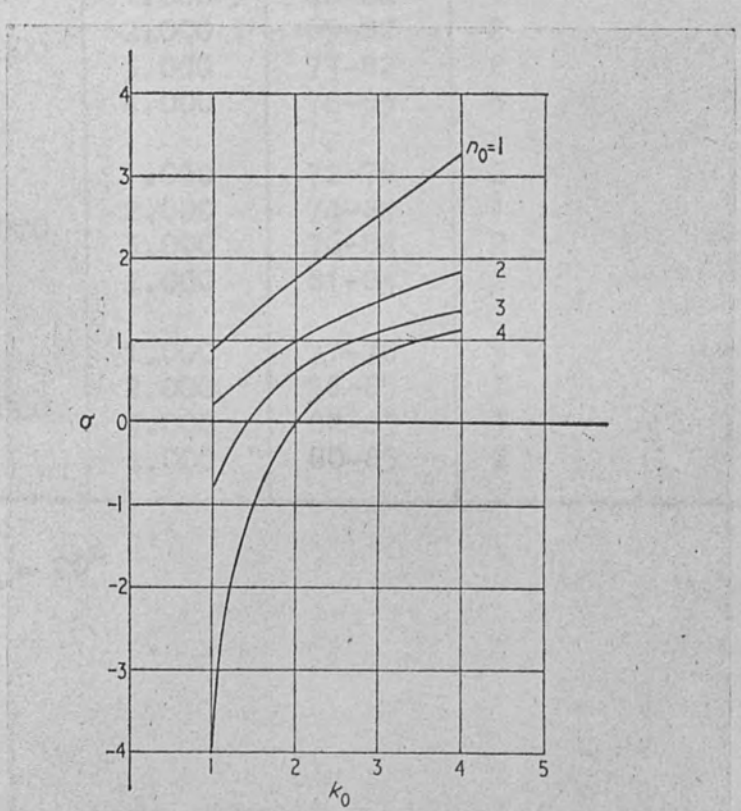

Figure 9: The variation of σ with n_o and k_o at the optimum angles, for $\gamma R = 0.002$ R.

Table 1

n_o	k_o	Optimum θ_1°	Maximum σ (%) for $\delta R = 0.002$ R	Maximum %Error in $(n_o k_o)$ due to angular errors of ± 0.1
1.000	1.000	70-77	1	2
	2.000	75-80	2	2
	3.000	78-84	3	3
	4.000	80-85	4	4
2.000	1.000	46-88	1	1
	2.000	69-82	2	2
	3.000	77-82	2	2
	4.000	78-83	3	2
3.000	1.000	72-78	2	3
	2.000	74-84	1	1
	3.000	76-84	2	2
	4.000	81-84	2	2
4.000	1.000	77-78	5	5
	2.000	56-85	1	1
	3.000	82-83	1	1
	4.000	80-85	2	2

$\theta_2 = 20^\circ$

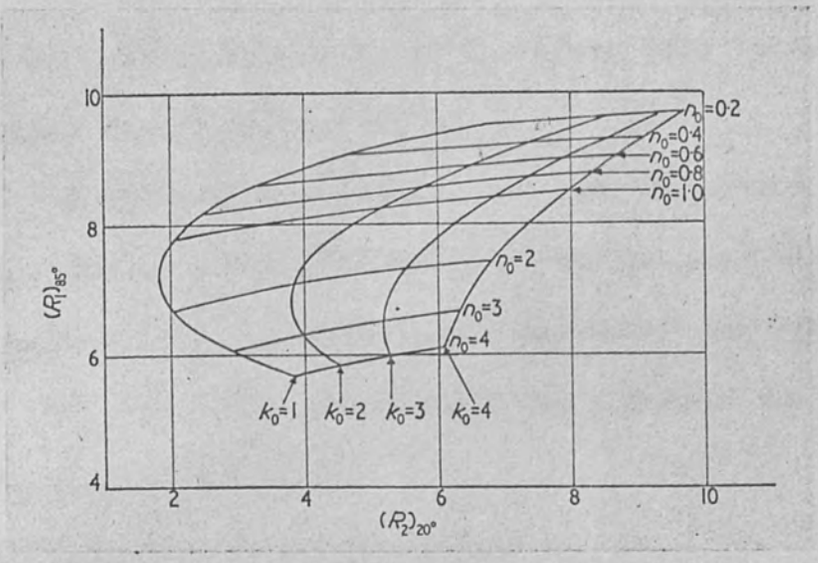

Figure 10: The sensitivity of total reflectance to n_o and k_o at 85° and 20°.

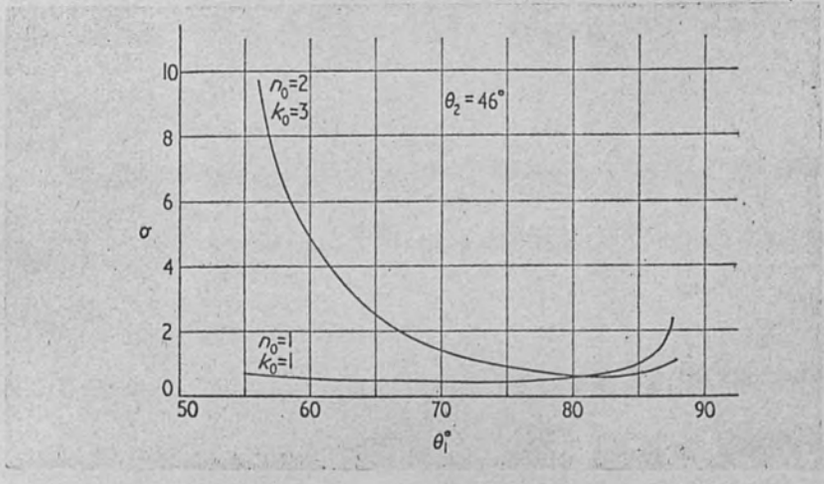

Figure 11: The variation of σ with θ_1 for $\phi = 0$, at $\theta_2 = 46°$.

close to 1.0 and Figure 10 is therefore constructed for the more generally optimized angles 85° and 20°.

A typical calculation time for the method is 0.18 seconds on CDC 6600 computer (FORTRAN IV), in the case where d (defined by equation 2.21) is made less than 0.0001 for the optimum angles ($\theta_1 = 85^\circ$, $\theta_2 = 20^\circ$), and n and k are computed to better than 0.1%, for $n_o = 2$, $k_o = 3$.

(b) Optimum angles for $R_{\parallel}$ method

Computation for σ for $\delta R = .002 R_{\parallel}$ and for various values of θ_1, θ_2, n_o and k_o, θ_1 and θ_2 from 1° to 88° shows that:

(i) The optimum values of θ_1 and θ_2 are both greater than 45°,

(ii) σ is almost independent of the lower angle θ_2. Table 2 shows σ for various optimum θ_1, at $\theta_2 = 46^\circ - 52^\circ$. In general, the minima in the curves relating σ to θ_1 are shallow, as indicated by Figure 11.

Finally the errors in product $(n_o k_o)$ produced by an error of $\pm .01^\circ$ in θ_1 and θ_2 were found at optimum angles. These were found to be $< 1\%$.

Computing time for this method is 0.02 seconds for $\theta_2 = 46^\circ$, $n_o = 2$, $k_o = 3$ and for $56^\circ < \theta_1 < 85^\circ$, on CDC 6600 computer.

3.3. Optimization of Three Angles Method

Since in the three angles method, described in Section 2.6., only two angles θ_1 and θ_2 have been used to calculate n and k, θ_1 and θ_2 can be taken in the ranges $58^\circ \leq \theta_1 \leq 67^\circ$ and $80^\circ \leq \theta_2 \leq 81^\circ$ (Miller et al

Table 2

n_o	k_o	Optimum θ_1°	Maximum σ for $\delta R=0.002\ R_{11}$
1.000	1.000	60-67	1
	2.000	72-76	1
	3.000	73-79	2
	4.000	81	2
2.000	1.000	58-86	1
	2.000	66-80	1
	3.000	74-81	1
	4.000	81-82	1
3.000	1.000	69-74	1
	2.000	69-85	1
	3.000	74-83	1
	4.000	79-83	1
4.000	1.000	75-76	1
	2.000	66-86	1
	3.000	76-85	1
	4.000	78-84	1

$46^\circ \leqslant \theta_2 < 52^\circ$

Error in $n_o k_o$ due to angular errors of 0.1° is $<1\%$

1972). The third angle θ_3 which has been used to calculate E_3', is optimized as follows:-

(i) We fix n_o, k_o, c_o, θ_1 and θ_2 (n_o, k_o and c_o being the actual values)

(ii) ρ_1 and ρ_2, and hence E_1 and E_2 are calculated using Fresnel reflectance equations.

(iii) ρ_3 and hence E_3 is calculated by taking n_o and k_o for all θ_3 in the range $1^\circ \leq \theta_3 \leq 85^\circ$.

(iv) ρ_{1e} and ρ_{2e} are calculated for θ_1 and θ_2 using equations

$$\rho_{1e} = c_o (E_1 + .002E_1)$$

and $$\rho_{2e} = c_o (E_2 - .002E_2)$$

(v) ρ_{1e} and ρ_{2e} are then used to calculate n and k (reflectance ratio method)

(vi) The calculated values of n and k are then used to calculate ρ_3' and hence E_3' for all angles $1^\circ \leq \theta_3 \leq 85^\circ$.

(vii) A graph is then plotted between $(E_3' - E_3)$ and θ_3 and is shown in figure 12 for some combinations of n_o, k_o and c_o, and for $\theta_1 = 60.0^\circ$, $\theta_2 = 80.0^\circ$.

(viii) Next using the same errors in E_1 and E_2, n and k are calculated using variable c around c_o.

(ix) For each c, $(E_3' - E_3)$ is calculated for θ_3.

(x) A graph is then plotted between $(E_3' - E_3)$ and c, and is shown in figure 13 for $n_o = 2$, $k_o = 3$, $c_o = 0.975$, $\theta_1 = 60^\circ$, $\theta_2 = 80^\circ$ and for three different θ_3.

Figure 12 shows that $(E_3' - E_3)$ is small and nearly constant at lower angles. At certain higher angles it increases sharply, goes through a maximum, and then decreases sharply, becomes negative and goes through a negative maximum. The angles at which it increases or decreases, and the sharpness depend on the values of n_o and k_o.

Figure 13 shows that for $\Theta_3 = 20^\circ$, the quantity $(E_3' - E_3)$ is zero for a value of c very near to the actual value c_o, whereas for $\Theta_3 = 50^\circ$ and 70°, it is zero for a value of c far from the actual value c_o.

Thus Θ_3 is so chosen that the errors in n_o and k_o produced by errors in E_1 and E_2 produce $(E_3' - E_3)$ less than the experimental error in E_3 (the experimental error may be taken as .002 E_3) for a value of c very nearly equal to the actual value c_o.

The whole procedure is done for $1 \leqslant n_o \leqslant 4$, $1 \leqslant k_o \leqslant 4$ and $0.900 \leqslant c_o \leqslant 1.100$ and it is found that $\Theta_3 \leqslant 21^\circ$ for the errors in the product $(n_o k_o)$ less than 2.5%.

The whole procedure is repeated for the error of $\pm .01^\circ$ in angles of incidence Θ_1, Θ_2 and Θ_3; the errors in the product $(n_o k_o)$ are again found to be less than 2.5%.

Computer time for this method is ~ 3 sec. on a CDC 6600 computer using FORTRAN IV compiler for $n_o = 2$, $k_o = 3$, $c_o = 1.025$ and for $\Theta_2 = 80^\circ$, $\Theta_1 = 60^\circ$ and $\Theta_3 = 20^\circ$.

3.4 Comparison of Non-Polarimetric Reflection Method Sensitivities

A general comparison is not possible, since the sensitivity varies from method to method with the particular values of n_o and k_o.

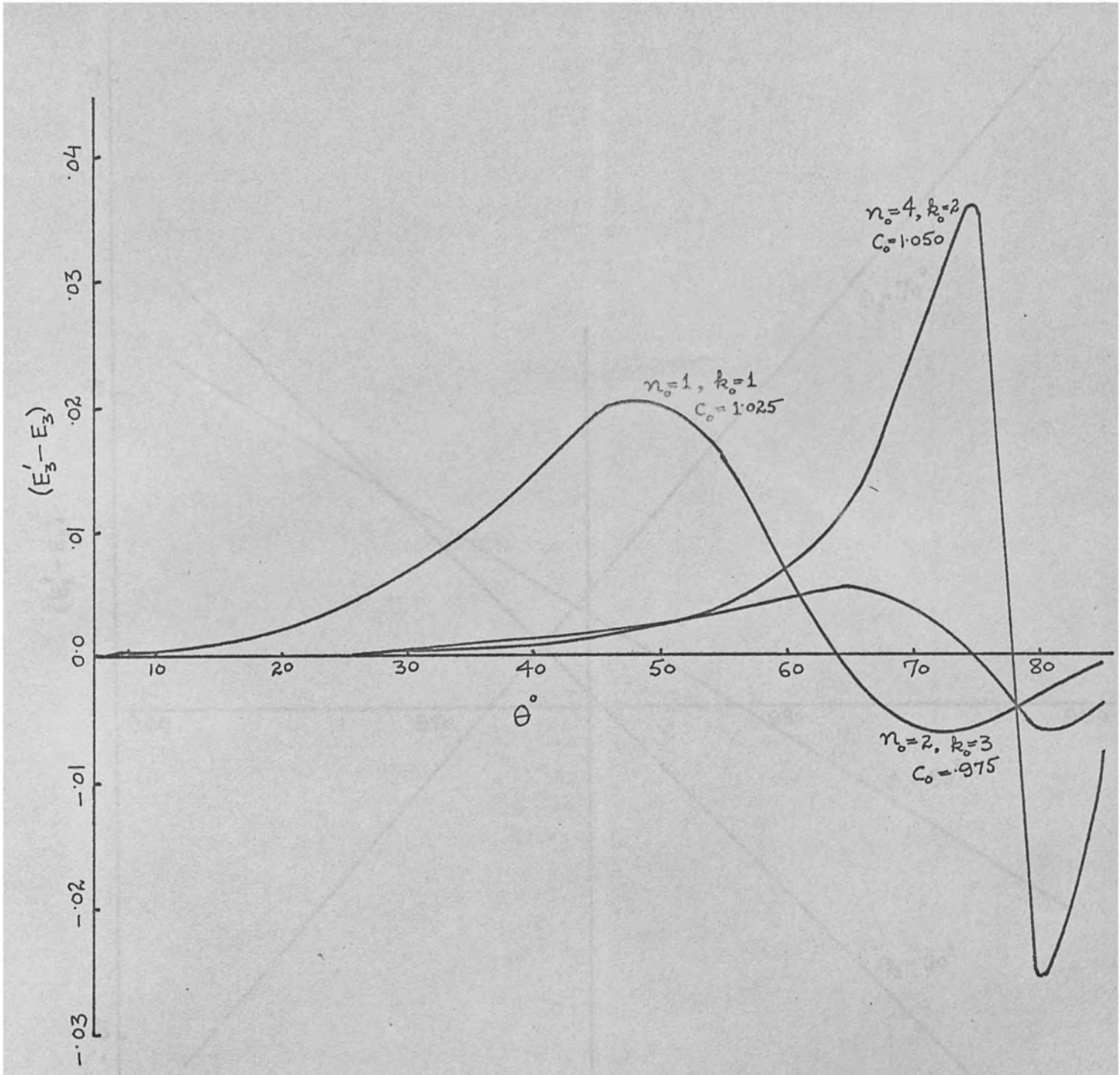

Figure 12: Variation of $(E_3' - E_3)$ with θ_3 for different combinations of n_o, k_o and C_o due to $\pm$ .2% error in E_1 and E_2. ($\theta_1 = 60^\circ$, $\theta_2 = 80^\circ$).

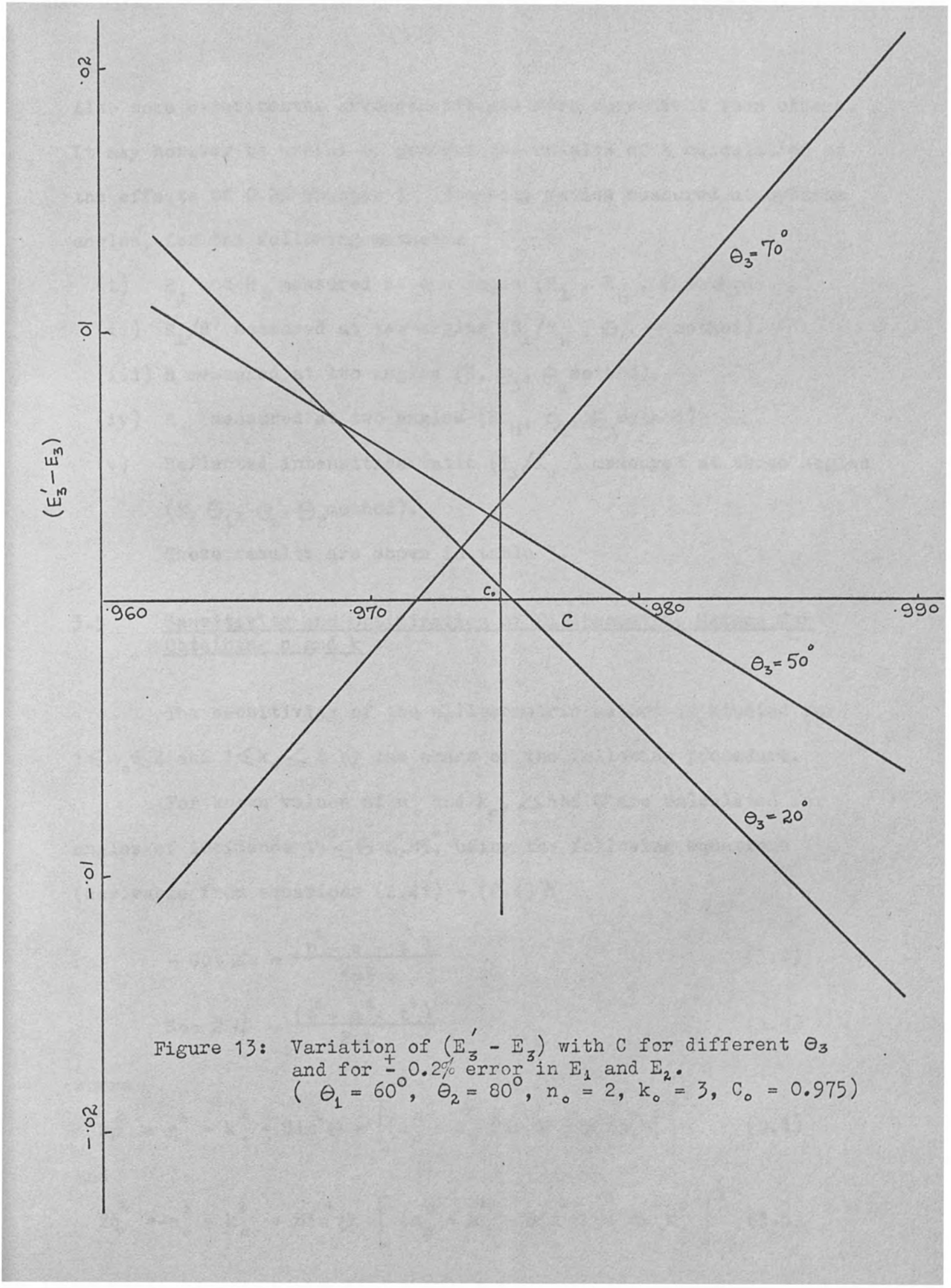

Figure 13: Variation of $(E_3' - E_3)$ with C for different θ_3 and for $\pm$ 0.2% error in E_1 and E_2.
($\theta_1 = 60^\circ$, $\theta_2 = 80^\circ$, $n_o = 2$, $k_o = 3$, $C_o = 0.975$)

Also some experimental arrangements are more convenient than others. It may however be useful to present the results of a calculation on the effects of 0.2% changes in intensity ratios measured at optimum angles, for the following methods:

(i) $R_\perp$ and $R_{||}$ measured at one angle ($R_\perp$, $R_{||}$, Θ method).

(ii) $R_\perp/R_{||}$ measured at two angles ($R_\perp/R_{||}$, Θ_1, Θ_2 method).

(iii) R measured at two angles (R, Θ_1, Θ_2 method).

(iv) $R_{||}$ measured at two angles ($R_{||}$, Θ_1, Θ_2 method)

(v) Reflected intensities ratio ($I_\perp/I_{||}$) measured at three angles (E, Θ_1, Θ_2, Θ_3 method).

These results are shown in table 3.

3.5 Sensitivity and Optimization of Ellipsometric Method for Obtaining n and k

The sensitivity of the ellipsometric method is studied for $1 \leqslant n_o \leqslant 4$ and $1 \leqslant k_o \leqslant 4$ by the means of the following procedure.

For known values of n_o and k_o, Δ and ψ are calculated for angles of incidence $15^\circ \leqslant \Theta \leqslant 85^\circ$, using the following equations (derivable from equations (2.41) - (2.43)):

$$-\operatorname{Cot}\Delta = \frac{(p^2 + q^2 - t^2)}{2qt} \tag{3.2}$$

$$\operatorname{Sec} 2\psi = \frac{(p^2 + q^2 + t^2)}{2pt} \tag{3.3}$$

where

$$2p^2 = n_o^2 - k_o^2 - \operatorname{Sin}^2\Theta + \left[(n_o^2 - k_o^2 - \operatorname{Sin}^2\Theta)^2 + 4n_o^2k_o^2\right]^{\frac{1}{2}} \tag{3.4}$$

and

$$2q^2 = -n_o^2 + k_o^2 + \operatorname{Sin}^2\Theta + \left[(n_o^2 - k_o^2 - \operatorname{Sin}^2\Theta)^2 + 4n_o^2k_o^2\right]^{\frac{1}{2}} \tag{3.5}$$

Table 3

Method		$(R_\perp, R_\parallel, \theta)$			$(R_\perp/R_\parallel, \theta_1, \theta_2)$			(R, θ_1, θ_2)			$(R_\parallel, \theta_1, \theta_2)$			$(E, \theta_1, \theta_2, \theta_3)$		
		% error in			% error in			% error in			% error in			% error in		
n_o	k_o	n_o	k_o	$(n_o k_o)$	n_o	k_o	$(n_o k_o)$	n_o	k_o	$(n_o k_o)$	n_o	k_o	$(n_o k_o)$	n_o	k_o	$(n_o k_o)$
1.000	1.000	0.347	0.868	1.218	0.039	2.515	2.563	0.590	0.451	1.038	0.297	0.321	0.619	0.197	0.778	0.967
	2.000	0.968	1.504	2.487	0.436	0.617	1.050	1.057	0.714	1.764	0.385	0.365	0.752	0.591	0.619	1.202
	3.000	2.252	2.924	5.242	0.484	0.622	1.103	1.511	1.095	2.589	0.708	0.604	1.317	0.964	0.771	1.721
	4.000	4.054	5.644	9.927	1.257	1.187	2.429	1.904	1.464	3.340	0.955	0.841	1.804	1.435	1.036	2.445
2.000	1.000	0.252	0.747	1.000	0.116	0.130	0.246	0.676	0.383	0.296	0.133	0.045	0.178	0.208	0.087	0.295
	2.000	0.600	1.110	1.716	0.236	0.346	0.581	0.787	0.299	1.083	0.185	0.170	0.356	0.285	0.194	0.479
	3.000	1.130	2.092	3.246	0.377	0.416	0.791	0.955	0.580	1.529	0.308	0.282	0.591	0.403	0.281	0.682
	4.000	2.148	3.453	5.675	0.644	0.565	1.205	1.136	0.814	1.941	1.667	0.924	2.606	0.651	0.434	1.081
3.000	1.000	0.420	1.354	1.780	0.070	0.091	0.161	0.627	1.534	0.898	0.107	0.089	0.197	0.108	0.110	0.200
	2.000	0.793	1.108	1.910	0.183	0.164	0.347	0.714	0.014	0.728	0.188	0.134	0.322	0.163	0.059	0.222
	3.000	1.246	1.869	3.138	0.290	0.249	0.539	0.810	0.374	1.181	0.272	0.223	0.495	0.274	0.146	0.420
	4.000	2.941	3.010	5.009	0.765	0.493	1.274	0.914	0.583	1.492	0.424	0.337	0.763	0.425	0.248	0.672
4.000	1.000	0.498	9.157	9.700	0.104	0.227	0.330	0.991	4.964	3.924	0.231	0.533	0.303	0.068	0.014	0.075
	2.000	0.712	3.814	4.553	0.193	0.134	0.327	1.955	2.028	0.033	0.230	0.080	0.310	0.122	0.025	0.147
	3.000	1.143	3.175	4.353	0.305	0.210	0.514	0.747	0.212	0.957	0.292	0.192	0.484	0.217	0.081	0.298
	4.000	1.906	3.477	5.449	0.404	0.269	0.672	0.813	0.458	1.267	0.336	0.283	0.621	0.387	0.165	0.551

Using $\Delta = \Delta + 0.1^\circ$ and $\psi = \psi - 0.1^\circ$, n and k are calculated from equations (2.41) - (2.43). The quantity σ (defined by equation 3.1) is then calculated for angles of incidence $15^\circ \leq \theta \leq 85^\circ$.

The variation of σ with θ for some combinations of n_o and k_o is shown in figure 14. It is evident from the figure that for some combinations of n_o and k_o, the percentage error in the product $(n_o k_o)$ can be large at certain angles of incidence. Thus the optimum angles are found for $1 \leq n_o \leq 4$ and $1 \leq k_o \leq 4$ and are given in Table 4.

The whole procedure is repeated for an error of 0.1° in θ, it is found that $0.9 < \sigma < 2.0$ for $1 \leq n_o \leq 4$, $1 \leq k_o \leq 4$ and for all optimum angles given in Table 4. For $52^\circ \leq \theta \leq 57^\circ$ the errors are less than 1%.

Thus if the approximate values of optical constants are known, an optimum angle (not very close to the Brewster angle) can be chosen.

If only one angle of incidence is to be used for different specimens, then it is recommended to use an angle between 55° and 57°, because

i) The Brewster angle does not lie in this range for $1 \leq n_o \leq 4$ and $1 \leq k_o \leq 4$.

ii) Δ and ψ have been commonly measured to better than $\pm 0.02^\circ$, and in that case σ due to these errors in Δ and ψ will be much less than mentioned in Table 4. The percentage error in product $(n_o k_o)$ due to an error in angle of incidence will then be dominant, and is less than 1% at these angles for an error of $.1^\circ$ in θ and for $1 \leq n_o \leq 4$ and $1 \leq k_o \leq 4$.

iii) The percentage errors in the product $(n_o k_o)$ due to an error

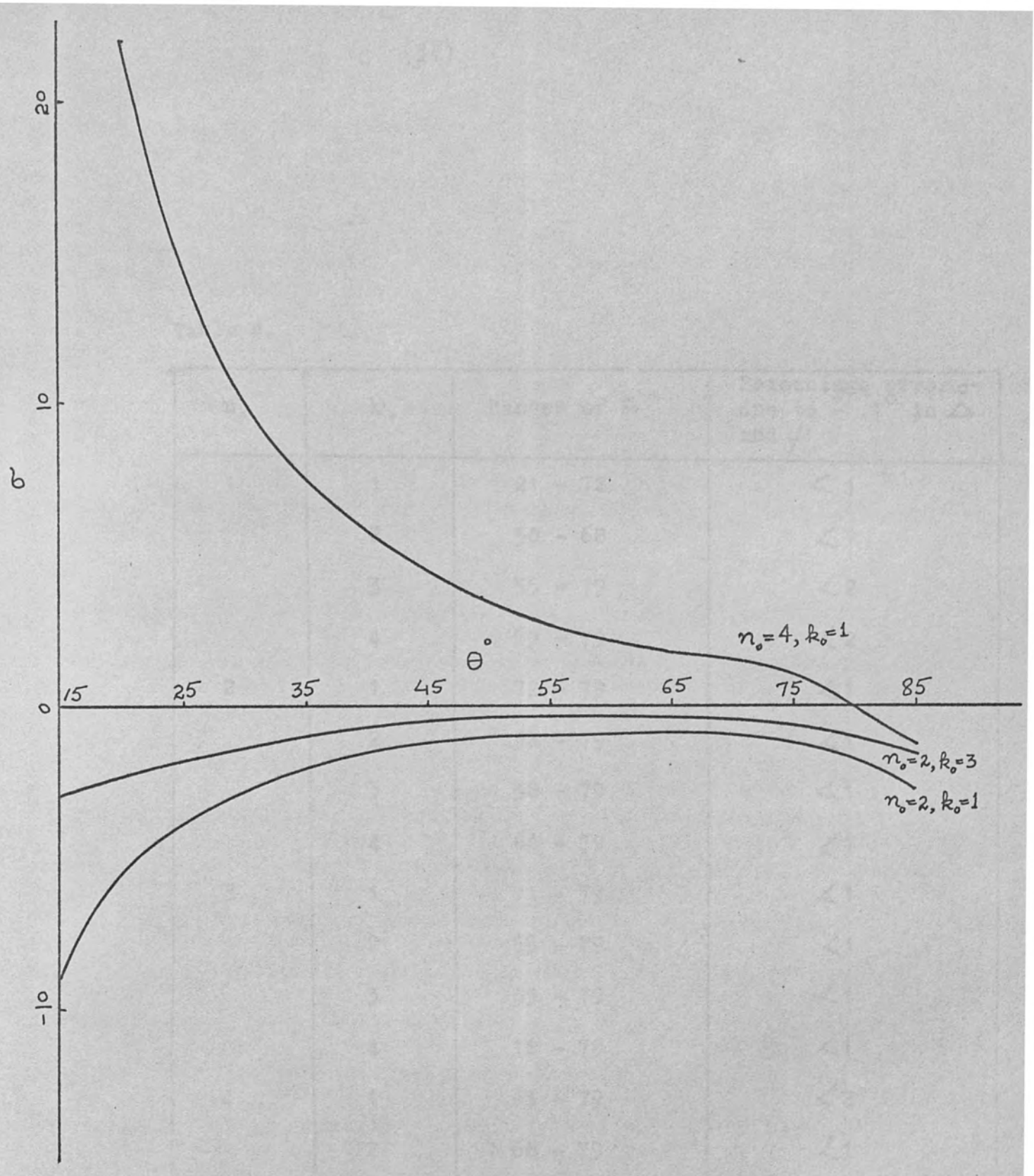

Figure 14: Variation of σ with angle of incidence θ for errors of $\pm 0.1^{\circ}$ in Δ and ψ .

Table 4.

n_o	k_o	Ranges of θ°	Percentage error σ due to $\pm .1^\circ$ in Δ and ψ
1	1	21 - 72	<1
	2	58 - 68	<1
	3	55 - 79	<2
	4	69 - 79	<2
2	1	72 - 79	<1
	2	32 - 79	<1
	3	38 - 79	<1
	4	64 - 79	<1
3	1	71 - 79	<1
	2	55 - 79	<1
	3	39 - 79	<1
	4	18 - 79	<1
4	1	63 - 79	<2
	2	68 - 79	<1
	3	58 - 79	<1
	4	45 - 79	<1

Percentage error σ due to $.1^\circ$ in θ is less than 2% for all n_o and k_o.

of $\pm$ .1° in Δ and ψ are less than 2% at these angles, except for $n_o = 1$, $k_o = 4$ and $n_o = 4$, $k_o = 1$, where σ is less than 3.5%.

3.6 Comparison of Sensitivities of Polarimetric and Non-Polarimetric Methods

A direct comparison of sensitivities is difficult because of the experimental conditions involved in the two methods.

In ellipsometry, the problem of measuring Δ and ψ for a perfectly clean surface has been discussed by Archer (1968). Even for the cleanest surfaces maintained in the ultra high vacuum, measurements are complicated by the effect on Δ and ψ of strain birefringence in cell windows. It is necessary with windows to measure independently the strain double refraction and correct Δ and ψ empirically (Archer, 1968). With or without windows, the thickness of the unavoidable surface film must be stabilised during the measurement and must be known with sufficient accuracy to correct Δ and ψ (the procedure is discussed in "Manual on Ellipsometry" by Archer).

Thus polarimetric methods can yield more information about surface films often with greater accuracy, than non-polarimetric methods. However, the polarimetric methods when compared with non-polarimetric methods, are experimentally more cumbersome if dispersion measurements are required, and are certainly more expensive. Moreover, the very sensitivity of the method to surface films can prove a disadvantage if measurements of the bulk material properties are required.

3.7 Optimum Angles of Incidence for the Determination of Magneto-Optical Parameters

An optimization study has been performed for the derivation of magneto-optical parameters in visible and ultra-violet regions of the spectrum from experimental measurements of the transverse Kerr effect. The optimization is carried out using the largest available range of experimental n, k, Q_1, and Q_2 (i.e. $1 \leq n \leq 3$, $2 \leq k \leq 4$, $0.002 \leq Q_1 \leq 0.055$, $-0.01 \leq Q_2 \leq 0.01$) (Krinchik, 1959, a and b) and for angles of incidence. To assist in the calculations, computer programmes were written in FORTRAN IV and run on CDC 6600 computer.

Equation (2.62) can be written as

$$\gamma = RQ_1 - SQ_2 \tag{3.6}$$

where

$$R = \frac{2 \sin 2\Theta \left(2nk \cos^2\Theta - \frac{2nk \sin^2\Theta}{(n^2+k^2)^2}\right)}{\left(2nk \cos^2\Theta - \frac{2nk \sin^2\Theta}{(n^2+k^2)^2}\right)^2 + \left((n^2-k^2)\cos^2\Theta - 1 + \frac{(n^2-k^2)\sin^2\Theta}{(n^2+k^2)^2}\right)^2} \tag{3.7}$$

and

$$S = \frac{2 \sin 2\Theta \left((n^2-k^2)\cos^2\Theta - 1 + \frac{(n^2-k^2)\sin^2\Theta}{(n^2+k^2)^2}\right)}{\left(2nk \cos^2\Theta - \frac{2nk \sin^2\Theta}{(n^2+k^2)^2}\right)^2 + \left((n^2-k^2)\cos^2\Theta - 1 + \frac{(n^2-k^2)\sin^2\Theta}{(n^2+k^2)^2}\right)^2} \tag{3.8}$$

The effect of R and S on γ, and the variation of γ with Θ are first considered. Calculation of R for all values of n_o, k_o, (the actual values) and Θ shows R to be positive for most Θ but negative for higher values of Θ. The results are summarized in Table 5. For ferromagnetic metals $k > n$ and hence S is always negative (equation 3.8).

Calculation of γ for angles of incidence in the range 0° to 90° at 0.5° intervals, and all available Q_1 and Q_2 (Q_1 and Q_2 are taken in

small steps over the range defined above)shows that γ is positive for Q_2 positive, and positive or negative for Q_2 negative. (No experimental values of Q_1 were negative). Figure 15 shows the three general shapes of the curves for the variation of γ with θ. The positions of the peaks and intercepts vary accordingly to n_o, k_o, Q_1 and Q_2, such that (referring to Figure 15)

curve (a) γ +ve — max. γ in range 57° - 82°

(b) γ -ve — min. γ in range 69° - 82°

(c) γ +ve, or, γ-ve — max. in range 34° - 74°

intercept in range 51° - 87°

min. in range 76° - 89°

Table 5.

Angles of incidence at which R becomes negative for different n_o, k_o combinations

n_o	k_o	θ°
1	2	78
1	3	85
1	4	87
2	3	86
2	4	88
3	4	88

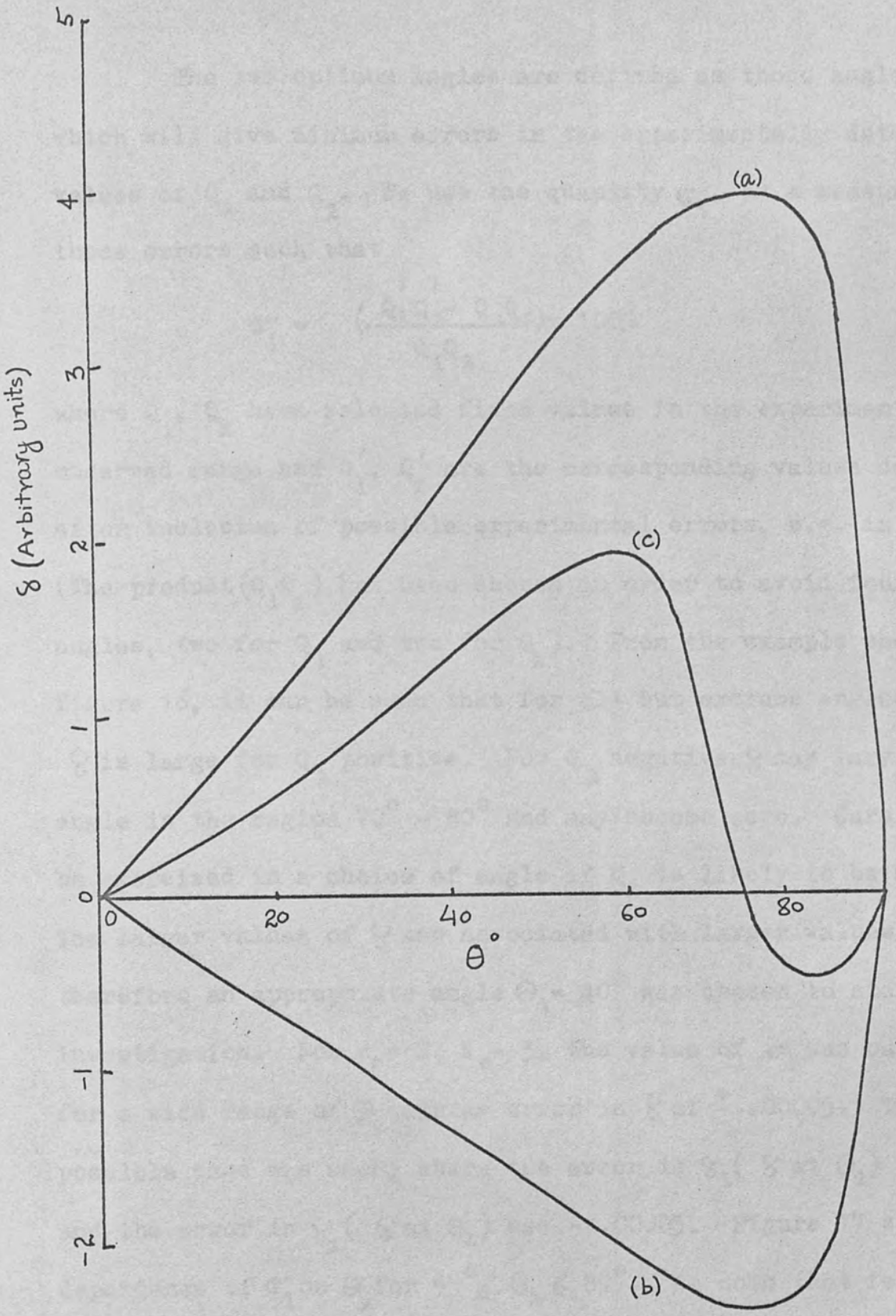

Figure 15: General shape of curves of δ vs. θ.

The two optimum angles are defined as those angles which will give minimum errors in the experimentally determined values of Q_1 and Q_2. We use the quantity σ_1, as a measure of these errors such that

$$\sigma_1 = \frac{(Q_1 Q_2 - Q_1' Q_2')}{Q_1 Q_2} \times 100\% \qquad (3.9)$$

where Q_1, Q_2 have selected fixed values in the experimentally observed range and Q_1', Q_2' are the corresponding values calculated after inclusion of possible experimental errors, e.g. in γ, Θ, n_o and k_o. (The product $(Q_1 Q_2)$ has been chosen in order to avoid four optimum angles, two for Q_1 and two for Q_2). From the example shown in figure 16, it can be seen that for all but extreme angles of incidence, γ is large for Q_2 positive. For Q_2 negative γ may vary rapidly with angle in the region 70° - 80° and may become zero. Care must therefore be exercised in a choice of angle if Q_2 is likely to be negative. The larger values of γ are associated with larger values of R and therefore an appropriate angle $\Theta_1 = 40^\circ$ was chosen to start the investigation. For $n_o = 2$, $k_o = 3$, the value of σ_1 was calculated for a wide range of Θ_2 with an error in γ of $\pm$ .00005. The worst possible case was used, where the error in γ_1 (γ at Θ_1) was + .00005 and the error in γ_2 (γ at Θ_2) was - .00005. Figure 17 shows the dependence of σ_1 on Θ_2 for $55^\circ \leq \Theta_2 \leq 89^\circ$. We note that for $1^\circ \leq \Theta_1 \leq 54^\circ$, $\sigma_1 > 100\%$ and σ_1 is minimum for $80^\circ \leq \Theta_2 \leq 85^\circ$. σ_1 was then calculated for a range of Θ_1, using $\Theta_2 = 83^\circ$ so as to produce figure 18, from which a better optimum value of $\Theta_1 (\approx 60^\circ)$ was obtained. More

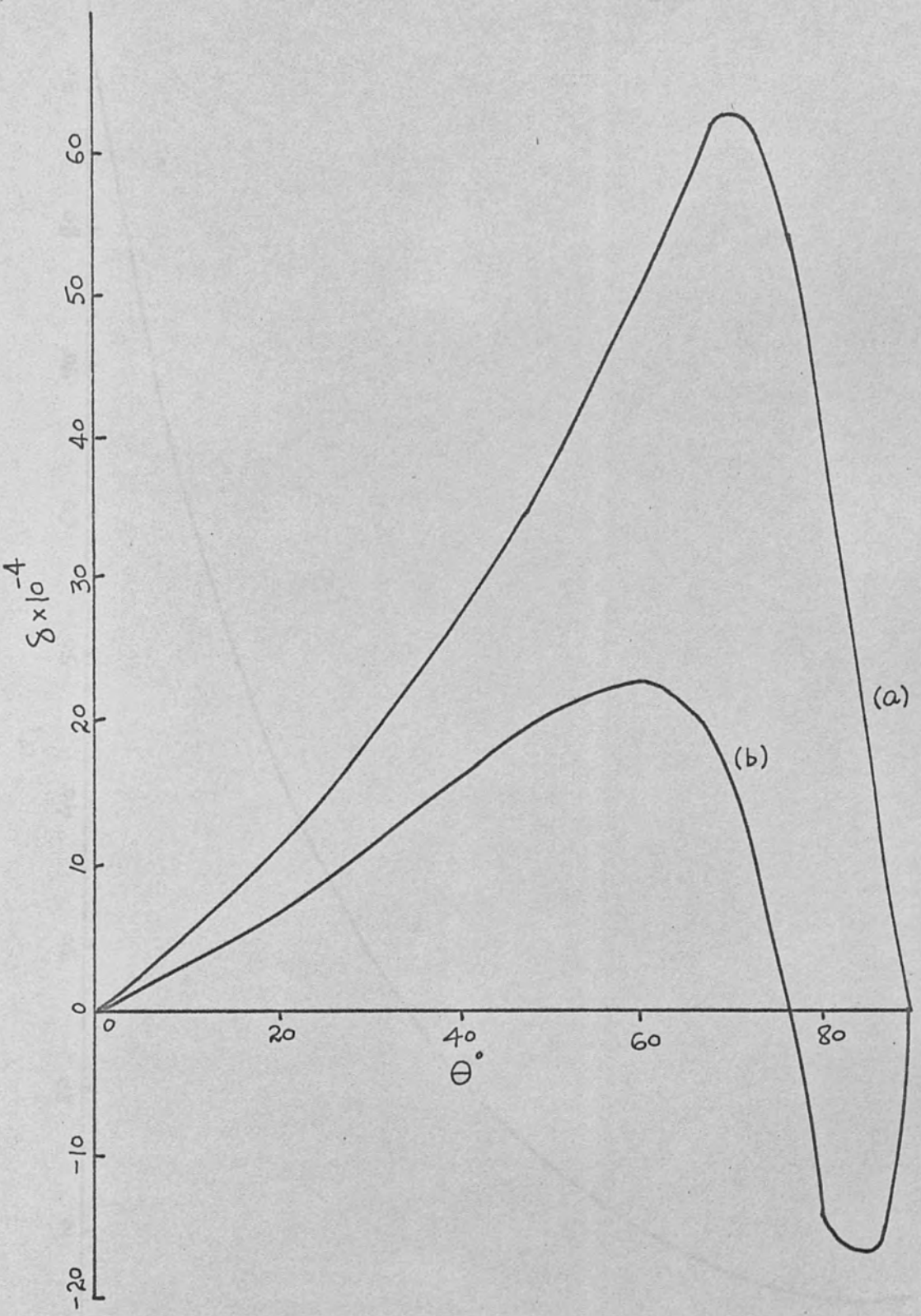

Figure 16: δ versus θ ($n_o = 2$, $k_o = 3$)

curve (a): $Q_1 = 0.01$, $Q_2 = 0.005$

curve (b): $Q_1 = 0.01$, $Q_2 = -0.005$

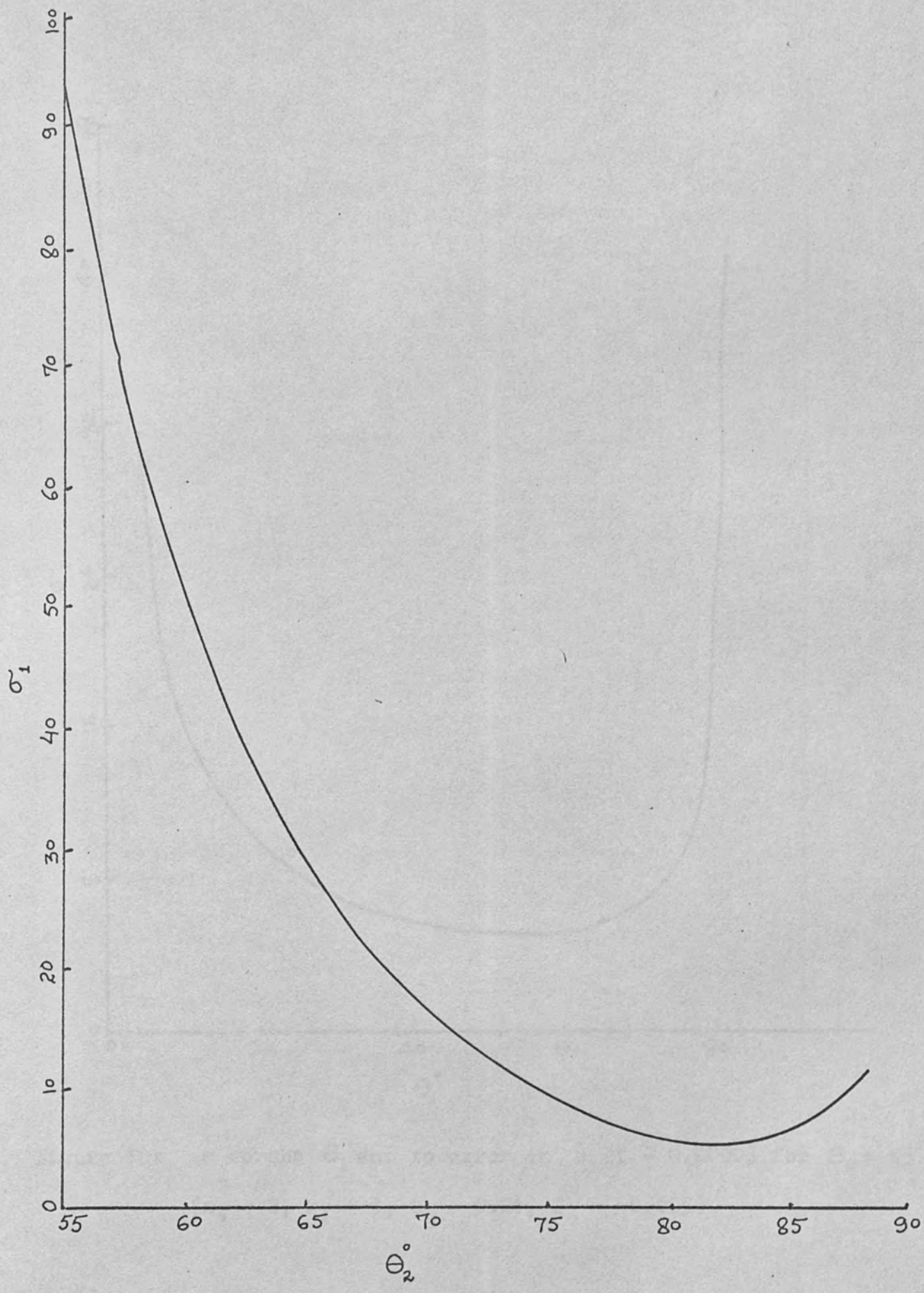

Figure 17: σ_1 versus θ_2 due to error in δ of $\pm$ 0.00005 for $\theta_1 = 40^0$.
($n_o = 2$, $k_o = 3$, $Q_1 = 0.01$, $Q_2 = -0.005$)

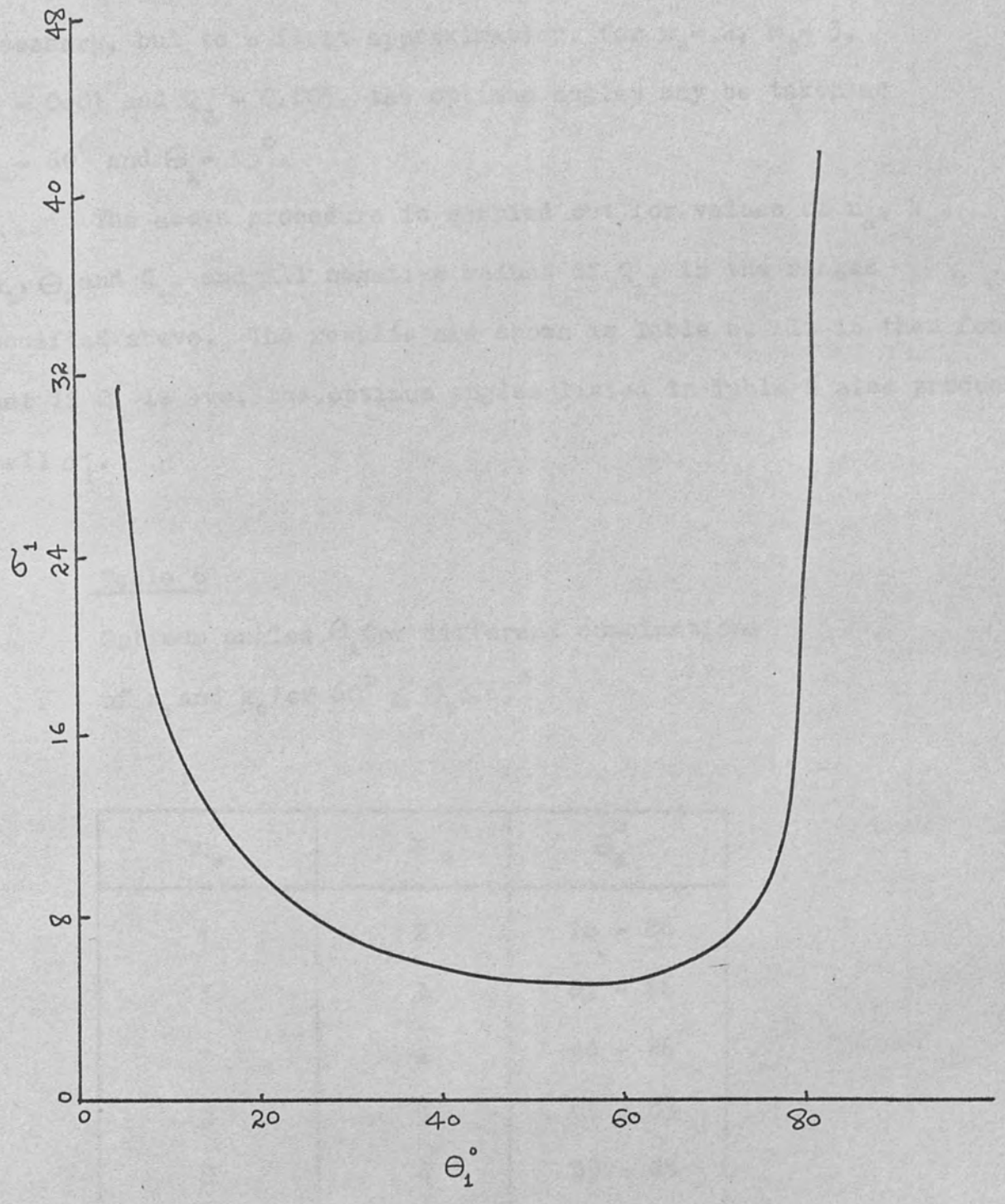

Figure 18: σ versus θ_1 due to error in δ of $\pm$ 0.00005 for $\theta_2 = 83^\circ$

($n_o = 2$, $k_o = 3$, $Q_1 = 0.01$, $Q_2 = -0.005$)

precise optimization of Θ_2 may be performed, using $\Theta_1 = 60^\circ$, if necessary, but to a first approximation, for $n_o = 2$, $k_o = 3$, $Q_1 = 0.01$ and $Q_2 = 0.005$, the optimum angles may be taken as $\Theta_1 = 60^\circ$ and $\Theta_2 = 83^\circ$.

The above procedure is carried out for values of n_o, k_o, Θ_1, Θ_2 and Q_1, and all negative values of Q_2, in the ranges specified above. The results are shown in Table 6. It is then found, that if Q_2 is +ve, the optimum angles listed in Table 6 also produce small σ_1.

Table 6

Optimum angles Θ_2 for different combinations of n_o and k_o for $60^\circ \leq \Theta_1 \leq 65^\circ$

n_o	k_o	Θ_2°
1	2	78 - 86
1	3	83 - 86
1	4	83 - 86
2	3	83 - 85
2	4	83 - 86
3	4	83 - 86

It is now desirable to examine the inherent errors in the experimentally determined values of Q_1 and Q_2 using the determined optimum angles. The result showed that as Q_2 became very small σ_1 increased. When Q_1 and Q_2 were both very small σ_1 was also large. In general for $Q_1 < 0.01$ and $-0.002 \leq Q_2 \leq 0.002$ the σ_1 was found to be greater than 10%.

The effect on σ_1 of an error in (n,k) values from which Q_1 and Q_2 were calculated was now considered. σ_1 was calculated for an error in n_o and k_o of $\pm$ .05 throughout the whole range of Q_1 and Q_2 values. As before, the worst case for error was used i.e. where the error in n_o was + .05 and the error in k_o was - .05. The angles of incidence are taken from Table 6 such that $60^\circ \leq \Theta_1 \leq 65^\circ$ and $83^\circ \leq \Theta_2 \leq 85^\circ$. σ_1 was found to be extremely small for all Q_1, Q_2 combinations mentioned above. The range of Q_1 and Q_2 values for which $\sigma_1 > 10\%$ fell within the range of Q_1 and Q_2 values stated in the above paragraph of this section.

σ_1 was also calculated for an error of $\pm 0.1^\circ$ in the setting of the optimum angles of incidence (again the worst case is considered where the error was $+0.1^\circ$ in Θ_1 and -0.1° in Θ_2). The combinations of Q_1 and Q_2 where $\sigma_1 > 10\%$ is again found to fall within the exclusion range stated above.

Thus the optimum angles of incidence are $60^\circ \leq \Theta_1 \leq 65^\circ$ and $83^\circ \leq \Theta_2 \leq 85^\circ$ for the range of magneto-optical parameter values typical of ferromagnetic materials in the visible and ultra-violet range of spectrum.

3.8 Errors in Reflectances and Reflectance Ratio due to an Error in Polarizer Setting

The errors in $R_{\parallel}$, $R_{\perp}$ and ψ ($=\frac{R_{\perp}}{R_{\parallel}}$) due to an error in polarizer setting have been investigated for $1^{\circ} \leq \theta \leq 85^{\circ}$.

If $R_{\parallel}$, $R_{\perp}$ and ψ are the real values, and $R_{\parallel e}$, $R_{\perp e}$ and ψ_e are the values obtained due to an error in incident polarization azimuth then

$$\% \text{ error in } R_{\parallel} = \frac{|R_{\parallel} - R_{\parallel e}|}{R_{\parallel}} \times 100$$

$$\% \text{ error in } R_{\perp} = \frac{|R_{\perp} - R_{\perp e}|}{R_{\perp}} \times 100 \qquad (3.10)$$

$$\% \text{ error in } \psi = \frac{|\psi - \psi_e|}{\psi} \times 100$$

Using known values of n_o, k_o, the quantities $R_{\parallel}$, $R_{\perp}$ and ψ are calculated for a given θ from equations (2.6) - (2.9). The error in ϕ is then taken as $\pm 1.0^{\circ}$ and $R_{\parallel e}$, $R_{\perp e}$ and hence ψ_e are calculated using equation (2.22). The percentage error is then found using the above equations.

The above procedure was performed for all $1^{\circ} \leq \theta \leq 85^{\circ}$ and for $1 \leq n_o \leq 4$ and $1 \leq k_o \leq 4$. The% errors in $R_{\parallel}$, $R_{\perp}$ and ψ vary with angle of incidence θ. The maximum percentage errors in $R_{\parallel}$, $R_{\perp}$ and ψ for different combinations of n_o and k_o are given in Table 7.

It is evident from Table 7 that for metals ($k > n$) the errors are very small ($\ll .2\%$ as taken for Table 4), whereas for dielectrics the errors are relatively large. Hence for a dielectric a more

Table 7

n_o	k_o	Maximum % errors in $R_{\parallel}$	Maximum % errors in $R_{\perp}$	Maximum % errors in φ
1	1	0.082	0.022	0.104
	2	0.039	0.017	0.056
	3	0.025	0.014	0.039
	4	0.019	0.012	0.030
2	1	0.370	0.029	0.398
	2	0.122	0.025	0.146
	3	0.068	0.021	0.089
	4	0.046	0.019	0.065
3	1	0.931	0.030	0.961
	2	0.265	0.027	0.292
	3	0.135	0.025	0.160
	4	0.086	0.023	0.109
4	1	1.742	0.030	1.772
	2	0.467	0.029	0.496
	3	0.227	0.027	0.254
	4	0.140	0.025	0.165

$1 \leq \theta \leq 85$

accurate polarizer setting is needed than for a metal.

CHAPTER IV

THE REFLECTOMETER SYSTEM FOR DETERMINING OPTICAL AND MAGNETO-OPTICAL CONSTANTS FOR THICK ABSORBING FILMS

4.1 Introduction:

The difficulties associated with the determination of optical constants from separate reflectances are discussed in this chapter and the reasons given for choosing a reflectance ratio method. The reflectometer was a modified version of the instrument used by Taylor (1972) and is capable of yielding data which is analyzable by various non-polarimetric methods (Chapter II) to obtain optical constants of opaque or transparent absorbing films

4.2 Reflectance Ratio Measurements

The measurement of absolute reflectances presents some difficulties which will be briefly discussed below.

(a) When measuring absolute reflectances some spatial re-arrangement of the system is necessary in order to measure the incident beam under near identical conditions (e.g. same photo-sensitive surface of the detector, same intensity of the source while taking measurements) to those for which the reflected intensity is measured. Rearrangement is likely to introduce errors into the determination through small differences in optical path for the two measurements.

(b) Another problem associated with absolute reflectance measurements is the large decrease in effective aperture of the

reflecting surface as the angle of incidence is increased. As in many cases where the optical constants of single crystals, etc. are being determined, the specimens available tend to be rather small, and since in no case must the specimen itself become the limiting aperture of the optical system, it follows that the beam cross section used must be very small, with consequent loss in intensity if beams of only small divergence are to be employed.

The reflectance ratio method and the "three angles" intensity ratio method (described in Chapter II) have, however, the following advantages:

i) No absolute measurements of light intensity are required, provided that for the reflectance ratio method, the components of light incident on the polarizer in the two planes of polarisation are of equal intensity or in a known ratio. This can be arranged by a suitable depolarizer (Portigal 1969) or an initial calibration.

ii) No errors are introduced if the specimen becomes the limiting aperture at high angles of incidence, because the aperture is the same for both components of polarisation.

iii) In these methods, only a simple rotation of the polarizer is needed, rather than the most complex rearrangements required in accurate absolute reflectance measurements.

iv) These methods are particularly suitable for measurement on a sample in vacuum or other enclosure when the source and detector optics are outside the sample cell. Whereas the windows must be calibrated for most other methods of obtaining n and k under these conditions, this is not necessary for the ratio

methods, because the optical geometry is identical for each component in the ratio, provided that the light passes normally through nondichroic windows.

The reasons for preferring the reflectance ratio method to the "three angles" method will be given in the next section.

4.3 Variation of Reflectance and Reflected Intensity with Incident Polarization Azimuth ϕ for Thick Specimens

Differentiating equation (2.22) and putting $\frac{dR_\phi}{d\phi} = 0$ for maximum and minimum in R_ϕ, we have

$$\cos\phi \sin\phi (R_\perp - R_{||}) = 0 \qquad (4.1)$$

Since $(R_\perp - R_{||}) = 0$ is only true for normal incidence, either $\cos\phi = 0$ or $\sin\phi = 0$ for non-normal incidence.

Substituting $\cos\phi = 0$ in equation (2.22), we have

$$R_\phi = R_\perp \qquad (4.2)$$

and substituting $\sin\phi = 0$ in equation (2.22), we have

$$R_\phi = R_{||} \qquad (4.3)$$

Calculation of $R_\perp$ and $R_{||}$ from Fresnel reflectance equations over a wide range of values for $n \leq 4$, $k \leq 4$ and $\theta (\neq 0)$, indicates that $R_\perp$ is always greater than $R_{||}$. This implies that R_ϕ will have a maximum value $R_\perp$ at $\phi = 90^\circ$ and a minimum value $R_{||}$ at $\phi = 0^\circ$. Figure 19 shows the variation of R_ϕ with ϕ for $n = 2$, $k = 3$ and for two angles of incidence 60° and 80°.

Writing equation (2.22) in terms of reflected and incident intensities

$$\frac{I_\phi}{I_{o\phi}} = \frac{I_{||}}{I_{o||}} \cos^2\phi + \frac{I_\perp}{I_{o\perp}} \sin^2\phi$$

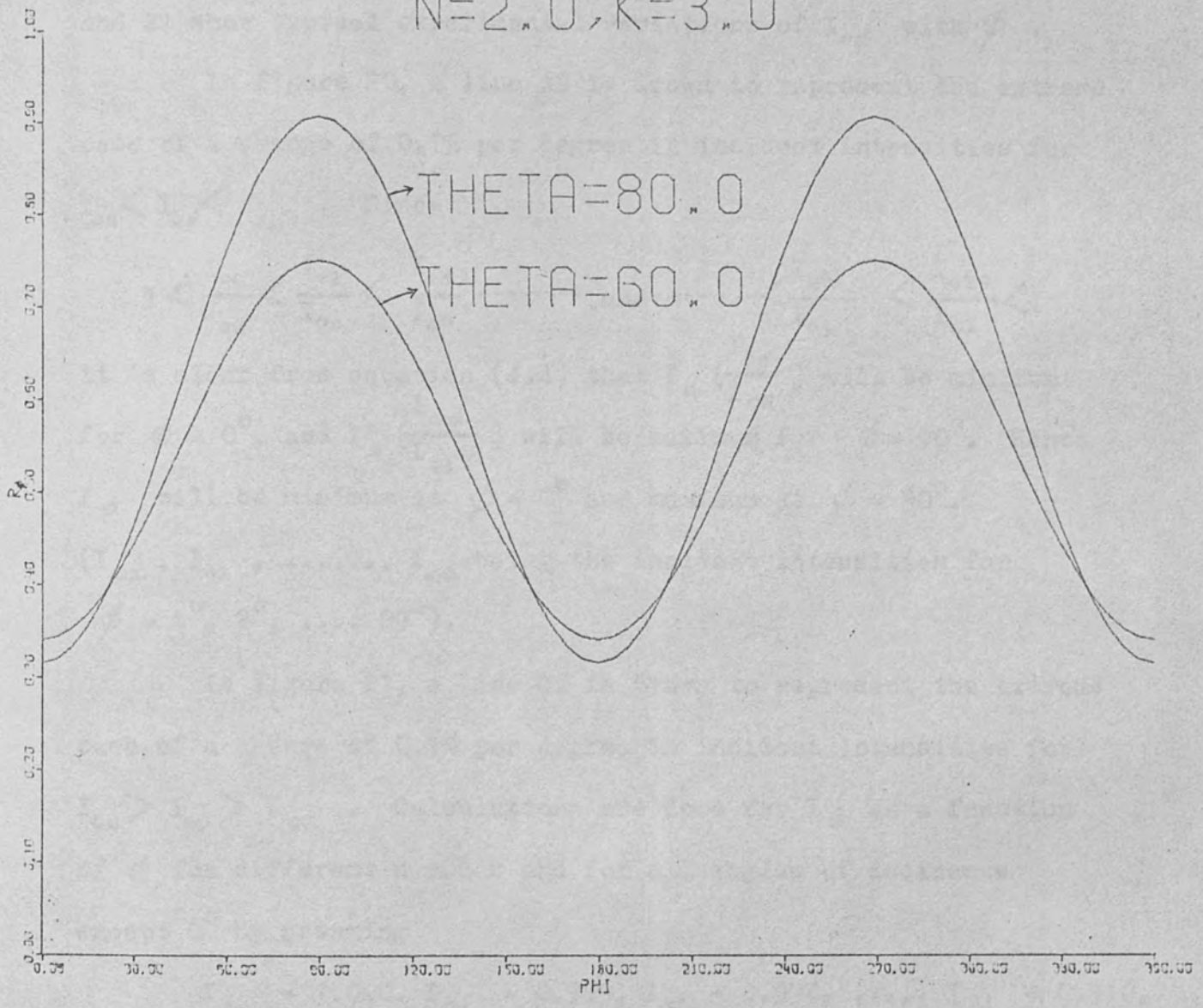

Figure 19: Variation of R_ϕ with ϕ .

or $$I_\phi = I_{\parallel} \left(\frac{I_{o\phi}}{I_{o\parallel}}\right) \cos^2\phi + I_{\perp}\left(\frac{I_{o\phi}}{I_{o\perp}}\right) \sin^2\phi \qquad (4.4)$$

If $I_{o\phi} = I_{o\parallel} = I_{o\perp}$, I_ϕ will vary with ϕ exactly in the same way as R_ϕ. In practice this condition is difficult to obtain, $I_{o\phi}$ variesrandomly with ϕ and a change of not more than 0.1% per degree of the rotation of polarizer is generally observed. Figure 20 and 21 show typical experimental variations of $I_{o\phi}$ with ϕ.

In Figure 20, a line AB is drawn to represent the extreme case of a change of 0.1% per degree in incident intensities for $I_{o\parallel} < I_{o\phi} < I_{o\perp}$. Since

$$1 < \frac{I_{o1}}{I_{o\parallel}} < \frac{I_{o2}}{I_{o\parallel}} < \frac{I_{o3}}{I_{o\parallel}} \text{ --------, and --------} < \frac{I_{o88}}{I_{o\perp}} < \frac{I_{o89}}{I_{o\perp}} < 1$$

it is clear from equation (4.4) that $I_{\parallel}\left(\frac{I_{o\phi}}{I_{o\parallel}}\right)$ will be minimum for $\phi = 0^\circ$, and $I_{\perp}\left(\frac{I_{o\phi}}{I_{o\perp}}\right)$ will be maximum for $\phi = 90^\circ$. Hence I_ϕ will be minimum at $\phi = 0^\circ$ and maximum at $\phi = 90^\circ$. (I_{o1}, I_{o2}, ..., I_{o89} being the incident intensities for $\phi = 1^\circ, 2^\circ, \ldots. 89^\circ$).

In Figure 21, a line CD is drawn to represent the extreme case of a change of 0.1% per degree in incident intensities for $I_{o\parallel} > I_{o\phi} > I_{o\perp}$. Calculations are done for I_ϕ as a function of ϕ for different n and k and for all angles of incidence except 0° by assuming

$$I_{o\parallel} = 1.000,\ I_{o1} = 0.999,\ I_{o2} = 0.998,\ \ldots.,\ I_{o\perp} = 0.910,$$

which shows that $I_\perp$ and $I_\parallel$ can be taken as the maximum and minimum values of I_ϕ for $45^\circ \leq \theta \leq 85^\circ$ and for all thick specimens for which $n \geq 1$ and $k \leq 4$. The maximum% errors in reflectance ratios

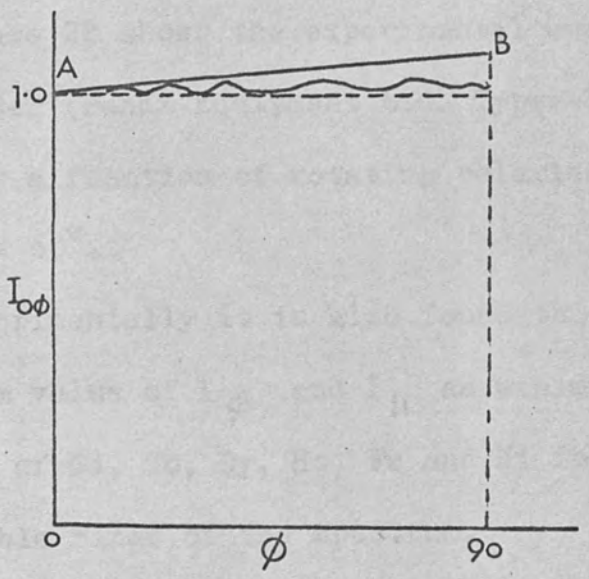

Figure 20: Variation of $I_{o\phi}$ with ϕ $(I_{o\perp} > I_{o\parallel})$

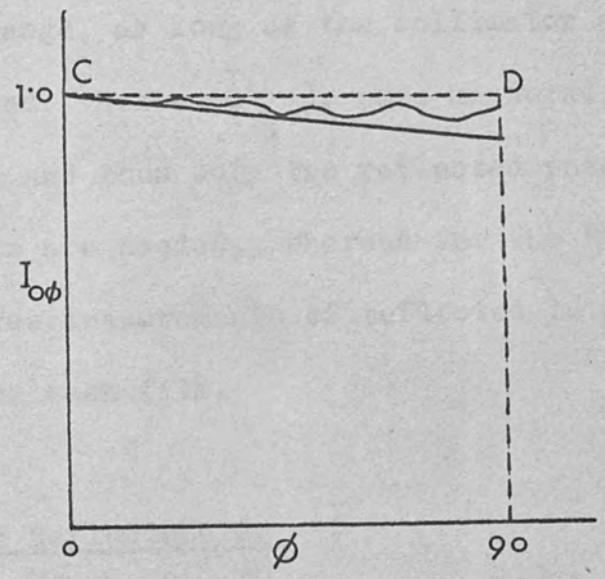

Figure 21: Variation of $I_{o\phi}$ with ϕ $(I_{o\perp} < I_{o\parallel})$

arising in taking $I_{\perp}$ and $I_{\parallel}$ as maximum values and minimum values of I_{ϕ} are shown in Table 8.

Figure 22 shows the experimental curve obtained on a chart recorder (Panax Equipment Ltd. Type:-SREC2P) for reflected intensity as a function of rotating polarizer for a thick holmium film at $\Theta = 60^{\circ}$.

Experimentally it is also found that $I_{\perp}$ can be taken as a maximum value of I_{ϕ} and $I_{\parallel}$ as minimum value of I_{ϕ} for thick films of Gd, Tb, Dy, Ho, Fe and Ni for all the wavelengths in the visible range of the spectrum.

Since angles of incidence $\leqslant 21^{\circ}$ (range of one of the optimum angle for three angles method) fell outside the range mentioned above, the reflectance ratio method is preferred over the three angles method. Also it is found that the ratio $(\frac{I_{o\perp}}{I_{o\parallel}})$ does not change, as long as the collimator and polarizer are not disturbed. Hence $(\frac{I_{o\perp}}{I_{o\parallel}})$, once measured, can be used for many films, and thus only two reflected intensities ratio measurements are needed, Whereas for the "three angles" method, three measurements of reflected intensities ratio are required for each film.

4.4. The Reflectometer

A reflectometer was devised and constructed for measuring reflectance ratios of metal films at non-normal incidence.

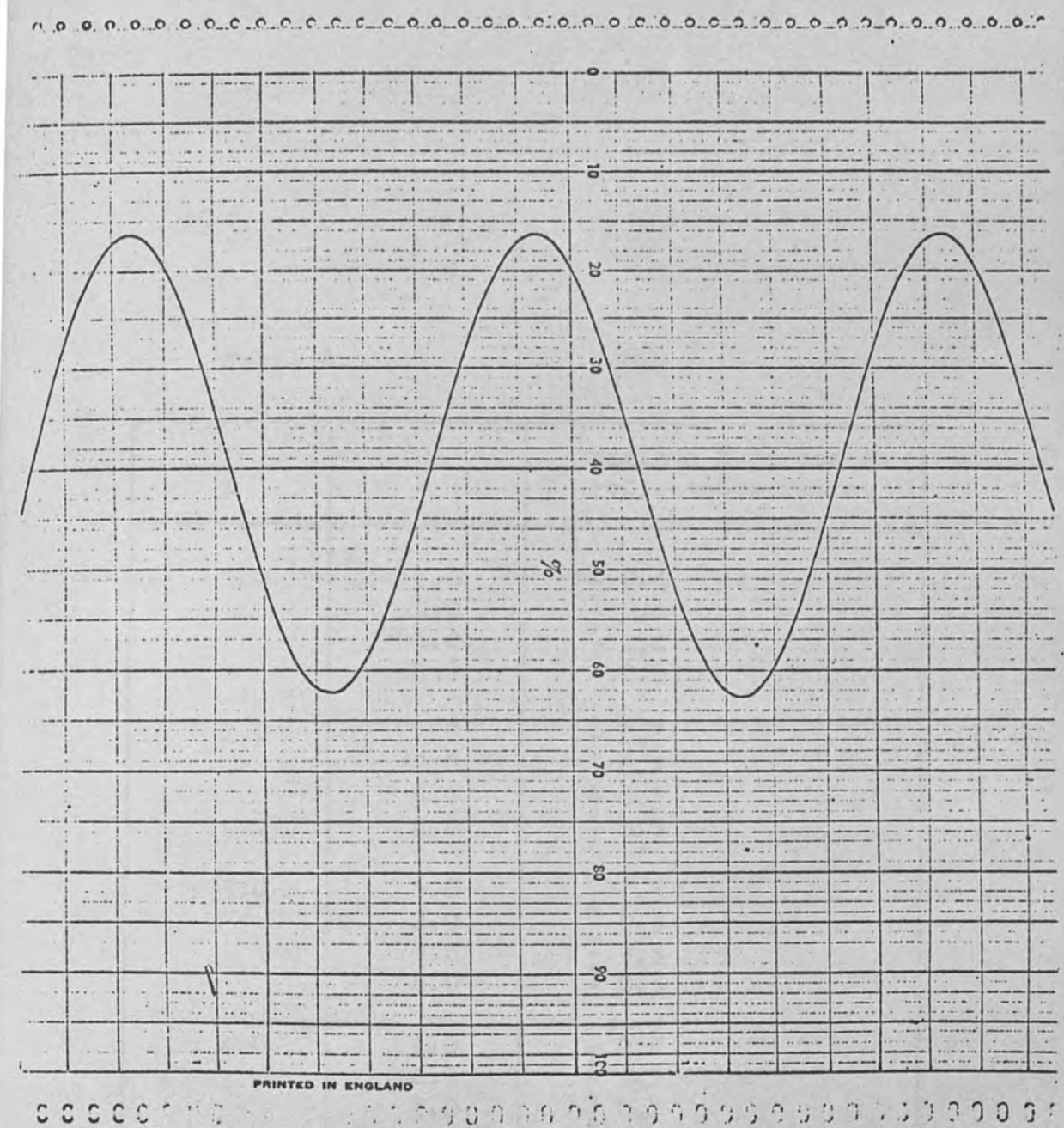

Figure 22: Experimental curve on a chart recorder of reflected intensities with the rotation of polarizer for Ho film at $\theta = 60^{\circ}$.

Table 8

n	k	maximum % errors in reflectance ratio
1.0	1.0	± 0.4
	2.0	± 0.4
	3.0	± 0.4
	4.0	± 0.5
2.0	1.0	± 0.3
	2.0	± 0.2
	3.0	± 0.3
	4.0	± 0.3
3.0	1.0	± 0.3
	2.0	± 0.3
	3.0	± 0.3
	4.0	± 0.3
4.0	1.0	± 0.2
	2.0	± 0.2
	3.0	± 0.2
	4.0	± 0.2
3.0	0.2	± 0.2

$45 \leqslant \theta \leqslant 85$

In addition, using a special optical cell (described in Section 4.6), optical and magneto-optical measurements could be obtained for films in vacuum and at low temperatures, using the same reflectometer.

The essential components of the reflectometer were a source, a collimator with a filter, a rotating polarizer, a $7\frac{1}{2}$ inch circular scale spectrometer table and a detecting system. The reflectometer is shown in Figure 23.

The light source used was a quartz halogen lamp enclosed in a water-cooled housing. The lamp was powered by a highly stabilized direct current supply (Farnell Ltd, Type: B30/20) capable of delivering up to 30 amps. The intensity drift using this 200 watt halogen lamp and stabilized power supply was generally found to be less than 1% per hour.

The collimator comprised a slit, and a lens of focal length 20 cms. manufactured from spectrosil B. A circular graded filter (Barr and Stroud Type: CGS 1) was used to produce monochromatic radiation in the range 4000A° - 7000A°. The band-width of the filter was typically 150A° and the transmission of the filter 25% throughout the spectral range. The whole range could be obtained for a 300° rotation of the filter. The filter was mounted on a bearing, the axis of which was made parallel to the optical axis of the system. The bearing was rotated by a bi-directional electric motor mounted co-axially with a precision circular potentiometer. The speed of the motor was fixed at 0.2 revolutions/minute. The output from the potentiometer indicated

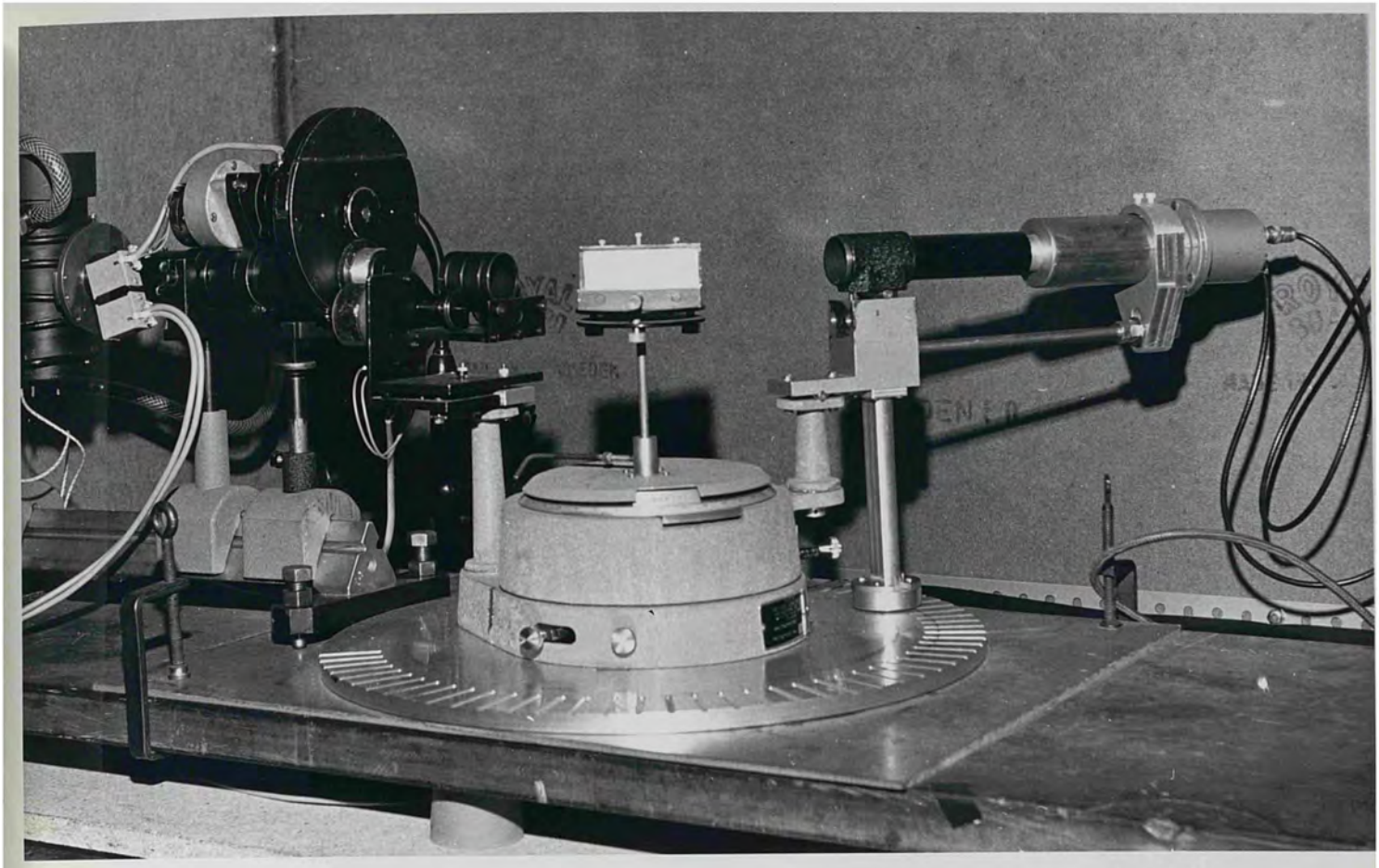

FIGURE 23

the angular setting of the filter to a degree of precision much better than the bandwidth of the filter.

The rotating polarizer system consisted of a polaroid sheet mounted on a brass cylinder of diameter 3.5 cm. and length 4.2 cm. The cylinder which had three locating grooves around its circumference, was rested on rubber rings fitted on three metal discs, one on the left hand side and the other two on the right hand side when seen from the detector side. A metal plate was fixed to the arm of the spectrometer table (the arm on which the collimator is fixed in the normal spectrometer) with the help of two screws and a small cylindrical rod. The whole rotating arrangement was attached to this plate by a cylindrical rod of diameter 0.62 cm, two springs and two screws. By adjusting these screws the polaroid sheet could be adjusted so that the incident beam fell nearly normal to it. The cylinder containing the polaroid sheet could be rotated by means of a uni-directional electric motor driving the disc on the left-hand side. There was no beam movement when the cylinder was rotated. The time taken by the cylinder for one complete rotation was $80.5 \pm .5$ secs. Figure 24 shows the rotating system for the polarizer together with the lamp, collimator and filter.

The base of the spectrometer table (Ealing Scientific Ltd. Type No: A26/4580) was fixed coaxially, by means of screws, to a circular duralumin base of thickness 1.2 cm and diameter 45 cm.

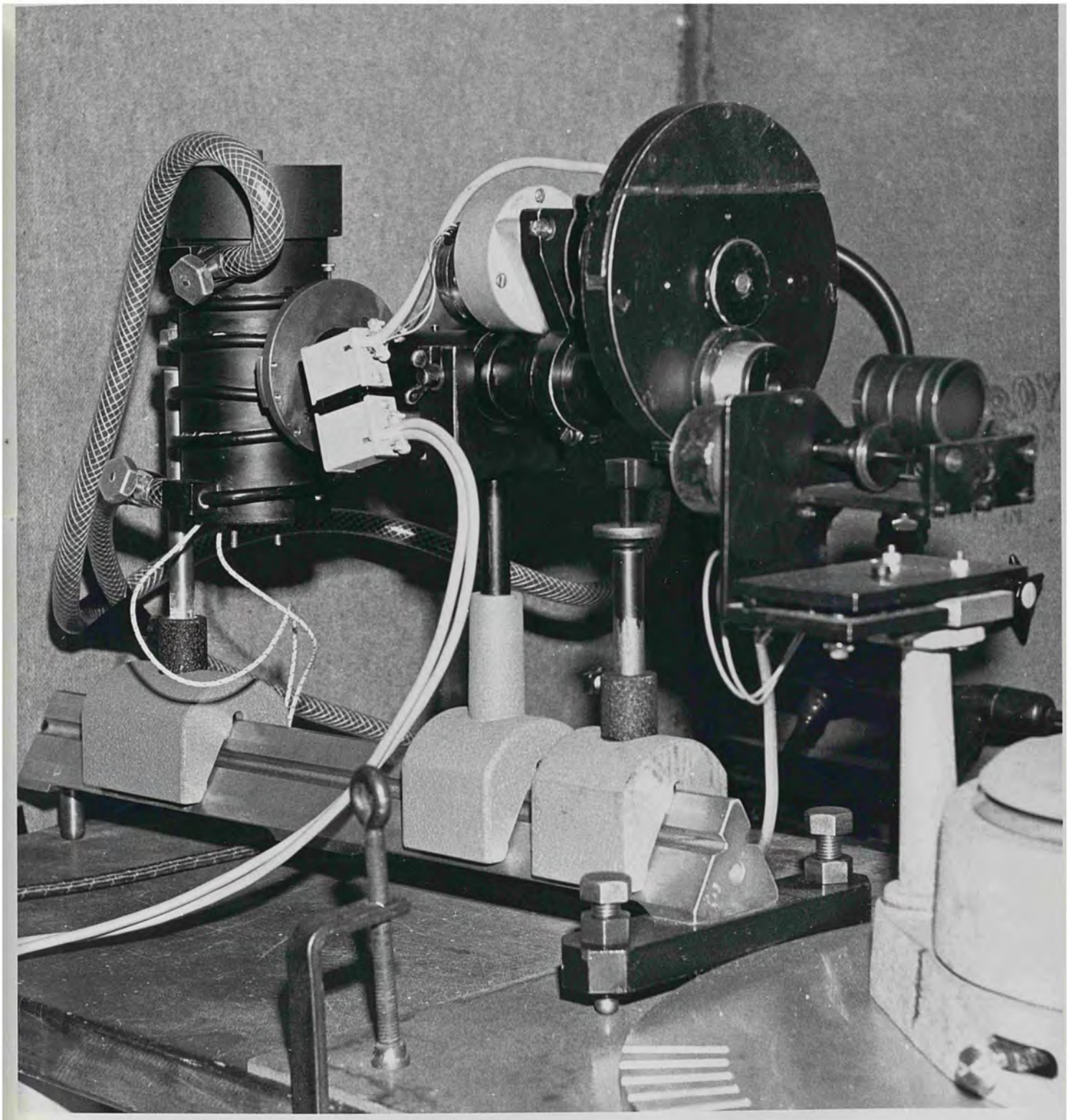

FIGURE 24

57 radial grooves 4.2 cm long, 0.2 cm deep and V-shaped in cross-section, were milled in the upper face of duralumin base, so as to meet the circumference and locate the angular position of the detector.

The detecting system consisted of telescope tube (without lens and eye piece) fixed to the rotating arm of the spectrometer table, by means of L-shaped duralumin block at a height such that the incident beam passed through the centre of the tube. An I - sectioned block of duralumin, with two spring-loaded ball bearings in one end, was fixed at its other end to the underside of the L-shaped block so that the ball bearings were in contact with the upper face of the duralumin base. When the telescope tube was rotated, one of the ball bearings remained in contact with the duralumin base plate and the other traversed the milled grooves. The I - sectioned component also provided extra support for the telescope tube. A photomultiplier (EMI, Type: 9529B, S10 Cathode) together with its dynode resistor chain, was magnetically shielded by mu-metal, placed in a duralumin case, which was also covered by mu-metal. The duralumin case was screwed into the telescope tube. Recommendations, supplied by EMI (1968), for the design of the dynode resistor networks were followed. The output current from the photomultiplier passed to earth through a 510K Ω high stability resistor and the voltage developed across this resistor was the signal recorded. A diffusing screen was mounted in front

of and parallel to the photomultiplier window, and separated from it by a cylindrical tube aluminised on the inside. The diffusing screen was a flat disc of flint glass with both faces ground. The purpose of this arrangement is to reduce sensitivity of the photomultiplier to any changes in incident beam size. A supporting cradle for the photomultiplier assembly was screwed on a L-shaped block attached to the rotating arm of the spectrometer table. A digital voltmeter (Solartron LM1010.2) was used to measure the output voltage from the photomultiplier.

The incident intensities were measured by setting the rotating polarizer to produce $\parallel$ and $\perp$ components using the method of Rowell et.al (1969). The absolute alignment differed by 0.2° for the extreme ends of the wavelength range (400 - 700 nm) for both polarization planes (Taylor, 1972). The reflected intensities for $\parallel$ and $\perp$ components were measured by noting the maximum and minimum intensities while the polarizer was rotating.

Using this reflectometer the reflectance ratios could be measured to better than 0.5%, and the angles of incidence to better than 0.03°.

The whole reflectometer was shrouded in a light-tight box. Once the angle of incidence was fixed, there was no need to open the box to set the polarizer or filter for measuring the reflected intensities at different wavelengths. A typical time was 45 minutes to measure reflected intensities for fifteen different wavelengths at a given angle of incidence.

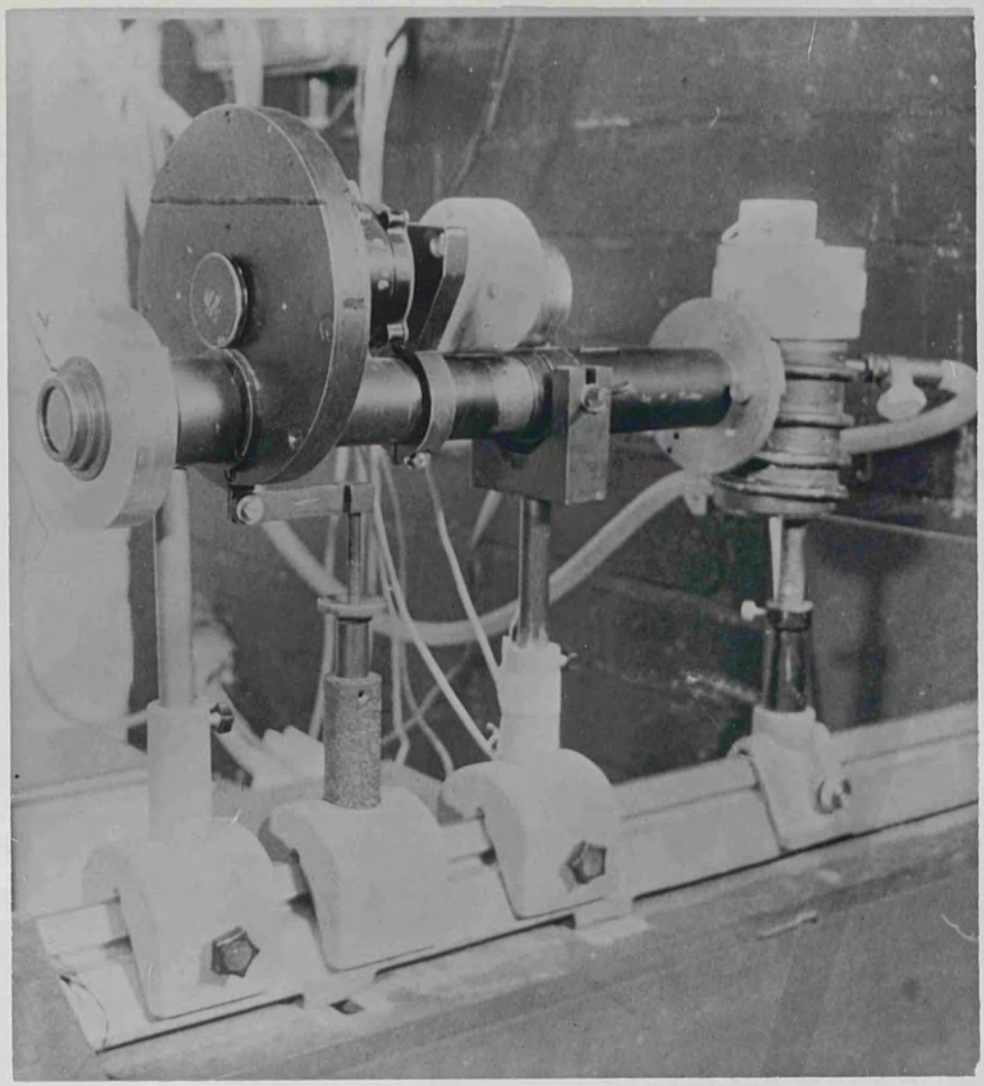

FIGURE 25

By removing the rotating polarizer and attaching a calibrated circular scale polarizer to the collimator (Figure 25), the reflectometer could be used for all the other non-polarimetric methods described in Chapter II.

4.5 The Substrate Holder for Optical Measurements in Air

The substrate holder (Figure 26) consisted of a block A containing bronze bushes to act as guides for steel rods B attached to a solid rectangular base C, was screwed to the prism table. A glass substrate could be clamped into position on a light frame-work D fixed on base C, perpendicular to the prism table top, by three nylon screws E, F and G. The lateral position of the specimen, relative to the reflectometer axis, could be adjusted by moving C relative to A by means of a 0.5 mm pitch brass screw threaded into C and free to move in bronze bearing in A. This substrate holder, together with the prism table levelling screws, allowed the surface of a specimen to be brought into coincidence with the rotational axis of the reflectometer.

4.6 The Optical Cell for Optical and Magneto-Optical Measurements in Vacuum

An optical cell (Figure 27) was designed and constructed for keeping films under low vacuum, and to obtain reflection measurements while the films are cooled to liquid nitrogen temperatures.

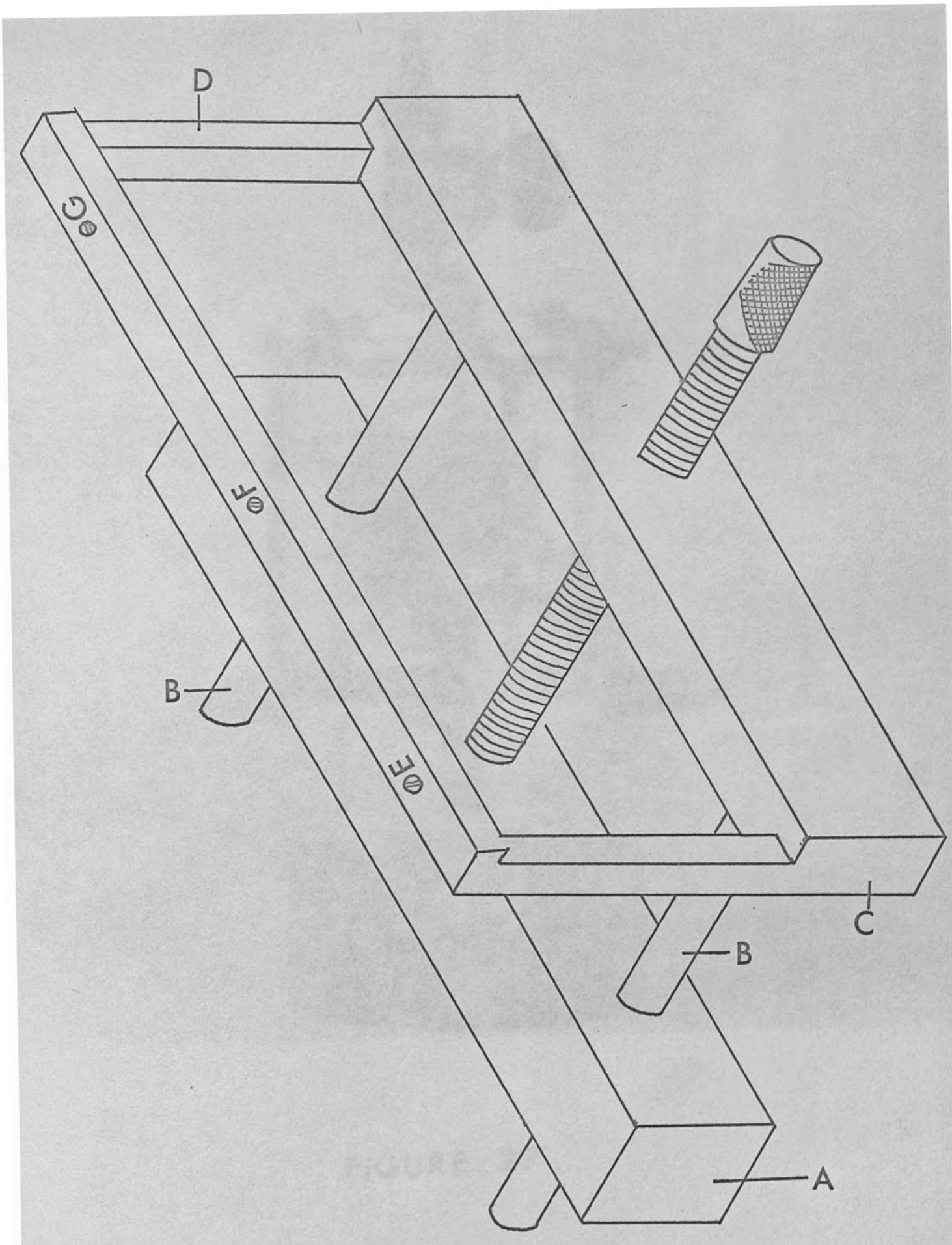

Figure 26: Isometric drawing of specimen holder for measurements in air.

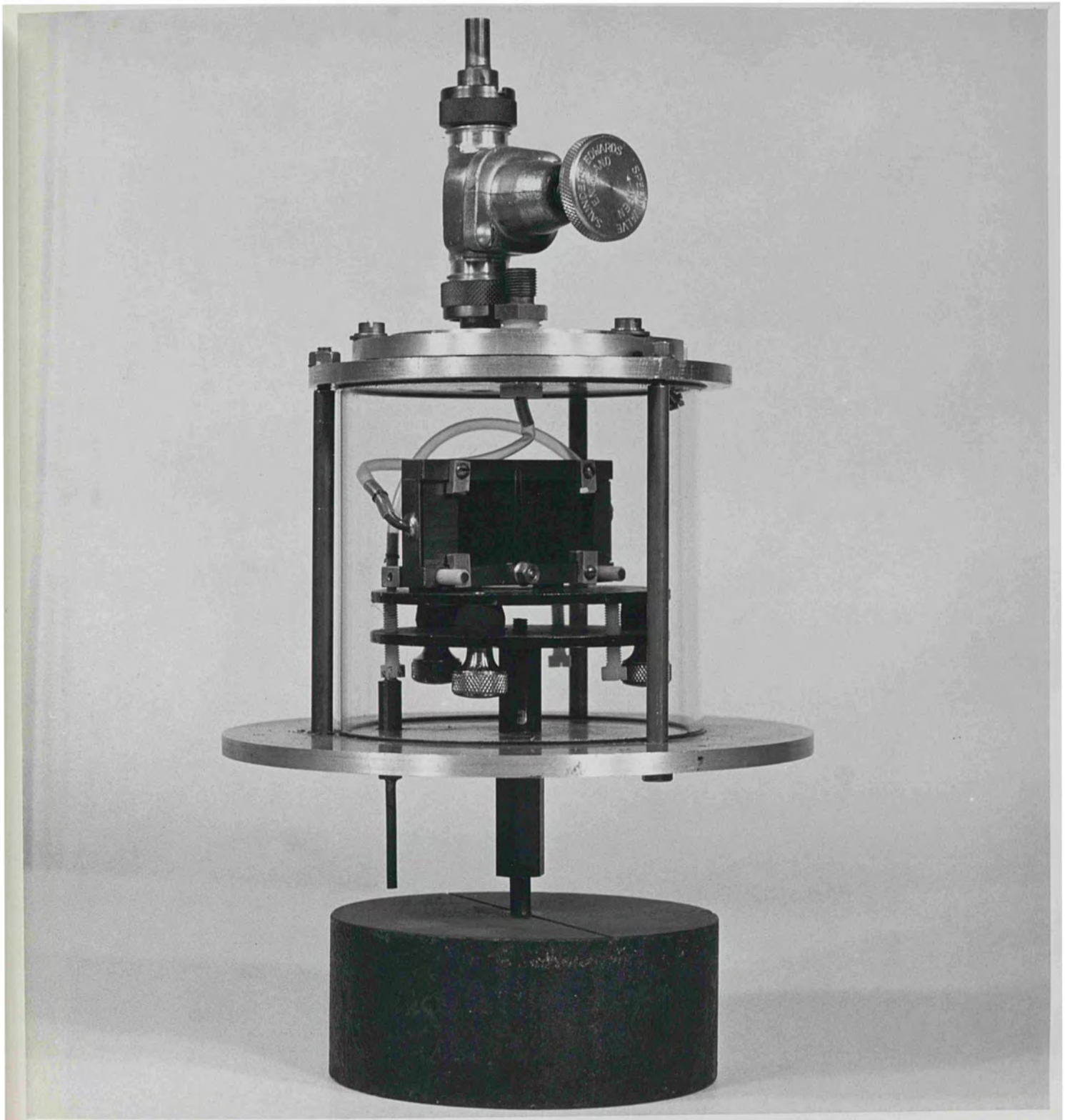

FIGURE 27

The cell can be fitted snugly, in place of prism table, into the working space between the telescope tube and rotating polarizer and can also be used for low temperature optical and magneto-optical studies.

Figure 28 shows a schematic section of the cell. It consists of a prism table A fitted with the arrangement for adjusting the lateral position of the specimen described in Section 4.5. A copper box B, having an inlet and an outlet for liquid nitrogen is used, in place of the frame-work, to hold the substrate. By means of four screws, the specimen can be held perpendicular to the prism table top. The leg E of the prism table is screwed into rod D through a hole in the duralumin base C and an 'O' ring used as a vacuum seal. The outlet tube F for liquid nitrogen is vacuum-sealed into C. The transparent envelope G is a fused quartz (Vitreosil, 066 quality) tube of wall thickness 2.4 mm. This tube, manufactured by Thermal Syndicate Ltd., was trepanned from a block of the 066 Vitreosil and highly polished both inside and outside. It was necessary to have the tube prepared in this manner because any imperfections in the wall of the tube would not only distort the beam of light passing through but would also perturb the state of polarization of the beam. This envelope G rests on a large diameter 'O' ring (the diameter of the 'O' ring being equal to the diameter of the envelope G) partially inset in the top face of C.

The top H of the cell is also made of duralumin. In the

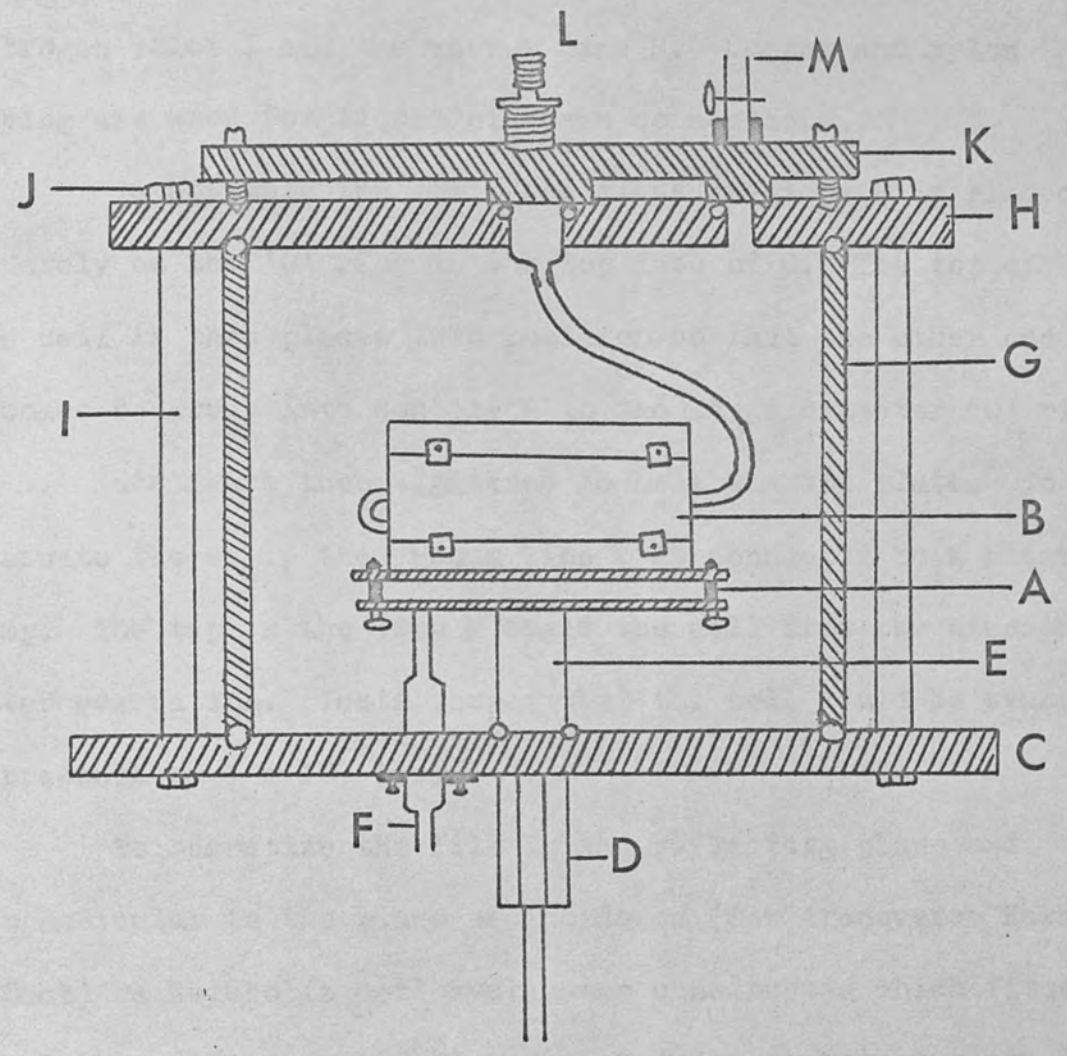

Figure 28: Schematic section of the optical cell

underside of H another large diameter 'O' ring was partially inset to provide a vacuum seal with the top end of the tube G. Extra support to the top H is provided by brass rods I which were screwed into C. Another duralumin top K is fixed to H by three screws in order to provide vacuum seal for liquid nitrogen inlet L and the vacuum line M. Copper and nylon tubing are used for liquid nitrogen connections.

To assemble the cell, the glass envelope G is placed squarely on the 'O' ring in the top face of C. The top of the cell is then placed into position so that the other end of G comes squarely into contact with the large diameter 'O' ring in H. Nuts J are then tightened to hold the top plate. To evacuate the cell, the vacuum line M is connected to a rotary pump. The tap in the line M seals the cell from the atmosphere after evacuation. Tests showed that the cell could be evacuated to a pressure of 1×10^{-3} torr.

To magnetize the film in the reflecting plane and perpendicular to the plane of incidence (for transverse Kerr effect) a Helmholtz coil system was constructed which fitted snugly around the cell wall and rested on the bottom plate C. The dimensions of this coil were such that when placed in position, the centre of the coil system was automatically aligned with the plane of reflecting surface. With a current of 10 amps flowing through the coil a uniform field of value 450 Oe was produced over the central area of the film. Figure 29 shows the optical cell with the Helmholtz coil.

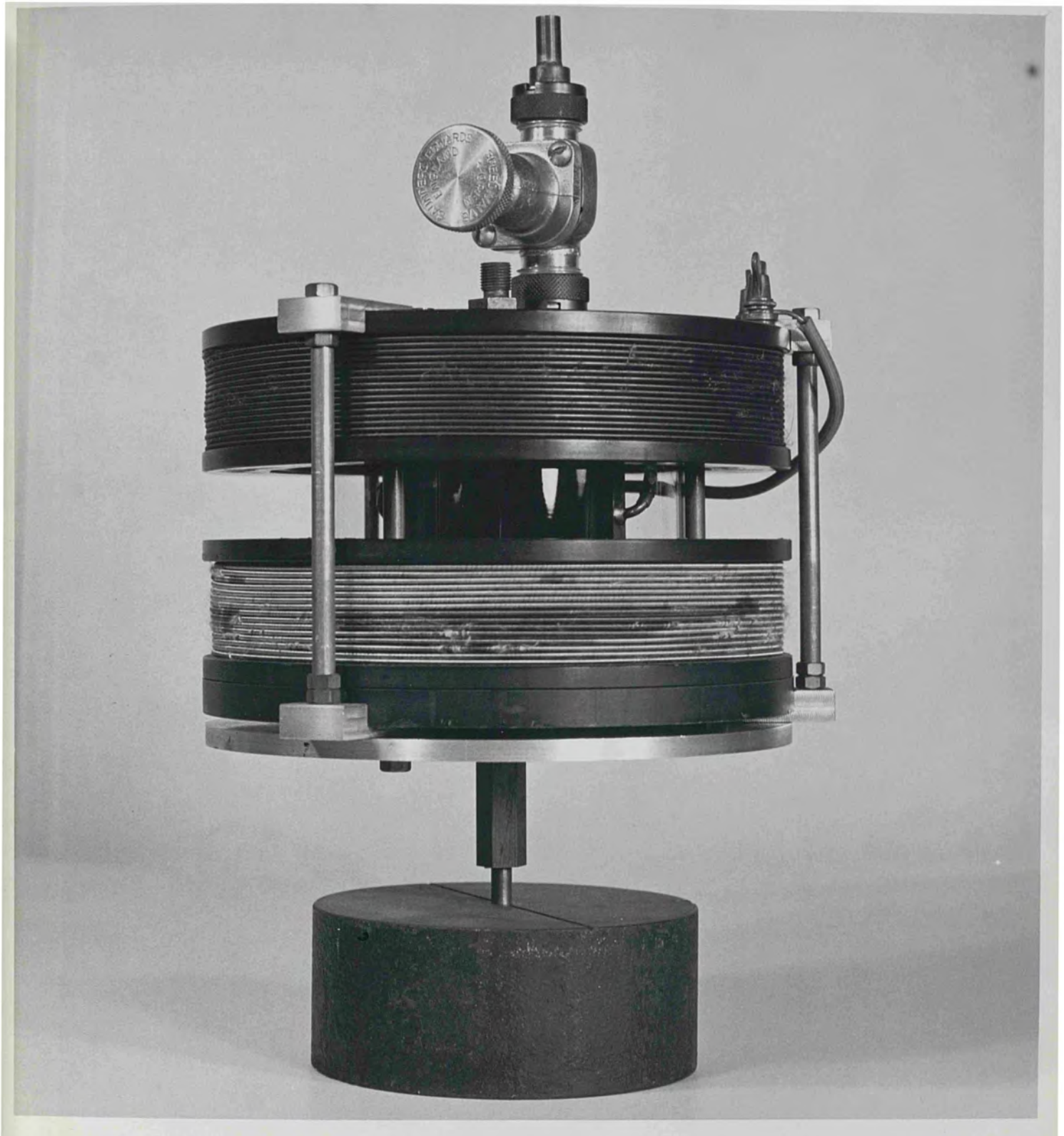

FIGURE 29

CHAPTER V

SPECIMEN PREPARATIONS

5.1. Introduction

Any determination of the optical constants of a material requires the preparation of a flat, strain-free and clean surface. The possible adverse effects of surface roughness on reflectance measurements have been discussed in the literature, with regard to diffuse scattering of reflected light (Bennett and Porteus 1961), and more recently, with regard to possible anomalies in reflectance near resonant frequencies of the specimen (Berreman, 1970).

This chapter briefly reviews the methods and related techniques used for preparing solid films, suitable for optical measurements, by thermal evaporation. Other methods of depositing films have been discussed in detail by Chopra (1969, Chapter II). The advantages of the thermal evaporation method over other methods and the conditions which must be realized in order that the deposition of a film from vapour may take place with a minimum of interfering factors have been discussed by Heavens (1955, Chapter II). The high reactivity of the metals studied also made this method the most suitable.

In order to prepare the films three different vacuum evaporation units were used: two ordinary high vacuum (O.H.V.) and one ultra high vacuum (U.H.V.) All the films were deposited onto float glass substrate.

5.2. Substrate Preparation

One of the requirements to obtain a clean film surface is that the supporting surface (substrate) must be free from contaminant films such as grease, absorbed water etc. Different methods used to clean substrates have been discussed by Holland (1956, Chapter III). The method used for the present work to clean the float-glass substrate of dimension 76 x 25 x 1 mm^3 is given below.

The substrate (soda glass microscope slide) was first selected for its freedom from scratches by looking under a bright light source. It was then placed in a beaker of degreasing agent (DECON 90), making an acute angle with the base of the beaker and ultrasonically cleaned for about 30 minutes. The degreasing agent was then displaced with distilled water and the substrate was rinsed for five minutes. It was then clamped onto a crocodile clip, attached to a stand and washed under the stream of distilled water for three to five minutes. It was checked that water flowed uniformly from the substrate surface. The substrate was then allowed to dry in air, covered loosely with lens tissue.

5.3. Ordinary High Vacuum (O.H.V.) Preparation of Films

The two ordinary vacuum evaporation systems used for growing films were Edwards 12EA/424 and Birvac T4-150. They both consisted of 12 inch diameter glass bell jars sealed to the base plates by means of L-shaped viton-gaskets. The bell jars were evacuated by

water cooled oil vapour diffusion pumps and oil rotary pumps. The rotary pumps were capable of evacuating to <0.005 torr. The ultimate pressure of the diffusion pumps were better than 5×10^{-6} for Edwards system and 5×10^{-7} for Birvac system. Pirani gauges were used to measure the backing pressures over the pressure range 0.5 - 0.001 torr. A Phillips ionization gauge, incorporated in the Edwards system measured pressures down to 1×10^{-6} torr, whereas a Birvac penning gauge measured pressures down to 1×10^{-7} torr for Birvac system.

Electrical feed-through , passing through the base plates of the vacuum chambers, provided electrical access to apparatus inside the bell jars. The apparatus to be used in vacuo was constructed from stainless steel where possible. The tungsten filament or boat was connected by stainless steel rods to the heavy current feedthroughs. The filament could be shielded from the substrate by means of a shutter, activated from outside the chamber by a vacuum rotary drive. The substrate could be either held in a stainless steel holder provided with a tungsten filament (for growing films on heated substrates) or could just be rested on two stainless steel strips (for growing films on cold substrate). The holder or the strips were supported by a system of adjustable clamps, so that the height of the substrate could be set as required.

Before using a filament or boat for evaporation it was thoroughly outgassed in vacuo to the base pressure better than 1×10^{-5} torr, by passing a current of at least 40 amperes through it. After allowing about 20 minutes for the filament to

cool, it was loaded with the material to be evaporated. Details of growth of films in these systems using filaments and boats are given in Chapter VI.

A Birvac electron ring-gun (type: RG2) could be used in the Birvac vacuum system in place of filament or boat, to evaporate materials from refractory crucibles using electron bombardment. Electron bombardment has been described in general terms by Francombe (1966). The ring-gun consisted of a stainless steel cylindrical hollow box with one of its ends plain. The other end was conical and each had a hole provided centrally and coaxial with the other. A filament of molybdenum (electron emitter) was in the form of a loop supported at each end of its diameter by suitable connections across which the filament voltage could be applied. One end of the filament was connected to the box and the other end was insulated from it. The whole assembly was mounted onto posts which insulated it from earth. The other ends of these posts were located onto a table and between this table and the box the variable H.T. voltage from the Birvac ring-gun console (Type: RG) was applied. Beneath the box a small rotating turntable was mounted, capable of holding six cermet (Al_2O_3) type crucibles mounted on molybydenum clips and rotatable from outside the vacuum chamber. Both the turntable and crucible were at earth potential. Details of growth of iron films using electron bombardment are given in Chapter VII.

5.4. Preparation of Films in Ultra-High Vacuum (U.H.V.)

The U.H.V. system used in the laboratory was manufactured by Edwards High Vacuum Ltd. for filament evaporations of metals.

A 12 inch diameter stainless steel chamber containing 8 ports (Figure 30) was rough pumped with an Edwards alumina-trapped rotary pump. At a pressure of approximately 10^{-3} torr a Varian Triode ion pump was started. This pump had a pumping speed of 140 litres/sec. at high pressure and a pressure of 10^{-6} torr was quickly attained with the system isolated from the rotary pump with a bakeable valve. At this stage the Bayard-Alpert gauge, used for total pressure measurement, was outgassed by electron bombardment. Titanium sublimation pump filaments were also outgassed at this stage. The system was then baked at 250°C until a pressure $\sim 5 \times 10^{-8}$ torr (indicated by the ion pump current) was attained. The length of time needed to achieve this depended critically on the cleanliness of the system. The system was allowed to cool and the gauge again outgassed. The pressure after cooling was generally found to be $\sim 10^{-9}$ torr. The titanium sublimation pump (T.S.P.) was then used for ~12 hours with the ion pump to reduce pressure to $\sim 10^{-10}$ torr. At this stage liquid nitrogen was fed to a stainless steel baffle inside the chamber. This baffle was situated directly above the T.S.P. filament. The condensation of gas onto this baffle further reduced the pressure up to 5×10^{-11} torr. Low pressure measurements were made with a modulated Bayard-Alpert ionization gauge.

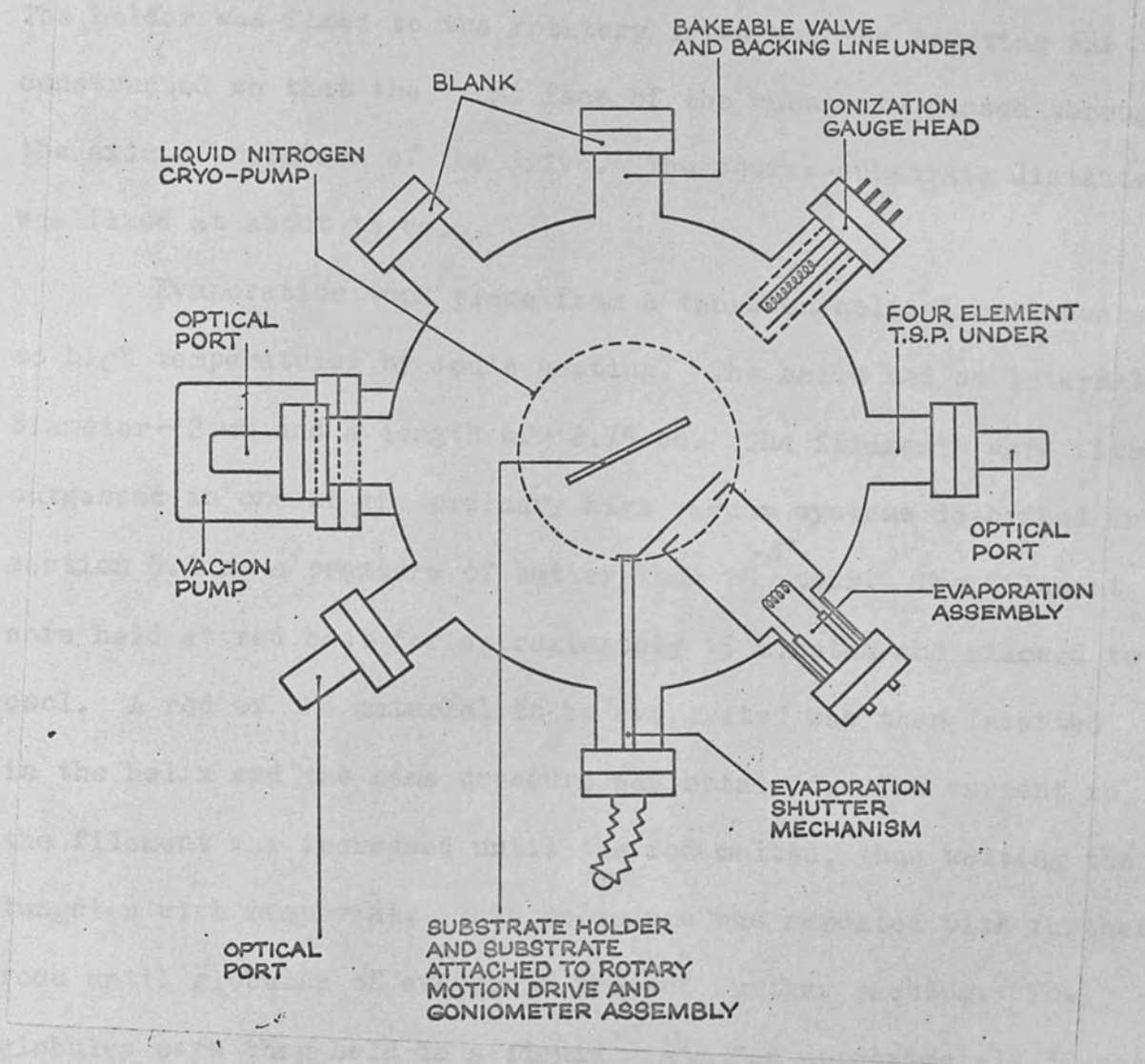

Figure 30: Schematic plan view of U.H.V. system.

Either copper con-flat gaskets or gold wire seals were used on all the ports. The system was normally let up to atmospheric pressure with dry nitrogen, and was sealed as quickly as possible in order to reduce the time taken to achieve minimum pressure.

The substrate was mounted onto a stainless steel holder. The holder was fixed to the rotatory drive and the mounting was constructed so that the front face of the substrate passed through the axis of rotation of the drive. The source-substrate distance was fixed at about 14 cm.

Evaporation took place from a tungsten helical coil heated to high temperatures by Joule heating. The coils had an internal diameter $\sim$2 mm and a length of $\sim$2.75 cm. The filaments were first outgassed in one of the ordinary high vacuum systems described in section 5.3 at a pressure of better than 10^{-5} torr. The filament were held at red heat for approximately 15 minutes and allowed to cool. A rod of the material to be evaporated was then inserted in the helix and the same pressure was obtained. The current in the filament was increased until the rod melted, thus wetting the tungsten with evaporant. This procedure was repeated with further rods until globules of evaporant prevent further packing. The globules were then held in a liquid state for approximately 30 seconds to complete the outgassing. The filament was then taken out from O.H.V. system and installed in the U.H.V. system. Outgassing of the filament was again done in U.H.V. system by increasing the current up to 45 amperes while the shutter was in between the

filament and substrate. The current was switched off if the pressure rose to approximately 10^{-6} torr. The system was allowed to return to its base pressure. This procedure was repeated until no pressure burst was observed. The filament was then left to outgass at 45 amps. for a few minutes. Details of growth for individual metals are given in Chapter VI.

CHAPTER VI

OPTICAL PROPERTIES OF GADOLINIUM, TERBIUM AND HOLMIUM IN THE VISIBLE REGION

6.1. Introduction:

The optical properties of heavy rare earth metals gadolinium (Gd), terbium (Tb) and holmium (Ho), as experimentally observed in air, in the visible region of the spectrum, are described in this chapter. The optical conductivity curves for Gd and Tb are also discussed directly in terms of their electronic band structures.

Since no relativistic band structure calculations for Ho had been published by the time this experimental work was done, some comparison was sought with dysprosium (Dy), whose band structure calculation had been published (Keeton and Loucks, 1968).

The optical conductivity curve for Dy, as experimentally observed in air is discussed in terms of its electronic band structure. The optical conductivity curve for Ho is then discussed in relation to the optical conductivity curve for Dy.

Electron diffraction analysis in reflection on a number of samples prepared in U.H.V. showed some semi-circular rings which indicated the film to be randomly polycrystalline with crystallite size of the order of $\sim$ 1000 Å.

The effects of ageing in air for some of these metal films were also observed, and are discussed in this chapter.

6.2. The Heavy Rare Earth Metals

The rare earth metals, alternatively known as the Lanthanides, are the fifteen elements in the periodic table with atomic numbers 57-71. The first seven elements namely lanthanum (La), cerium (Ce), praseodymium (Pr), neodymium (Nd), prometheum (Pm), samarium (Sm) and europium (Eu) with atomic numbers 57 - 63 are classified as light rare earths, whereas the last eight, namely gadolinium (Gd), terbium (Tb), dysprosium (Dy), holmium (Ho), erbium (Er), thulium (Tm), ytterbium (Yb) and lutetium (Lu) with atomic numbers 64 - 71 are classified as heavy rare earths. All the heavy rare earth metals have hexagonal closed-packed (h.c.p.) crystal structures, with the exception of ytterbium, which has face centred cubic (f.c.c.) crystal structure.

Gadolinium (z=64) is the first of the heavy rare earth metals in the periodic table with the configuration

$$1s^2 2s^2 2p^6 3s^2 3p^6 3d^{10} 4s^2 4p^6 4d^{10} 4f^7 5s^2 5p^6 5d^1 6s^2$$

At gadolinium the half-filled 4f state has a higher energy than the 5d level, so that the 4f state has the same population as its predecessor in the periodic table, europium (z=63). The addition of another electron and proton to the system makes it energetically favourable for the electron to enter the half-filled 4f state. There is also a tendency for the electron in the 5d level to be transferred to the 4f level; hence the configuration of terbium (z=65) is

$$1s^2 2s^2 2p^6 3s^2 3p^6 3d^{10} 4s^2 4p^6 4d^{10} 4f^9 5s^2 5p^6 6s^2$$

The rest of the heavy rare earths are typified by progressive filling of the 4f level. The configuration of the last rare earth element lutetium (z=71) is

$$1s^2\,2s^2\,2p^6\,3s^2\,3p^6\,3d^{10}\,4s^2\,4p^6\,4d^{10}\,4f^{14}\,5s^2\,5p^6\,5d^1\,6s^2$$

The appearance of the 4f electrons at the beginning of the lanthanide series clearly means that the nuclear charge becomes sufficiently large for them to be bound at that point. However, it might be supposed that the 4f electrons would occupy the outermost orbitals, whereas all the evidence indicates that they lie inside the 5s shells. This is because an electron added to the 4f shell cannot screen the remaining 4f electrons from the added positive nuclear charge. This phenomenon, known as lanthanide contraction, causes the atomic radius to decrease with increasing atomic number.

Because the 4f electrons are so well embedded within the core orbitals the valence electrons are readily transferred to other ions, while in metals they form the conduction band. Hence in most practical circumstances the rare earth ions are tripositive, in which case all electrons are in closed shells, and therefore inactive except for the 4f electrons.

The properties of the conduction band in rare earth metals play a dominant role in determining the interactions between the ions, and hence the magnetic properties of these metals. They also, of course, determine their electric, optical, and transport properties, as for any other metal.

6.3 Gadolinium (Gd)

Gadolinium is the first of the heavy rare earth metals with atomic number 64. Its melting point is 1593°K, density is 8.0 gm/c.c. and ferromagnetic Curie temperature is 292°K.

In all, optical measurements were made on 12Gd films. Reflectances $R_{\perp}$ and $R_{\parallel}$ were measured at an angle of incidence near about 74° (Section 2.4) on the first seven films. These earlier measurements were performed using a different, rectangular graded wavelength filter (Barr and Stroud Ltd.), whose bandwidth was twice the bandwidth of the circular wavelength filter (described in Chapter IV). The optical conductivity curves for these films indicated some structure which it was thought worthwhile to investigate with better resolution, using a more sensitive method.

Of the five films on which reflectance ratio measurements at two angles of incidence were made, using the circular wavelength filter, one is discussed in detail together with its growth condition. The optical conductivity curves of three of the remaining four films are also given in this chapter.

6.3.1. Growth of Gd film

The film was grown in the U.H.V. system described in Chapter V. The growth conditions for the film were as follows:-

(i) The film was grown from 99.9% pure sample obtained from Goodfellow Metals Ltd.

(ii) An evaporation current of 50 amperes was passed for 60 seconds through the loaded tungsten filament.

(iii) The pressure at the time of growth was better than 4×10^{-8} torr as measured on the linear scale of the Bayard-Alpert gauge.

(iv) The film was grown at room temperature on a microscope slide with nichrome contacts on its ends for electrical measurements by other workers.

(v) The film was taken out from U.H.V. system after six days, before which time electrical and some other optical measurements were made by other workers using the film. Optical measurements were made in air on the day of removal.

(vi) The thickness of the film as measured after the optical measurements in air, using multiple beam Fizeau fringes (Tolansky, 1970) was 1020A°. The step in the film necessary for such determination was introduced by placing a microscope slip in the substrate holder at the time of loading the U.H.V. system.

6.3.2. Optical Properties of Gd film

Reflectance ratios were measured on the above grown Gd film in air, four hours after it was taken out from the U.H.V. system. The measurements were made at angles of incidence 65.0° and 80.0° using the reflectometer described in Chapter IV. The narrow beam of light was made to fall on the area of film well within the

nichrome contacts for both the angles. The area of the film on the glass substrate between the nichrome contacts was 45 x 21 mm^2 .

Figure 31 shows the variation of reflectance ratios with incident energy in the visible region of the spectrum for angles of incidence 65° and 80°. We note the large variation in reflectance ratio for an angle of incidence of 80° compared with that at 65°. The maximum error in the reflectance ratio calculated from the errors of 0.1% in the intensity measurement was found to be 0.5%. The uncertainty in the measurements was estimated by measuring the same ratio several times and was found to be $<$0.5%. The values of n and k shown in Figure 32 were derived from the observed reflectance ratios (Section 2.5.1). The errors in n and k were obtained by taking an error of +0.5% in the reflectance ratio at one angle of incidence and an error of -0.5% in the reflectance ratio at the other angle of incidence. This combination accounted for the maximum possible errors in n and k. The calculated optical conductivity curve is shown in Figure 33. We notice the structure occuring in this curve, which will be interpreted in the next section.

Figure 34 shows the spectral dependence of optical conductivity, for Gd at room temperature, obtained by different authors. This figure illustrates the general disagreement that exists in the literature of the optical behaviour of rare earth metals. The basic reason for this disagreement probably lies in the reactive nature of rare earth metals (It is observed that the optical conductivity changes by as much as 10% after 68 hours from the

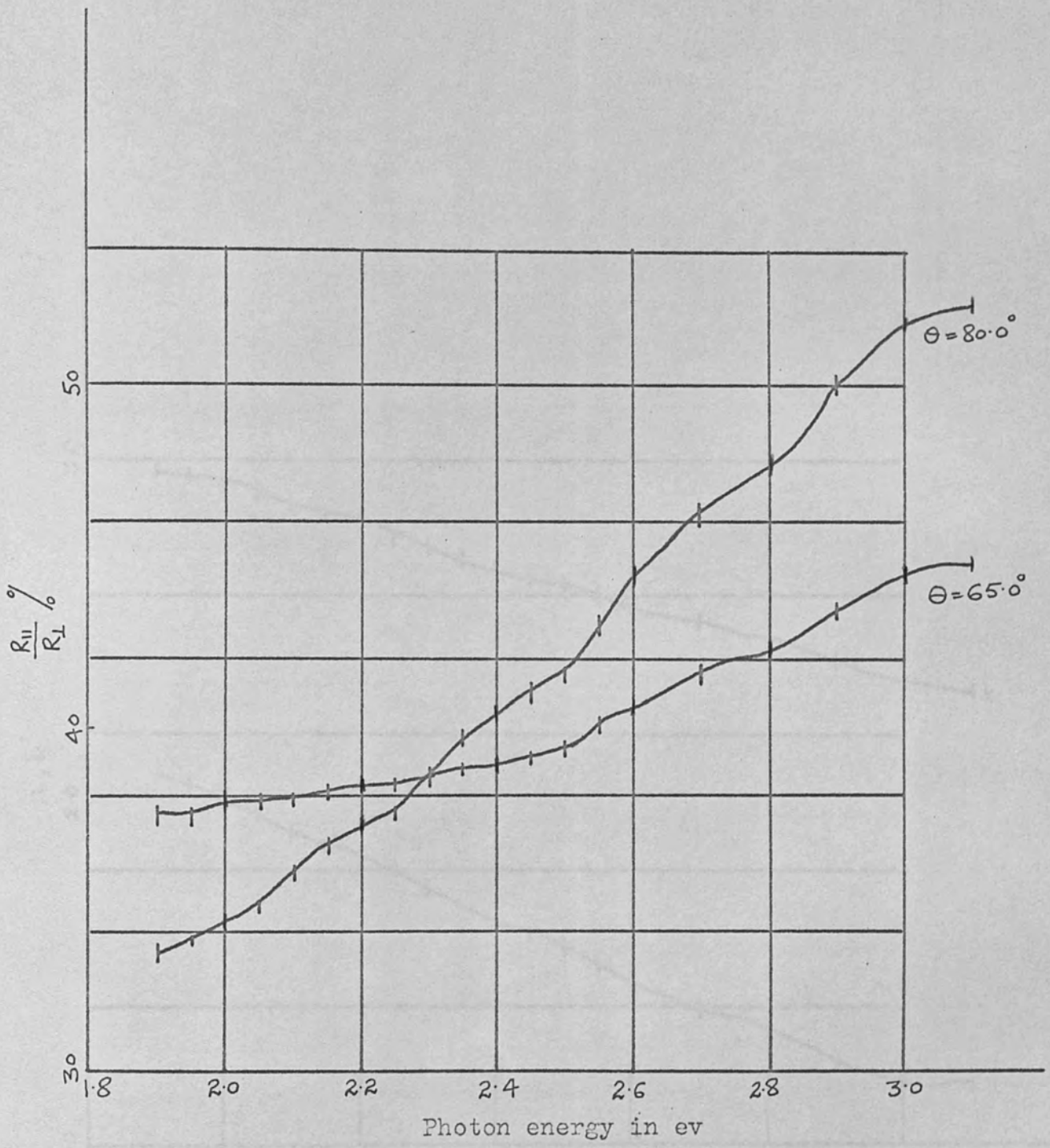

Figure 31: Reflection ratios at 80° and 65° measured for Gd film in air.

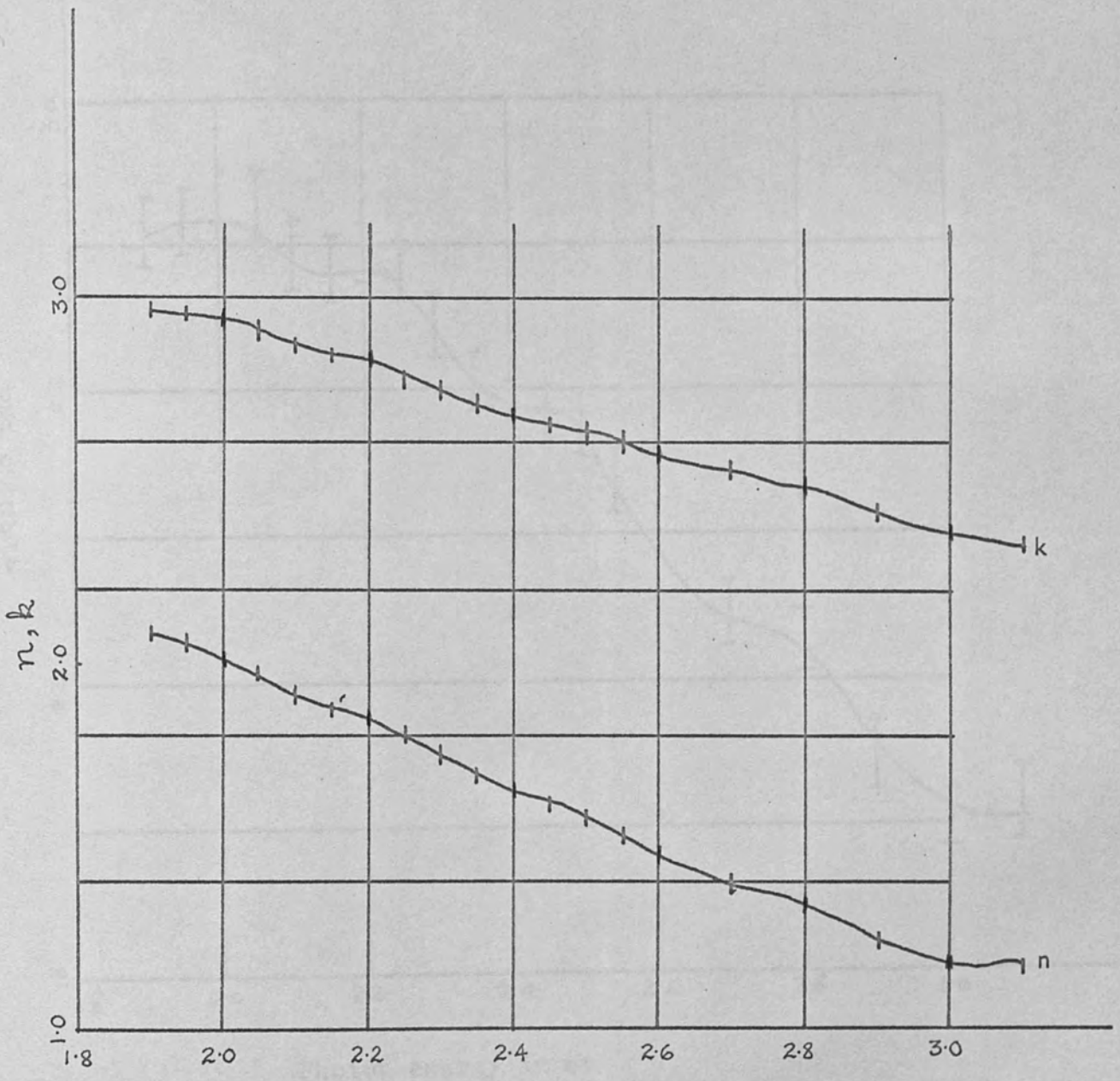

Figure 32: Optical constants n and k for Gd film in air.

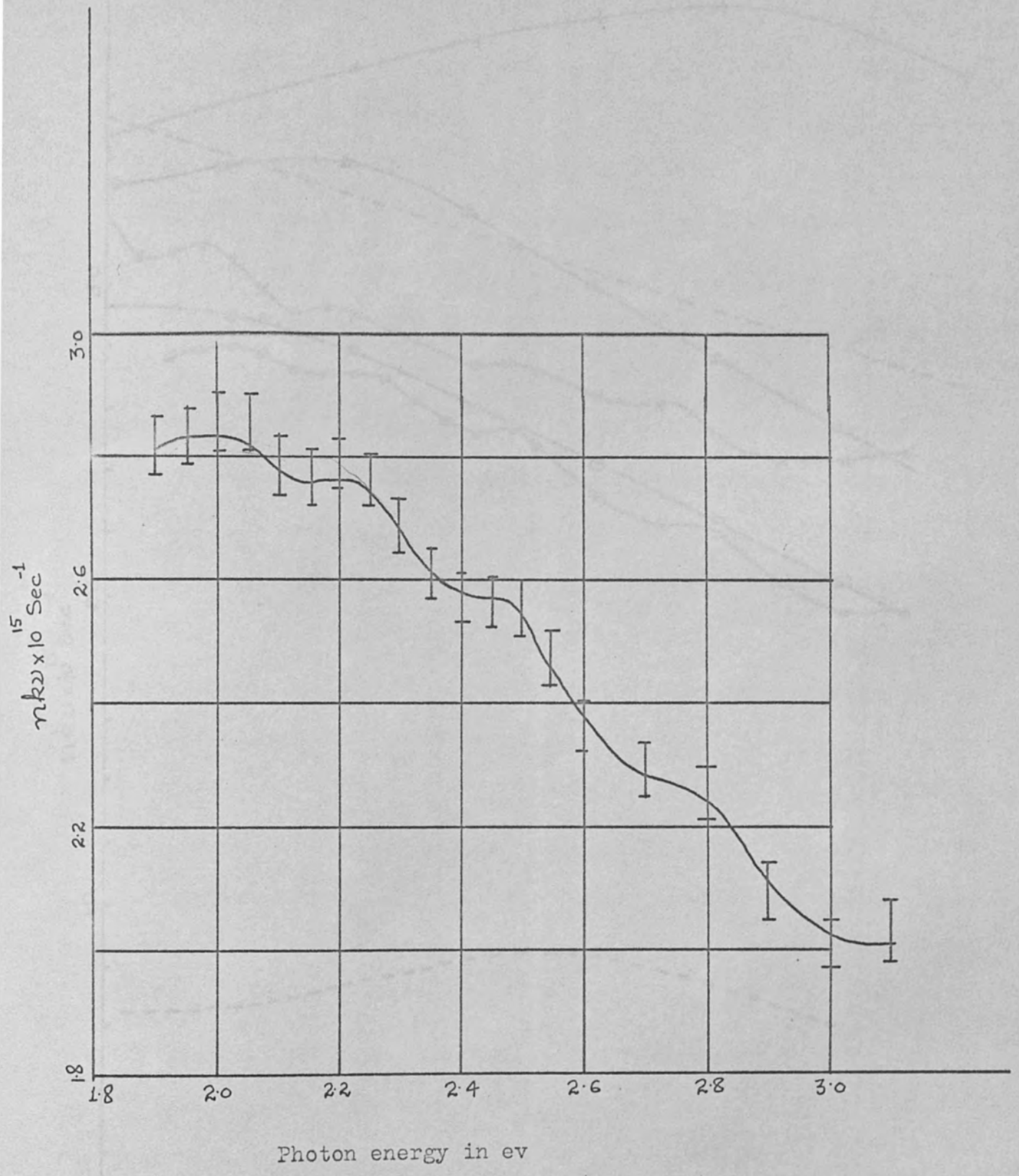

Figure 33: Optical conductivity of Gd in air at room temperature

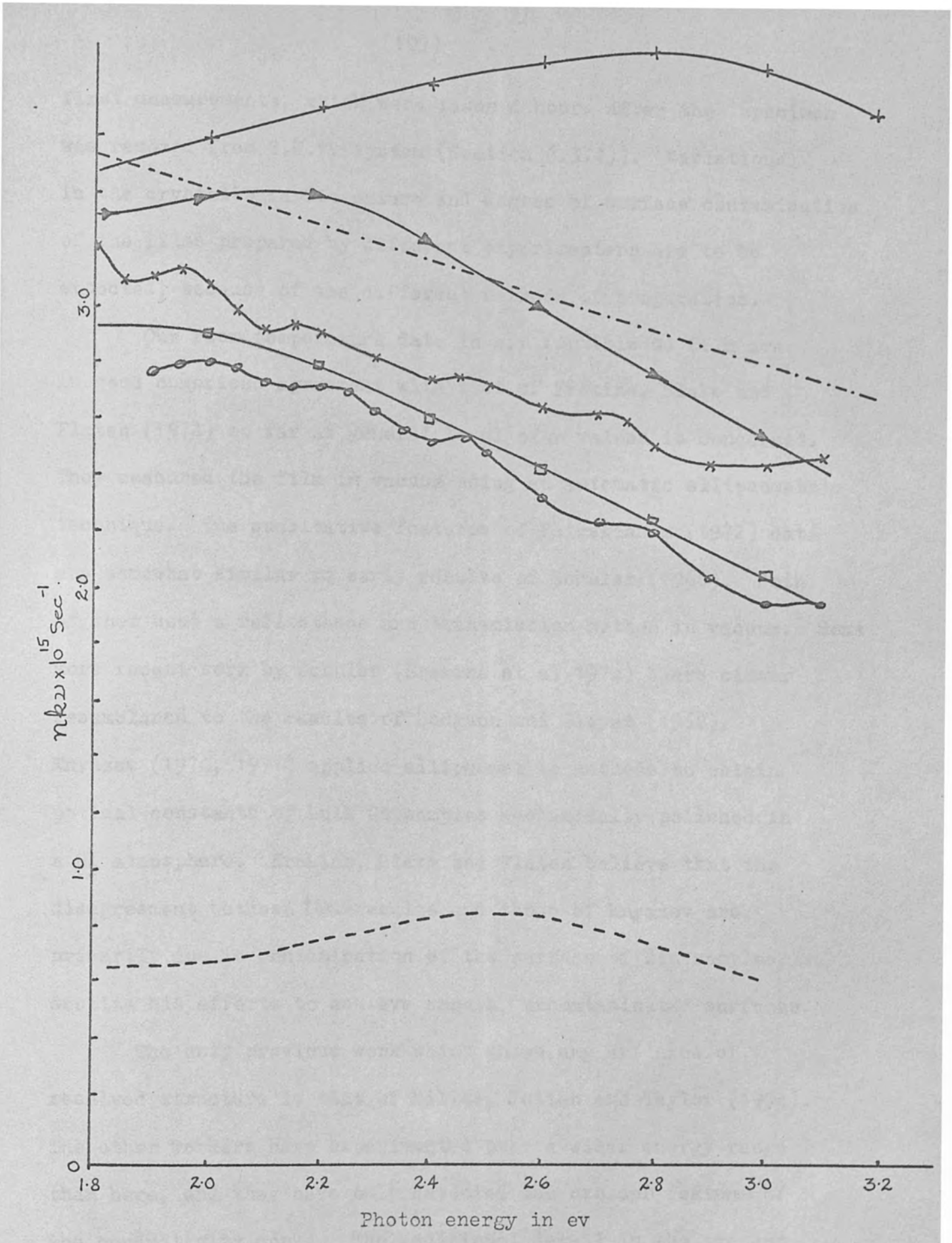

Figure 34: Optical conductivity of Gd at room temperature by several authors.

+ Petrakian; ➢ Schuler; —·— Hodgson and Cleyet; × Miller, Julien and Taylor; ▫ Erskine, Blake and Flaten; ∘ Present work; --- Knyazev.

first measurements, which were taken 4 hours after the specimen was removed from U.H.V. system (Section 6.3.4)). Variations in the crystallographic nature and degree of surface contamination of the films prepared by different experimenters are to be expected, because of the different methods of preparation.

Our room temperature data in air for this Gd film are in good numerical agreement with that of Erskine, Blake and Flaten (1974) so far as general level of σ values is concerned. They measured the film in vacuum using an automatic ellipsometric technique. The qualitative features of Petrakian's (1972) data are somewhat similar to early results of Schuler (1966). Both of them used a reflectance and transmission method in vacuum. Some more recent work by Schuler (Erskine et al 1974) bears closer resemblance to the results of Hodgson and Cleyet (1968). Knyazev (1970, 1971) applied ellipsometric methods to obtain optical constants of bulk Gd samples mechanically polished in a N_2 atmosphere. Erskine, Blake and Flaten believe that the disagreement between their results and those of Knyazev are primarily due to contamination of the surface of his samples, despite his efforts to achieve smooth, uncontaminated surfaces.

The only previous work which shows any evidence of resolved structure is that of Miller, Julien and Taylor (1974). The other workers have experimented over a wider energy range than here, and they have only detected the broader features of the conductivity curve. The additional detail in the present

curves may be due to higher energy resolution, and optimization of the reflectance measurements.

Because, the general numerical level of optical conductivity values changes with the exposure time of the Gd film in air (See Section 6.3.4.), it is the structure in the curve which is interpreted in terms of electronic transitions and compared with the results of Miller, Julien and Taylor in the next section.

6.3. Theoretical Interpretation of the Optical Conductivity Curve of Gd

As stated in Chapter I, the optical conductivity dispersion curve for visible wavelengths should be interpretable in terms of the energy band diagram. Non-relativistic band structure calculations have been performed by Dimmock and Freeman (1964) using augmented plane wave method (Slater, 1937) and their results are shown in Figure 35. The free-atom configuration $4f^7 5d^1 6s^2$ was used in constructing the potential. Figure 36 shows the appropriately labelled 1st Brillouin zone of the hexagonal close-packed crystal lattice. Each band is labelled according to the irreducible representation according to which the eigen functions, which generate the eigen values, transform. The crystal symmetry limits the type of wave function which satisfies the Schroedinger equation for an electron moving in a potential having the symmetry of the crystal lattice. The labels in Figure 35 indentify the different types of wave function.

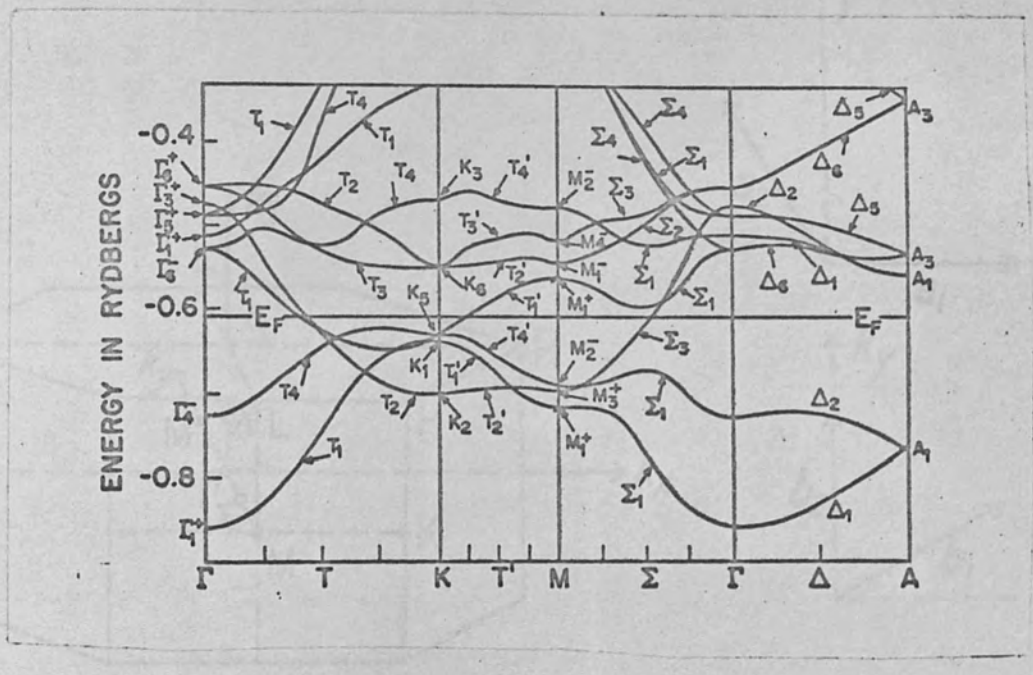

Figure 35: Electronic band structure diagram of bulk h.c.p. Gadolinium (Dimmock and Freeman, 1964).

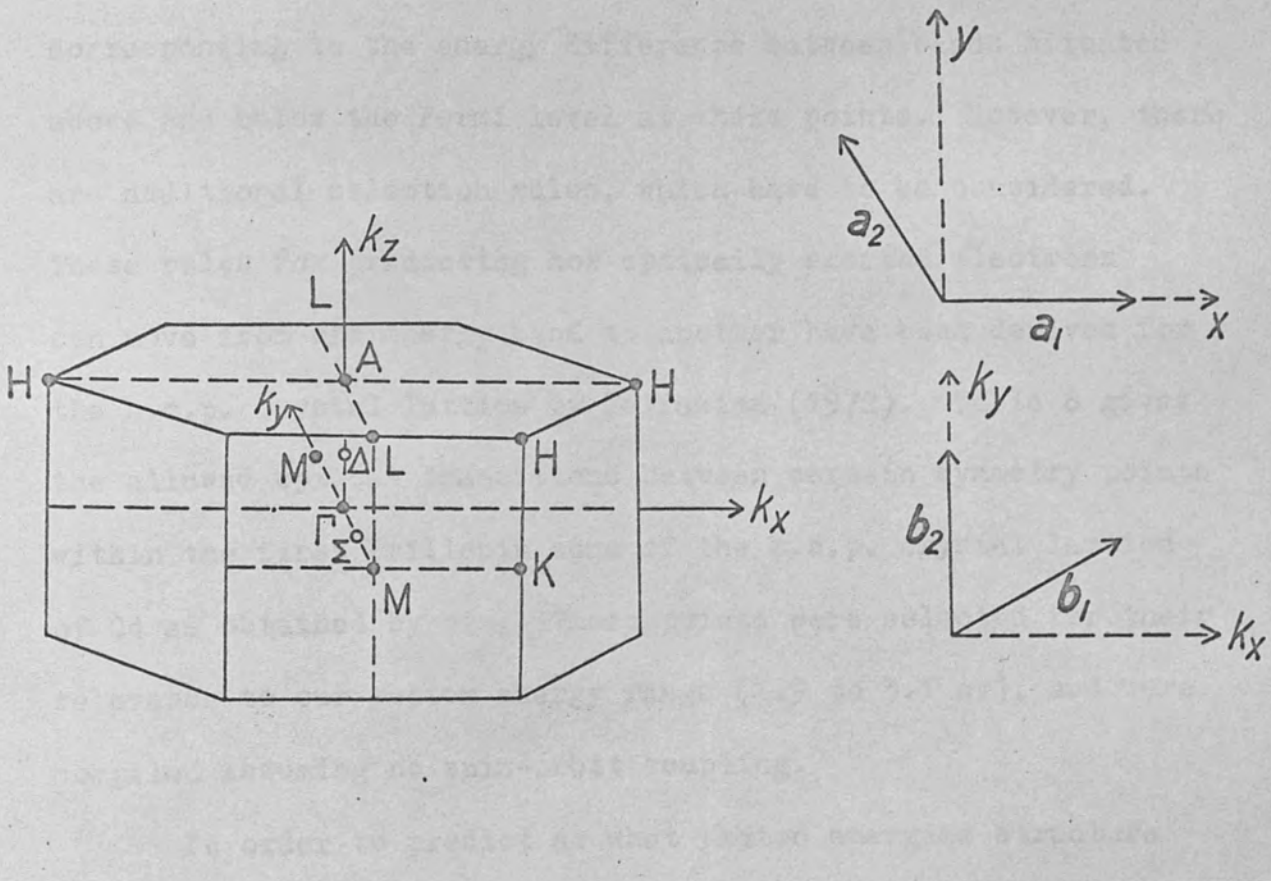

Figure 36: First Brillouin zone of the hexagonal close-packed crystal lattice.

From the symmetry conditions, we would expect the bands to be of zero slope, and therefore parallel, at symmetry, interband points: thus at these points there is a high joint density of states. Where the joint density of states is high, optical transitions are likely to occur. Thus, we might expect structure to occur in the optical conductivity curve at energies corresponding to the energy difference between bands situated above and below the Fermi level at these points. However, there are additional selection rules, which have to be considered. These rules for predicting how optically excited electrons can move from one energy band to another have been derived for the h.c.p. crystal lattice by Petrakian (1972). Table 8 gives the allowed optical transitions between certain symmetry points within the first Brillouin zone of the h.c.p. crystal lattice of Gd as obtained by him. These points were selected for their relevance to our photon energy range (1.9 to 3.1 ev), and were compiled assuming no spin-orbit coupling.

In order to predict at what photon energies structure should occur in the optical conductivity curve, the procedure of Miller, Julien and Taylor (1974) is adopted. They made the following simple assumptions.

i) All the allowed transitions given in table were equally probable.

ii) The optical absorption arising from interband electronic transitions at a photon energy E was proportional to the number of allowed transitions in the range $E \pm \delta E$.

Table 8. Allowed optical Transitions between certain symmetry points for first Brillouin zone of h.c.p. Gd.

Symmetry direction	Symmetry points of allowed transitions	Associated energy (ev)
M	$M_3^+ \rightarrow M_1^-$	2.045
K	$K_2 \rightarrow K_6$	2.045
K	$K_5 \rightarrow K_3$	2.24
M	$M_3^+ \rightarrow M_4$	2.385
H	$H_2 \rightarrow H_1$	2.44
L	$L_1 \rightarrow L_1$	2.44
L	$L_1 \rightarrow L_2$	2.48
H	$H_1 \rightarrow H_1$	2.58
M	$M_1^+ \rightarrow M_4^-$	2.79
A	$A_1 \rightarrow A_1$	2.84
M	$M_3^+ \rightarrow M_2^-$	2.93
K	$K_2 \rightarrow K_3$	3.17
A	$A_1 \rightarrow A_3$	3.185

A plot of the number of allowed transitions in the range $E \pm 0.05$ ev at each photon energy E versus photon energy obtained by them is shown in Figure 37. Clearly the peak positions shown in figure will have an uncertainty of $\pm$ 0.05 ev, which is equal to the experimental uncertainty in the positions of our observed peaks.

A list, similar to the one produced by Miller, Julien and Taylor, is produced and shown in Table 9. Each observed peak is assigned to the likely interband transition points within the first Brillouin zone. Table 9 also shows the peaks observed by Miller, Julien and Taylor. We notice the good agreement (within $\pm$ 0.05 ev) between the sets of results for the energy positions of the peaks.

We thus reach the surprising conclusion that even though the present measurements were made in air, they still show the structure in the optical conductivity curve, and the positions of peaks are in good agreement with those obtained by Miller, Julien and Taylor in ultra high vacuum.

6.3.4 Effect of Ageing on Gd Film in Air

Optical properties of Gd were also studied as a function of ageing. The film was kept in moist air and the reflectance ratio measurements at angles of incidence 65° and 80° were made after 72 and 168 hours from the first measurements in air. The optical constants were deduced from the reflectance ratio measurements (Section 2.5.1). It is found that the refractive

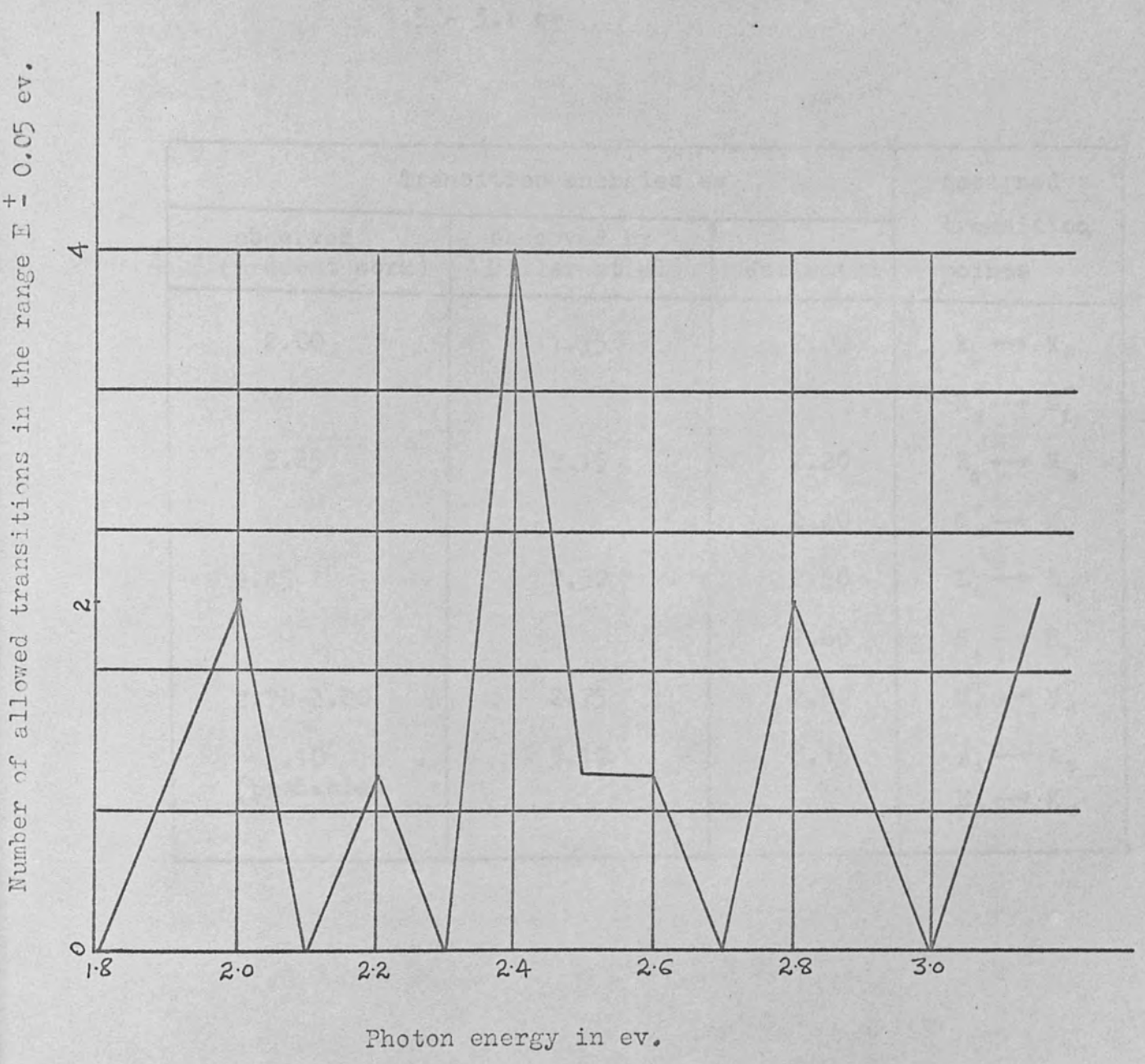

Figure 37: Theoretically estimated peak positions for Gd (Miller, Julien and Taylor, 1974).

Table 9. Optical transitions in Gd for the range 1.9 - 3.1 ev

Transition energies ev			Assigned transition points
observed (present work)	observed by Miller et al	Estimated	
2.00	1.95	2.00	$K_2 \rightarrow K_6$
			$M_3^+ \rightarrow M_1^-$
2.25	2.15	2.20	$K_5 \rightarrow K_3$
		2.40	$M_3^+ \rightarrow M_4^-$
2.45	2.50	2.50	$L_1 \rightarrow L_2$
		2.60	$H_1 \rightarrow H_1$
2.70-2.80	2.75	2.80	$M_1^+ \rightarrow M_4^-$
3.10 (probable)	3.10	3.15	$A_1 \rightarrow A_3$
			$K_2 \rightarrow K_3$

index n and extinction coefficient k both decrease with the exposure time of the film in air. The optical conductivity curves for these two exposure times in air together with the original one (the curve obtained 4 hours after the film was removed from the U.H.V. system) are shown in Figure 38. We notice that the optical conductivity decreases by about 10%, when the film is left in air for 72 hours after the first measurements and it decreases by as much as 15% for some photon energies, when it is left for 168 hours after the first measurements. This suggests a non-linear behaviour of optical conductivity with exposure time in air. We also notice the existence of structures in all the curves at the same photon energies.

In order to explain the above results, a theoretical model is constructed, in which it is assumed that a dielectric layer is formed on the surface of Cd film, when it is exposed in air and its thickness increases with the exposure time. Figure 39 shows a diagram of such a model, in which

$\tilde{n}'$ and $\tilde{n}$ are the complex refractive indices of the dielectric layer and the Cd film respectively,

d is the thickness of the dielectric layer,

θ and γ are the angles of incidence and refraction at air-dielectric layer interface,

ξ is the angle of refraction at dielectric layer-Cd interface,

r_i and t_i are the ratios of reflected and transmitted amplitudes to the incident amplitude for propagation from air to dielectric layer,

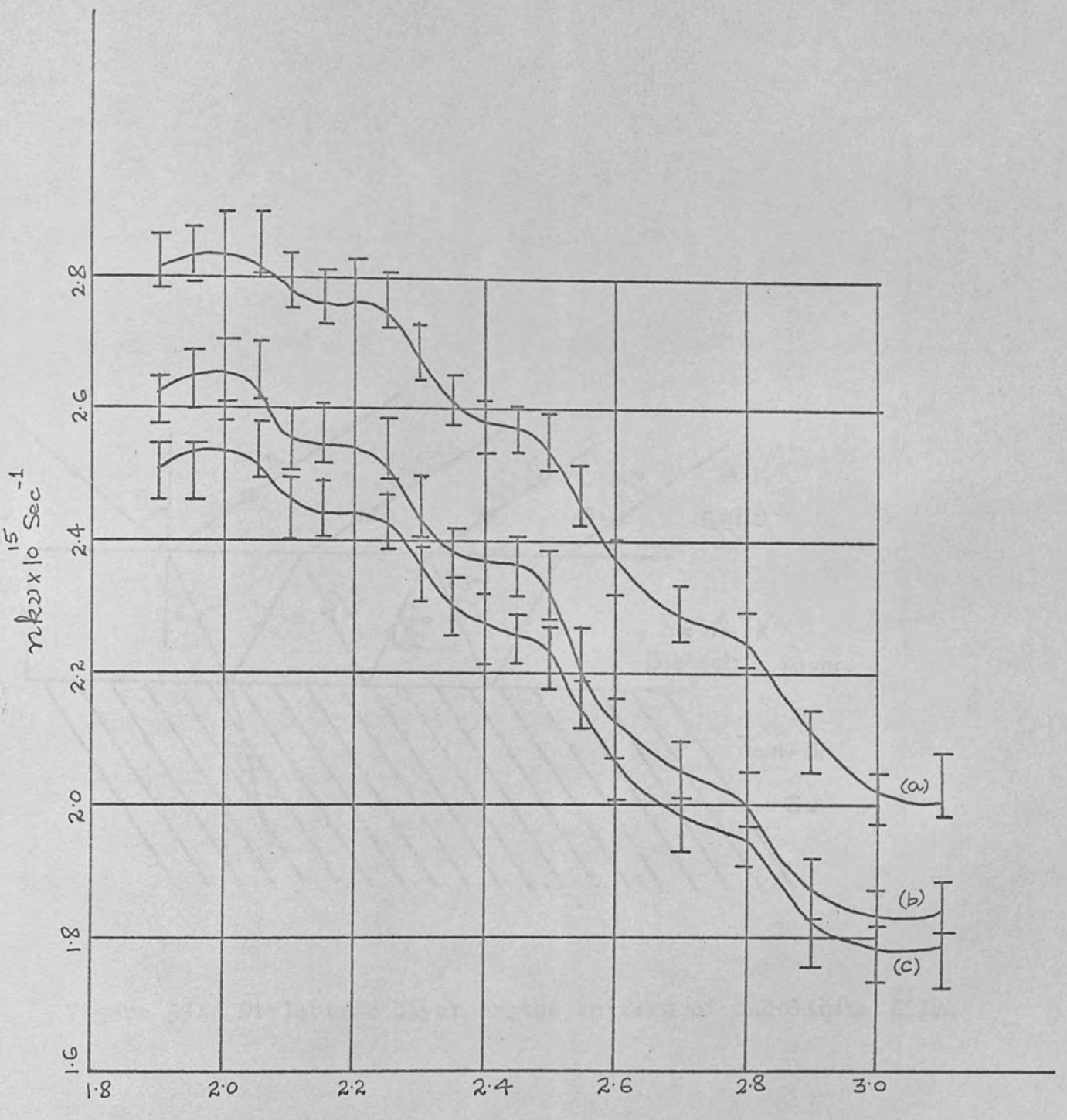

Figure 38: Optical conductivity of Gd in air as a function of ageing.

(a) 4 hours after taking out from U.H.V. (b) 76 hours after taking out from U.H.V. (c) 172 hours after taking out from U.H.V.

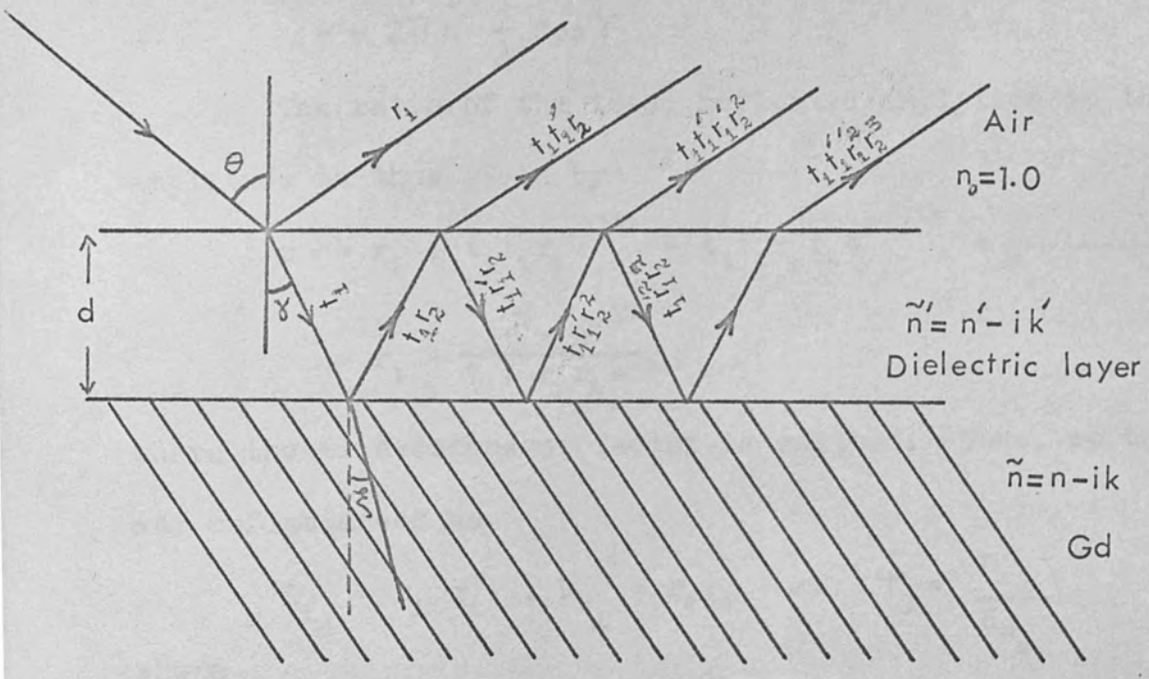

Figure 39: Dielectric layer on the surface of Gadolinium film.

r_1' and t_1' are the corresponding ratios for propagation from dielectric layer to air, and

r_2 is the ratio of the reflected amplitude from the metal surface to the incident amplitude on it.

The quantities r_1, r_1', r_2, t_1 and t_1' can be written in the form of equations (2.1)-(2.4). From the form of the equations (2.1) and (2.2) we see that r_1' is equal to $-r_1$. Writing δ, for the change in phase of the beam on traversing the dielectric layer

$$\delta = 2\pi \tilde{n}' \frac{d}{\lambda} \cos\gamma \qquad (6.1)$$

The ratio of the total reflected amplitude to the incident amplitude is thus given by

$$r = r_1 + t_1 t_1' r_2 e^{-2i\delta} - t_1 t_1' r_1 r_2^2 e^{-4i\delta} + \cdots\cdots\cdots\cdots$$

$$= r_1 + \frac{t_1 t_1' r_2 e^{-2i\delta}}{1 + r_1 r_2 e^{-2i\delta}} \qquad (6.2)$$

where the time-dependent factor is omitted. Thus, we can write our reflectances as

$$R_{\perp_d} = r_\perp r_\perp^* \quad , \quad R_{\parallel_d} = r_\parallel r_\parallel^* \quad \text{and} \quad \rho_d = \frac{R_{\perp_d}}{R_{\parallel_d}} \qquad (6.3)$$

where

$$r_\perp = r_{1\perp} + \frac{t_{1\perp} t_{1\perp}' r_{2\perp} e^{-2i\delta}}{1 + r_{1\perp} r_{2\perp} e^{-2i\delta}}$$

$$r_\parallel = r_{1\parallel} + \frac{t_{1\parallel} t_{1\parallel}' r_{2\parallel} e^{-2i\delta}}{1 + r_{1\parallel} r_{2\parallel} e^{-2i\delta}} \qquad (6.4)$$

$$t'_{1\perp} = \frac{2\tilde{n}' \cos\gamma}{\tilde{n}' \cos\gamma + \cos\theta} \quad , \quad t_{1\perp} = \frac{2\cos\theta}{\cos\theta + \tilde{n}' \cos\gamma}$$

$$t'_{1\parallel} = \frac{2\tilde{n}' \cos\gamma}{\tilde{n}' \cos\theta + \cos\gamma} \quad , \quad t_{1\parallel} = \frac{2\cos\theta}{\cos\gamma + \tilde{n}' \cos\theta} \qquad (6.5)$$

$$r_{1\perp} = -\frac{\tilde{n}' \cos\gamma - \cos\theta}{\tilde{n}' \cos\gamma + \cos\theta} \quad , \quad r_{2\perp} = -\frac{\tilde{n} \cos\varepsilon - \tilde{n}' \cos\gamma}{\tilde{n} \cos\varepsilon + \tilde{n}' \cos\gamma}$$

$$r_{1\parallel} = -\frac{\tilde{n}' \cos\theta - \cos\gamma}{\tilde{n}' \cos\theta + \cos\gamma} \quad , \quad r_{2\parallel} = -\frac{\tilde{n} \cos\gamma - \tilde{n}' \cos\varepsilon}{\tilde{n} \cos\gamma + \tilde{n}' \cos\varepsilon}$$

$$\cos\gamma = \frac{\sqrt{\tilde{n}'^2 - \sin^2\theta}}{\tilde{n}'} \qquad \text{and} \qquad \cos\varepsilon = \frac{\sqrt{\tilde{n}^2 - \sin^2\theta}}{\tilde{n}}$$

A computer programme using FORTRAN IV language was written and is given in appendix 1. This programme first calculatesn and k of a fresh Gd film from the reflectance ratio measurements at two angles of incidence θ_1 and θ_2. These n and k values are then used to calculate ρ_{d_1} and ρ_{d_2} at θ_1 and θ_2, using equations (6.3)-(6.5) for different thickness of dielectric layer and for certain assumed values of n' and k' for the dielectric layer. These ρ_{d_1} and ρ_{d_2} are then used to calculate n_e and k_e of the film with the dielectric layer using the method of Section 2.5.1.

First of all we assumed that there was no dielectric layer on the surface of Gd film, when the first measurements were made after 4 hours of taking out from U.H.V. system. We then assumed that when dielectric layer is formed, it has the same value of n as the original Gd film and has a value of 0.5 for k (dielectrics generally have small values of k). This is the order of values experimentally obtained for a gadolinium oxide film prepared by heating a thin Gd film (370Å) in air.

The values of n_e and k_e were then calculated using the computer programme mentioned above. The values of n_e and k_e were found to be smaller than the values of n and k for the fresh film. This is what we experimentally observed.

The calculated optical conductivity curves for different thickness d of the dielectric layer together with the optical conductivity curve of the fresh Gd film (d = 0) are shown in Figure 40(a). We notice the decrease in optical conductivities with the increasing thickness of the dielectric layer. We also notice the structure in all the curves at the same photon energies. By comparing the experimental results with the theoretical results based on the above model, we can conclude that the Gd film behaves as if a dielectric layer of thickness in the range 10-20A° is formed in 72 hours.

The optical conductivities for some other combinations of optical constants n' and k' of the dielectric layer were calculated for $\sim$20A° thick dielectric layer. The results are shown in Figure 41. These graphs show that variation of n' and k' slightly change the average slope of the conductivity curve. All the structures still exist in every curve. The average slope of the conductivity curve for $n' = 1.6$ and $k' = 0.5$ is more nearly the same as that of the optical conductivity curve for fresh film than the average slope of the other two optical conductivity curves, for d = 20Å. From the experimental results we also see that the average slope of the optical conductivity curve obtained after 72 hours from the first measurements is nearly the same as that

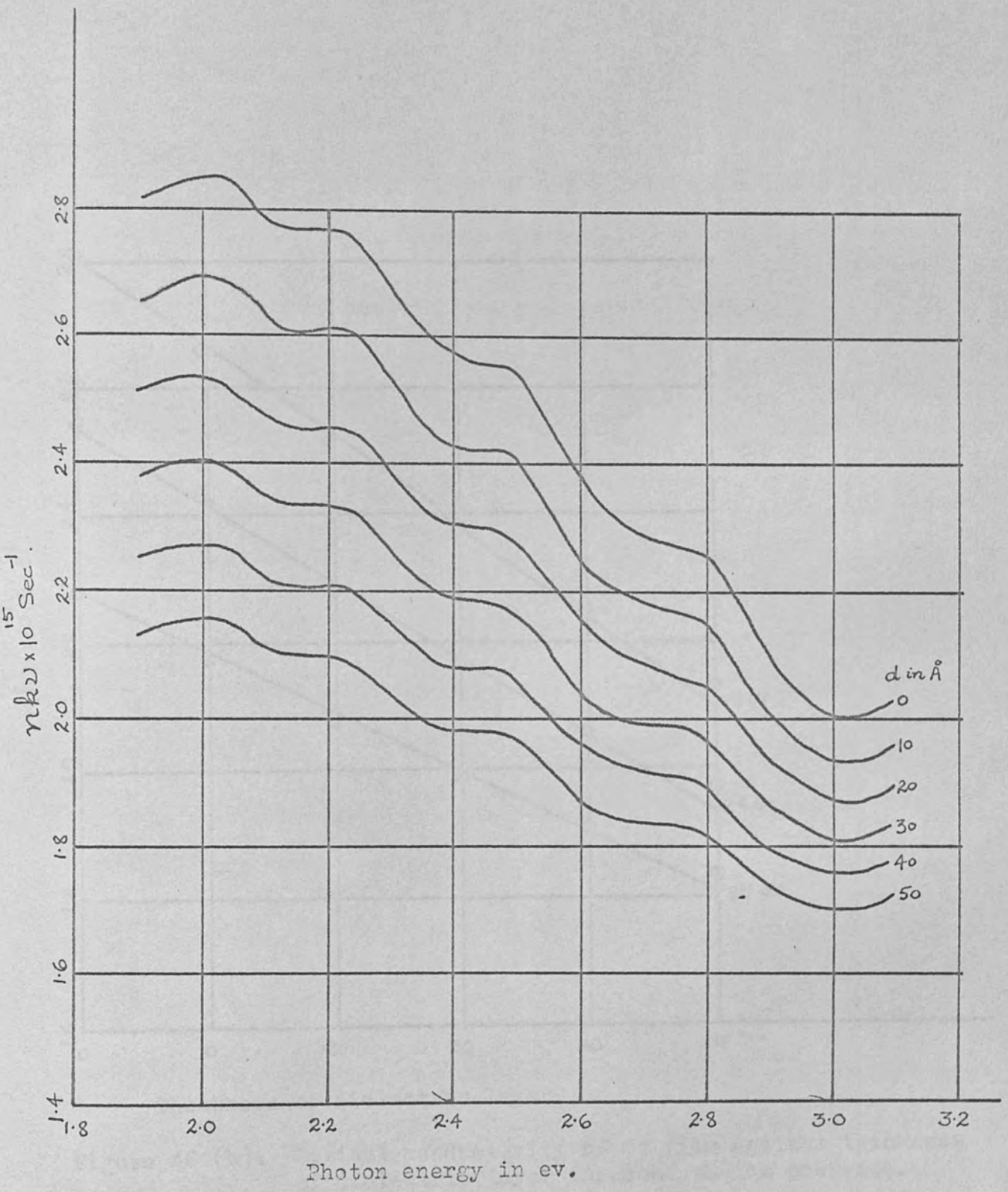

Figure 40 (a): Optical conductivity of Gd film as a function of thickness of dielectric layer. ($n' = n$, $k' = 0.5$)

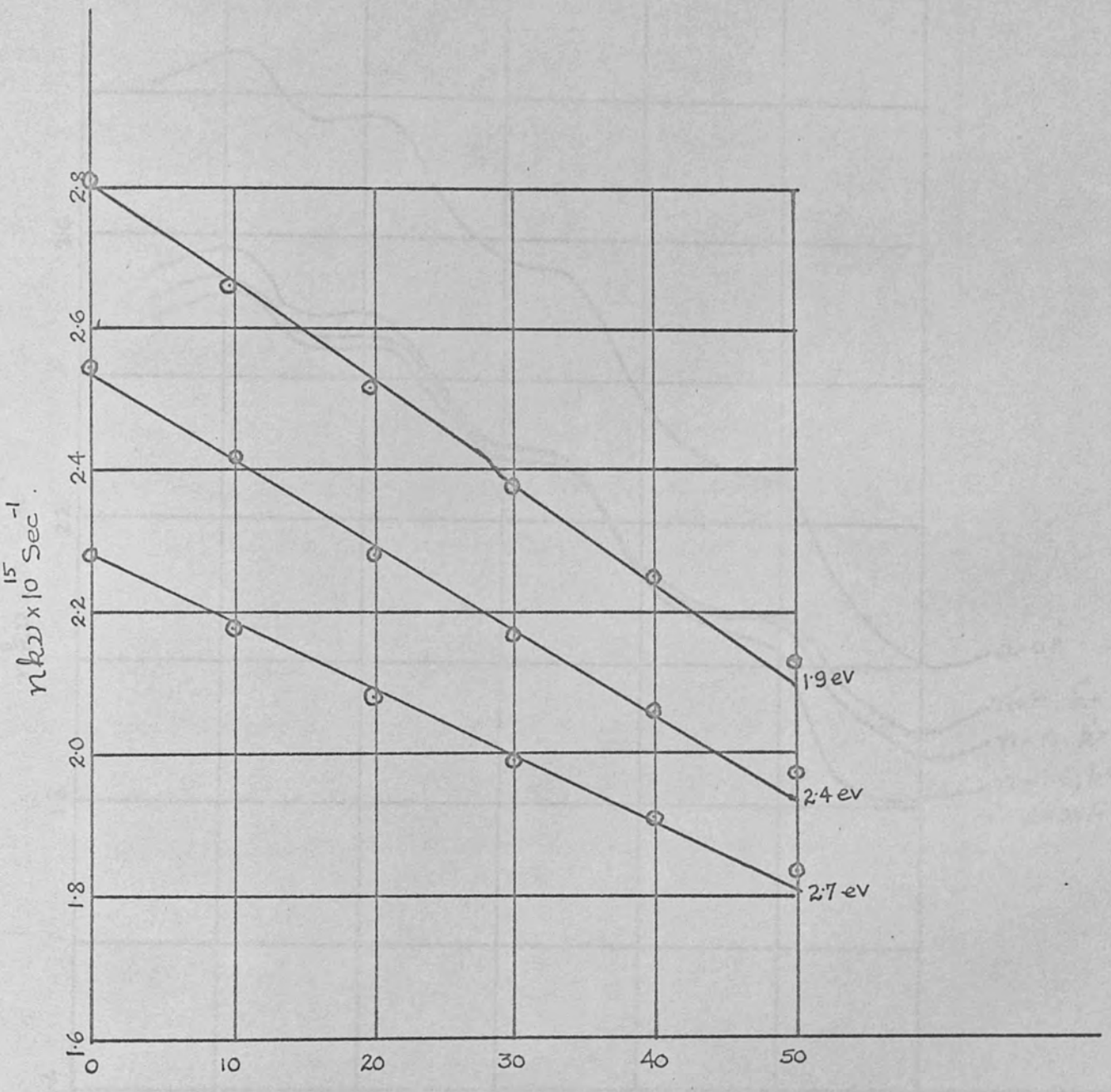

Figure 40 (b): Optical conductivity of Gd film against thickness of dielectric layer for some photon energies.

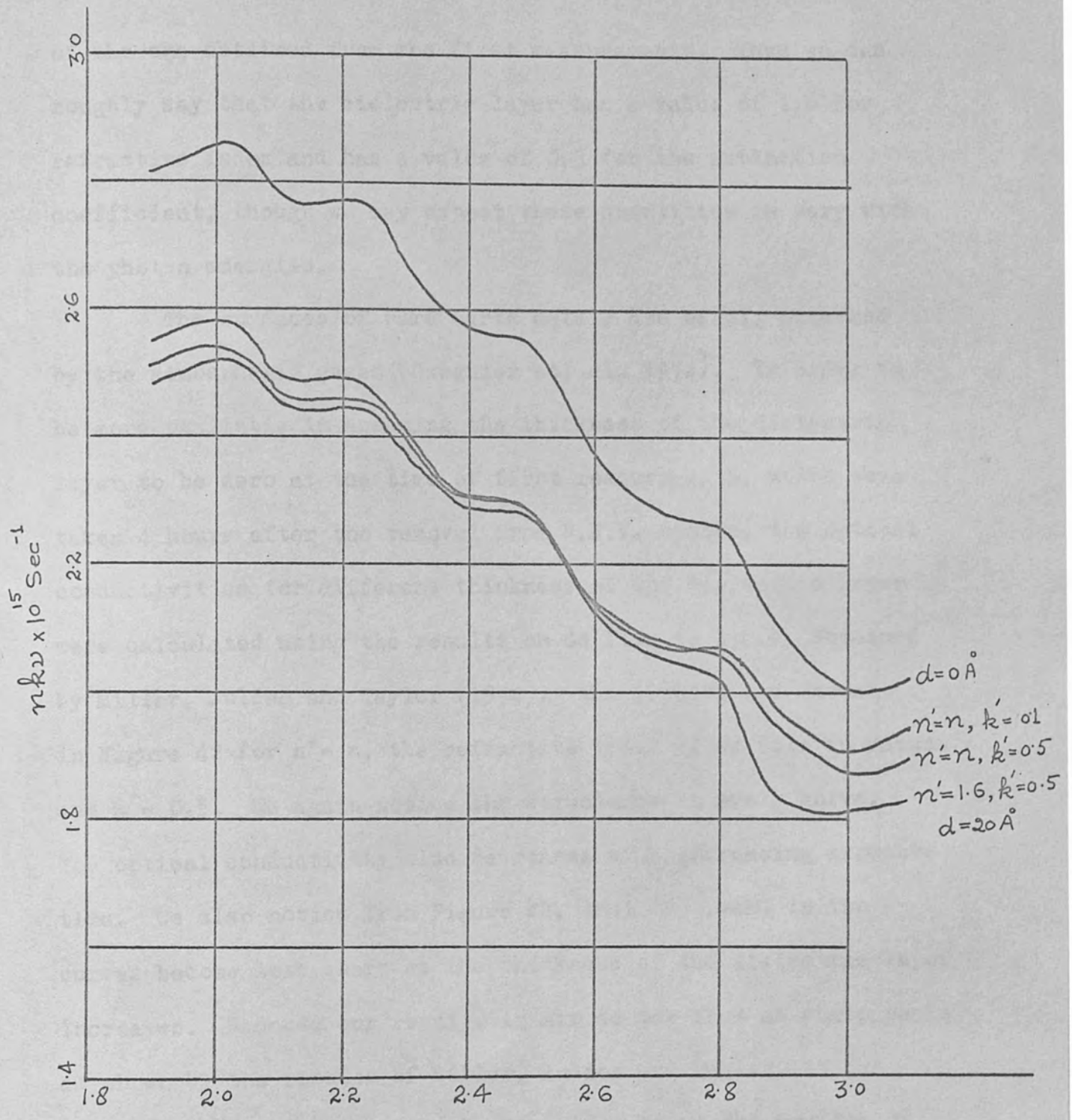

Figure 41: Optical conductivity of Cd film as a function of n′ and k′ of dielectric layer.

of the one obtained from the first measurements. Thus we can roughly say that the dielectric layer has a value of 1.6 for refractive index and has a value of 0.5 for the extinction coefficient, though we may expect these quantities to vary with the photon energies.

The surfaces of rare earth metals are easily attacked by the atmospheric gases (Gasgnier et. al. 1974). In order to be more realistic in assuming the thickness of the dielectric layer to be zero at the time of first measurements, which were taken 4 hours after the removal from U.H.V. system, the optical conductivities for different thickness of the dielectric layer were calculated using the results on Gd film in U.H.V. obtained by Miller, Julien and Taylor (1974). The results are shown in Figure 42 for $n' = n$, the refractive index of Gd film in vacuum and $k' = 0.5$. We again notice the structures in every curve. The optical conductivity also decreases with increasing exposure time. We also notice from Figure 42, that the peaks in the curves become less sharp as the thickness of the dielectric layer increases. Because our results in air do not show as sharp peaks as shown by the results of Miller, Julien and Taylor, it can be assumed that a dielectric layer is formed on the surface of the Gd film as soon as it is taken out from the ultra high vacuum.

Since the optical conductivity varies approximately linearly with the thickness of the dielectric layer (Figure 40(b)), and it varies non-linearly with the exposure time as Figure 38 suggests, we can predict a non-linear behaviour of the formation of the

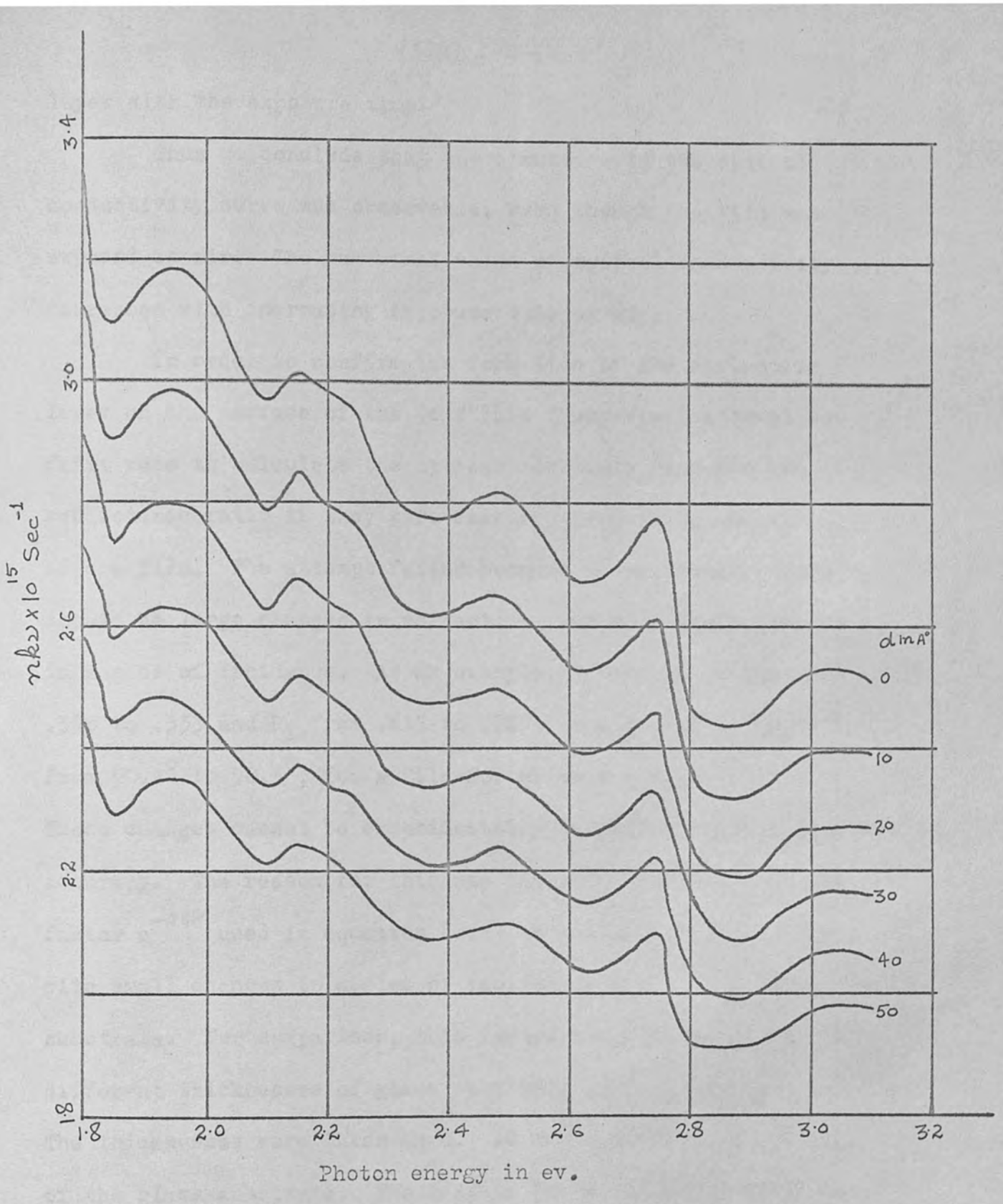

Figure 42: Optical conductivity of Gd film as function of thickness of the dielectric layer calculated from the measurements of Miller, Julien and Taylor (1974) in U.H.V. ($n' = n$, $k' = 0.5$).

layer with the exposure time.

Thus we conclude that the structure in the optical conductivity curve was observable, even though the film was exposed in air. The numerical value of optical conductivity decreases with increasing exposure time in air.

In order to confirm the formation of the dielectric layer on the surface of the Gd film a theoretical attempt was first made to calculate the optical constants from the two reflectance ratio if they were measured from the glass side of the film. The attempt failed because theoretically there should be large changes in reflectance for very small changes in angles of incidence. As an example, $R_{\parallel}$ should change from .398 to .333 and $R_{\perp}$ from .613 to .228 for a change in angle from 50.2° to 50.3°, for a film for which n = 2 and k = 3. These changes cannot be experimentally determined with sufficient accuracy. The reason for this was the large variation in the factor $e^{-2\beta\delta}$ used in equation (6.4) to calculate reflectances, with small changes in angles of incidence, for 0.1 cm thick glass substrate. For comparison, this factor was calculated for two different thicknesses of glass substrates at a wavelength $4000A^{\circ}$. The thicknesses were taken as 0.1 cm and 0.000005cm for n = 1.51 of the glass substrate. The results for a randomly chosen range of angles of incidence are shown in Table 10. For the reasons clear from the table no experimental measurements were made from the glass substrate side of the film.

Table 10. The quantity $e^{-2i\delta}$ for two different thicknesses at some angles

Angle of incidence θ°	$e^{-2i\delta}$ for n = 1.51, λ = 4000A$^\circ$			
	thickness = .00005cm		thickness = .1cm	
	real part	imaginary part	real part	imaginary part
50.0	-.456	-.890	-.290	-.957
50.5	-.451	-.892	+.255	+.967
51.0	-.446	-.895	-.305	-.925
51.5	-.442	-.897	+.464	+.886
52.0	-.437	-.899	-.723	-.691
52.5	-.433	-.901	+.968	+.249
53.0	-.428	-.904	-.887	+.461
53.5	-.423	-.906	+.109	-.994
54.0	-.419	-.908	+.916	+.401
54.5	-.414	-.910	-.386	+.922
55.0	-.409	-.912	-.999	-.029

6.3.5. Further Data on Gd

Because of the importance of the observed structure, it is desirable to present some further optical conductivity curves. These are shown in Figure 43. Some of the results were taken using a lower energy resolution and chronologically these are the first curves measured for Gd. The growth pressure and the time measurements were started after the removal of the film from U.H.V. system are given for each film. All these curves show structures of energies observed before. The effect of ageing on one of the filmsin air is also shown in the figure.

We notice the consistency in the results as far as the structure in optical conductivity curve. We also notice the different values of optical conductivity for different films. The optical conductivity decreases with increasing exposure time of the film in air.

6.4 Terbium (Tb)

Terbium is the second of the heavy rare earth metals with atomic number 65. Its melting point is 1723^{o}K, density is 8.2gm/cc and ferromagnetic Curie temperature is 221^{o}K.

In all, optical measurements were made on 18 Tb films. On the first 12 films, measurements were performed at one angle of incidence using the rectangular graded wavelength filter. On the last 6 films reflectance ratio measurements were made at two angles of incidence using the circular wavelength filter.

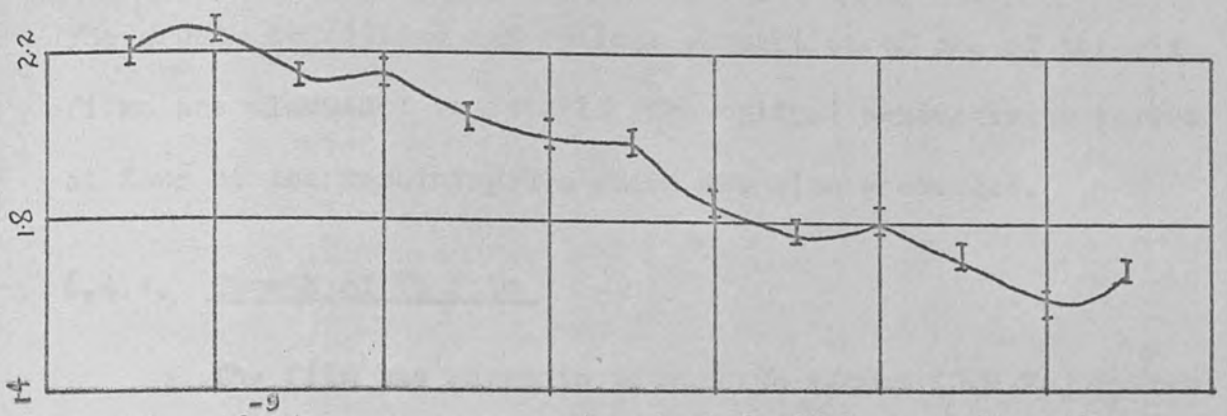

$p < 8 \times 10^{-9}$ torr, measurements started ~ 24 hours after the removal from U.H.V. , thickness of the film ~ 820Å .

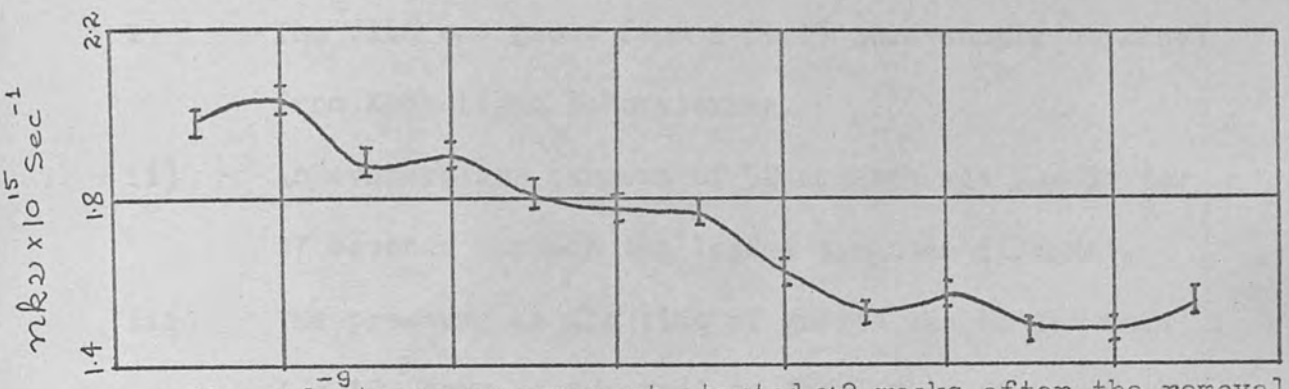

$p < 2 \times 10^{-9}$ torr, measurement started ~ 2 weeks after the removal from U.H.V., thickness of the film not measured.

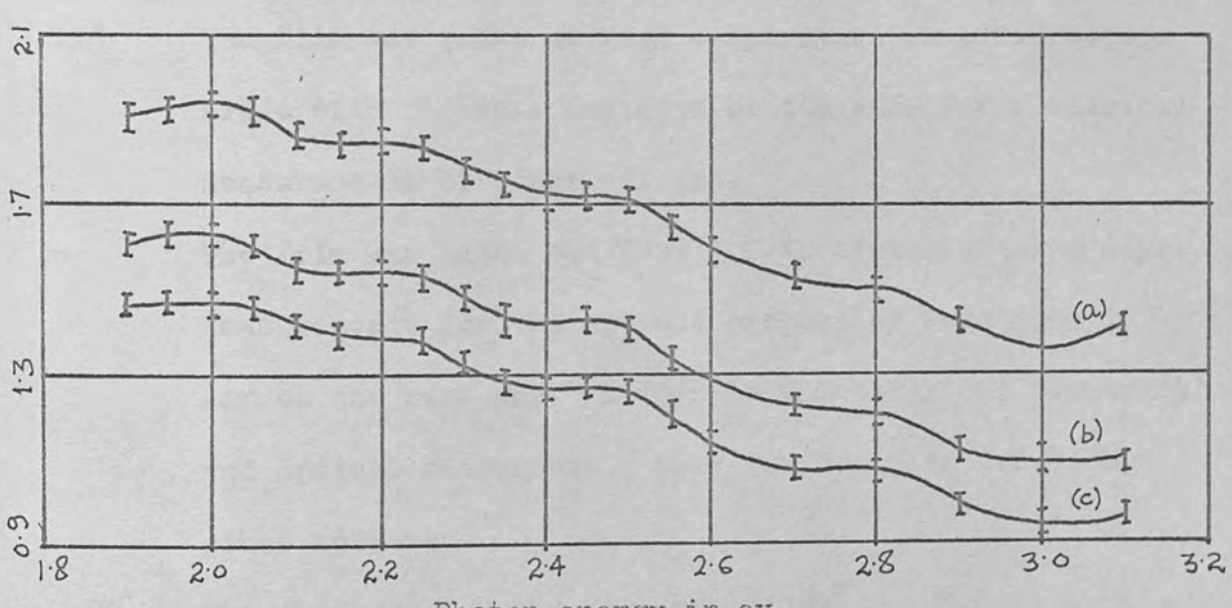

$p < 4 \times 10^{-8}$ torr, measurements started (a) 5 hours, (b) 56 hours, (c) 198 hours, after removal from U.H.V., thickness of the film ~ 760Å .

Figure 43: Optical conductivity curves for three different Gd films grown in U.H.V. and measured in air.

The growth conditions and optical properties of one of the six films are discussed in detail. The optical conductivity curves of four of the remainingfive films are also presented.

6.4.1. Growth of Tb film

The film was grown in ultra high vacuum (U.H.V.) system. The growth conditions for the film were as follows:-

i) The film was grown from a 99.9% pure sample obtained from Koch-Light Laboratories.

ii) An evaporation current of 50 amperes was passed for 87 seconds through the loaded tungsten filament.

iii) The pressure at the time of growth was better than 3×10^{-8} torr as measured on the linear scale of the Bayard-Alpert gauge.

iv) The film was grown at room temperature on a microscope slide with nichrome contacts on its ends for electrical measurements by other workers.

v) The film was taken out from U.H.V. system after 4 days. Measurements for the optical properties were made in air on the same day. Before it was taken out electrical and optical measurements were performed in U.H.V. by other workers.

vi) The thickness of the film was 1110A^{o}.

6.4.2 Optical properties of Tb Film

Reflectance ratios were measured on the above grown Tb film in air, four hours after its removal from the U.H.V. system.

The measurements were made on the central area of the film at angles of incidence 80.3° and 60.3°.

Figure 44 shows the variation of reflectance ratios with incident energy in the visible region of the spectrum for the above mentioned angles of incidence. We note the large variation in reflectance ratio for angle of incidence 80.3° compared with that at 60.3°. The values of n and k of the film derived from the measured reflectance ratios are shown in Figure 45. The calculated optical conductivity curve is shown in Figure 46. We notice the structure occuring in this curve, which will be interpreted in the next section.

The optical properties of terbium have not been so extensively studied as that of Gd. Figure 47 shows the spectral dependence of optical conductivity, for Tb at room temperature, obtained by some authors. As for Gd, we again find the disagreement in the values of optical conductivity. More surprisingly, the values of optical conductivity obtained by us, for this Tb film in air are greater for most incident energies than those obtained by Miller, Julien and Taylor (1974) in U.H.V. But their further results on Tb films (L.S. Julien, Ph.D.Thesis, 1973) show the variation of optical conductivity between 3.2×10^{15} to 2.0×10^{15} sec^{-1} for the whole range of photon energies under investigation. The general disagreement in their values of optical conductivity for different Tb films in comparison to Gd films, they thought, was due to more chemically reactive nature of Tb than Gd.

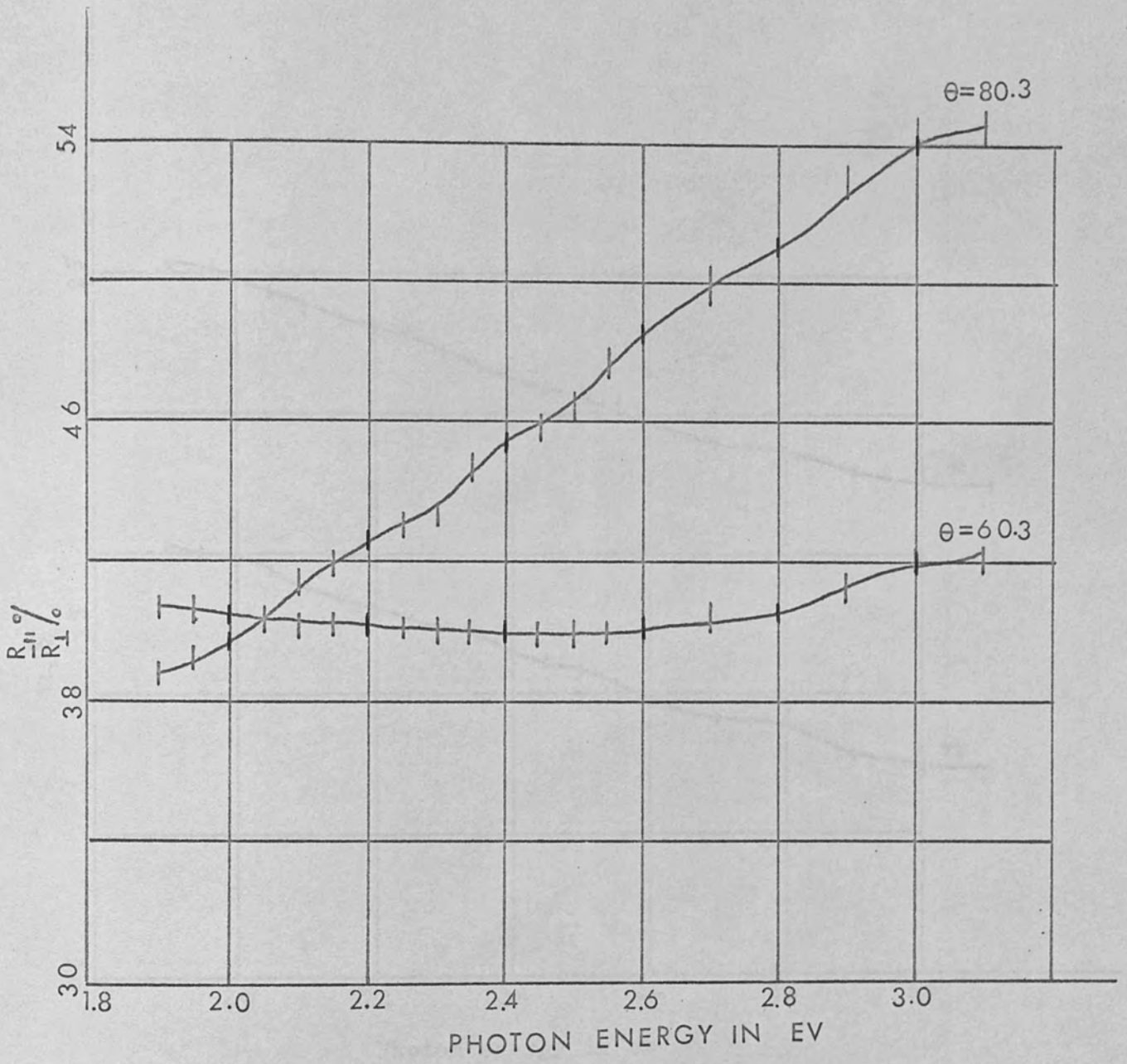

Figure 44: Reflectance ratios at 80.3° and 60.3° measured for Tb film in air.

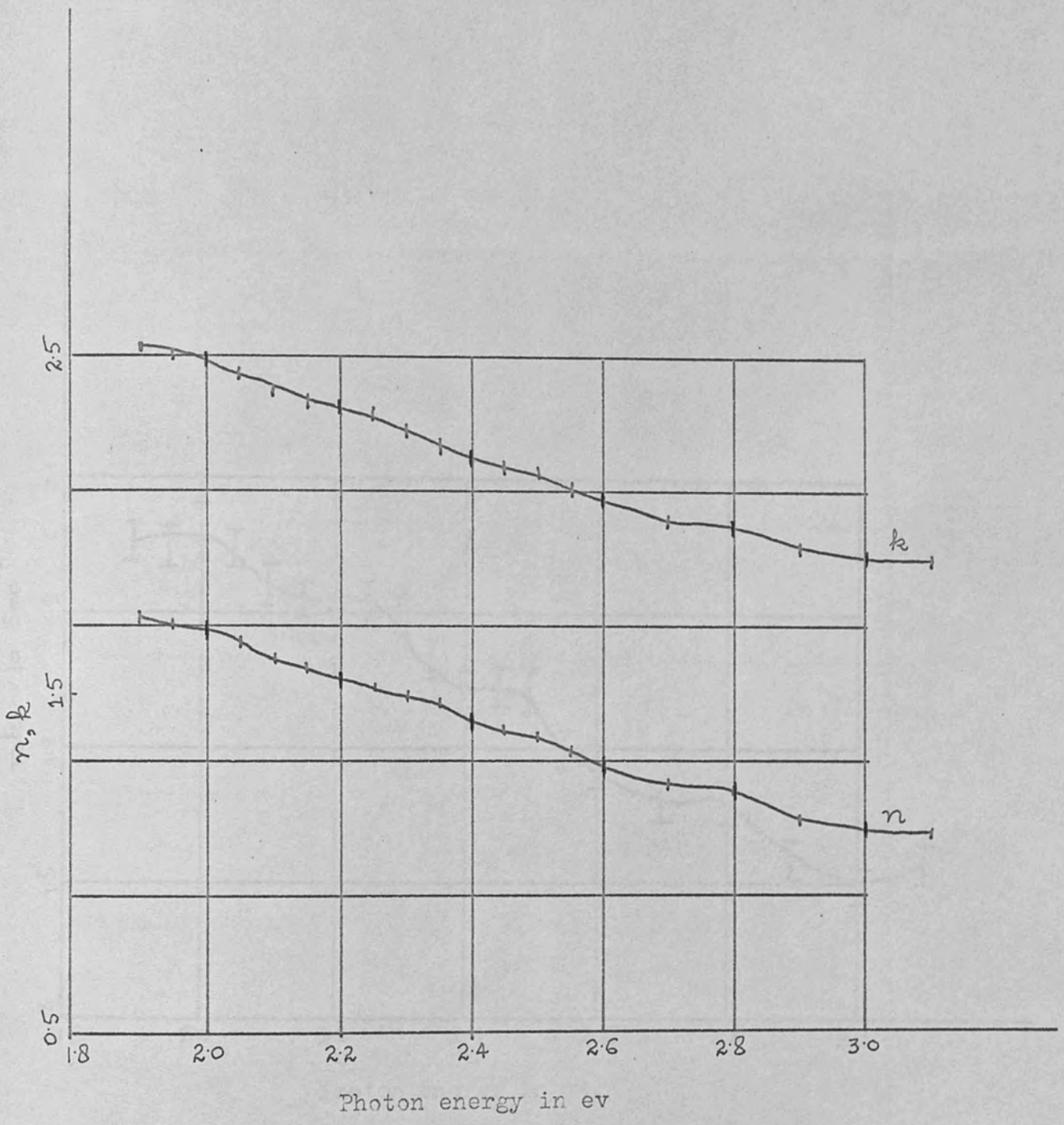

Figure 45: Optical constants n and k for Tb film in air.

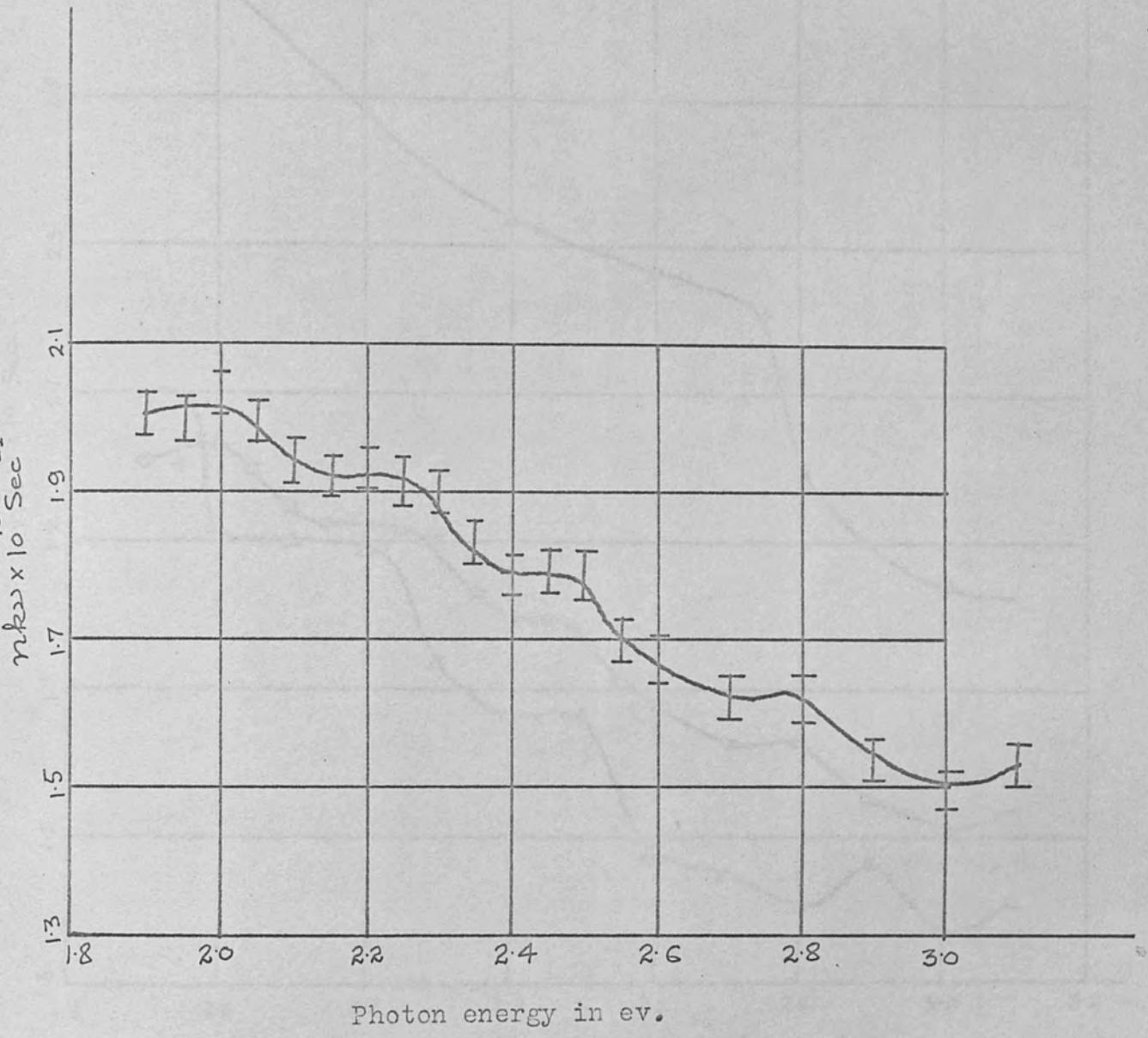

Figure 46: Optical conductivity of Tb in air at room temperature.

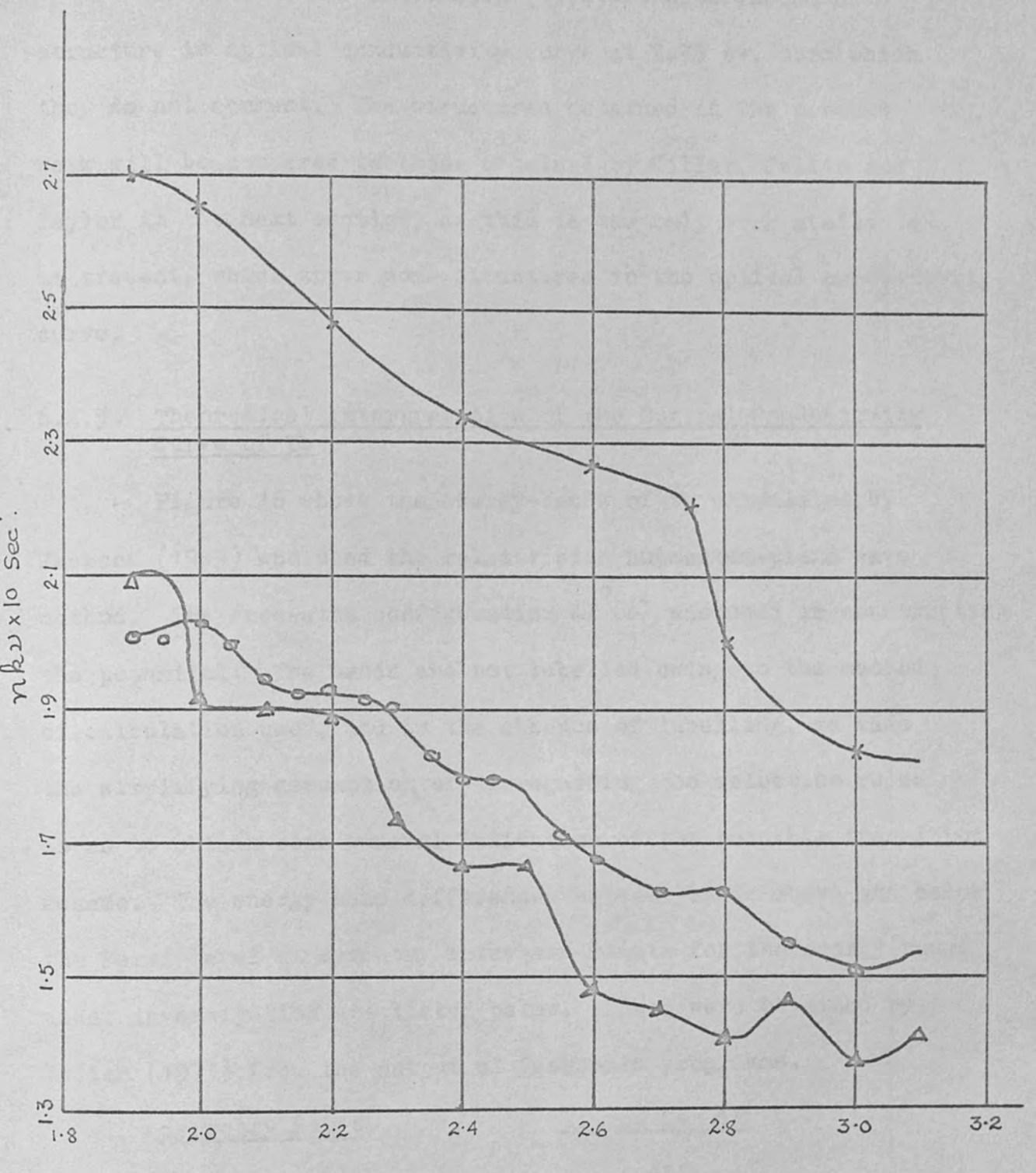

Figure 47: Optical conductivity of Tb at room temperature by some authors.

× Erskine, Blake and Flaten; o Present work;
▵ Miller, Julien and Taylor.

Erskine, Blake and Flaten (1974) results indicate structure in optical conductivity curve at 2.75 ev. upon which they do not comment. The structures obtained in the present work will be compared to those obtained by Miller, Julien and Taylor in the next section, as this is the only work available at present, which shows some structures in the optical conductivity curve.

6.4.3. Theoretical Interpretation of the Optical Conductivity Curve of Tb

Figure 48 shows the energy-bands of Tb calculated by Jackson (1969) who used the relativistic augmented-plane wave method. The free-atom configuration $4f^9 6s^2$ was used in constructing the potential. The bands are not labelled owing to the method of calculation used, and in the absence of labelling, we made the simplifying assumption of disregarding the selection rules so as to obtain some general indication of the possible transition scheme. The energy band differences between bands above and below the Fermi level at symmetry interband points for the energy range under investigation are listed below. These were obtained by Julien (1973) from the output of Jackson's programme.

Symmetry Point	Energy Gap ΔE
M	1.836
	2.992
	2.788
	2,380
	2.788

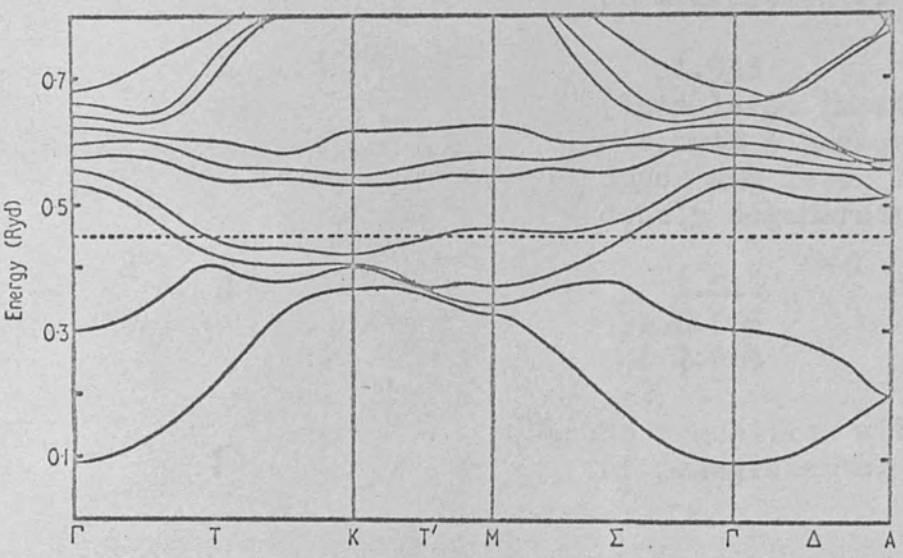

Figure 48: Electronic band structure diagram for h.c.p. Terbium (Jackson, 1969).

Symmetry Point	Energy Gap ΔE
K	2.230 2.462 1.754 1.986 2.924 1.822 1.918 2.856 2.652
A	No transition within range of measurements.
L	1.938 (This level is assigned a strength 4 because both the upper and lower levels are doubly degenerate)
H	3.046 3.005 2.965
Γ	No transition within range of measurements.

The estimated peaks are shown in Figure 49 (Miller, Julien and Taylor, 1974). We see immediately that the peak positions are similar to the estimated positions for Gd. In the theoretical diagrams the low energy peak for Tb is shifted to lower energy by 0.1 ev, whereas in the experimental curve it is still at the same value as that for Gd. This can be explained if we consider the number of transitions at 1.95 ev in the range 1.95 ± 0.05 ev instead of number of transitions at 1.90 ev in the range 1.90 ± 0.05 ev. There will be six possible transitions at 1.95 ev and we will have a big peak at 1.95 ev. Since there is an uncertainty of ± 0.05 ev in our measurements, we conclude that the estimated peaks are in good

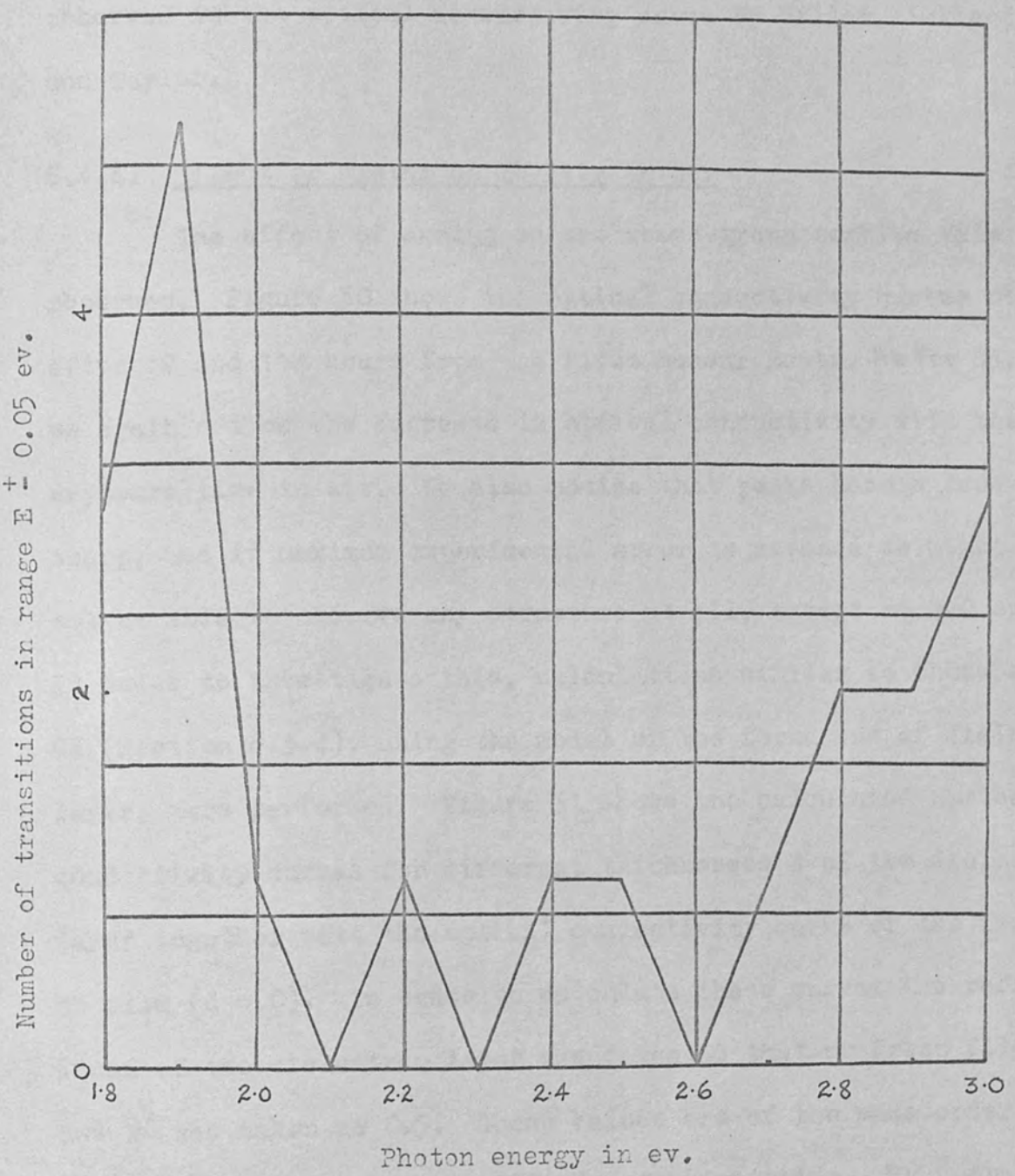

Figure 49: Theoretically estimated peak positions for Tb.

agreement with the observed peaks in the experimental curve. The results are summarized in Table 11, which also shows the energies observed in the optical conductivity curve by Miller, Julien and Taylor.

6.4.4. Effect of Ageing on Tb Film in Air

The effect of ageing on the above-grown terbium film was observed. Figure 50 shows the optical conductivity curves obtained after 12 and 114 hours from the first measurements. As for Gd, we again notice the decrease in optical conductivity with the exposure time in air. We also notice that peaks become less sharp, and if maximum experimental error is assumed we might not be able to observe any structure at all, except at 2.0 ev. In order to investigate this, calculations similar to those for Gd (Section 6.3.4), using the model of the formation of dielectric layer, were performed. Figure 51 shows the calculated optical conductivity curves for different thicknesses d of the dielectric layer together with the optical conductivity curve of the fresh Tb film (d = 0). In order to calculate these curves the refractive index of the dielectric layer was taken as that of fresh film and k' was taken as 0.5. These values are of the same order as those obtained by Taylor (1972) for terbium oxide. By comparing the experimental results with the theoretical results, we can roughly estimate that a dielectric layer of thickness in the range 30-50A^{o} is formed on the Tb film in 12 hours. Comparison of this with the thickness of the dielectric layer estimated for Gd,

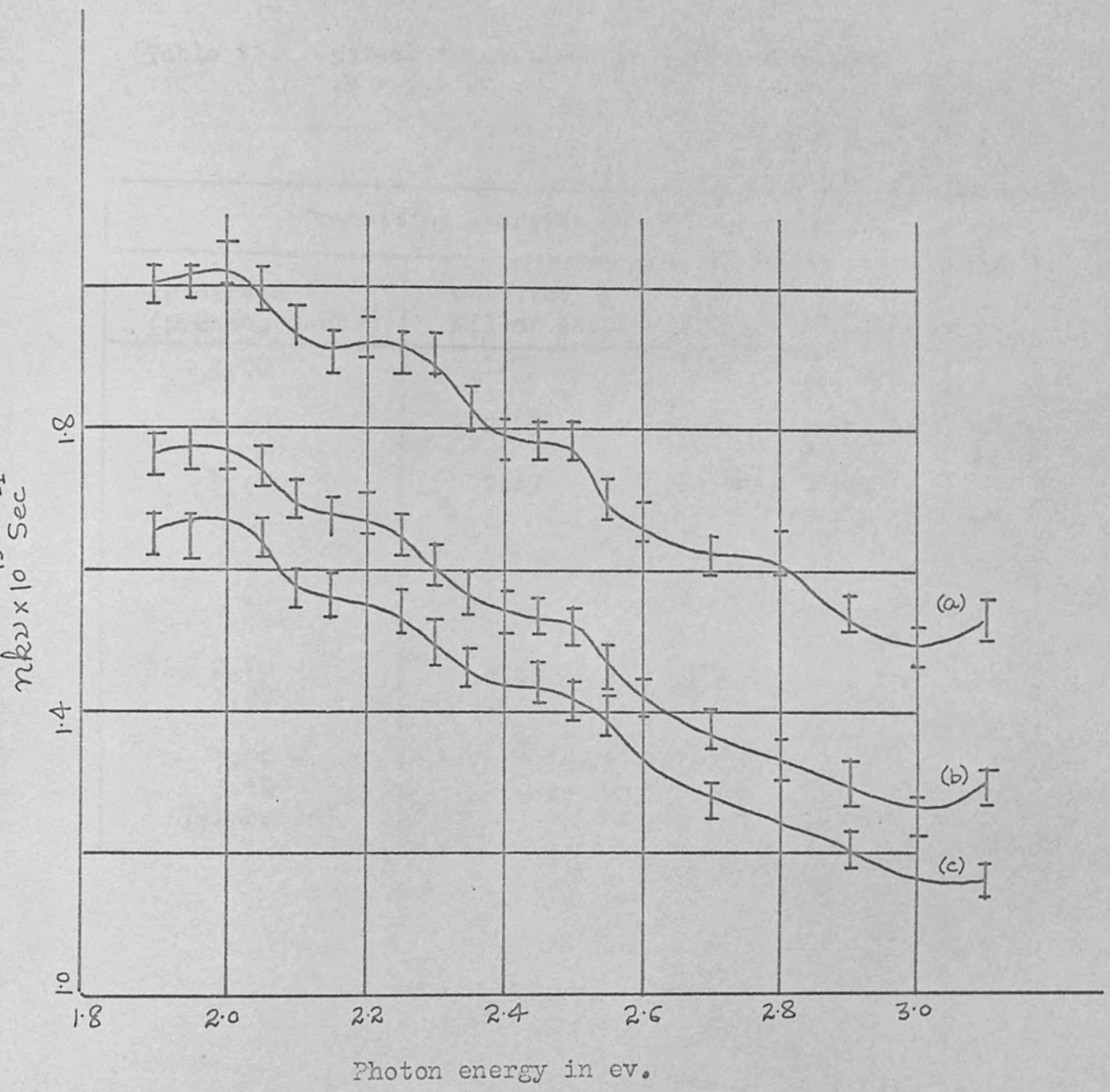

Figure 50: Optical conductivity of Tb in air as a function of ageing.

(a) 4 hours after taking out from U.H.V. (b) 16 hours after taking out from U.H.V. (c) 118 hours after taking out from U.H.V.

Table 11. Optical transitions in Tb for the range 1.9 - 3.1 ev

Transition energies ev			Symmetry Points
observed (present work)	observed by Miller et.al.	Estimated	
2.00	1.95	1.95	K, L
2.20	2.15	2.20	K
2.45	2.45	2.40	M
		2.50	K
		2.80	M
2.70 - 2.80	2.90	2.90	K
3.00 - 3.10 (probable)		3.00	M, H

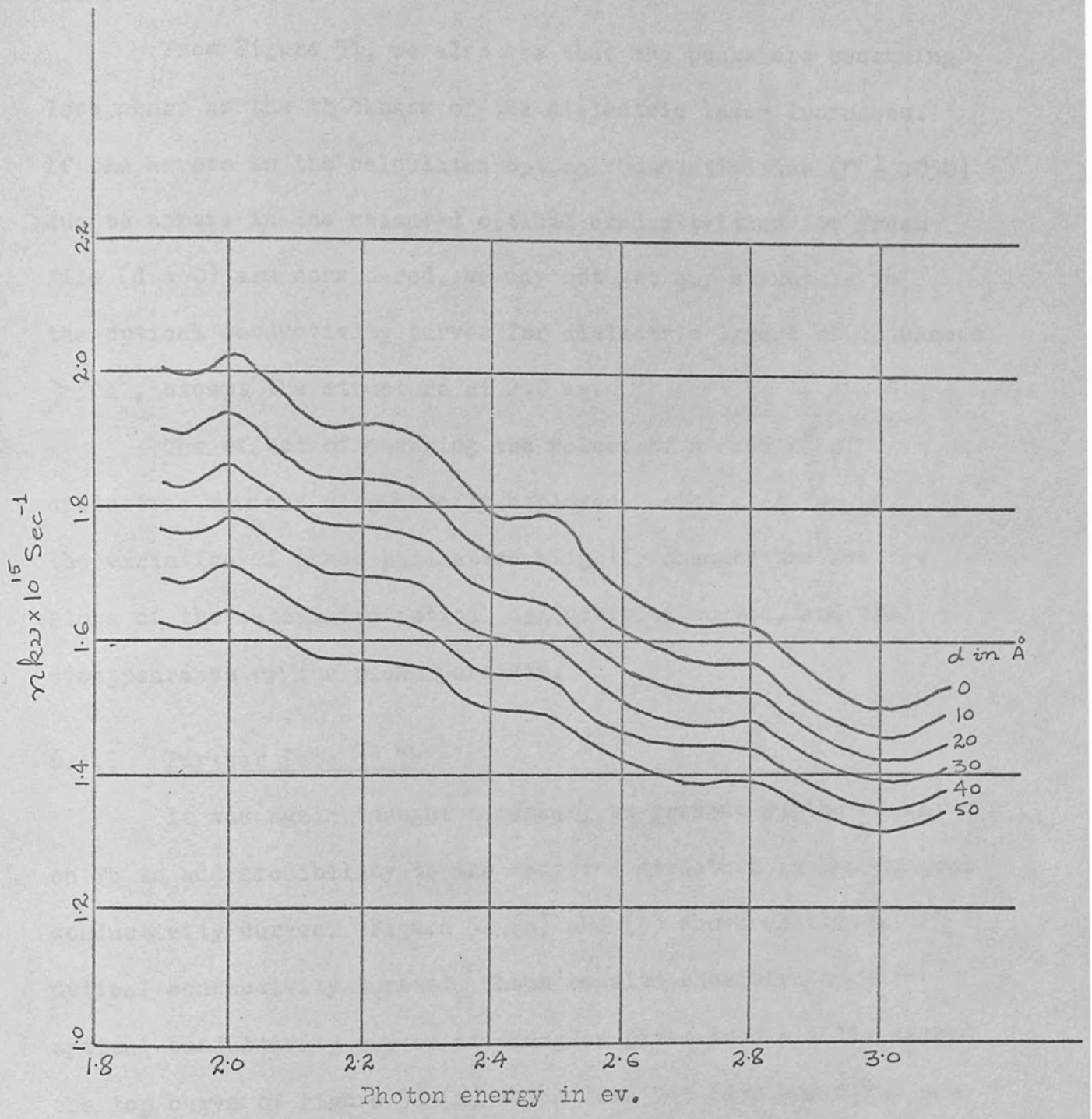

Figure 51: Optical conductivity of Tb film as a function of thickness of dielectric layer. ($n' = n$, $k' = 0.5$).

suggests the correct relative order of reactiveness for Gd and Tb.

From Figure 51, we also see that the peaks are becomming less sharp as the thickness of the dielectric layer increases. If the errors in the calculated optical conductivities ($\sim \pm .030$) due to errors in the measured optical conductivities for fresh film (d = 0) are considered, we may not get any structure in the optical conductivity curves for dielectric layers of thickness $> 30A^{o}$, except the structure at 2.0 ev.

The effect of changing the values of n' and k' of dielectric layer was also briefly explored. Like that for Gd, the variation of these parameters slightly changes the average slope of the calculated optical conductivity curves, and the disappearance of the peaks persists.

6.4.5 Further Data on Tb

It was again thought necessary to present further data on Tb to add credibility to the observed structure in the optical conductivity curves. Figure 52 (a) and (b) shows additional optical conductivity curves. These results show structure in optical conductivity curves at energies given in Table 11, except the top curve of Figure 52 (a) which does not show any structure at 2.2 ev. This was either due to long exposure time of the film in air or due to large energy steps taken in the measurements. The disappearance of the structure between 2.7 - 2.8 ev for the top curve of Figure 52 (a), under the error bars was probably due to the long exposure time of the film in air.

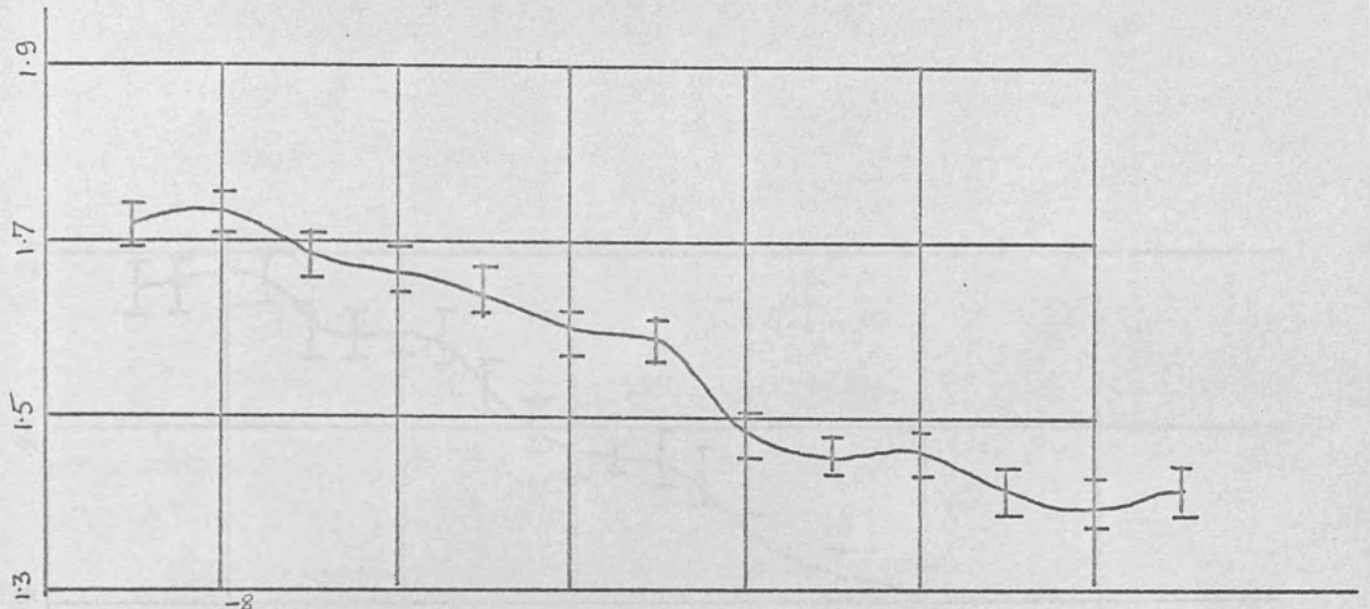

$p < 2 \times 10^{-8}$ torr, measurement started ~72 hours after removal from U.H.V., thickness of the film not measured.

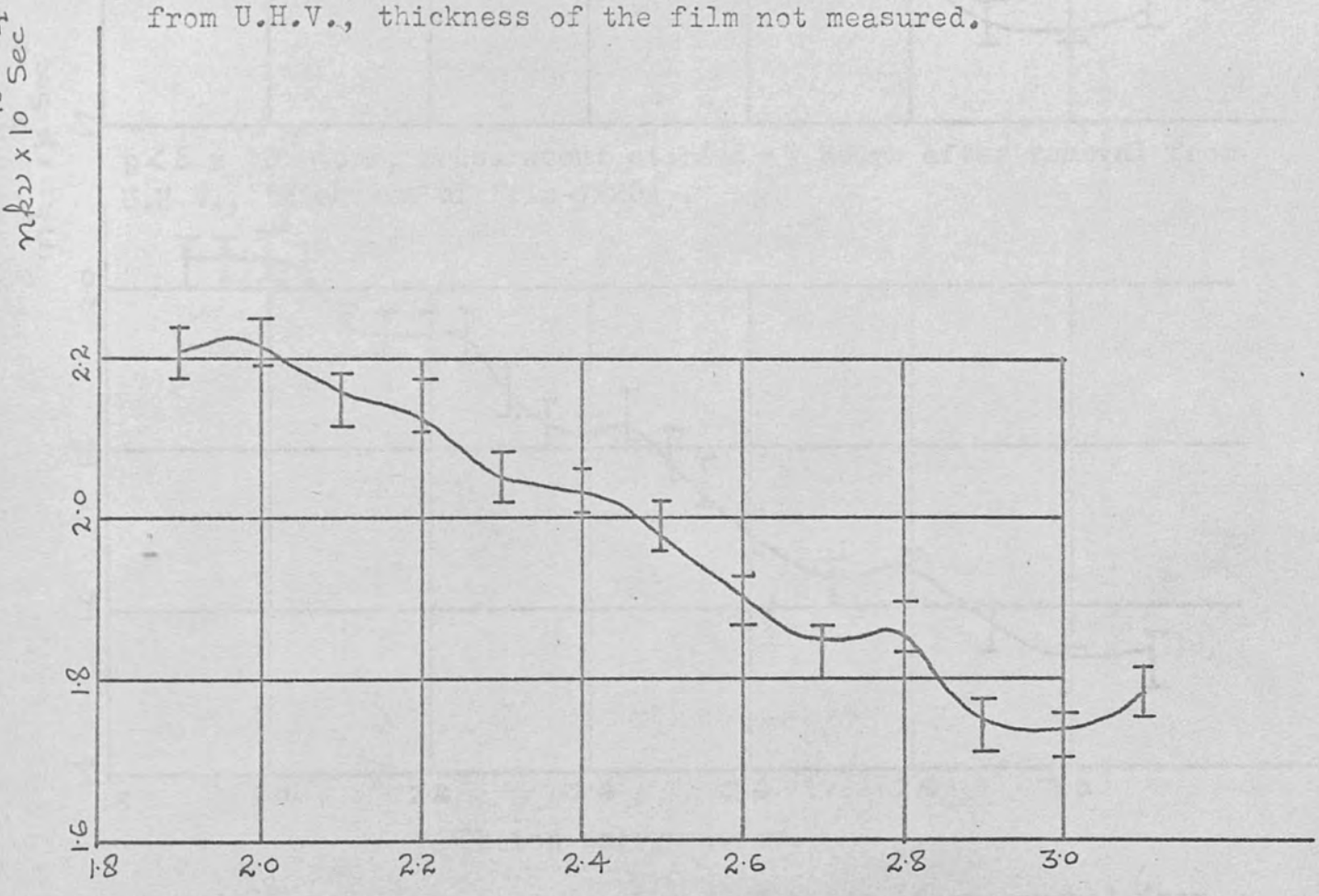

$p < 5 \times 10^{-8}$ torr, measurement started ~6 hours after removal from U.H.V., thickness of the film ~1340Å .

Figure 52 (a): Optical conductivity curves for some Tb films grown in U.H.V. and measured in air.

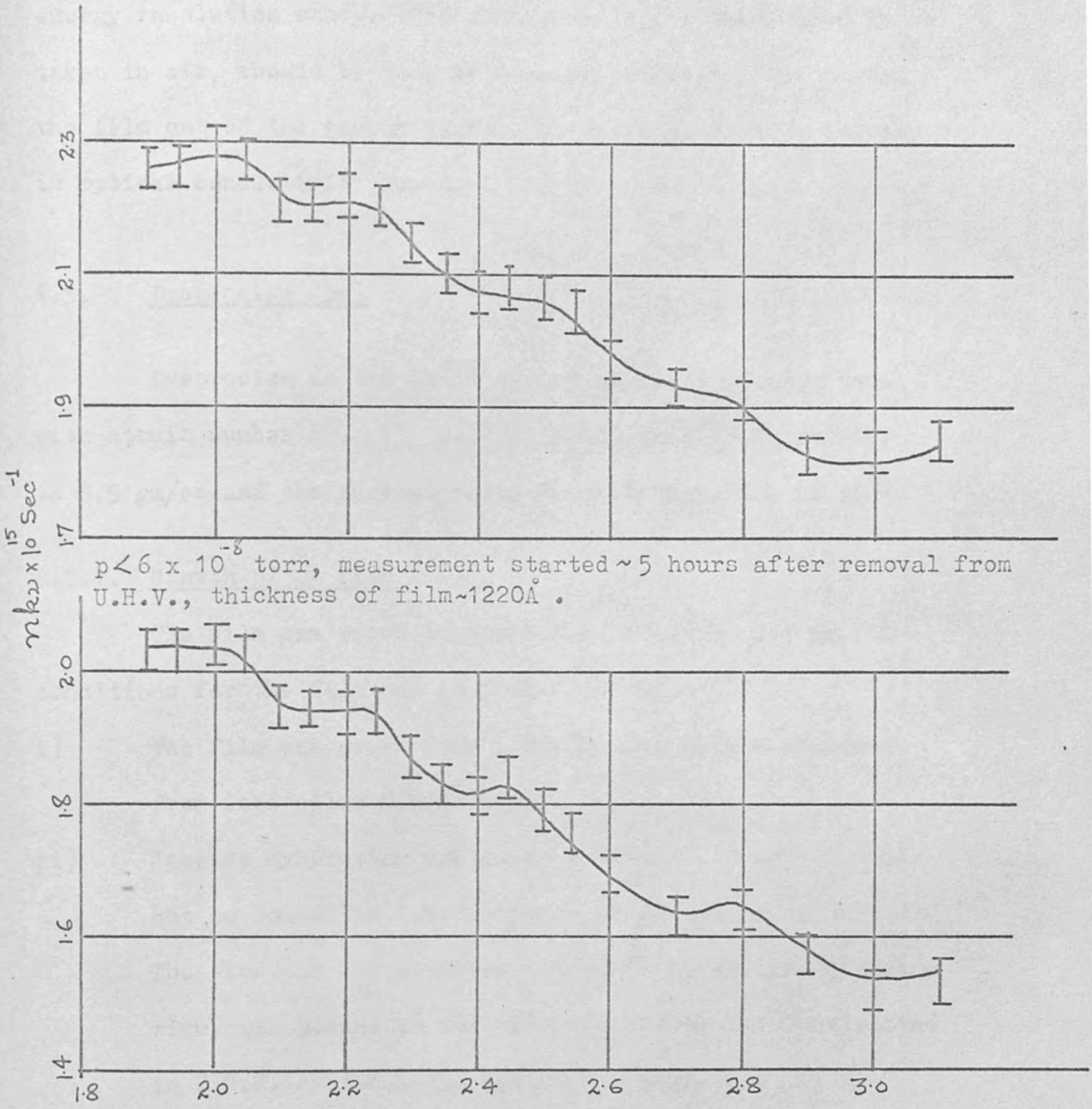

$p < 6 \times 10^{-8}$ torr, measurement started ~ 5 hours after removal from U.H.V., thickness of film ~ 1220Å .

$p < 2 \times 10^{-8}$ torr, measurement started ~ 5 hours after removal from U.H.V., thickness of the film ~ 1125Å .

Figure 52 (b): Optical conductivity of some more Tb films grown in U.H.V. and measured in air.

The above sets of data provide the motive for a higher energy resolution study. The measurements, if these have to be taken in air, should be made as soon as possible after taking the film out of the vacuum system, in order to observe structure in optical conductivity curve.

6.5. Dysprosium (Dy)

Dysprosium is the third of the heavy rare earth metals with atomic number 66. Its melting point is 1773^{o}K, density is 8.5 gm/cc and the ferromagnetic Curie temperature is 85^{o}K.

6.5.1. Growth of Dy film

The film was grown in the U.H.V. system. The growth conditions for the film was as follows:-

i) The film was grown from a 99.9% pure sample obtained from Goodfellow Metals Ltd.

ii) Because dysprosium sublimes, a tungsten filament could not be loaded in O.H.V. system as was done for Gd and Tb. Instead the material, in the form of 1 mm diameter wire, was placed in the filament, which was then placed in U.H.V. system. The system was evacuated and a pressure of about 1 x 10^{-10} torr was obtained.

iii) The filament with the material was outgassed with pulsing current up to 40 amperes. The pulsing current was used in order to keep the pressure below 10^{-7} torr.

iv) A pulsing current up to 60 amperes was passed through the filament till no material was left in the filament.

v) The pressure at the time of growth was better than 3×10^{-8} torr as measured on the linear scale of the Bayard-Alpert gauge.

vi) The film was grown at room temperature on a microscopeslide with nichrome contacts on its ends for electrical measurements by other workers.

(vii) The film was taken out from U.H.V. system after 4 days. Measurements for optical properties were made in air on the same day. Before it was taken out electrical and optical measurements were performed in U.H.V. by other workers.

(viii) The thickness of the film was 690A°.

6.5.2 Optical Properties of Dy film

Reflectance ratios were measured on the above grown Dy film in air, four hours after its removal from U.H.V. system. The measurements were made on the central area of the film at angles of incidence 80.6° and 60.6°.

Figure 53 shows the variation of reflectance ratios with incident energy in the visible region of the spectrum for angles of incidence 80.6° and 60.6°. The values of n and k of the film derived from the measured reflectance ratios are shown in Figure 54. The calculated optical conductivity curve is shown in Figure 55. We notice the structure in this curve, which is very similar to that in the optical conductivity

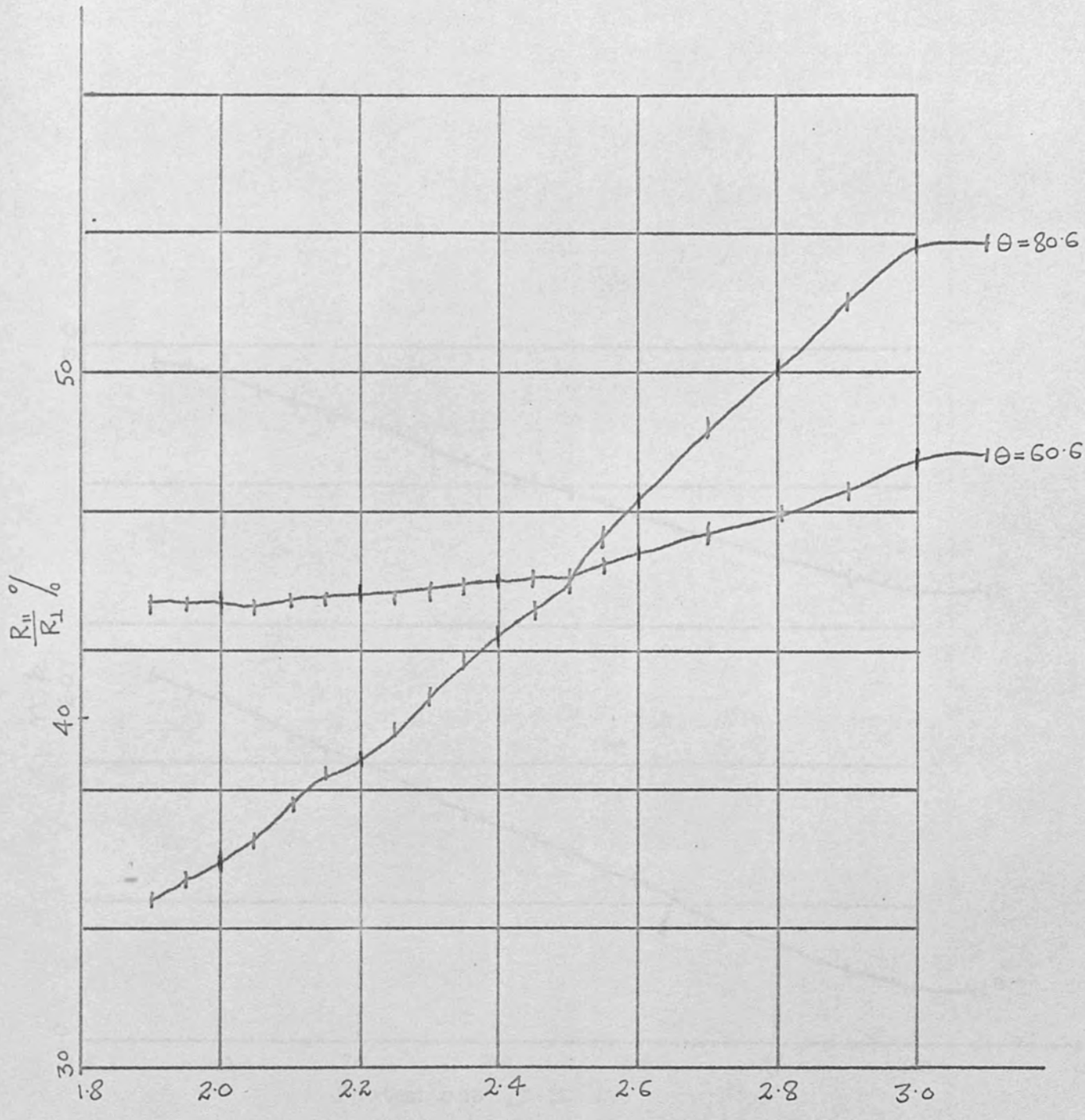

Figure 53: Reflectance ratios at 80.6° and 60.6° measured for Dy film in air.

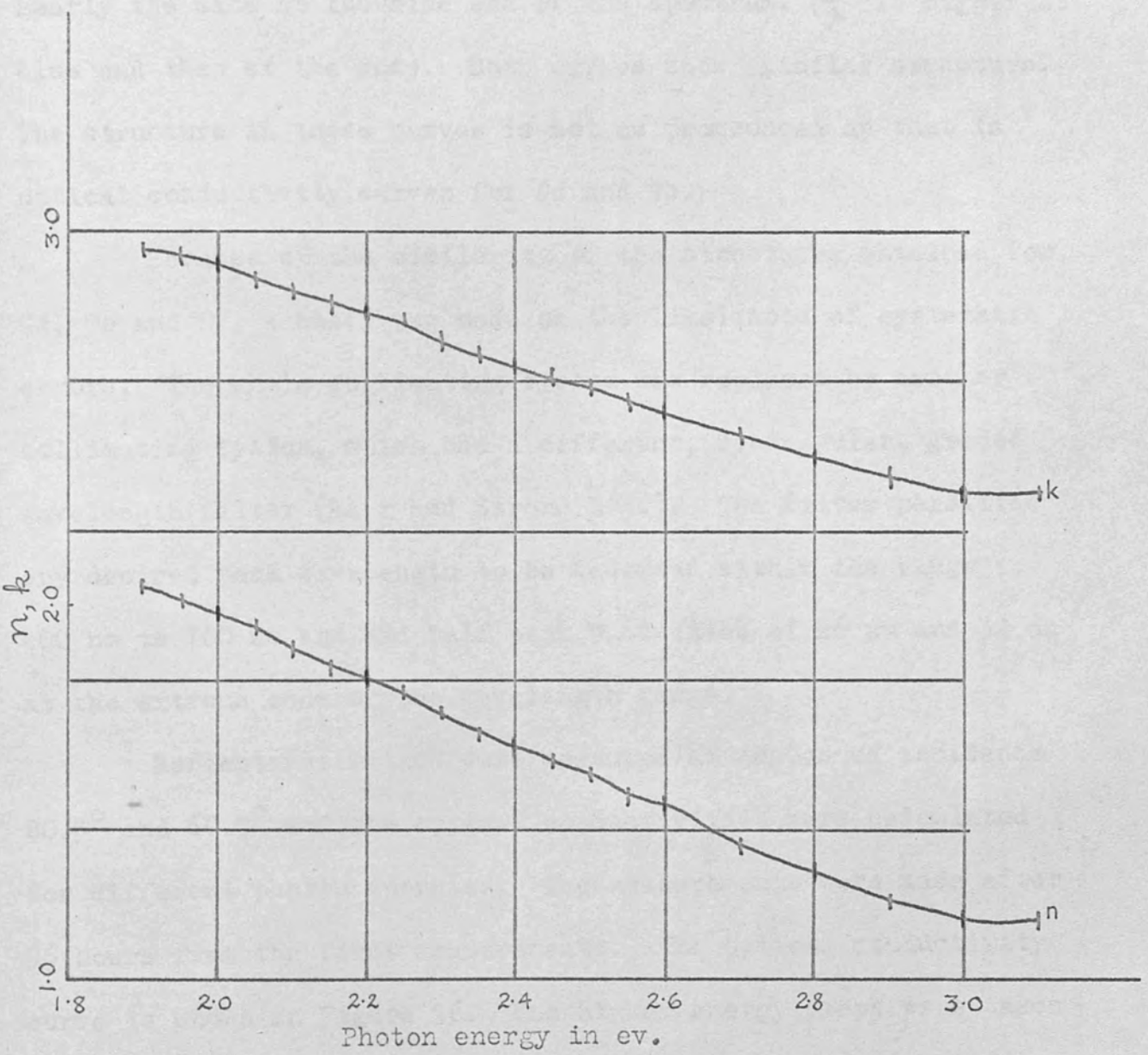

Figure 54: Optical constants n and k for Dy film in air.

curves for Gd and Tb. Figure 55 also shows the optical conductivity curve calculated using thin film formulae (Section 2.8). We note the difference in optical conductivity at the red end of the visible spectrum. The values of optical conductivity are nearly the same at the blue end of the spectrum. ($\frac{d}{\lambda}$ is bigger at blue end than at the red). Both curves show similar structure. The structure in these curves is not as pronounced as that in optical conductivity curves for Gd and Tb.

Because of the similarity of the structures obtained for Gd, Tb and Dy, a check was made on the likelihood of systematic errors. The whole collimating system was replaced by another collimating system, which had a different, rectangular, graded wavelength filter (Barr and Stroud Ltd.). The filter permitted any desired peak wavelength to be selected within the range 400 nm to 700 nm and had half peak bandwidths of 26 nm and 32 nm at the extreme ends of the wavelength range.

Reflectance ratios were measured at angles of incidence 80.5° and 60.5° and the optical conductivities were calculated for different photon energies. The measurements were made after 96 hours from the first measurements. The optical conductivity curve is shown in Figure 56. The higher energy steps were taken because the bandwidth of this filter was twice that of circular filter. The curve again shows the structures at nearly the same energies as before. The structures are rather less sharp, which may be due to the effect of leaving the film in air for a long time

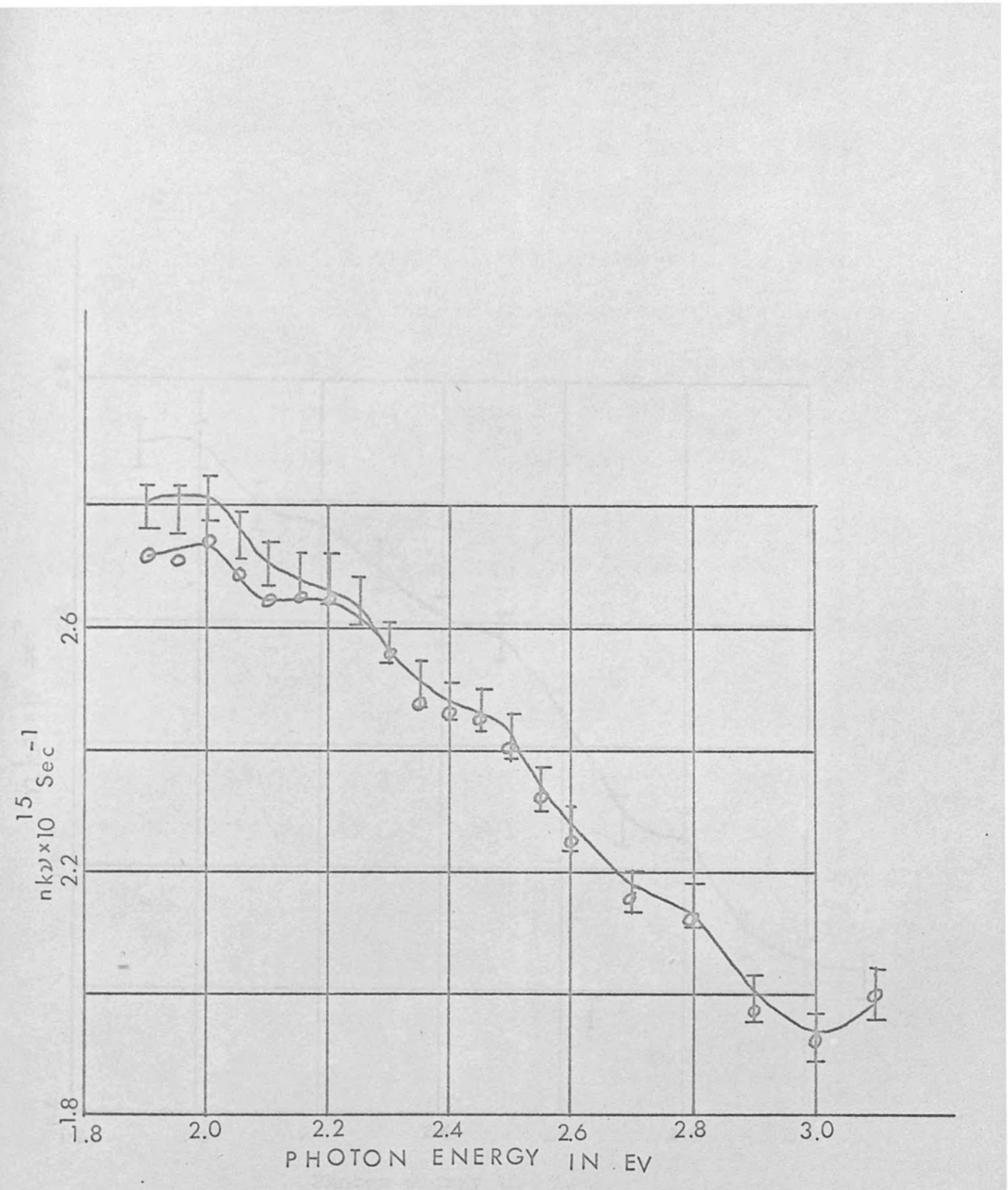

Figure 55: Optical conductivity of Dy in air at room temperature.

I using thick film formulae, o using thin film formulae.

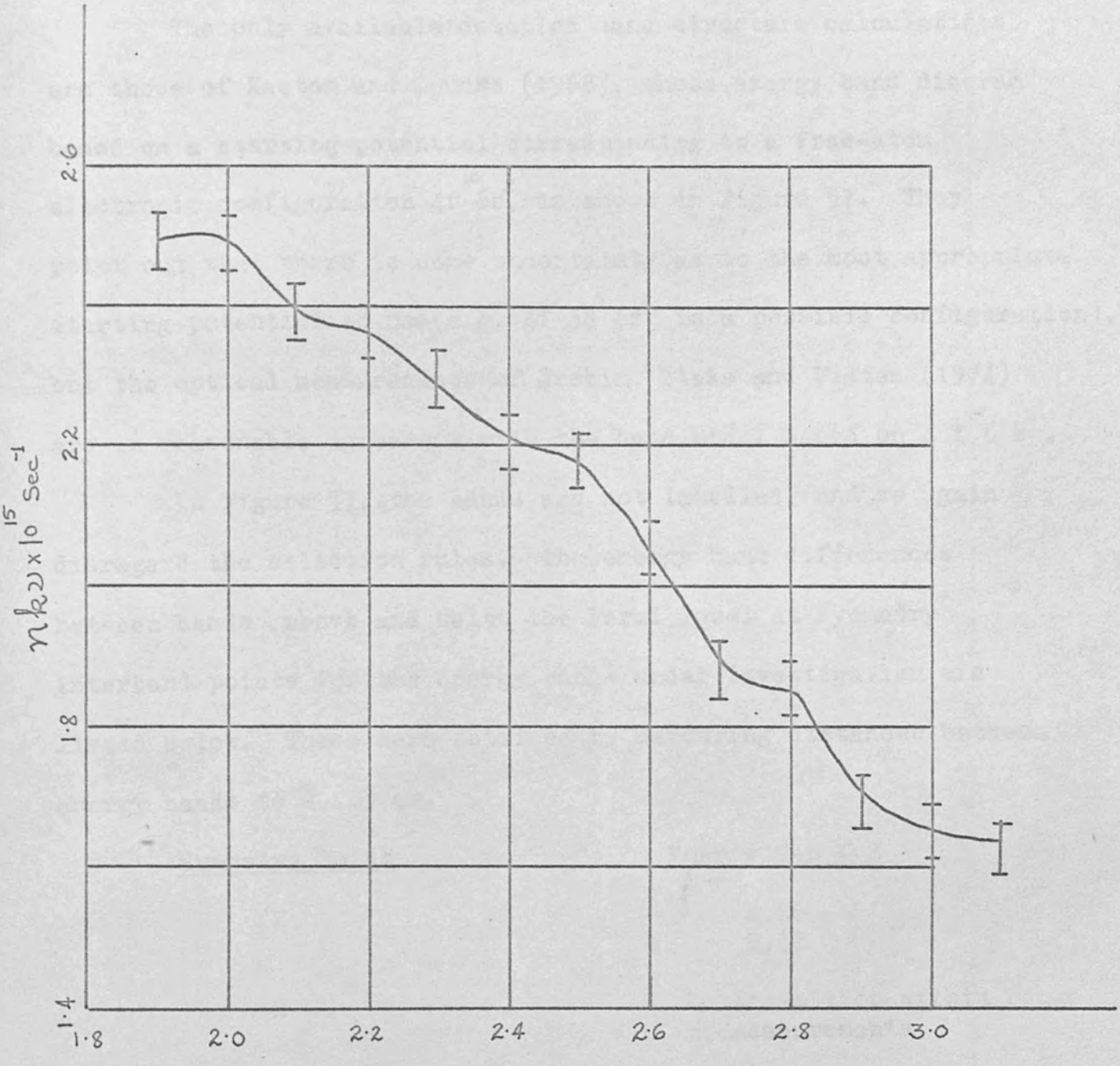

Figure 56: Optical conductivity of Dy film obtained 100 hours after removal from U.H.V. using a collimating system with a rectangular filter.

before taking those measurements (see Section 6.5.4.)

6.5.3 Theoretical Interpretation of the Optical Conductivity Curve of Dysprosium

The only available detailed band structure calculations are those of Keeton and Loucks (1968), whose energy band diagram based on a starting potential corresponding to a free-atom electronic configuration $4f^{10}6s^2$, is shown in Figure 57. They point out that there is some uncertainty as to the most appropriate starting potential to use (e.g. $4f^9 5d^1 6s^2$ is a possible configuration), but the optical measurements of Erskin, Blake and Flaten (1974) are in reasonable agreement with the band model based on $4f^{10}6s^2$.

In Figure 57, the bands are not labelled, and we again disregard the selection rules. The energy band differences between bands above and below the Fermi level at symmetry interband points for the energy range under investigation are listed below. These were obtained by measuring distances between energy bands to $\pm$ .03 ev.

Symmetry Point	Energy Gap ΔE
K	2.08 2.42
H	No transition within range of measurements
L	2.24
A	No transition within range of measurements
Γ	3.03
M	2.28 2.76 2.69

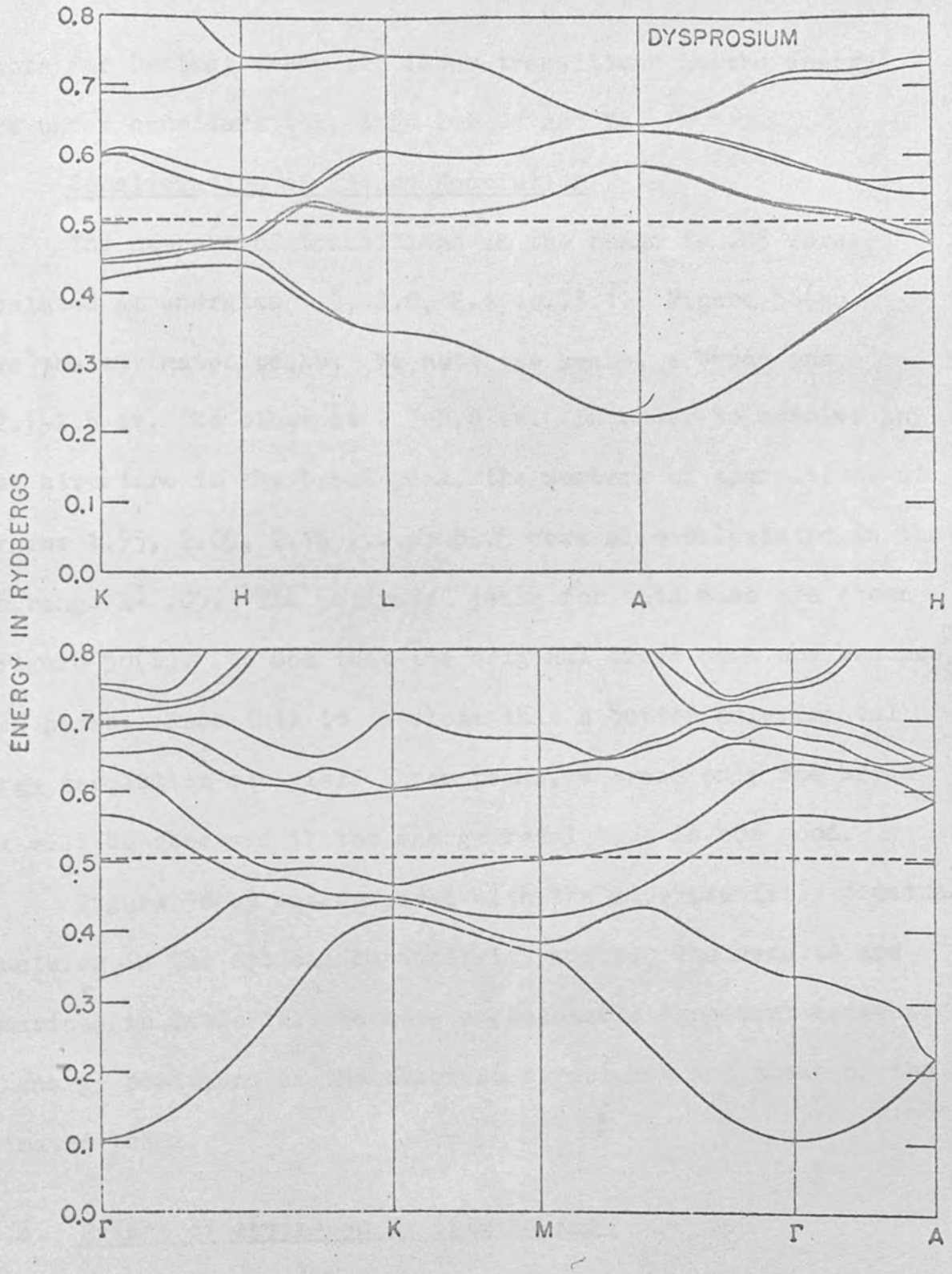

Figure 57: Energy bands for Dy along the symmetry axes of Brillouin zone using potential constructed from $4f^{10}\,6s^2$ free-atom configuration (Keeton and Loucks, 1968).

We note for Dy that there are fewer transitions in the energy range under consideration, than for Gd and Tb.

Consideration of Energy Resolution

The numbers of transitions in the range $E \pm .05$ were calculated at energies 1.9, 2.0, 2.1,....3.1. Figure 58(a) shows the estimated peaks. We note two peaks, a broad one at 2.1-2.5 ev, the other at 2.7-2.8 ev. In order to resolve any finer structure in the broad peak, the numbers of transitions at energies 1.95, 2.05, 2.15 ....., 3.05 were also calculated in the same range $E \pm .05$. The estimated peaks for this case are shown in Figure 58(b). We see that the original broad peak now becomes three peaks. From this it is clear that a better experimental energy resolution can yield three peaks, whereas only one broad peak will be observed if the energy resolution is not good.

Figure 58(b) was compared with the experimentally obtained structures in the optical conductivity curve. The results are summarized in Table 12. We note a reasonable agreement between the energy positions of the observed structures and those of the estimated peaks.

6.5.4. Effect of Ageing on Dy film in Air

The effect of ageing on the above grown Dy film was examined. Figure 59 shows the optical conductivity curves obtained after 12 hours and 176 hours from the first measurements. We again note the decrease in optical conductivity with the increasing

(a) at energies multiple of 0.10

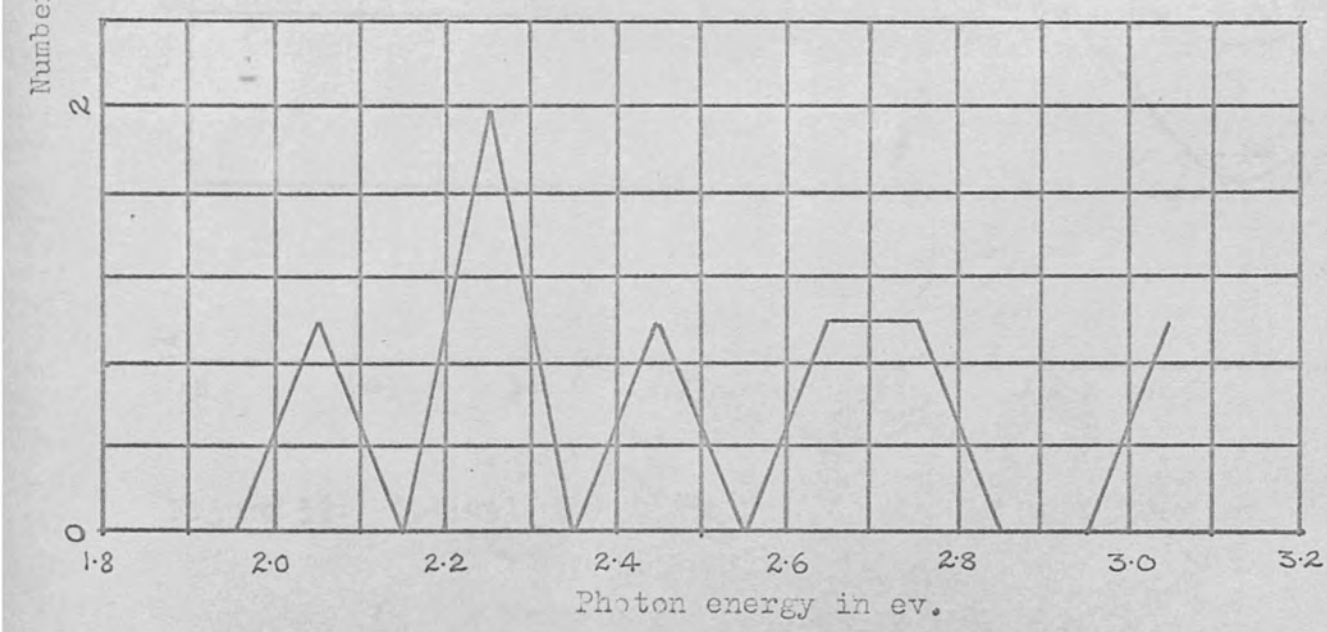

(b) at energies multiple of 0.05.

Figure 58: Theoretically estimated peak positions for Dy.

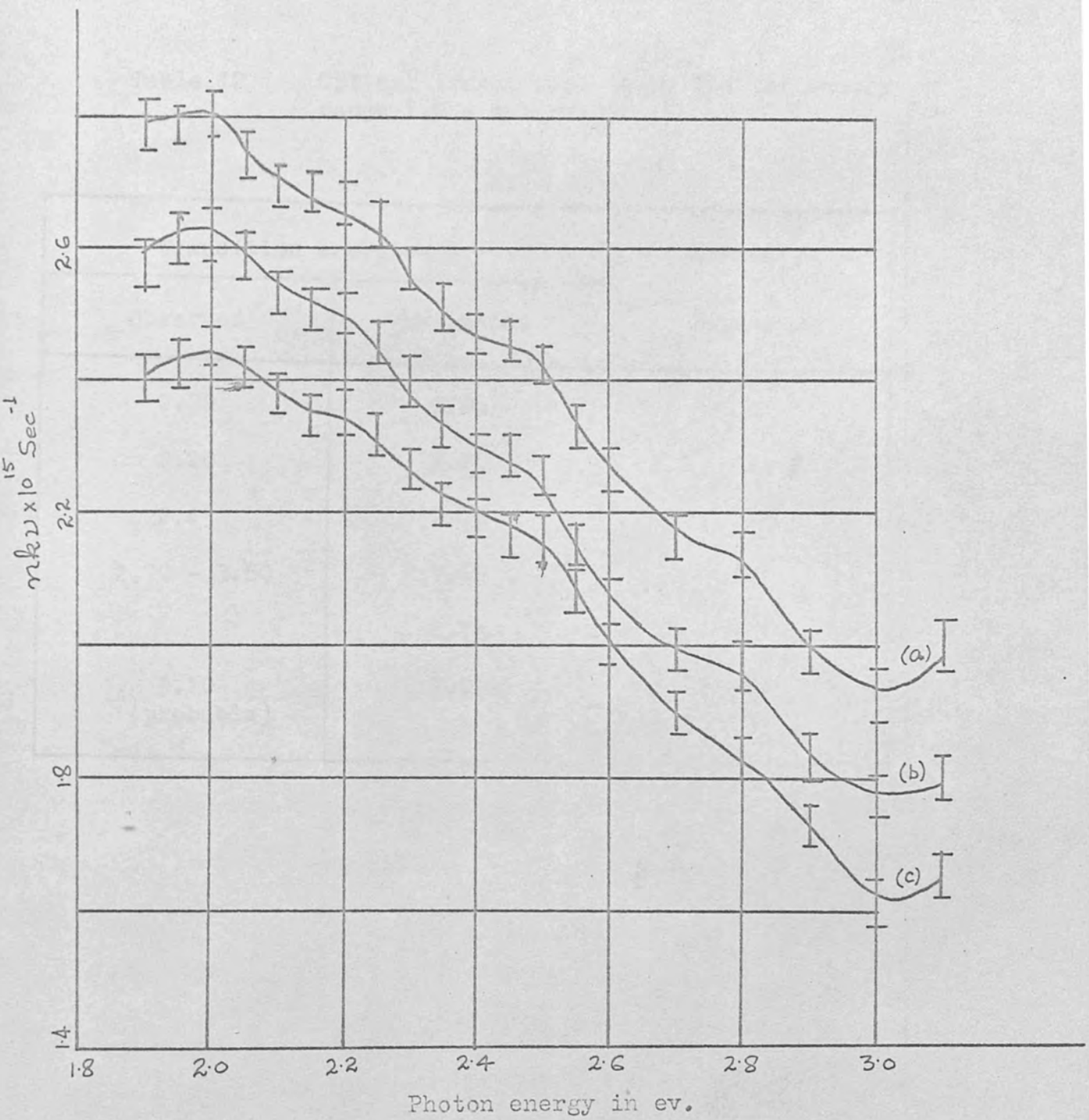

Figure 59: Optical conductivity of Dy in air as a function of ageing.

(a) 4 hours after removal from U.H.V.
(b) 16 hours after removal from U.H.V.
(c) 180 hours after removal from U.H.V.

Table 12 Optical transitions in Dy for the energy range 1.9 - 3.1 ev

Transition energies ev		Symmetry Points
Observed	Estimated	
2.00	2.05	K
2.20	2.25	L, M
2.45	2.45	K
2.70 - 2.80	2.65	M
	2.75	
3.10 (probable)	3.05	Γ

exposure time in air. As for Tb, we also note that peaks become less sharp and that eventually the structures at 2.2 and 2.8 ev may become unobservable.

6.6. Holmium (Ho)

Holmium is the fourth of the rare earth metals (heavy) with atomic number 67. Its melting point is 1773°K, density is 8.8 gm/cc

6.6.1 Growth of Ho films

A Ho film was first grown in ordinary high vacuum (O.H.V.) system using a tungsten filament. Because Ho rapidly sublimes when heated on a tungsten filament, another film was grown in O.H.V. using a tungsten boat. It was found that Ho evaporates in a more controlled fashion if the tungsten boat is used. Optical measurements were made on both these films, which were grown on ultrasonically clean microscope slides without any nichrome contacts, at room temperature. The films were grown from a 99.9% pure sample obtained from Goodfellow Metals Ltd. The growth conditions for two differently grown films were as follows:-

(a) Growth Conditions for Film Grown Using Tungsten Filament

i) The filament was first degassed by passing a current of 50 amperes for 10 minutes

ii) The material in the form of 1mm diameter wire was placed in the filament and the system was evacuated.

iii) The distance between the filament and substrate was 9.0 cm.

iv) A current of 34 amperes was passed for 5 minutes. The low current was tried to melt the material first.

v) The growth pressure was $< 5 \times 10^{-6}$ torr.

b) Growth Conditions for Film Grown Using Tungsten Boat

i) The boat was first degassed by passing a current of 80 amperes for 3 minutes.

ii) The material in the form of wire was cut into small pieces and the pieces were placed in the boat, and the system was evacuated.

iii) The distance between the boat and the substrate was 7.0 cm.

iv) A current of 70 amperes was passed for 30 seconds.

v) The growth pressure was $< 2 \times 10^{-6}$ torr

6.6.2. Optical Properties of Two Differently Grown Ho Films

Reflectance ratios were measured in air, at angles of incidence 80.0° and 65.0°, on two above grown films, just after their removal from O.H.V. system. Figure 60 shows the variation of reflectance ratios with incident energy in the visible range of the spectrum for two films. We again note the large variation in reflectance ratio for angle of incidence 80.0° compared with that at 65.0°. We also note the difference in values of reflectance ratio for two films at each angle.

The values of n and k of the films derived from the measured reflectance ratios are shown in Figure 61. We note the

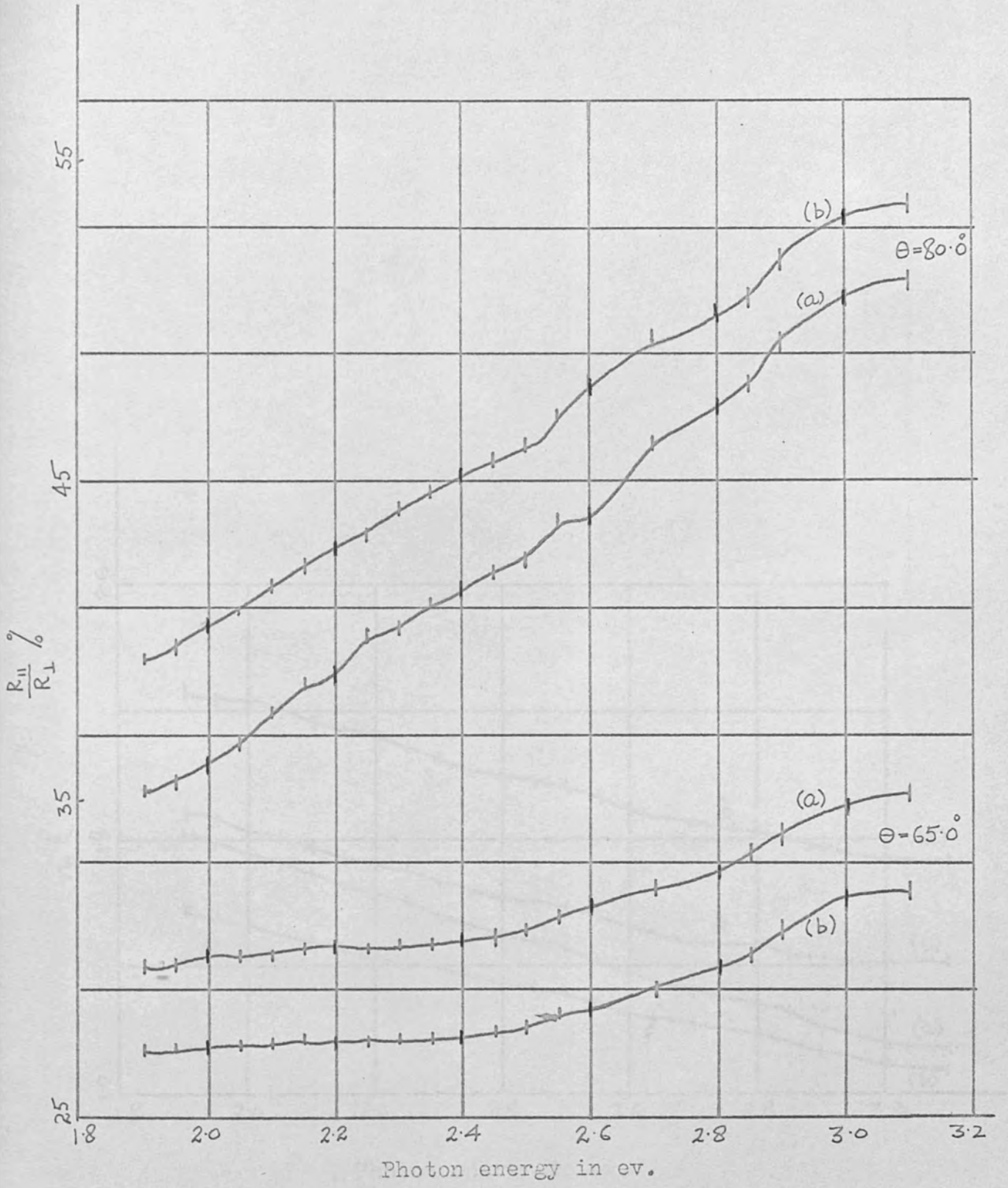

Figure 60: Reflectance ratios at 80.0° and 65.0° measured in air for two Ho films grown (a) using a filament and (b) using a boat.

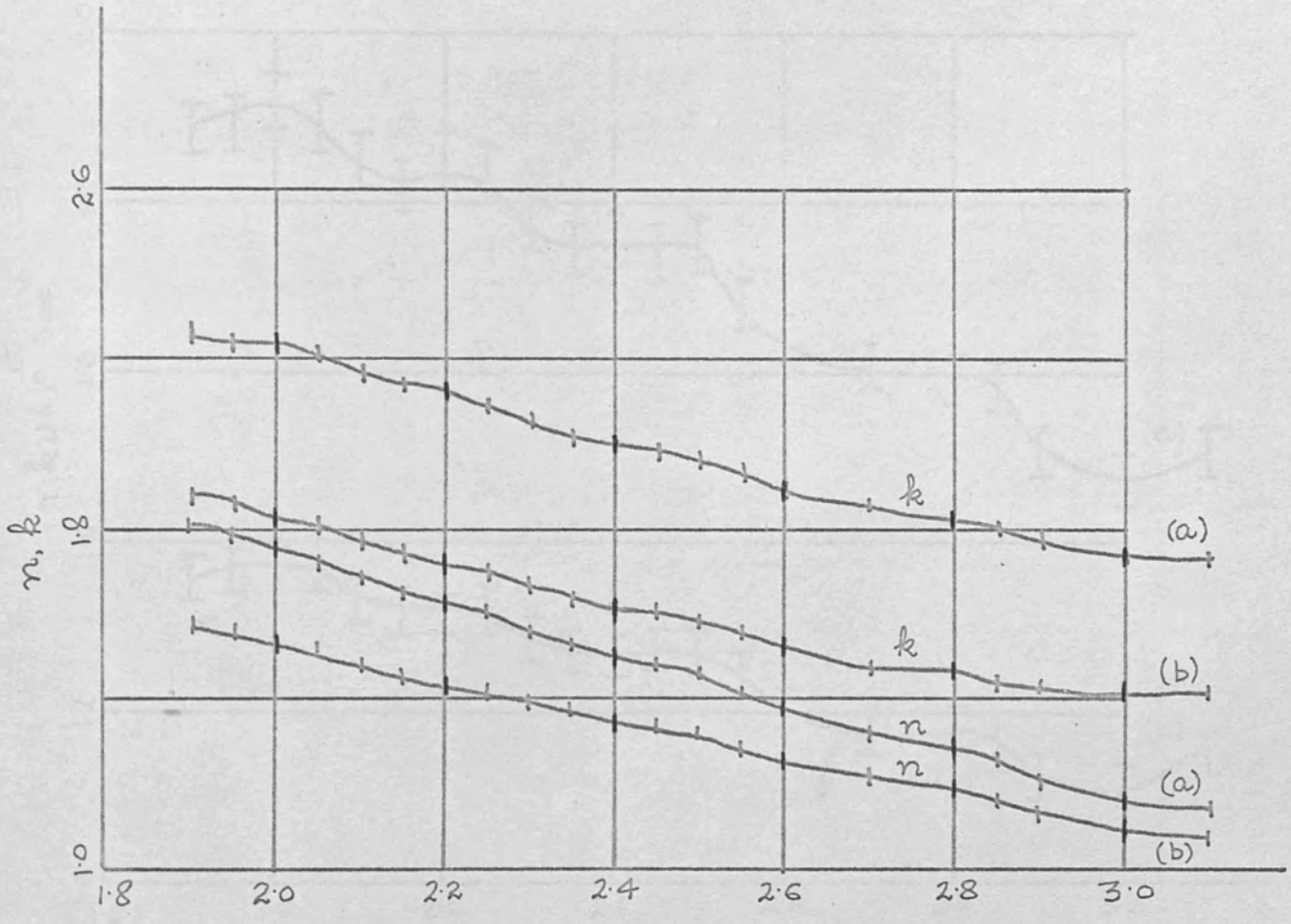

Figure 61: Optical constants n and k for two Ho films grown (a) using a filament and (b) using a boat.

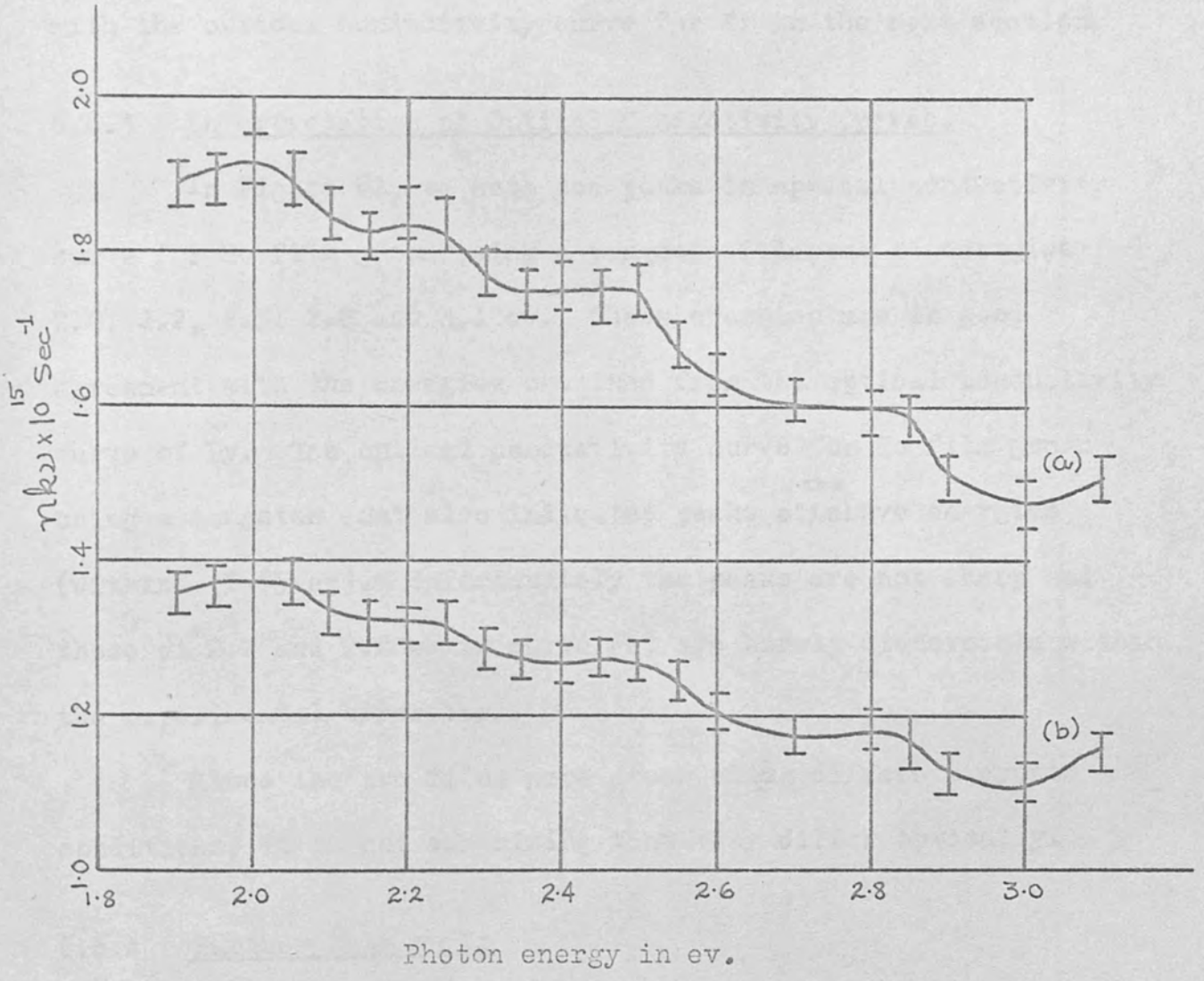

Figure 62: Optical conductivity for Ho films in air at room temperature grown (a) using a filament and (b) using a boat.

difference in values of n and k for the two films. This we may expect, because the growth conditions for the two films were different (Heavens, 1955).

Figure 62 shows the optical conductivity curves for two differently grown Ho films. We note the difference in optical conductivity curves, which will be discussed and compared with the optical conductivity curve for Dy in the next section.

6.6.3 Interpretation of Optical Conductivity Curves.

In Figure 62, we note the peaks in optical conductivity curve for Ho film grown using a tungsten filament at energies 2.0, 2.2, 2.5, 2.8 and 3.1 ev. These energies are in good agreement with the energies obtained from the optical conductivity curve of Dy. The optical conductivity curve for Ho film grown using a tungsten boat also indicates peaks at the above energies (within $\pm$ 0.05 ev). Unfortunately the peaks are not sharp and those at 2.2 and 2.8 ev in curve (b) are barely discernible within the experimental error bars.

Since the two films were grown using different growth conditions, it is not surprising that they differ optically.

6.6.4 Further Data on Ho

Figure 63 shows additional optical conductivity curves. The results indicate structure in these curves at energies mentioned in the previous section. Again the peaks are not as sharp for film grown using a tungsten boat as for film grown using a tungsten filament.

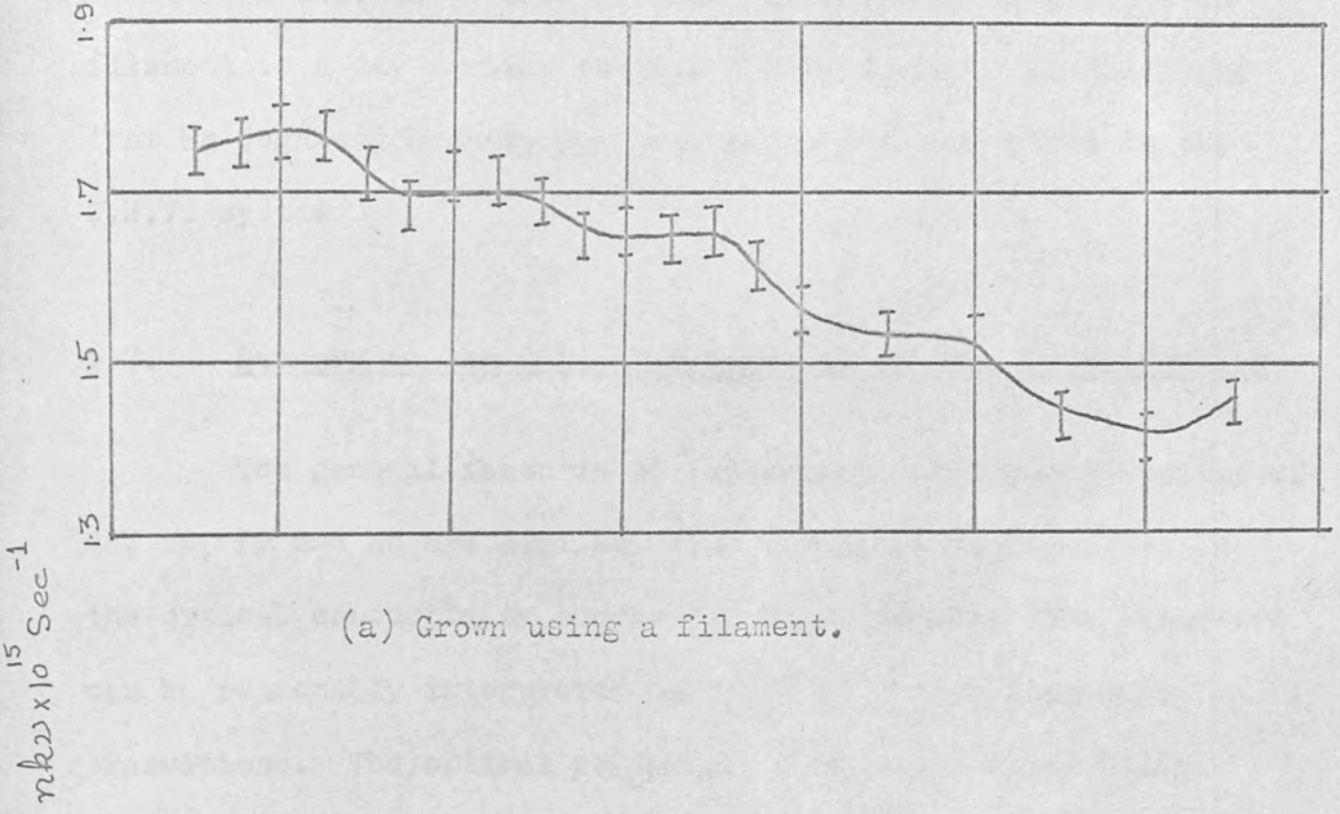

(a) Grown using a filament.

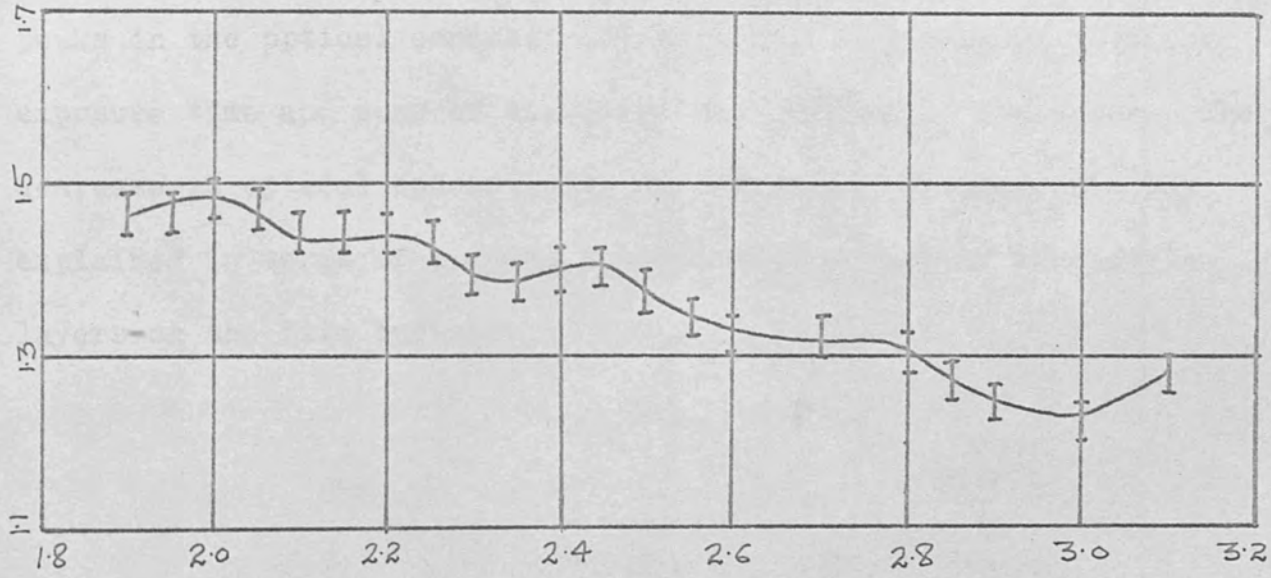

(b) Grown using a boat.

Figure 63: Optical conductivity curves for Ho films in air.

An attempt to grow Ho film in U.H.V. using a tungsten filament in a way similar to that for Dy failed. It was found that Ho degassed heavily and produced a pressure burst in the U.H.V. system.

6.7. Summary on the Optical Properties of Rare Earths in Air

The general features of the optical absorption spectra of Gd, Tb, Dy and Ho are similar. The results show structure in the optical conductivity curves for these metals. The structure can be reasonably interpreted in terms of direct interband transitions. The optical conductivity of these metal films decreases with exposure time in air. The sharpness of the peaks in the optical conductivity curves also decreases with the exposure time and some of the peaks may eventually disappear. The decrease in optical conductivity and sharpness of peaks can be explained in terms of a model based on the growth of dielectric layers on the film surface.

CHAPTER VII

OPTICAL AND MAGNETO-OPTICAL PROPERTIES OF IRON IN THE VISIBLE REGION

7.1 Introduction

The optical and magneto-optical properties of iron, as experimentally observed in air, in the visible region of the spectrum are described in this Chapter. The purpose of the magneto-optical measurements was to obtain new data and to correlate, where possible, features in the optical spectra with electronic transitions associated with the band structure of iron.

Iron was chosen because (a) it is strongly ferromagnetic and produces a large transverse Kerr effect parameter δ at room temperature, and (b) the optical and magneto-optical properties have not previously been discussed in terms of electronic band structure, in as much detail, as for example, nickel.

The transverse Kerr effect was used to determine the magneto-optical properties because of its simplicity, as it only involves intensity measurements. The quantity of interest is the change in reflected intensity of the parallel component of light (Chapter II) on reversing the sense of magnetisation.

The optical constants of iron have been reported, in visible part of the spectrum, by Meyer (1962) and Ferguson and Romagnoli (1969). Their results are given for comparison.

The magneto-optical properties have been studied by Krinchik and Artemev (1960) and Ferguson & Romagnoli (1969) using transverse Kerr Magneto-optical effect. Their results are not compared owing to the (a) different magneto-optical parameter used by different workers (b) large difference in values of the parameter obtained largely due to the difference in optical constants.

7.2 Growth of Iron Films

Iron films were grown in Birvac ordinary high vacuum system (described in Chapter V) using electron bombardment. The films were grown on soda glass microscope slides of dimension 76 x 25 x 1mm^3, at room temperature, from a 99.999% sample obtained from Johnson Matthey Metals Limited. Iron pieces cut from a wire were placed in a cermet (Al_2O_3) crucible. The source-substrate distance was 12.5 cm. When the system was under high vacuum (2 x 10^{-6} torr) a low voltage was applied to the filament, causing the filament to glow and emit electrons. The negative H.T. (up to 3 KV) was then applied to the surrounding box, which focussed electrons on to the crucible. The bombardment resulted first in melting of the iron and consequently its evaporation as filament current and H.T. were increased. The maximum typical pressure at the time of growth was 6 x 10^{-6} torr.

In all, five films were grown. The first film was grown to estimate the amount of material required for a thick film. It was found that the wire of length ~ 3.00 cm and diameter 0.046 cm produced a film of thickness ~ 2600A$^{\circ}$ (as measured using multiple beam Fizeau fringes (Tolansky, 1970)).

Optical and magneto-optical measurements were made on all the remaining four films. The optical and magneto-optical properties of one of the films are discussed in detail. The optical conductivity curves of the other three films and magneto-optical conductivity ($\omega \sigma_{xy}^{2}$) of two films are also presented in the Chapter. The magneto-optical conductivity curve of the first film is not given because the magneto-optical measurements made on this film were preliminary, and the first aim was to get an idea of the order of magnitude of δ at some angles of incidence for a few wavelengths.

7.3. Optical Properties of Iron

Reflectance ratios were measured for the iron film in air, just after its removal from O.H.V. system. The measurements were made at angles of incidence 64.6° and 80.4°, using the reflectometer described in Chapter IV.

Figure 64 shows the variation of reflectance ratios with incident energy in the visible region of the spectrum. Like rare earth metals, we again note the large variation in reflectance ratio for an angle of incidence of 80.4° compared with that at 64.6°. The optical constants n and k, derived from the observed reflectance ratios are shown in Figure 65. The calculated optical conductivity curve is shown in Figure 66 (a). We observe a broad peak in the optical conductivity curve at about 2.5 ev. A possible explanation for this peak will be suggested in terms of electronic band structure of iron, in the next section.

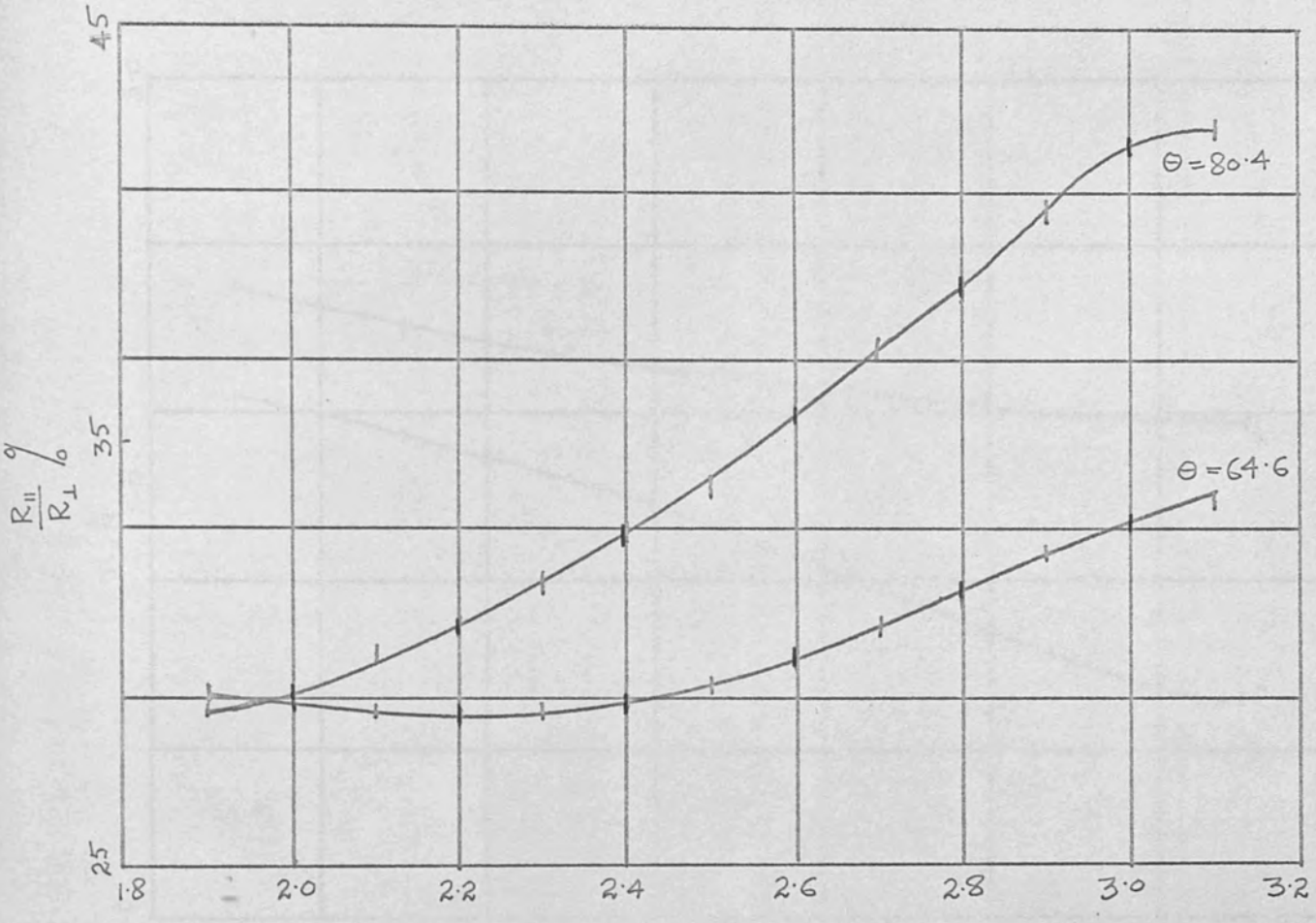

Figure 64: Reflectance ratios at 80.4° and 64.6° measured for iron film in air.

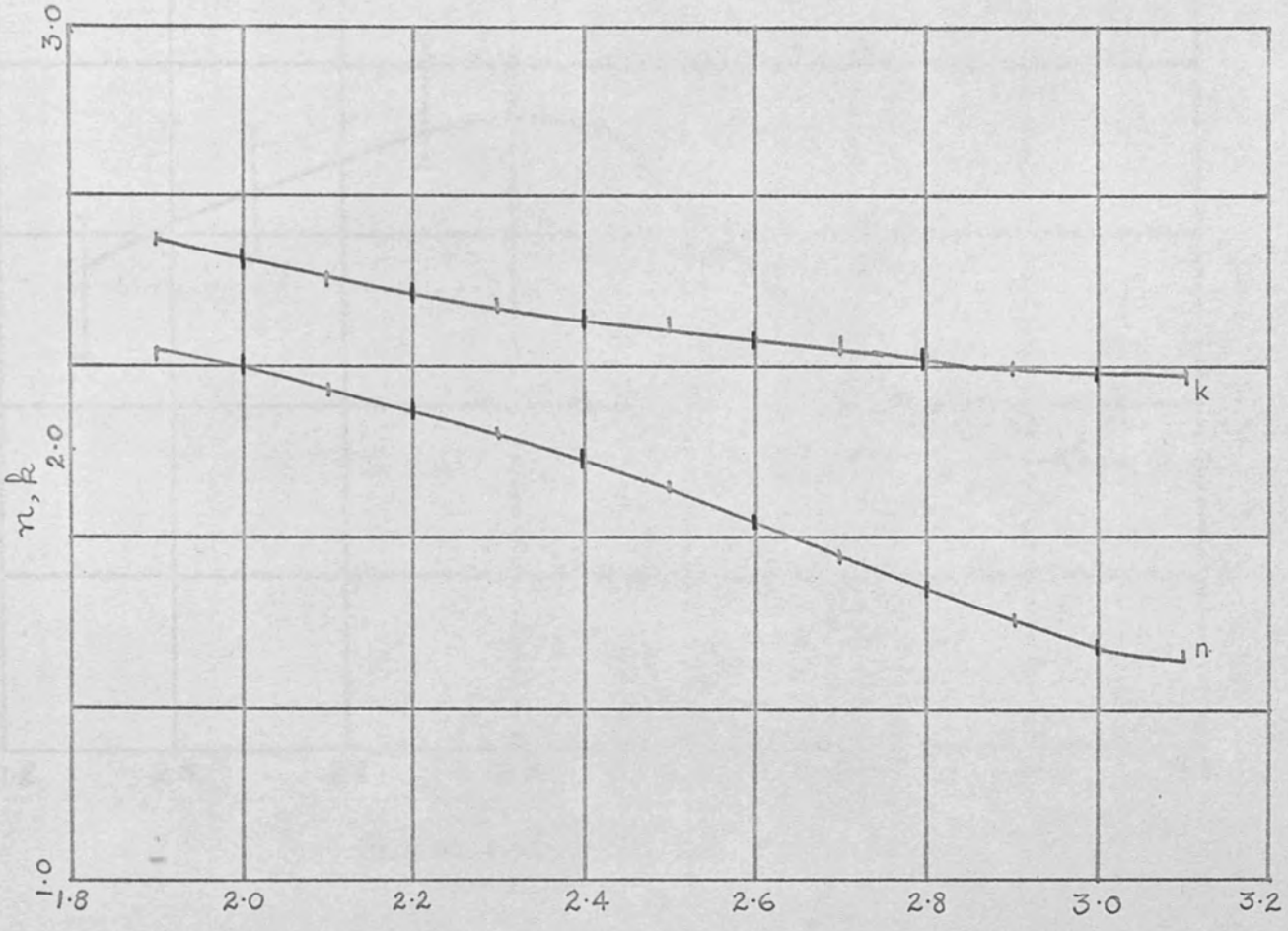

Figure 65: Optical constants n and k for iron film in air.

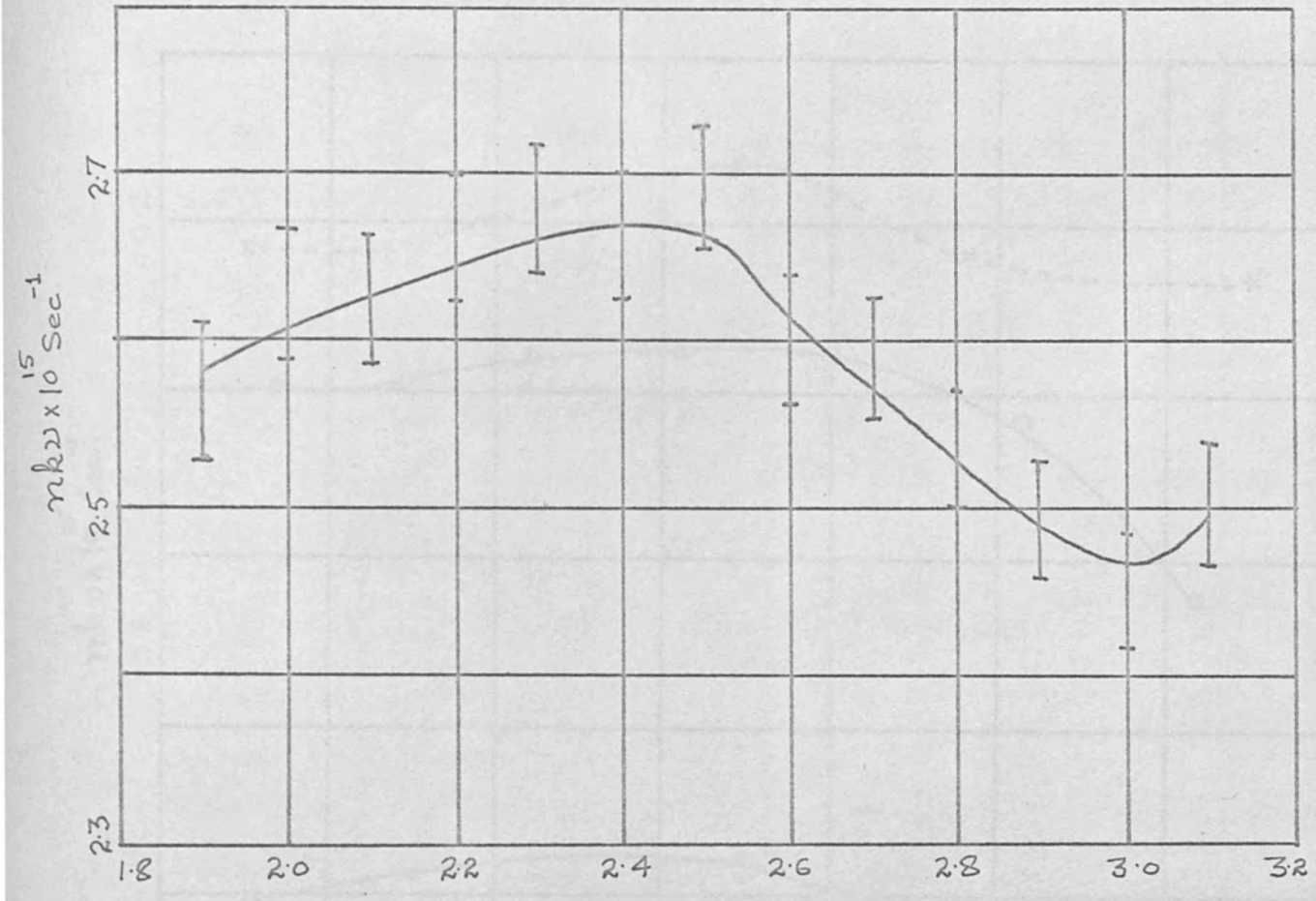

Figure 66 (a): Optical conductivity of iron in air at room temperature.

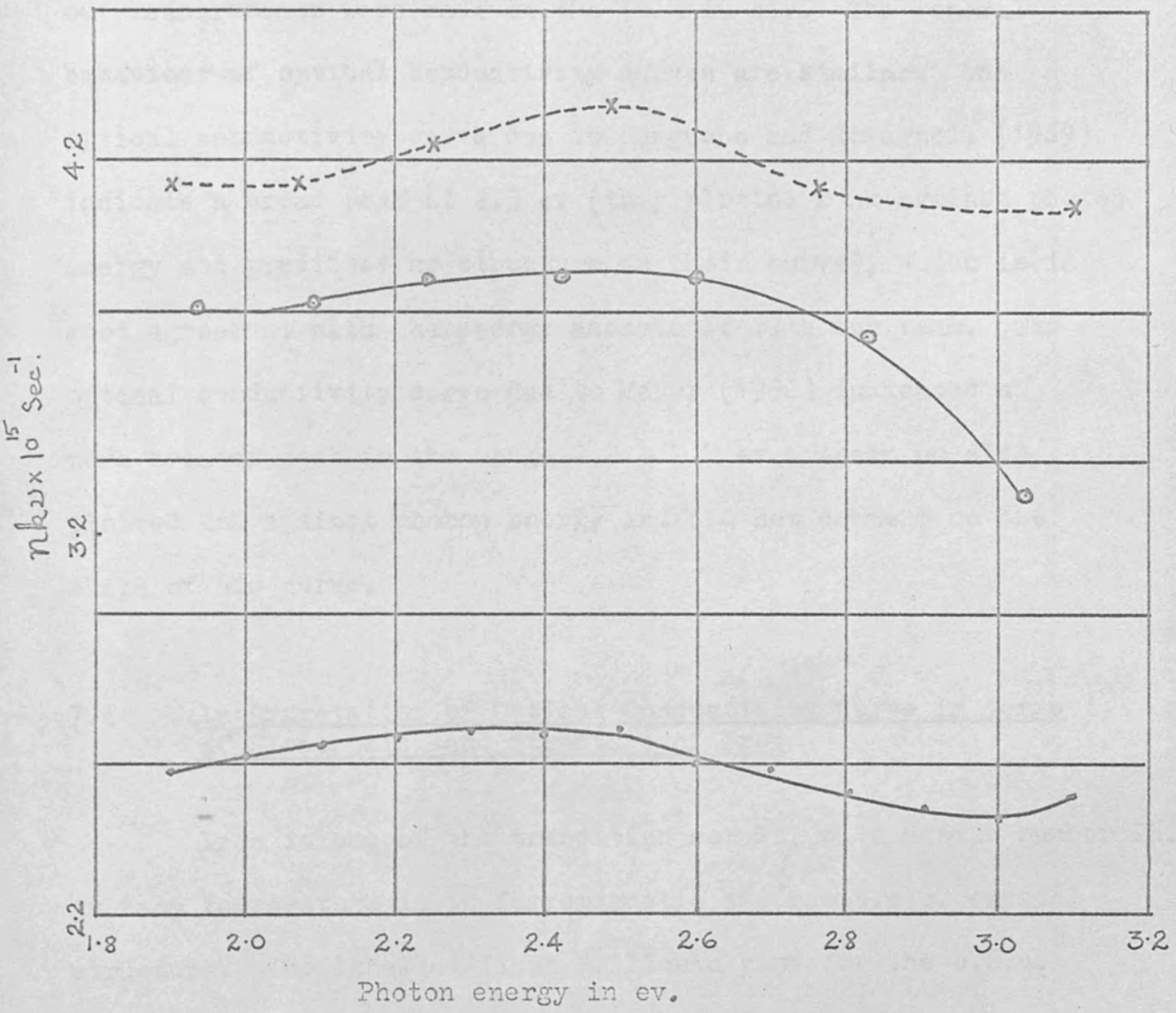

Figure 66(b): Optical conductivity curves due to different workers.

× Ferguson and Romagnoli; ⊙ Meyer; • Present work.

Figure 66(b) shows the optical conductivity curves calculated from the results of other workers, together with our optical conductivity curve. We note the difference in values of optical conductivity, which is not surprising because our measurements were made on the film in air. The general behaviour of optical conductivity curves are similar. The optical conductivity curve due to Ferguson and Romagnoli (1969) indicate a broad peak at 2.5 ev (they plotted 2 nk against photon energy and predicted no structure in their curve), which is in good agreement with the energy associated with our peak. The optical conductivity curve due to Meyer (1962) indicates a more broader peak in the range 2.2 - 2.7 ev. Again he also plotted 2nk against photon energy and did not comment on the shape of his curve.

7.4 Interpretation of Optical Conductivity Curve in Terms of Electronic Band Structure of Iron

Iron is one of the transition metals, with atomic number 26. At room temperature it is ferromagnetic and has b.c.c. crystal structure. The labelled first Brillouin zone for the b.c.c. lattice is shown in Figure 67.

Recently, a new band structure calculation for ferromagnetic iron has been reported by Duff and Das (1971). In their calculation they incorporated features which had emerged as a consistent pattern in band structures reported by several other workers. Their band structure calculation has been chosen to explain the structure in

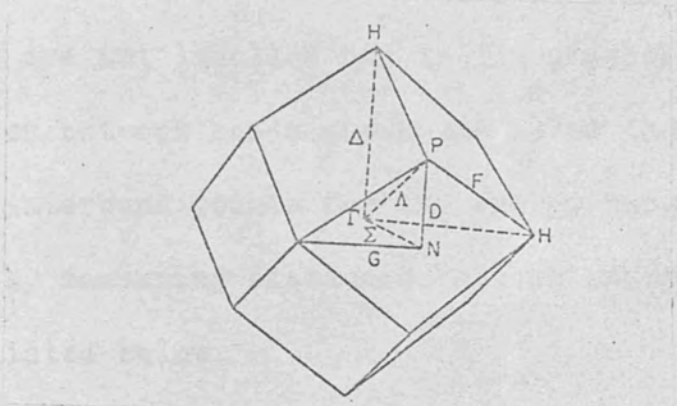

Figure 67: First Brillouin zone for b.c.c. lattice.

optical conductivity curve as this is the only calculation which leads to self-consistency with the observed magnetic moment. The electron configuration $3d^7 4s^1$ was used. The wave functions were expanded in terms of tight binding functions (Colloway, 1964) and orthogonalized plane waves (Colloway, 1964). Their results are shown in Figure 68.

Figure 68(a) shows the band structure for majority spin and Figure 68(b) shows the band structure for minority spin. The bands are not labelled and in the absence of labelling, differences between bands above and below the Fermi level at symmetry interband points for the energy range under investigation were obtained by measuring distances between energy bands to $\pm$ 0.03 ev and are listed below.

Symmetry Point	Energy Gap ev	Spin
N	2.43	Majority
	2.76	Majority
	2.77	Minority
	3.18	Minority
Γ	2.45	Minority
H	(No transition within	
P	(range of measurements	

The observed peak at 2.5 ev in the optical conductivity curve can be assigned to either (a) a transition at the N symmetry point in the majority spin band, or (b) a transition at Γ symmetry point in the minority spin band, or (c) both optical transitions (a) and (b) together. To be more definite about the exact case we require to know the selection rules and hence allowed transitions.

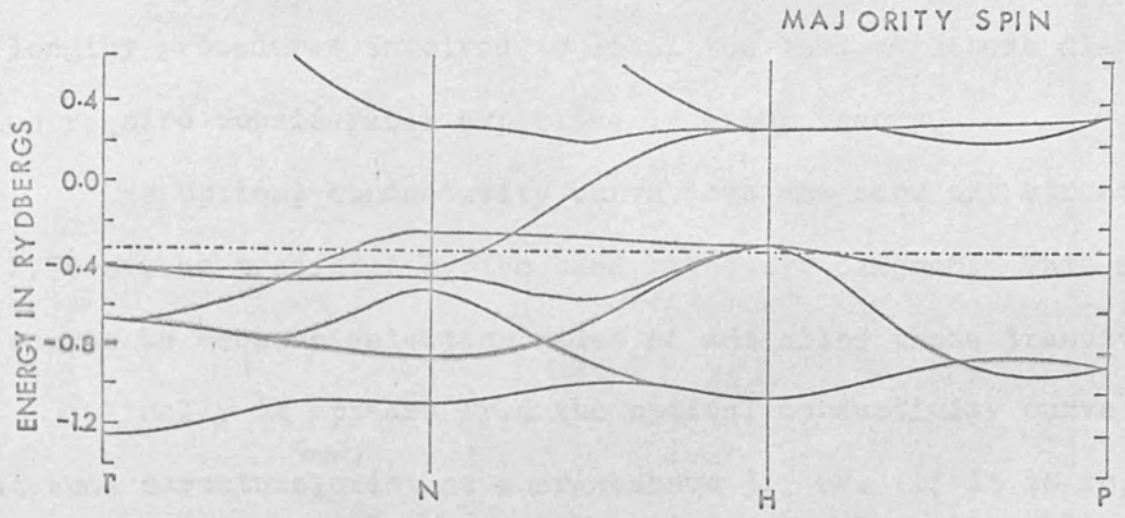

Figure 68 (a): Band structure for ferromagnetic iron for majority spin, E_F = -0.314Ry.

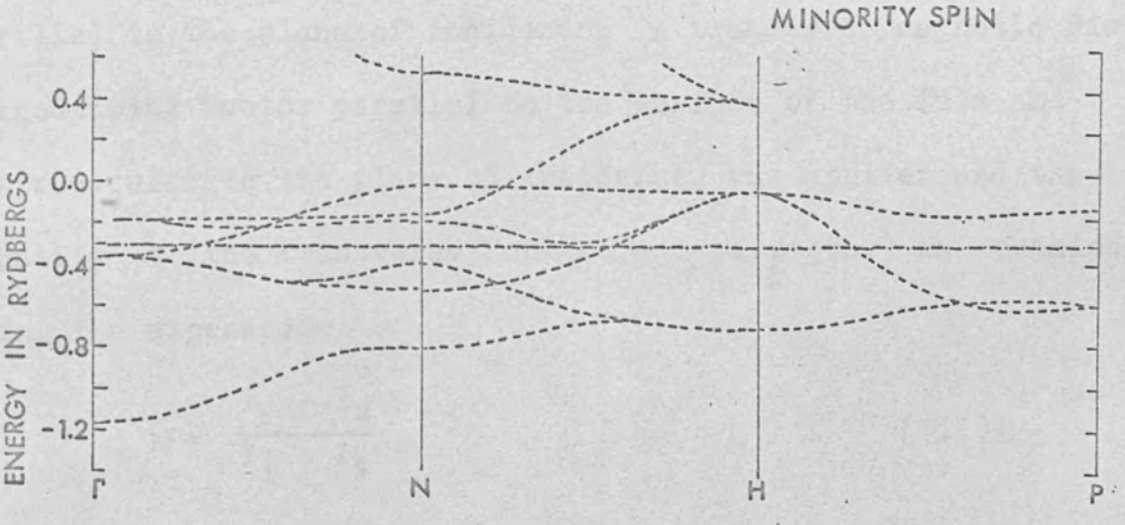

Figure 68 (b) : Band structure for ferromagnetic iron for minority spin, E_F = -0.314 Ry.

(Duff and Das, 1971).

No attempt was made to calculate allowed transitions because of lengthy procedures involved to label the band structure diagram, which require considerable expertise in group theory.

The optical conductivity curve does not show any structure at 2.75 ev, as predicted by the band structure diagram. This may of course be because selection rules do not allow these transitions.

Finally it appears from the optical conductivity curve that some structure may exist at energies above 3.1 ev. If it is so, it may be assigned to the optical transition at N symmetry point in minority spin band.

7.5 Magneto-Optical Properties of Iron Film

The iron film was placed in the optical cell described in Chapter IV. The polarizer was set to produce light polarized parallel to the plane of incidence. A transverse magnetic field (magnetising vector parallel to the surface of the film and perpendicular to the plane of incidence) was applied and the quantity δ (the transverse Kerr effect parameter) was obtained using the expression

$$\delta = \frac{I_1 - I_2}{I_1 + I_2} \qquad (7.1)$$

where

I_1 = intensity of reflected light for magnetic field in one direction, and

I_2 = intensity of reflected light for magnetic field in the opposite direction.

Figure 69 shows the variation of δ with angle of incidence for a wavelength of 5893A°. The errors in δ were calculated using 0.1% error in the measured intensities. We note that δ is maximum at about 63°, zero at abour 81° and minimum (or absolute maximum in the negative quadrant) at about 85°.

Figure 70 shows the variation of δ with incident energy for two angles of incidence 64.6° and 85.5°, which were chosen to be near the optimum angles (Section 3.7). We note a peak in curve for 64.6° at a photon energy in the range 2.0 to 2.2 ev. A similar peak was reported by Krinchik and Artemev (1968) at about 2.0 ev in their δ curve for 70° angle of incidence.

The quantities ϵ_1' and ϵ_2' (magneto-optical parameters) were calculated from measured δ's at two angles of incidence using equation (2.63) and are shown in Figure 71. The values of optical constants n and k for the film necessary to calculate the above quantities were taken from Section 7.3. We note that ϵ_2' is positive for all the photon energies under investigation whereas ϵ_1' is positive for some photon energies and negative for others. No structure is evident from these curves.

The magneto-optical conductivity $\omega\sigma_{xy}^{i}$ $(= \frac{\omega^2}{4\pi}\epsilon_2')$ was also calculated and is shown in Figure 72. $\omega\sigma_{xy}^{i}$ is proportional to the joint density of states, if the optical matrix elements between all filled states and all empty states are constant (Chapter I). On this assumption, the approximate values of joint density of states were calculated from the total density of states histogram (Figure 73)

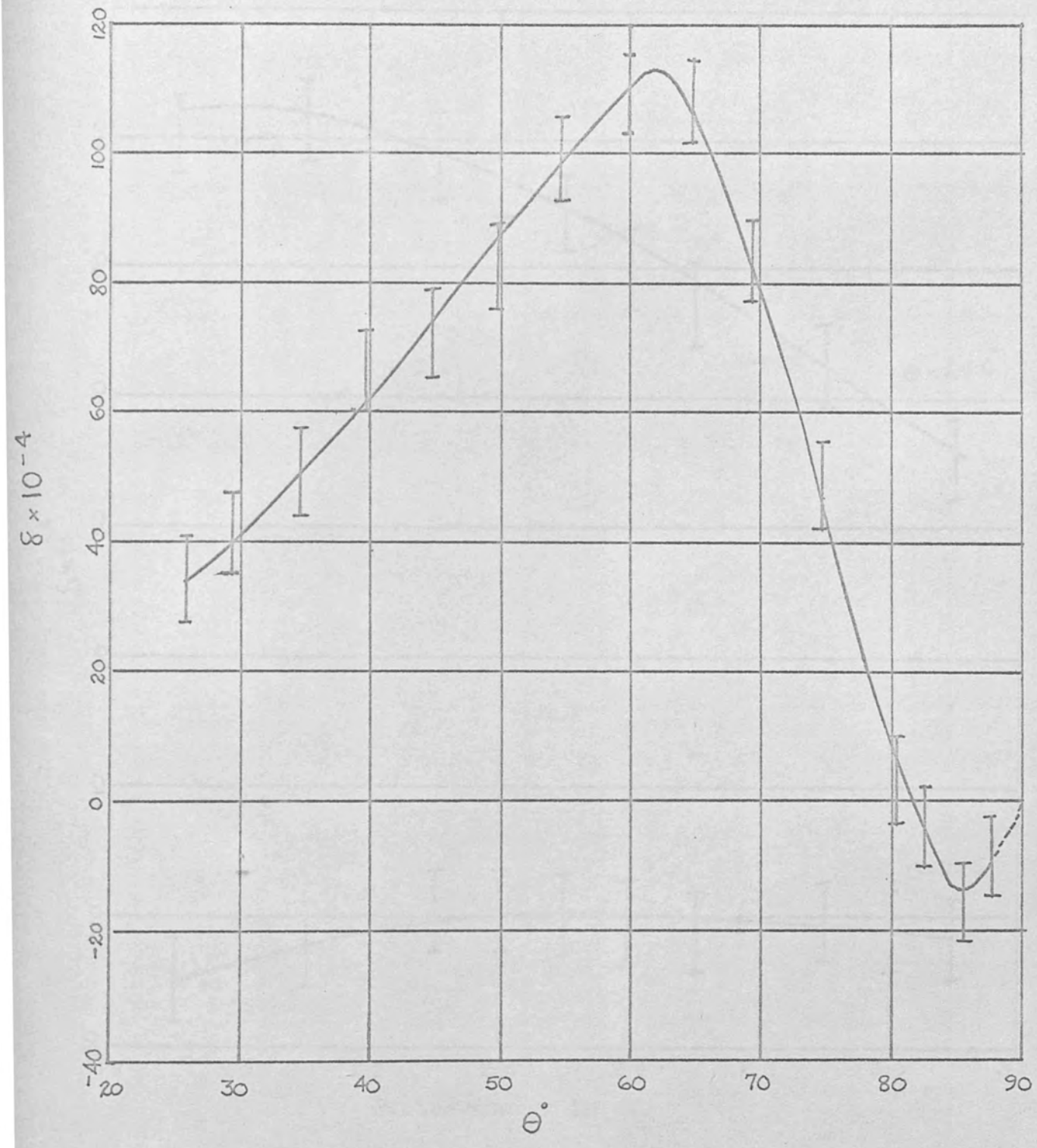

Figure 69: Variation of δ with angle of incidence Θ at $\lambda = 5893\text{A}^{\circ}$.

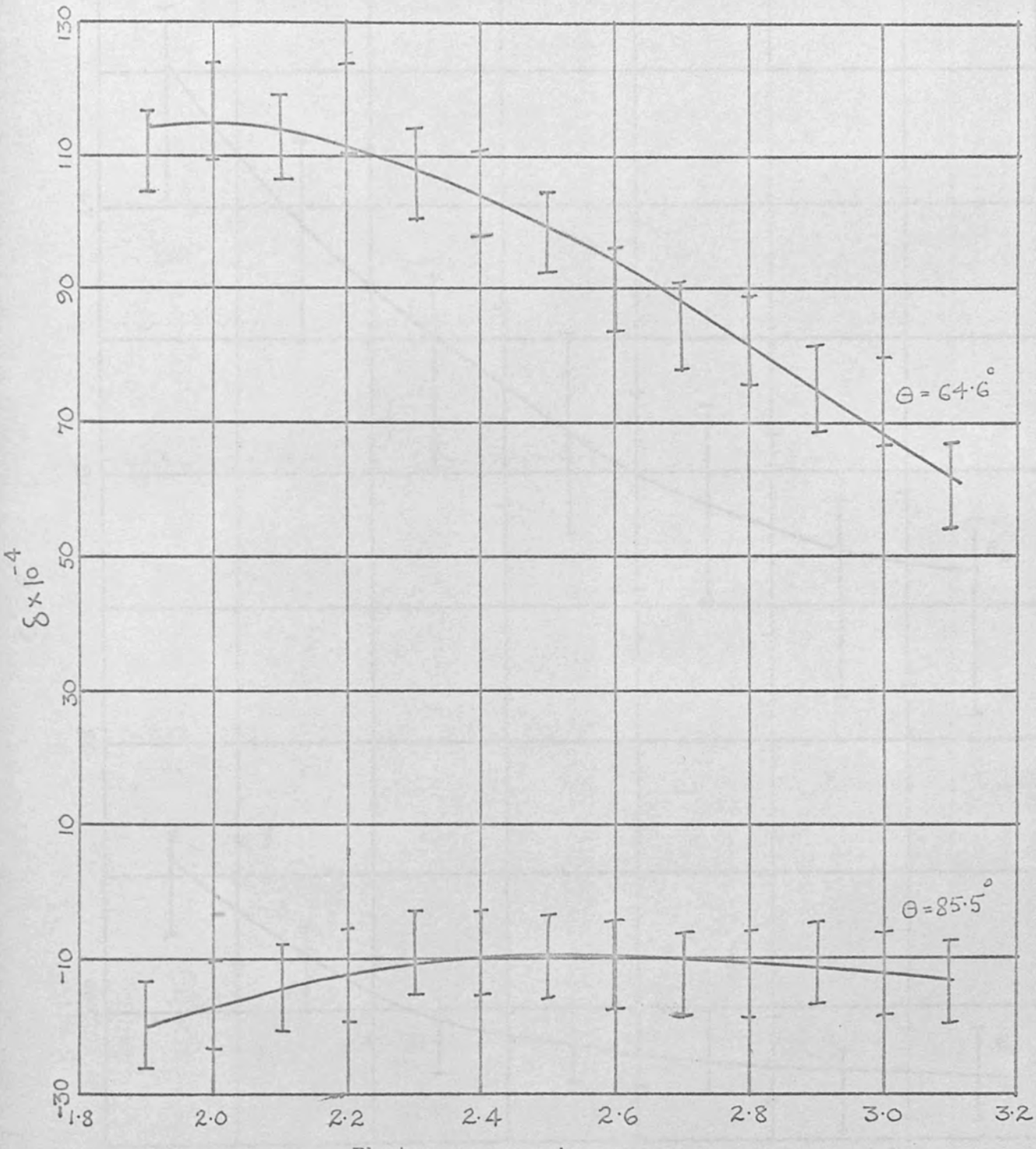

Figure 70: Variation of δ with incident energies for angles of incidence 64.6° and 85.5°.

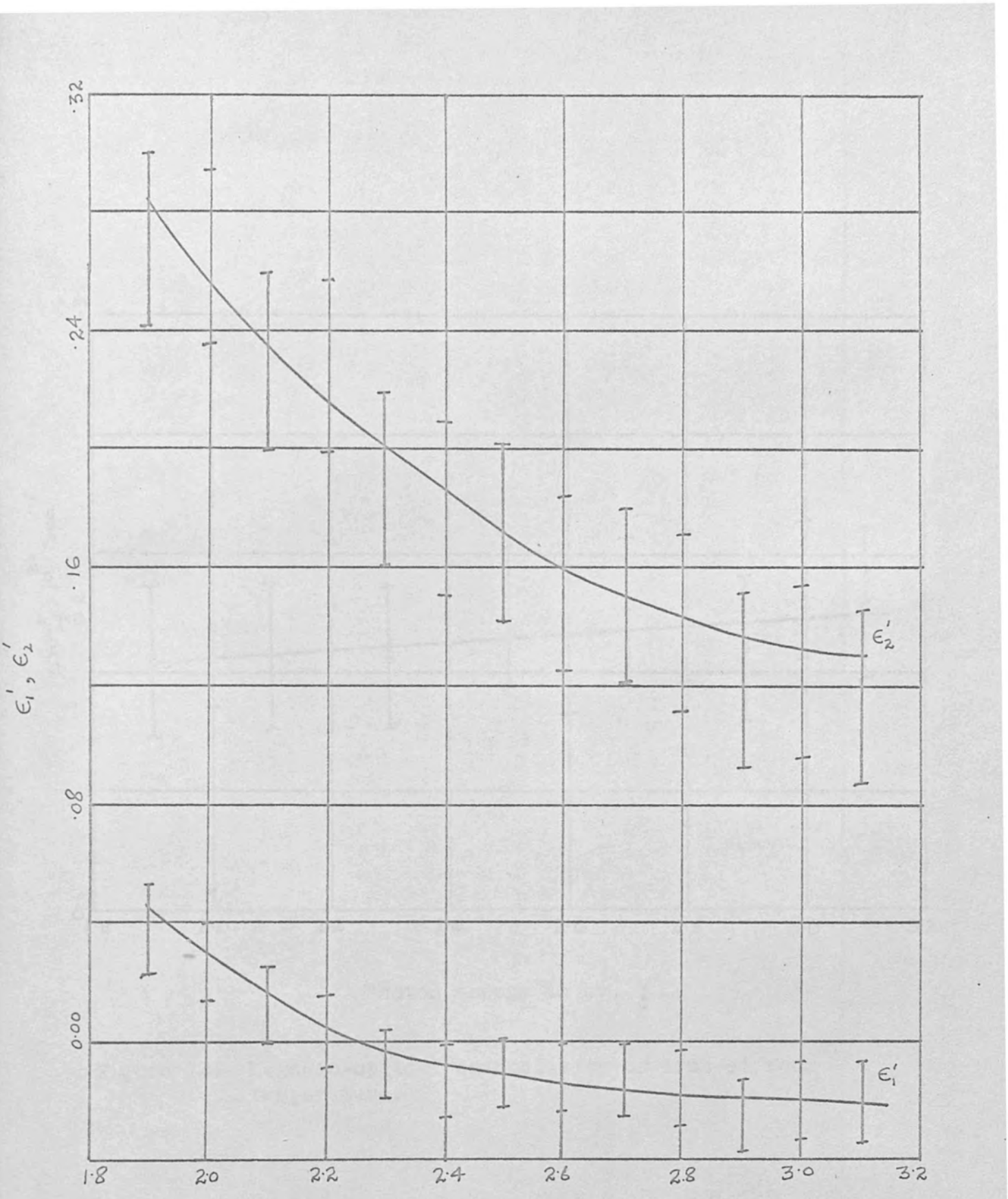

Figure 71: Magneto-optical parameters as a function of photon energy.

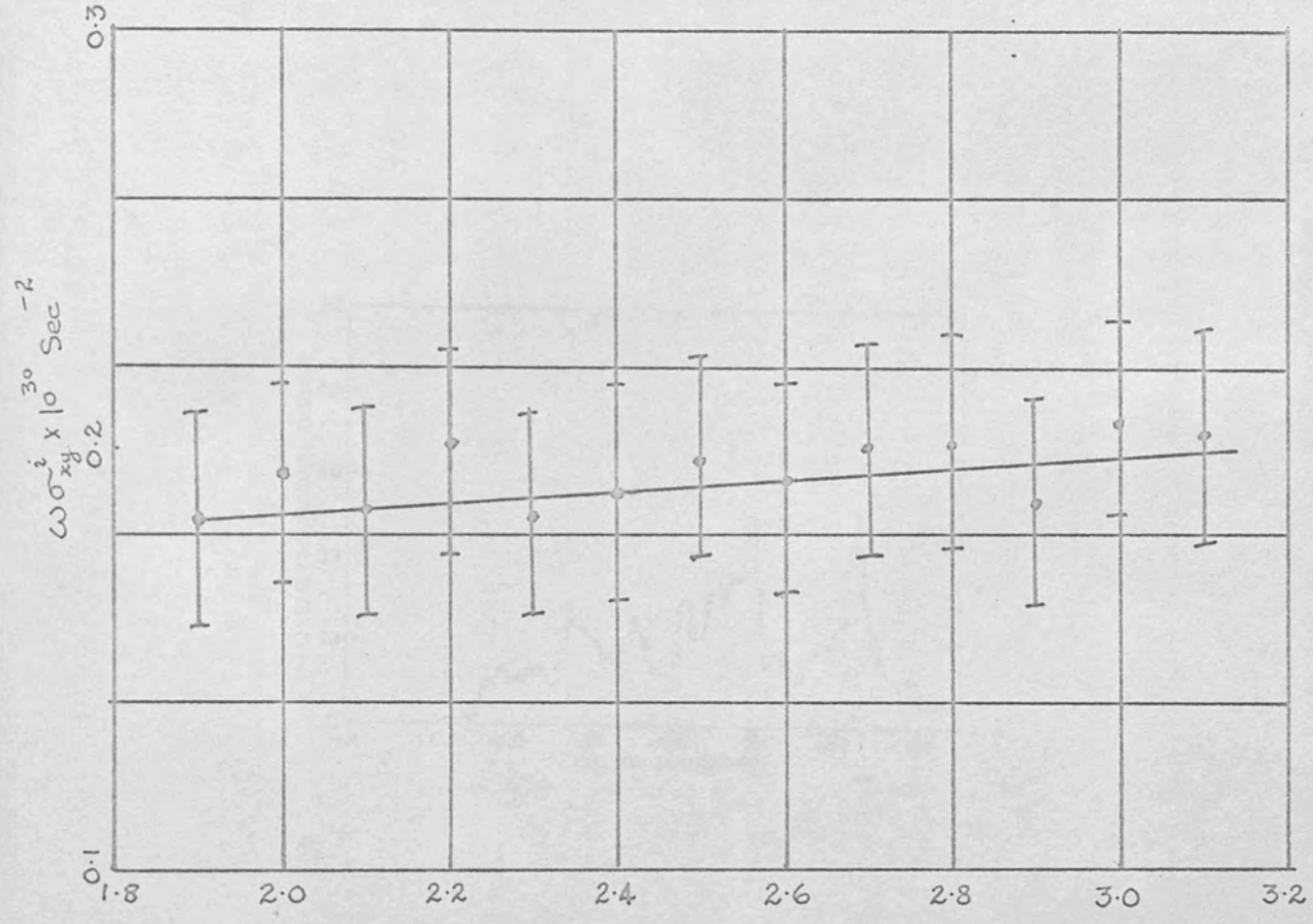

Figure 72: Magneto-optical conductivity of iron at room temperature.

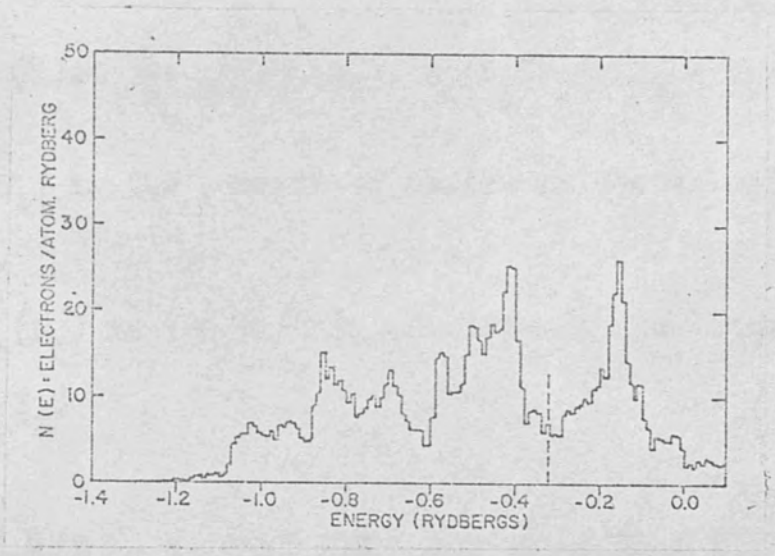

Figure 73: Total density of states for iron.

(Duff and Das, 1971).

of Duff and Das, at different energies, for comparison with $\omega\sigma_{xy}^{i}$ curve, by the following method:

The total density of states histogram was divided into strips of equal width of energy 0.02 rydberg. The approximate density of states (number of electrons/atom rydberg) for each energy associated with a strip were found, and the quantity directly proportional to the joint density of states were calculated using the summation

$$J(E) \propto \sum_{E_1=0}^{E_F} N_v(E_1) \cdot N_c(E_2) \cdot \delta(E_1 - E_2 + E)$$

where $N_v(E_1)$ is the density of states in the valence band at energy E_1.

$N_c(E_2)$ is the density of states in the conduction band at energy E_2.

and

$$\delta(E_1 - E_2 + E) = 0 \quad \text{for} \quad E_2 - E_1 \neq E$$
$$= 1 \quad \text{for} \quad E_2 - E_1 = E$$

Figure 74 shows the quantity proportional to the joint density of states calculated for some energies. We note the increase in the joint density of states with the increasing energy. This is what our experimental curve for $\omega\sigma_{xy}^{i}$ indicates.

7.6. Further Results on Iron

Figure 75 shows the optical conductivity curves for three more films. We note that all these curves show a peak at 2.5 ev

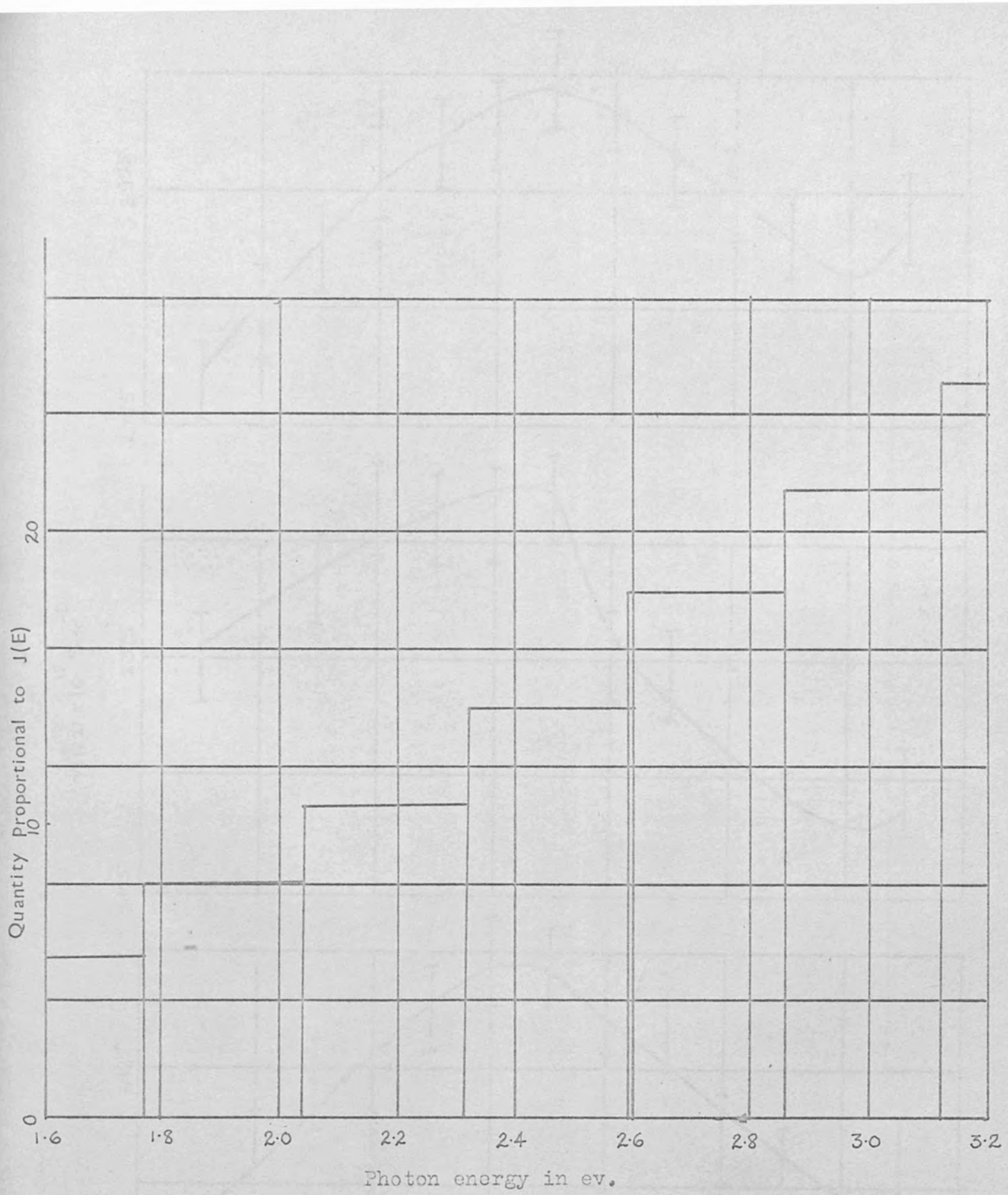

Figure 74: Joint density of states in arbitrary units for Iron.

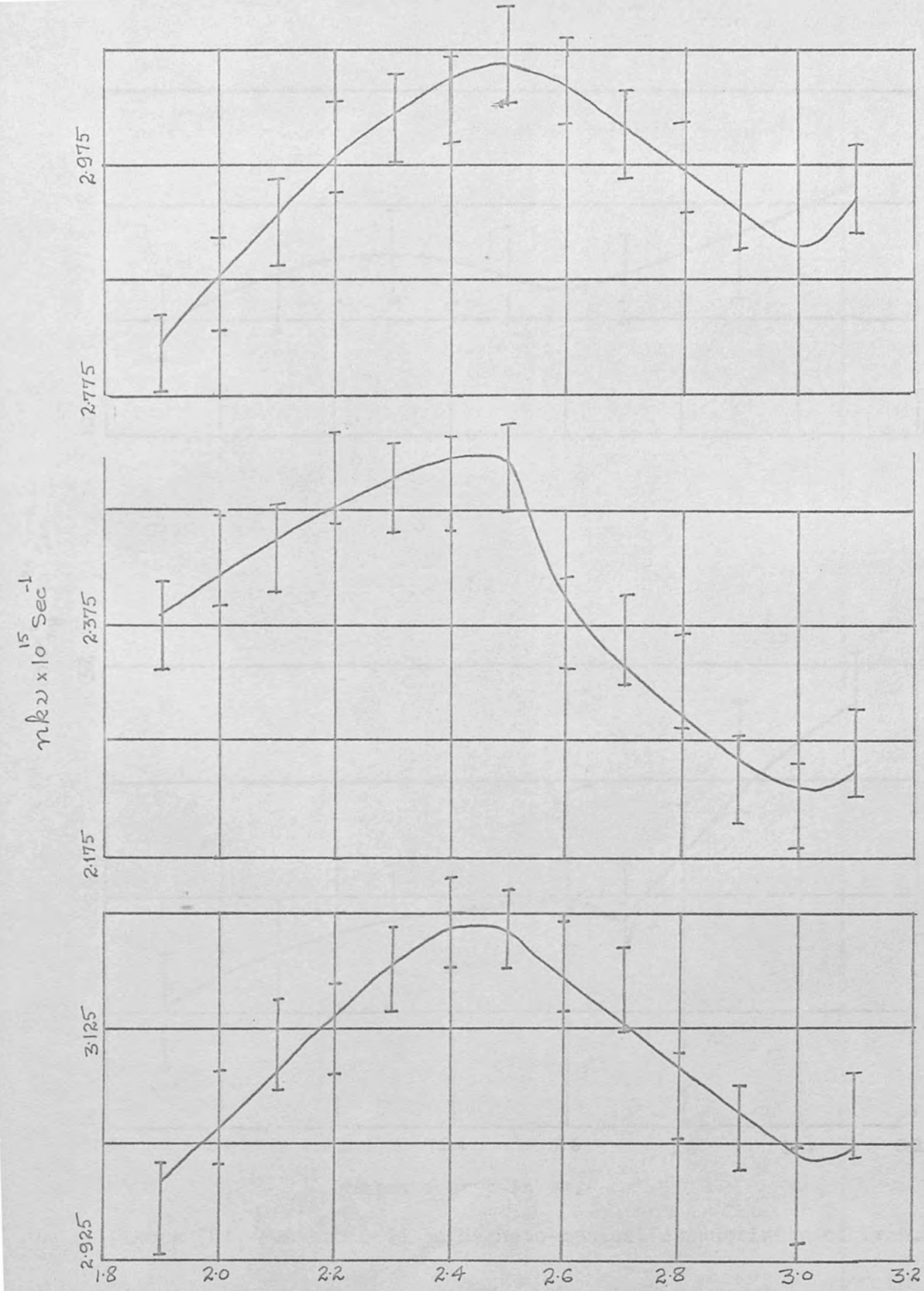

Figure 75: Further results on optical conductivity of Iron.

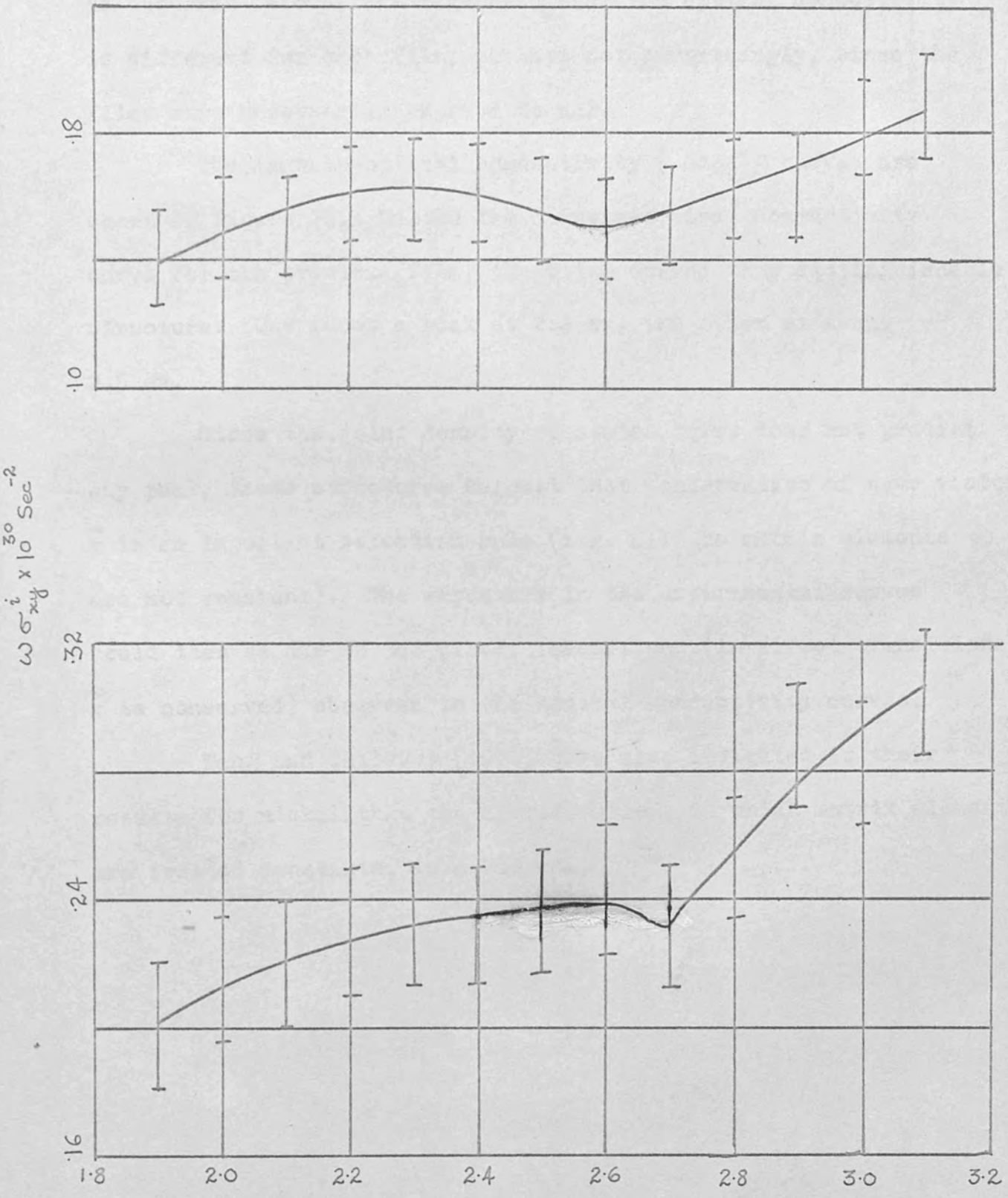

Figure 76: Further data on Magneto-optical conductivity of Iron.

as observed before. We also note that the optical conductivity is different for each film, perhaps not surprisingly, since the films were necessarily exposed to air.

The magneto-optical conductivity ($\omega\sigma_{xy}^{i}$) curves are shown in Figure 76. Unlike the magneto-optical conductivity curve for the previous film, these two curves show distinguishable structure. One shows a peak at 2.4 ev, the other at about 2.5 ev.

Since the joint density of states curve does not predict any peak, these structures suggest that conservation of wave vector $\vec{k}$ is an important selection rule (i.e. all the matrix elements are not constant). The structure in the experimental curves could then be due to the direct transitions (in direct transitions $\vec{k}$ is conserved) observed in the optical conductivity curves.

Wang and Callaway (1974) have also indicated in their results for nickel that the approximation, in which matrix elements are treated constants, is a bad one.

CHAPTER VIII

CONCLUSIONS AND SOME SUGGESTED FURTHER WORK

New methods for the determination of optical constants from reflectance measurements at two angles of incidence have been described. The existence of optimum angles of incidence for the determination of optical constants has been confirmed and their values estimated for $1 \leqslant n \leqslant 4$ and $1 \leqslant k \leqslant 4$. It has also been shown that large errors in optical constants can arise from the errors in the measured quantities if these are measured at angles well removed from optimum.

A new method for determining optical constants has been described, which does not require any incident intensity measurements. Measurements of the ratio of reflected intensities $\left(\frac{I_\perp}{I_\parallel}\right)$ at three angles of incidence are required to calculate optical constants n and k. Optimum angles of incidence have been obtained using a technique which can also yield an accurate value of the incident intensities ratio $\left(\frac{I_{o\parallel}}{I_{o\perp}}\right)$. The method could be useful for measurements on samples maintained in high vacuum, where it is often difficult to move the sample in order to get the incident beam on to the detector for incident intensity measurements, which are required for calculating reflectances or reflectance ratios.

The sensitivity of n and k to errors in (a) the measured values of change in phase Δ , (b) the arctangent of the factor by which the amplitude ratio changes Ψ , and (c) the angle of incidence θ , has been investigated and optimum angles of incidence have been found for $1 \leqslant n \leqslant 4$ and $1 \leqslant k \leqslant 4$.

A technique for obtaining optical constants n and k for thin absorbing films from reflectance ratios has been described, which can yield n and k in less time than the method of Miller and Taylor.

The sensitivity of the magneto-optical parameters Q_1 and Q_2 to errors in the measured values of complex refractive index, change in reflected light intensity, and angle of incidence has been investigated. The optimum angles of incidence have been determined for the range of magneto-optical parameter values typical of ferromagnetic materials in the visible and ultra-violet region of spectrum. It has been shown that measurements, if made at other angles, may produce large inherent errors in the determined values of magneto-optical parameters.

In order to investigate the optical and magneto-optical properties of opaque films, a simple, efficient and accurate reflectometer was constructed to allow the reflectance ratio ($\frac{R_\perp}{R_\parallel}$) method to be used to determineoptical constants. This reflectometer, with a slight modification could be used to yield data analysable by various non-polarimetric methods.

The preparation of films by thermal evaporation in different vacuum systems has been described.

The optical constants of heavy rare earth metals Gd, Tb, Dy and Ho, in the visible part of the spectrum, have been measured in air and compared with results obtained by other workers, for Gd and Tb. The values of optical constants found by other workers are not generally in good agreement with each other. In the present work, structure in the optical conductivity curves has been found to be in good agreement with that observed by Miller, Julien and Taylor. New structure in the optical conductivity of Dy has been observed. The structures in the optical conductivity curves of Gd, Tb and Dy have been accounted for fairly well using theoretical electronic band structure calculations for these metals on the basis of the simple model of Miller, Julien and Taylor. The good agreement of simple theory and experimental results lends credibility to the energy band structure calculations used in the model. Observations were carried out on Ho films and these measurements represent the first published data on Ho. Since no detailed band structure calculations on Ho were available at the time of writing this thesis, a comparison of the optical conductivity curve has been made with the optical conductivity curve of Dy. The results show similar structure.

The effect of ageing on some of the rare earth metal films has been studied. It was found that optical conductivity decreases with increasing exposure time in air. It was also found that peaks became less pronounced and some of these disappeared if the film was left for a long time in air before measurement.

These results have been explained on the basis of a theoretical model, which assumes the formation of a dielectric layer, the thickness of which was found to increase non-linearly with increasing exposure time. This work on the ageing of rare earth films suggests further work to be done, which is mentioned below:-

i) Confirmation of the formation of layer

This could be done by growing a thick film in U.H.V. on a prism and measuring reflectances in air from the glass and air side at one angle of incidence at different time intervals. A comparison of optical conductivities from the two sides should confirm the formation of a layer, though this technique might not provide all the peaks in optical conductivity curve, obtained in the present work. This is because a one-angle method is not as sensitive as the reflectance ratio method, which requires measurements at two angles of incidence, and hence growth of films under identical conditions on two prisms with different base angles.

ii) Variation of thickness of dielectric layer with increasing exposure time

As mentioned above, the thickness of the dielectric surface layer increases non-linearly with increasing exposure time. A graph of log thickness against exposure time indicated a non-exponential behaviour. The growth mechanisms involved in surface layers could be investigated by examining the time dependence of dielectric film thickness.

iii) Constituents in the dielectric layer

Chemical analysis of the surface layers is desirable. Information about likely constituents could be obtained by optical measurements before and after exposure to various atmospheric gases (e.g. H_2, N_2, O_2 etc.) on different samples maintained in high vacuum.

Additional work on the optical and magneto-optical properties of iron was carried out. The results experimentally observed in air have been described. A peak in the optical conductivity curve has been observed, which has not been reported before. The existence of this peak has been explained in terms of electronic band structure. Some magneto-optical results confirmed this peak.

Further extensions of this work are desirable. Optical measurements on Dy, Ho and Fe in U.H.V. are required to confirm the optical structures in the pure form of these metals. Further work in the infra-red region should lead to new information about intraband transitions. In view of the observed structure, studies with higher energy resolution should prove profitable. Low temperature measurements may be useful for information on the magnetic properties of rare earth metals. Magneto-optical measurements on rare earth metals may be useful to confirm some of the structures obtained in optical conductivity curves. An important future step to be taken is to perform experiments with high energy resolutions on single crystals of the rare-earth

metals which should provide a better experimental check on the band structure calculations, and should permit one to assign individual transitions to structure in the optical conductivity curve. Throughout this work there has been a deficiency of information on the structure of the films. The problems related to electron-optical surface studies are formidable. For example, the studies must usually be carried out in reflection and resulting diffraction patterns are of poor visibility. In recent years several new techniques of surface study have been developed: e.g. low energy electron diffraction (L.E.E.D.), which allows the first few layers of a surface to be studied. Using the diffraction pattern obtained from appropriately scattered electrons incident normally on the surface, one should obtain detailed information on the metal or dielectric surfaces. Almost all the other work on optical constants of rare-earth metals also suffers from this dearth of information on the surface structure.

REFERENCES

Archer, R.J., "Manual on Ellipsometry", Gaertner Scientific Corporation, Chicago, (1968).

Bennett, H.E. and Porteus, J.O., J. Opt. Soc. Am., 51, 123, (1961).

Berreman, D.W., J. Opt. Soc. A., 60, 499, (1970).

Bode, H.W., "Network Analysis and Feedback Amplifier Design", N.Y. Van Nostrand, (1945).

Calloway, J., "Energy Band Theory", Academic, New York, (1964).

Chopra, K.L., "Thin Film Phenonmenon", McGraw Hill Book Co., (1969)

Dimmock J.O., and Freeman, A.J., Phys Rev. Letters, 14, 1066, (1964).

Ditchburn, R.W.J., Opt. Soc. Am., 45, 743, (1955).

Duff, K.J. and Das, T.P., Phy. Rev, B3, 192, (1971).

E.M.I. Ltd., "EMI Photomultiplier Handbook", (1968).

Erskine, J.L., Blake, C.A., and Flaten C.J., J. Opt. Soc. Am., 64, 1332, (1974).

Erskine, J.L. and Stern, E.A., Phys. Rev., B8, 1239, (1973).

Ferguson, P.E., Romagnoli, R.J., J. App. Phys, 40, 1236, (1969).

Francombe, M.H. "The use of Thin Films in Physical Investigations", Ed. J.C. Anderson, Academic Press, London, (1966).

Greenwood, D.A., Proc. Phys. Soc., A71, 585, (1958).

Gasgnier, M., Chys, J., Schiffmacher, G., Henry La Blanchetais, Ch., Caro, P.E., Boulesteix, C., Loier, Ch. and Pardo B.J. Less-Common Metals, 34, 131, (1974).

Hadley, L.N. and Dennison, D.M., J. Opt. Soc. Am., 37, 451, (1947).

Harrison, W.A., "Solid State Theory", McGraw Hill Book Co., (1970)

Heavens, O.S., "Optical Properties of Thin Solid Films", Butterworth Scientific Publications, (1955).

Herman, F., Kortum, R.L., Kuglin, C.D. and Short, R.A., "Quantum Theory of Atoms, Molecules and Solid State" Ed. P. Lowdin, Academic Press, N.Y. (1967).

Hodgson, J.N. and Cleyet, B., J. of Phys. C, 2, 97, (1969).

Holland, L., "Vacuum Deposition of Thin Films", Chapmann and Hall Ltd., (1966).

Humphreys- Owen, S.P.F., Proc. Phys. Soc., 77, 949, (1961).

Jackson, C., Phys. Rev., 178, 949, (1969).

Julien, L.S., Ph.D. Thesis, London Univ., (1973).

Keeton, S.C. and Loucks T., Phys. Rev., 168, 672, (1968).

Kittel, C. "Quantum Theory of Solids", John Wiley and Sons, Inc., (1963).

Knyazev, Yu. V., Fiz. Met. Metall., 30, 214 (1970),

Knyazev, Yu. V., Fiz. Met. Metall, 31, 1099 (1971).

Knyazev, Yu. V., Fiz. Met. Metall, 32, 1189 (1971).

Krinchik, C.S., (a)Fiz. Met. Metalloved. 7, 181, (1959)

Krinchik, C.S., (b)Fiz. Met. Metalloved, 7, 460, (1959).

Krinchik, G.S., and Chetkin, M.V., Sov. Phys. JETP, 36, 1368, (1959).

Krinchik, G.S., and Artemev, V.A., Sov. Phy. JETP, 1080, (1968).

Kubo, R., J. Phy. Soc. Japan, 12, 570, (1957).

Loucks, T.L., "Augmented Plane Wave Method", W.A. Benjamin Ltd. (1967).

Loucks, T.L., Phys. Rev., A139, 1333, (1965).

Martin, D.H., Neal, K.F. and Dean, T.J., Proc. Phys. Soc., 86, 605, (1965).

Meyer, C., Zeitschift Fur Physik, 168, 169, (1962).

Miller, R.F., Taylor, A.J. and Julien, L.S. J. Phys. D, 3, 1957, (1970)

Miller, R.F., Julien, L.S. and Taylor, A.J., J. Phys. D. 4, 1100, (1971).

Miller, R.F. and Taylor, A.J., J. Phys. D., 4, 1419, (1971).

Miller, R.F., Julien, L.S. and Taylor, A.J. J. Phys. D., 5, 2288, (1972).

Miller, R.F., Julien, L.S. and Taylor, A.J., J. Phys. F, 4, 2338 (1974).

Petrakian, J.P., J. Opt. Soc. Am., 62, 401 (1972).

Pincherle, L., "Electronic Energy Bands in Solids", Macdonald and Co. Ltd., (1971).

Portigal, D.L., Appl. Opt., 8, 838, (1969).

Querry, M.R., J. Opt. Soc. Am., 59, 876, (1969).

Rose, M.E., "Relativistic Electron Theory", John Wiley and Sons Inc., N.Y., (1961).

Rowell, R.L., Levit, A.B. and Aval, G.M., Appl. Opt. 8, 1734, (1969).

Schuler, C. "Optical Properties and Electronic Structure of Metals and Alloys", Ed. F. Abèlès North Holland, Amsterdam, (1966).

Slater, J.C., Phys. Rev., 51, 846, (1937).

Slater, J.C., "Quantum Theory of Molecules and Solids", McGraw Hill Book Co., N.Y., (1965).

Sokolov, A.V., "Optical Properties of Metals", Blackie and Son Ltd., London, (1967)

Soven, P. Phys. Rev., A137, 1706, (1965).

Taylor, A.J., Ph.D. Thesis, London Univ., (1972).

Tolansky, S., "Multiple Beam Interferometry of Surface and Films" Dover, (1970).

Wang C.S. and Callaway, J., Phys. Rev., B9, 4897 (1974).

ACKNOWLEDGEMENTS

I greatly acknowledge the help of my supervisor, Dr. R.F. Miller, who has given much encouragement and has provided me with many things to think about throughout this work.

My thanks are also due to my colleagues, in particular to Dr. L.S. Julien, Mr. N. Chandler and Mr. R.B. Inwood, who all have, at various times, been co-users of the U.H.V. equipment. Some of the films for measurements were produced by them. Dr. L.S. Julien also deserves sincere thanks for some helpful discussions.

I also wish to thank all the technical staff at Royal Holloway College for their help. In particular, I wish to thank Mr. G. Hayward, Mr. M. Thyer and Mr. R. May.

Mr. G. Hayward has produced some of the diagrams and Mrs. S. Hayward has typed this thesis and they both deserve sincere thanks. My thanks are also due to Miss L.C. Winfield-Chislett, who has helped me in drawing some of the diagrams.

Finally, I wish to thank British Council and Royal Holloway College for financial assistance.

Appendix I

```
PROGRAM DAT(INPUT,OUTPUT)
COMPLEX CR1,CR2,CR3,CTHETA1,CTHETA2,CTHETA3,RE12,RA12,TE12,TA12
1,RE23,RA23,TE21,TA21,Z1,Z2,Z3,Z4,ARPE,ARPA
1,ARPE1,ARPA1,ARPE2,ARPA2
1,CR01
1,ATPE,ATPA
COMMON/A1/CTHETA1,CTHETA2,CTHETA3,RAT,CR1,CR3
READ 1,T1,T2
FORMAT(2F5.2)
PRINT 6,T1,T2
FORMAT(15X,*THETA1=  *,F5.2,5X,*THETA2=  *,F5.2)
PRINT 4
FORMAT(8X,*EV*,5X,*RHO1*,5X,*RHO2*,5X,*N*,5X,*K*,5X,*CON*,5X,*DN1*
7,5X,*DK1*,5X,*CON0*,5X,*RHO3 *,5X,*RHO4 *,5X,*T*)
CI=3.14159/180.
THETA1=T1*CI
THETA2=T2*CI
DO 8 I=1,20
READ 2,EV,RHO1,RHO2
FORMAT(F4.2,2F4.3)
PHO1=1./RHO1
PHO2=1./RHO2
CALL ANGLI(THETA1,THETA2,PHO1,PHO2,RR,RI)
D=1.60207/5.6252
CON=RR*RI*D*EV
AL=12406.36/EV
DO 8 N=1,6
T=10.*FLOAT(N)-10.
RAT=T/ALL
CR1=CMPLX(1.000,-0.000)
CR2=CMPLX(RR,-0.500)
CR3=CMPLX(RR,-RI)
CALL REFLET(T1,CR2,ARPE1,ARPA1)
RPE1=AMSQ(ARPE1)
RPA1=AMSQ(ARPA1)
RHO3=RPE1/RPA1
CALL REFLET(T2,CR2,ARPE2,ARPA2)
RPE2=AMSQ(ARPE2)
RPA2=AMSQ(ARPA2)
PHO4=RPE2/RPA2
CALL ANGLI(THETA1,THETA2,RHO3,RHO4,AN,AK)
CON0=AN*AK*D*EV
A=0.005*RHO3
B=0.005*RHO4
PHO5=RHO3-A
PHO6=RHO4+B
CALL ANGLI(THETA1,THETA2,RHO5,RHO6,BN,BK)
CON2=BN*BK*D*EV
DC2=ABS(CON2-CON0)
PHO3=1./RHO3
PHO4=1./RHO4
PRINT 3,EV,RHO1,RHO2,RR,RI,CON,AN,AK,CON0,PHO3,PHO4,T
FORMAT(8X,F4.2,8F8.3,2F8.3,F10.1)
CONTINUE
CONTINUE
STOP
END
```

```
      SUBROUTINE ANGL(THETA1,THETA2,RHO1,RHO2,RR,RI)
      TEST=1.0E+07
       STEP=.01
      RPA1=0.0000000
      RHO=-1.00000
      STEP=STEP*.1
   10 CONTINUE
      IF(TEST.LE..001) GO TO 40
      RPA1=RPA1+STEP
       IF(RPA1.GT.1.) GO TO 50
      RPE1=RPA1*RHO1
      CALL SOLVE(RPE1,RPA1,THETA1,RR,RI)
      IF(RP.EQ.-2.) GO TO 70
      CALL CHECK(THETA2,RPE,RPA,RR,RI)
      RHO=RPE/RPA
      A1=ABS(RHO2-RHO)
      IF(A1.LT.TEST) GO TO 20
      GO TO 30
   20 TEST=A1
      GO TO 10
   30 RPA1=RPA1-2.0*STEP
      RPE1=RPA1*RHO1
      CALL SOLVE(RPE1,RPA1,THETA1,RR,RI)
      CALL CHECK(THETA2,RPE,RPA,RR,RI)
      RHO=RPE/RPA
      TEST=ABS(RHO2-RHO)
      STEP=.1*STEP
      GO TO 10
   40 CONTINUE
      GO TO 60
   50 PRINT 250
  250 FORMAT(1X,'REFLECTION COEFF. OUT OF RANGE')
   60 CONTINUE
      GO TO 80
   70 IF(TEST.EQ.1.0E+07) GO TO 10
      GO TO 30
   80 CONTINUE
      RETURN
      END


      SUBROUTINE REFLET(THETA,CR2,ARPE,ARPA)
      COMPLEX CR1,CR2,CR3,CTHETA1,CTHETA2,CTHETA3,RE12,RA12,RE23,RA23
     1,TE12,TA12,TE21,TA21,ARPE,ARPA,ARY
      COMMON/A1/CTHETA1,CTHETA2,CTHETA3,RAT,CR1,CR3/A2/RE12,RA12,
     1RE23,RA23,TE12,TA12,TE21,TA21
      CALL COSES(THETA,CR2)
      CALL RAMPCO(CR1,CR2,CTHETA1,CTHETA2,RE12,RA12)
      CALL RAMPCO(CR2,CR3,CTHETA2,CTHETA3,RE23,RA23)
      CALL TAMPCO(CR1,CR2,CTHETA1,CTHETA2,TE12,TA12)
      CALL TAMPCO(CR2,CR1,CTHETA2,CTHETA1,TE21,TA21)
      ARPE=ARY(RE12,RE23,TE12,TE21,RAT,CR2,CTHETA2)
      ARPA=ARY(RA12,RA23,TA12,TA21,RAT,CR2,CTHETA2)
      RETURN
      END
```

```
      SUBROUTINE CHECK(THETA,RPE,RPA,RR,RI)
      APA=RR*RR-RI*RI-SIN(THETA)*SIN(THETA)
      REA=RR*RR*RI*RI
      DISC=SQRT(APA*APA+4.*REA)
      Q=SQRT((APA+DISC)/2.)
      P=SQRT((-APA+DISC)/2.)
      PSQ=P*P
      A1=Q-COS(THETA)
      A2=Q+COS(THETA)
      RPE=(A1*A1+PSQ)/(A2*A2+PSQ)
      B1=SIN(THETA)*SIN(THETA)/COS(THETA)
      A1=Q-B1
      A2=Q+B1
      RPA=(A1*A1+PSQ)/(A2*A2+PSQ)
      RPA=RPA*RPE
      RETURN
      END
```

```
      SUBROUTINE COSES(THETA,CR2)
      COMPLEX CR1,CR2,CR3,CTHETA1,CTHETA2,CTHETA3,CROT,Z1,Z2,Z3,Z4
      COMMON/A1/CTHETA1,CTHETA2,CTHETA3,RAT,CR1,CR3
      THETA IS THE ANGLE OF INCIDENCE IN DEGREES
    1 FORMAT(50X,*TEST COSES*,2F10.3)
      PHI=THETA*3.14159/180.
      CTHETA1=COS(PHI)
      Z4=1.-CTHETA1*CTHETA1
      Z1=CROT(Z4)
      Z2=CR1*Z1/CR2
      Z4=1.-Z2*Z2
      CTHETA2=CROT(Z4)
      Z3=CR2*Z2/CR3
      Z4=1.-Z3*Z3
      CTHETA3=CROT(Z4)
      RETURN
      END
```

```
      SUBROUTINE TAMPCO(A,B,C,D,E,F)
      COMPLEX CR1,CR2,CTHETA1,CTHETA2,ATPE,ATPA,Z1,Z2,Z3
     1,A,B,C,D,E,F
     THIS ROUTINE CALCULATES AMPLITUDE TRANSMISSION COEFFICIENTS FOR
      INPUT PARAMETERS AS DESCRIBED IN RAMPCO
PERPENDICULAR COMPONENT
      CR1=A
      CR2=B
      CTHETA1=C
      CTHETA2=D
      Z1=2.*CR1*CTHETA1
      Z2=CR1*CTHETA1+CR2*CTHETA2
      ATPE=Z1/Z2
      PARALLEL COMPONENT
      Z2=CR1*CTHETA2+CR2*CTHETA1
      ATPA=Z1/Z2
      E=ATPE
      F=ATPA
      RETURN
      END
```

```
      SUBROUTINE RAMPCO(A,B,C,D,E,F)
      COMPLEX CR1,CR2,CTHETA1,CTHETA2,Z1,Z2,Z3,ARPE,ARPA
     1,A,B,C,D,E,F
      CR1=A
      CR2=B
      CTHETA1=C
      CTHETA2=D
    PERPENDICULAR COMPONENT
      Z1=CTHETA2
      Z2=CR1*CTHETA1-CR2*Z1
      Z3=CR1*CTHETA1+CR2*Z1
      ARPE=Z2/Z3
       PARRALLEL COMPONENT
      Z2=CR1*Z1-CR2*CTHETA1
      Z3=CR1*Z1+CR2*CTHETA1
      ARPA=Z2/Z3
      E=ARPE
      F=ARPA
      RETURN
      END



      SUBROUTINE SOLVE(RPE,RPA,THETA,RR,RI)
    9 FORMAT(10X,5HCHECK)
      A1=RPE+1.
      A2=RPE-1.
      E=A1/A2
      A1=RPA+1.
      A2=RPA-1.
      G=A1/A2
      B1=E-G
      C1=2.*THETA
      B2=1./(TAN(C1))
      B3=E*G
      B4=1.-E*E
      B5=COS(THETA)*COS(THETA)
      A1=B1*SIN(THETA)*B2
      A2=B3+B4*B5-1.
      Q=A1/A2
      PS0=-Q*Q-2.*E*Q*COS(THETA)-B5
    TEST FOR NEGATIVE P SQUARED
      IF(PS0) 2,1,1
    1 P=SQRT(PS0)
      D1=2.*Q-PS0+SIN(THETA)*SIN(THETA)
      D2=2.*P*Q*Q
      DISC=SQRT(D1*D1+4.*D2)
      RR=SQRT((D1+DISC)/2.)
      RI=SQRT((-D1+DISC)/2.)
      GO TO 3
    2 RI=-2.
      RR=-2.
    3 RETURN
      END
```

```
      FUNCTION AMSO(Z)
      COMPLEX Z
      COCO=REAL(Z)*REAL(Z)+AIMAG(Z)*AIMAG(Z)
      AMSO=COCO
      RETURN
      END
```

```
      COMPLEX FUNCTION ARY(RAB,RBC,TAB,TBA,RAT,CR2,CTHETA2)
      COMPLEX RAB,RBC,TAB,TBA,CR2,CTHETA2,Z1,Z2,Z3,R
    1 FORMAT(40X,*TEST ARY*,F10.3)
    2 FORMAT(30X,*TEST2 ARY*,2F10.3)
      Z2=CMPLX(0.0,1.0)
      Z1=2.*3.14159*RAT*CR2*CTHETA2
      Z3=Z1*Z2
      Z3=-2.*Z3
      Z3=CEXP(Z3)
      Z1=TAB*TBA*RBC*Z3/(1.+RAB*RBC*Z3)
      R=RAB+Z1
      A1=AMSO(R)
      ARY=R
      RETURN
      END
```

```
      COMPLEX FUNCTION CROT(Z)
      COMPLEX Z
    1 FORMAT(1H1,10X,*TEST CROT*)
    2 FORMAT(10X,F10.4)
    3 FORMAT(20X,2F10.4)
      A1=REAL(Z)
      A2=AIMAG(Z)
      PHI=ATAN2(A2,A1)
      PHI=PHI/2.
      AMP=SQRT(A1*A1+A2*A2)
      A1=SQRT(AMP)
      B1=A1*COS(PHI)
      B2=A1*SIN(PHI)
      CROT=CMPLX(B1,B2)
      RETURN
      END
```

J. Phys. D: Appl. Phys., Vol. 7, 1974. Printed in Great Britain.

A general procedure for evaluating optical constants from functions of reflectance at two angles of incidence

R F Miller, W Hasan and L S Julien
Department of Physics, Royal Holloway College, University of London, Egham Hill, Egham, Surrey, TW20 0EX

Received 12 November 1973

Abstract. A general computational technique is described for deriving optical constants from observable functions of reflectances measured at two angles of incidence. The method is applied to the cases where reflectance is measured for light linearly polarized at azimuthal angles $\phi=\pi/4$ (equivalent here to unpolarized light), $\phi=0$ and $\phi=\pi/2$. Optimization procedures are used to show that the last case is relatively insensitive and optimum conditions are derived for the two other cases, for the range $1{\cdot}0\leqslant n\leqslant 4{\cdot}0$, $1{\cdot}0\leqslant k\leqslant 4{\cdot}0$. A table is presented which allows the accuracies of several optimized methods to be compared directly, over the range $1{\cdot}0\leqslant n\leqslant 4{\cdot}0$, $1{\cdot}0\leqslant k\leqslant 4{\cdot}0$.

1. Introduction

The refractive index n and the extinction coefficient k of a bulk material can be conveniently obtained from measurements of reflectance at two angles of incidence θ_1 and θ_2. Existing methods of analysis (Avery 1952, Miller *et al* 1970) normally require a determination of two reflectances, $R_\perp$ and $R_\parallel$, at each angle of incidence, for light polarized respectively perpendicular and parallel to the plane of incidence. By generalizing the computational procedure developed for deriving n and k from reflectance ratio measurements (Miller *et al* 1972) we now examine the derivation of the optical constants from only one reflectance measurement at each of θ_1 and θ_2. The sensitivities, analytical procedures, and optimum angles of incidence for several experimental configurations have been investigated for useful ranges of n and k.

2. General procedure for calculating n and k from reflectances at two angles

Let us suppose for a given angle of incidence that $F(R_\perp, R_\parallel)$ is an observable function of $R_\perp$ and $R_\parallel$ such that in the linear relationship

$$R_\perp=\alpha R_\parallel+\beta \tag{1}$$

the constants α and β are derivable from $F(R_\perp, R_\parallel)$. If $F(R_\perp, R_\parallel)_1$ and $F(R_\perp, R_\parallel)_2$ are measured at θ_1 and θ_2, then n and k may be obtained by the following procedure.

At angle θ_1:

$$R_\perp=\alpha_1 R_\parallel+\beta_1. \tag{2}$$

Sets of (n, k) pairs are calculated, using the analytical solutions to the Fresnel equations (Querry 1969), such that equation (2) is satisfied, and these values are used to calculate $F(R_\perp, R_\parallel)'_2$ at θ_2. Here, and subsequently, the calculated values are indicated by a prime.

$$d=F(R_\perp, R_\parallel)'_2-F(R_\perp, R_\parallel)_2 \tag{3}$$

is then made arbitrarily small with respect to the (n, k) values generated by equation (2). In practice d will be slightly less than the precision to which $F(R_\perp, R_\parallel)$ can be measured.

The case where $F(R_\perp, R_\parallel)=R_\perp/R_\parallel$, ie $\alpha=R_\perp/R_\parallel$ and $\beta=0$, has already been discussed in detail (Miller *et al* 1972). Here we examine the more general case, where the reflectance R_ϕ for plane polarized light is measured for any fixed incident polarization azimuth ϕ with respect to the plane of incidence:

$$R_\phi=R_\parallel \cos^2\phi+R_\perp \sin^2\phi. \tag{4}$$

This gives $\alpha=-\cot^2\phi$ and $\beta=R_\phi \operatorname{cosec}^2\phi$. The procedure used to obtain n and k from $F(R_\perp, R_\parallel)=R_\perp/R_\parallel$ can be applied, with minor modifications, to the general situation described by equation (4). Although, in principle, measurements of R_ϕ at θ_1 and θ_2, for any ϕ, can be used to obtain n and k, some experimental arrangements are more convenient than others, and it is desirable to establish under what conditions such arrangements are likely to be most sensitive, ie what are the optimum values of ϕ, θ_1 and θ_2. The above computational procedure permits this to be done, and the results are described in the following sections.

If we define the actual values of the optical constants as n_0 and k_0, and the experimentally observed values as n and k, we may calculate σ, the percentage error in n_0k_0 produced by an error δR in reflectance measurement, for various combinations of θ_1 and θ_2, ϕ and n_0 and k_0:

$$\sigma=\frac{n_0k_0-nk}{n_0k_0}\times 100\%. \tag{5}$$

$(R_\phi)_1$ and $(R_\phi)_2$, at θ_1 and θ_2, are computed for the given n_0 and k_0, using the Fresnel equations. Then it is assumed that $\delta R=0{\cdot}001\ R_\phi$, and the quantities $(R_\phi)_1+\delta R$ and $(R_\phi)_2-\delta R$ are used to compute n and k.

3. Variation of σ with φ

Figure 1 shows the variation of σ with ϕ for several values of n_0, k_0, θ_1 and θ_2. In general the curves indicate an initial gradual increase in σ with ϕ, rising steeply near $\phi=90°$. The curve for $n_0=2$, $k_0=3$ (typical of metals) and $\theta_1=85°$, $\theta_2=20°$ (values typically used in the reflectance measurements, and the optimum angles for method (*a*) below) is of particular interest in relation to the following experimental situations:

(*a*) $\phi=\pi/4$, when, as for unpolarized incident light, the reflectance is

$$R=\frac{R_\perp+R_\parallel}{2} \tag{6}$$

and

$$\alpha=-1,\ \beta=2R.$$

(*b*) $\phi=0$, when $-\beta/\alpha=R_\parallel$.

(*c*) $\phi=\pi/2$, when $\beta=R_\perp$, and $\alpha=0$.

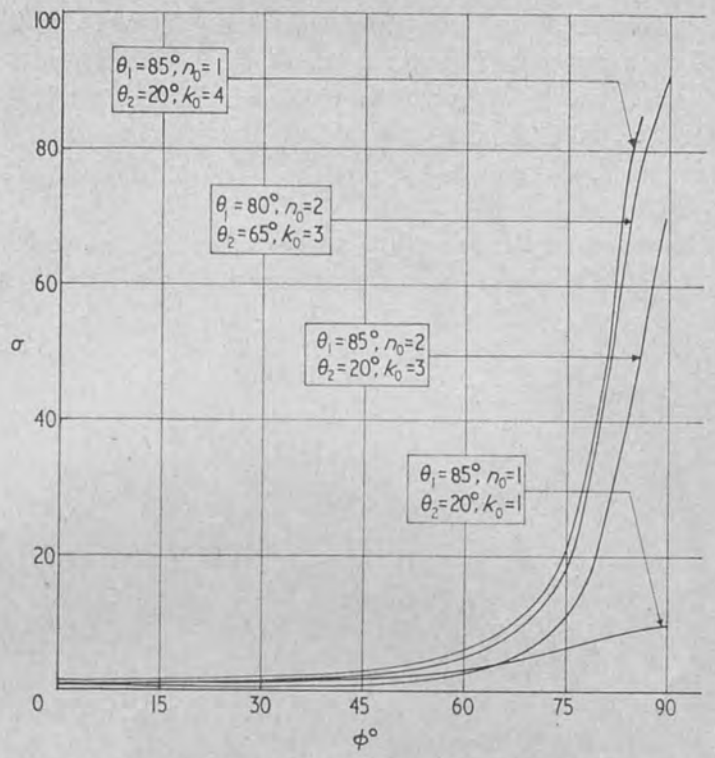

Figure 1. The variation of σ with ϕ.

Figure 1 indicates that method (*c*) (when only $R_\perp$ is being measured) is evidently liable to large errors, and is therefore not generally recommended.

Method (*b*), the measurement of $R_\parallel$, is generally the most accurate, and method (*a*), measurement of the total reflectance R of unpolarized incident light, is almost as good as (*b*) at the optimum angles. The latter method might be advantageous in spectral regions where polarization is not easily achieved, and also eliminates errors arising from inaccurate setting of the plane of polarization of the incident light.

The optimum reflection angles for the methods (*a*) and (*b*) will be considered in the following sections.

4. Measurement of total reflectance R at two angles of incidence: method (*a*)

If R_1 is the value of R for $\theta=\theta_1$, equation (6) becomes

$$R_\perp = -R_\parallel + 2R_1 \tag{7}$$

ie a straight line in $(R_\perp, R_\parallel)$ space, with gradient -1 and intercept $2R_1$ on the $R_\perp$ axis. Possible values of n and k are calculated at equispaced points on this line, using the analytical solutions to the Fresnel reflectance equations. These values of n and k are then used to generate the line

$$R_\perp = -R_\parallel + 2R_2 \tag{8}$$

for θ_2, and the calculation proceeds until $d=R'_2-R_2$ is made arbitrarily small.

The results of a computation of σ for many combinations of θ_1, θ_2, n_0 and k_0 may be summarized as follows.

(i) σ is found to be minimized by taking one angle below 45° and the other above 45°.

(ii) σ is practically independent of the lower angle, θ_2, for $2° < \theta_2 < 22°$; ie, it is determined by θ_1 for a given n_0 and k_0. Figure 2 shows how σ depends on θ_1, for $\theta_2 = 20°$ and various n_0 and k_0, for $\delta R = 0{\cdot}002\ R$. It is evident that the optimum value of θ_1 is generally about 85°. Specific optimum angles θ_1 are given in table 1, for different combinations of n_0 and k_0, at $\theta_2 = 20°$.

(iii) σ generally increases as the n_0 and k_0 values diverge from each other; figure 3 shows the variation of σ with n_0 and k_0, at the optimum angles, again for $\delta R = 0{\cdot}002\ R$.

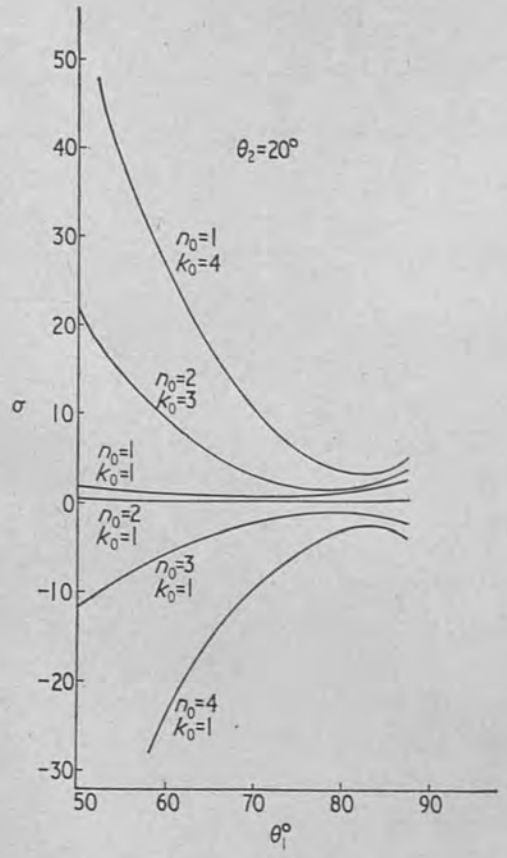

Figure 2. The variation of σ with θ_1 for $\phi = \pi/4$, at $\theta_2 = 20°$.

(iv) The errors in $(n_0 k_0)$ produced by an error of $\pm 0{\cdot}1°$ in θ_1 and θ_2 were found to be $< 3\%$, except for $n_0 = 3$, $k_0 = 1$ and $n_0 = 4$, $k_0 = 1$, where the error was between 3% and 5%.

The sensitivity of the method to changes in optical constants is indicated by figure 4, in which R_1 is plotted against R_2, with n_0 and k_0 as parameters. A similar diagram was produced by Humphreys-Owen (1961) for angles of 20° and 70°. As figure 2 indicates, $\theta_1 = 70°$ is the optimum angle only for values of n_0 and k_0 close to 1·0, and figure 4 is therefore constructed for the more generally optimized angles 85° and 20°. A typical calculation time for the method is 0·18 seconds on a CDC 6600 computer (FORTRAN IV), in the case where d is made less than 0·0001, and n and k are computed to better than 0·1%, for $n_0 = 2$, $k_0 = 3$.

If the incident light is not completely depolarized, then equation (6) does not hold, and the parallel component of incident intensity may be written

$$I_{\parallel} = \gamma I_{\perp} \tag{9}$$

Table 1

n_0	k_0	Optimum θ_1 °	Maximum σ (%) for $\delta R = 0{\cdot}002\,R$	Maximum % error in $(n_0 k_0)$ due to angular errors of $\pm 0{\cdot}1$
1·000	1·000	70–77	1	2
	2·000	75–80	2	2
	3·000	78–84	3	3
	4·000	80–85	4	4
2·000	1·000	46–88	1	1
	2·000	69–83	2	2
	3·000	77–82	2	2
	4·000	78–83	3	2
3·000	1·000	72–78	2	3
	2·000	74–84	1	1
	3·000	76–84	2	2
	4·000	81–84	2	2
4·000	1·000	77–78	5	5
	2·000	56–85	1	1
	3·000	82–83	1	1
	4·000	80–85	2	2

$\theta_2 = 20°$.

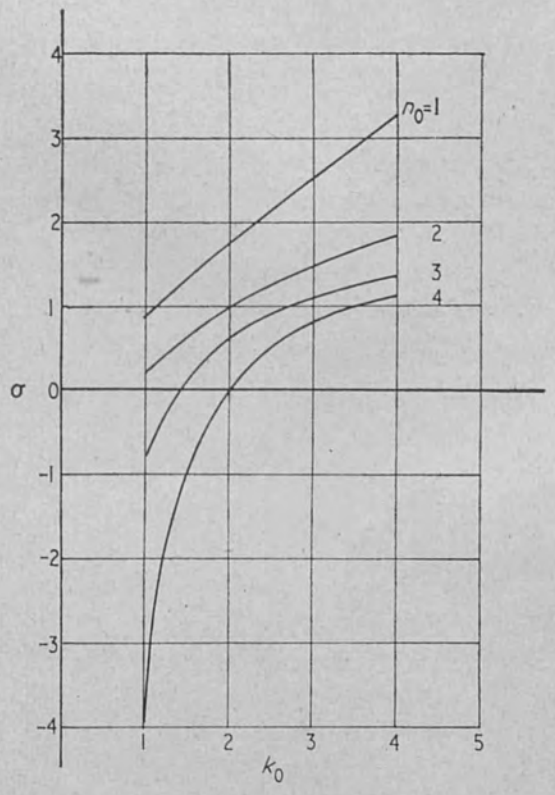

Figure 3. The variation of σ with n_0 and k_0 at the optimum angles, for $\delta R = 0{\cdot}002\,R$.

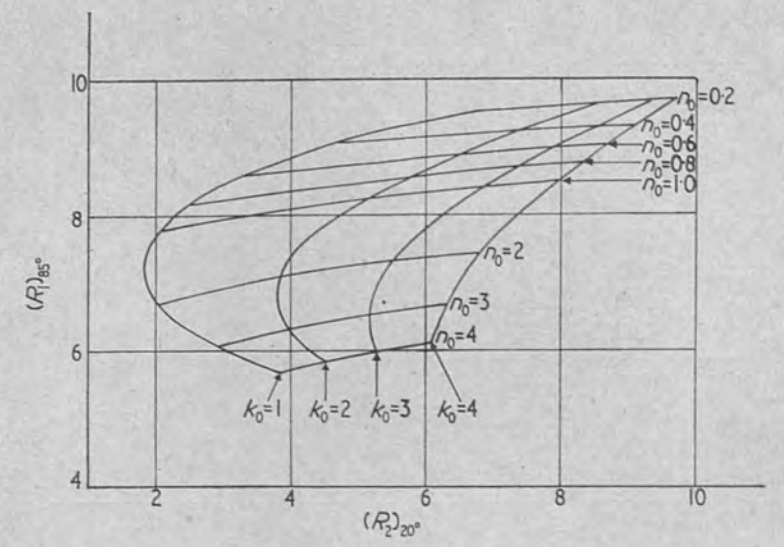

Figure 4. The sensitivity of total reflectance to n_0 and k_0 at 85° and 20°.

giving

$$R=\frac{R_\perp+\gamma R_\parallel}{1+\gamma}. \tag{10}$$

γ may be determined in a preliminary calibration experiment. Alternatively, light linearly polarized with $\phi=\pi/4$ may be used, and equation (6) then holds independently of the initial state of polarization of the light.

5. Measurement of $R_\parallel$ at two angles of incidence: method (*b*)

For a given angle θ_1, the equation

$$(R_\parallel)_1=-\beta_1/\alpha_1 \tag{11}$$

represents a straight line in $(R_\perp, R_\parallel)$ space, parallel to the $R_\perp$ axis. Possible values of n and k are calculated at equispaced points on this line as in §4 above. In this case, in order to reduce the computation time, the starting value of $R_\perp$ to be used in obtaining these points was chosen to lie at the point of intersection of equation (11) with the boundary in $(R_\perp, R_\parallel)$ space which encloses all possible solutions to the Fresnel reflectance equations (Miller *et al* 1970). The equation to this boundary is

$$aF^4+bF^3+cF^2+dF+e=0 \tag{12}$$

where

$$a=\cos^2\theta\sin^2\theta$$

$$b=-G$$

$$c=G^2+\sin^4\theta+\cos^4\theta+\cot^2 2\theta$$

$$d=-G\,(1+2\cot^2 2\theta)$$

$$e=G^2\cot^2 2\theta+\cos^2\theta\sin^2\theta$$

$$G=\frac{R_\parallel+1}{R_\parallel-1}$$

$$F=\frac{R_\perp+1}{R_\perp-1}.$$

A computer subroutine is used to solve (12) and thus obtain the smallest real value of $R_\perp$, which is then used as the starting value for a series of steps in $R_\perp$ of 0·001, for which n and k are found. These values of n and k are then used to generate lines

$$(R_\parallel)_2 = -\beta_2/\alpha_2 \tag{13}$$

in $(R_\perp, R_\parallel)$ space, for the angle θ_2, until $d=(R_\parallel)'_2-(R_\parallel)_2$ becomes $<0{\cdot}001$, the experimental error in $R_\parallel$.

Computation of σ for various values of θ_1, θ_2, n_0 and k_0 in the range $1 \leqslant n_0 \leqslant 4{\cdot}0$, $1 \leqslant k_0 \leqslant 4{\cdot}0$, θ_1 and θ_2 from 1° to 88° shows that:

(i) the optimum values of θ_1 and θ_2 are both greater than 45°;
(ii) σ is almost independent of the lower angle θ_2.

Table 2

n_0	k_0	Optimum θ_1 °	Maximum σ for $\delta R=0{\cdot}002\,R$
1·000	1·000	60–67	1
	2·000	72–76	1
	3·000	73–79	2
	4·000	81	2
2·000	1·000	58–86	1
	2·000	66–80	1
	3·000	74–81	1
	4·000	81–82	1
3·000	1·000	69–74	1
	2·000	69–85	1
	3·000	74–83	1
	4·000	79–83	1
4·000	1·000	75–76	1
	2·000	66–86	1
	3·000	76–85	1
	4·000	78–84	1

$46° \leqslant \theta_2 < 52°$.
Error in $n_0 k_0$ due to angular errors of 0·1° is $<1\%$.

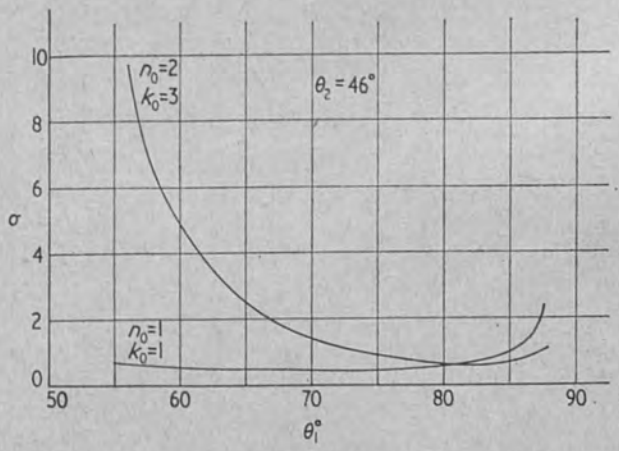

Figure 5. The variation of σ with θ_1 for $\phi=0$, at $\theta_2=46°$.

Table 3

Method		$(R_\perp, R_\parallel, \theta)$			$(R_\perp/R_\parallel, \theta_1, \theta_2)$			(R, θ_1, θ_2)			$(R_\parallel, \theta_1, \theta_2)$		
		% error in			% error in			% error in			% error in		
n_0	k_0	n_0	k_0	(n_0k_0)	n_0	k_0	(n_0k_0)	n_0	k_0	(n_0k_0)	n_0	k_0	(n_0k_0)
1·000	1·000	0·347	0·868	1·218	0·039	2·515	2·563	0·590	0·451	1·038	0·297	0·321	0·619
	2·000	0·968	1·504	2·487	0·436	0·617	1·050	1·057	0·714	1·764	0·385	0·365	0·752
	3·000	2·252	2·924	5·242	0·484	0·622	1·103	1·511	1·095	2·589	0·708	0·604	1·317
	4·000	4·054	5·644	9·927	1·257	1·187	2·429	1·904	1·464	3·340	0·955	0·841	1·804
2·000	1·000	0·252	0·747	1·000	0·116	0·130	0·246	0·676	0·383	0·296	0·133	0·045	0·178
	2·000	0·600	1·110	1·716	0·236	0·346	0·581	0·787	0·299	1·083	0·185	0·170	0·356
	3·000	1·130	2·092	3·246	0·377	0·416	0·791	0·955	0·580	1·529	0·308	0·282	0·591
	4·000	2·148	3·453	5·675	0·644	0·565	1·205	1·136	0·814	1·941	1·667	0·924	2·606
3·000	1·000	0·420	1·354	1·780	0·070	0·091	0·161	0·627	1·534	0·898	0·107	0·089	0·197
	2·000	0·793	1·108	1·910	0·183	0·164	0·347	0·714	0·014	0·728	0·188	0·134	0·322
	3·000	1·246	1·869	3·138	0·290	0·249	0·539	0·810	0·374	1·181	0·272	0·223	0·495
	4·000	1·941	3·010	5·009	0·785	0·493	1·274	0·914	0·583	1·492	0·424	0·337	0·763
4·000	1·000	0·498	9·157	9·700	0·104	0·227	0·330	0·991	4·964	3·924	0·231	0·533	0·303
	2·000	0·712	3·814	4·553	0·193	0·134	0·327	1·955	2·028	0·033	0·230	0·080	0·310
	3·000	1·143	3·175	4·353	0·305	0·210	0·514	0·747	0·212	0·957	0·292	0·192	0·484
	4·000	1·906	3·477	5·449	0·404	0·269	0·672	0·813	0·458	1·267	0·336	0·283	0·621

Table 2 shows σ for the various optimum θ_1, at $\theta_2=46°$–$52°$. In general, the minima in the curves relating σ to θ_1 are shallow, as indicated by figure 5.

Computing time is 0·02 s for $\theta_2=46°$, $n_0=2$, $k_0=3$, and for $56°<\theta_1<85°$.

6. Comparison of method sensitivities

A general comparison is not possible, since the sensitivity varies from method to method with the particular values of n_0 and k_0. It may however be useful to present the results of a calculation on the effects of 0·2% changes in intensity ratios measured at optimum angles, for the following methods:

(i) $R_\perp$ and $R_\parallel$ measured at one angle ($R_\perp$, $R_\parallel$, θ_1 method)
(ii) $R_\perp/R_\parallel$ measured at two angles ($R_\perp/R_\parallel$, θ_1, θ_2 method)
(iii) R measured at two angles (R, θ_1, θ_2 method)
(iv) $R_\parallel$ measured at two angles ($R_\parallel$, θ_1, θ_2 method)

These results are shown in table 3.

7. Conclusions

A computational procedure of general applicability has been described for deriving optical constants from observable functions of reflectance measured at two angles of incidence. The technique has been applied to the particular cases of $R_\parallel$ and R measured at two angles, and optimum angles derived for $1\leqslant n_0\leqslant 4{\cdot}0$ and $1\leqslant k_0\leqslant 4{\cdot}0$. A table has been produced, for this range of optical constants, from which the accuracies of four different reflectance methods for n and k may be compared.

Acknowledgments

We wish to acknowledge financial assistance from the Science Research Council and the British Council during the course of this work.

References

Avery D G 1952 *Proc. Phys. Soc.* B **65** 425–8
Humphreys-Owen S P F 1961 *Proc. Phys. Soc.* 77 949–57
Miller R F, Taylor A J and Julien L S 1970 *J. Phys.* D: *Appl. Phys.* **3** 1957–61
—— 1972 *J. Phys.* D: *Appl. Phys.* **5** 2288–91
Querry M R 1969 *J. Opt. Soc. Am.* **59** 876–7

corrections

In figure 3, the two boxes containing "STEP = .01" should be removed and a box containing "STEP = .01" should be included just after the box containing "TEST = 10^7".